

Silesian University of Technology
Faculty of Mechanical Engineering
Department of Fundamentals of Machinery Design

Doctoral Dissertation

Optimization method for ultralight aerial composite structures

MSc, Eng. Ramesh Kumpati

Supervisor:

PhD, DSc, Eng. Wojciech Skarka, Prof. SUT

Gliwice, 2024

Content

Contents.....	2
List of Acronyms and Symbols.....	4
List of figures.....	5
List of tables.....	8
1. Introduction.....	10
1.1. Aim and thesis.....	12
1.2. Scope of the work.....	12
1.3. Scientific problem.....	14
1.4. Author's publications.....	14
1.5. Acknowledgment.....	16
2. Literature Review.....	17
2.1 Structural optimization.....	17
2.2 Parametric (size) optimization.....	18
2.3 Geometric (shape) optimization.....	19
2.4 Topology optimization.....	20
2.5 Parametrization of constitutive mechanical properties.....	22
2.5.1. Continuous fiber angle optimization.....	22
2.5.2. Free material optimization.....	24
2.5.3. Discrete material optimization.....	25
2.6 Buckling analysis.....	28
2.6.1. Linear buckling analysis of structures.....	30
2.6.2. Non-linear analysis of structures.....	33
2.7 Natural fibers.....	33
2.8 Classical laminated plate theory.....	37
3. Methodology.....	41
3.1. Material selection.....	43
3.2. E-glass reinforcement.....	44
3.3. Type of Adhesive.....	44
3.4. Optimization procedure.....	45
3.5. Research methodology.....	45
3.6. Geometrical modelling procedure.....	46
3.7. Load and boundary strategy.....	47
3.8. Multi-objective optimization methodology by GA.....	48
3.8.1 Optimization statement.....	48
3.8.2 Optimization methodology.....	49
3.8.3 Design recommendations.....	49
3.8.4 Analysis setup.....	50
3.8.5 Fabrication of composite laminate.....	50
3.9. Sandwich structure design and analysis.....	51
3.9.1. Material design methodology.....	52
3.9.2. Design constraints.....	52
3.9.3. Stiffness terms since laminate theory.....	53

3.9.4. In-Plane Constants (Engineering).....	54
3.9.5. Extensional Stiffnesses matrix of sandwich panel.....	55
3.9.6. Bending Stiffness of sandwich structure.....	56
3.9.7. Transverse Shear Stiffness of sandwich structure.....	56
3.10. Light aircraft wing skin as a carrier for photovoltaic cells.....	57
3.11. Wing construction methodology.....	58
4. Case study_1&2.....	59
4.1. Design of composite sandwich T-joint	60
4.2. Design methodology.....	60
4.3. Structural failure of the laminate.....	62
4.4. Optimization methodology.....	63
4.5. Analytical information of composite bonded T-joints.....	64
4.6. Bio-composite validation.....	66
4.7. Highlights of case study.....	67
5. Case study_3.....	69
5.1 Design of composite wing for TS-17 UAV.....	69
5.2 Homogenization approach.....	73
5.3 Homogenization Analysis.....	74
5.4 Rule of Mixture for Composite material.....	74
5.5 Preliminary Design Methodology.....	81
5.6 FEA of UAV wing skin Stiffeners.....	81
6. Manufacturing of bio-composite and validation	85
6.1. Composite laminate fabrication strategy.....	85
6.2. Mechanical characterization of composite materials.....	89
6.3. Compression test.....	89
6.4. Tensile test.....	91
6.5. Three-point bending test.....	94
6.6. Microscopic surface assessment.....	96
7. Results.....	99
7.1. Case study_1.....	99
7.2. Case study_2.....	105
7.2.1. Sandwich structure design and analysis (approach_1)	105
7.2.2. Sandwich structure design and analysis (approach_2)	109
7.2.3. Light aircraft wing skin as a carrier for photovoltaic cells results.....	115
7.3. Case study_3.....	119
7.4. Stability analysis of composite laminate.....	130
7.5. Fiber orientation and stacking sequence.....	133
7.6. Structural optimization method.....	137
8. Summary.....	150
8.1. Conclusion.....	150
8.2. Future work.....	157
References.....	158
Abstract.....	171
Polish.....	172

List of Acronyms and Symbols

E_1	Composite ply modulus in the longitudinal direction
E_2	Composite ply module in the transverse direction
G_{ij}	Composite ply shear modulus in the i-j plane
ν_{12}	Composite ply Poisson's ratio in the 1-2 plane
X_t	Tensile strength in the fiber direction
X_c	Compressive strength in the fiber direction
Y_t	Tensile strength in the fiber transverse direction
Y_c	Compressive strength in the fiber transverse direction
σ_1, σ_2	Composite ply stress in the 1 or 2- direction
τ_{12}	Composite ply shear stress in the 1-2 direction
$\varepsilon_1, \varepsilon_2$	Composite ply strain in the 1-2 direction
γ_{12}	Composite ply shear strain in the 1-2 direction
CFAO	Continuous Fiber Angle Optimization
FMO	Free Material Optimization
DMO	Discrete Material Optimization
FEA	Finite Element Analysis
RTM	Resin Transfer Moulding
ASTM	American Society for Testing and Materials
FEM	Finite Element Model
FMLS	Fiber Metal Laminates
CFRP	Carbon Fiber Reinforced Composites
UAV	Unmanned Arial Vehicle
GA	Genetic Algorithm
PVC	Polyvinyl chloride
CAD	Computer-aided design
UD	Unidirectional
UPCS	Ultra-lightweight photovoltaic composite structure

List of figures

1. Figure 1. Composite laminate layout	10
2. Figure 2. Composite reinforcements, (a) carbon, (b) E-glass and (c) Jute fiber respectively	11
3. Figure 3. Types of reinforcements, (a) Continues fibers, (b) Discontinues fibers, (c) Particles	23
4. Figure 4. Line diagram of DMO.	26
5. Figure 5. The buckling shape, (a) Geometrical sandwich structure, (b) Buckling mode shape	29
6. Figure 6. The line diagram of snap distribution, (a) Snap through, (b) snapback	31
7. Figure 7. (a) Composite laminate general loading configuration (b) Laminate stacking sequence layout.	38
8. Figure 8a. The overview of the research work	41
Figure 8b. The process flow chart for TS17 UAVs wing,	42
Figure 8c. The material selection layout,	43
9. Figure 9. NFRC optimization layout.	45
10. Figure 10. Configuration of ply-orientation for NFRC laminates, (a), (b), (c) Ply- orientation with 2, 3 and 4mm, HNRC laminates (d), (e), (f) Ply- orientation with 2, 3 and 4mm at 0°	46
11. Figure 11. The geometrical configuration of various composite laminates, (a) NFRC, (b) HNRC and (c) Geometrical dimensions.	47
12. Figure.12. (a) Geometrical dimensions of laminate, (b) Boundary conditions	47
13. Figure 13. Multi- objective optimization strategy	48
14. Figure 14. Loading and boundary conditions.	50
15. Figure 15. Optimization strategy (a) Laminate 1, (b) Laminate 2, (c) Laminate 3.	51
16. Figure 16. Novel sandwich structure schematic diagram.	52
17. Figure 17. The geometrical parameters with corrugated (z) -core sandwich panel	53
18. Figure 18. Deformation of a corrugated (z)-core sandwich panel subjected to transverse shear in planes perpendicular to the corrugation.	55
19. Figure 19. (a) Design concept of the photovoltaic cell embedded into the wing, (b) Exploded view of the photovoltaic cell and (c) Ply orientation configuration for laminate_1, 2, 3 and 4.	58
20. Figure 20. Process flow layout for Sandwich T-joint.	60
21. Figure 21. Sandwich T-joint, (a) CAD model parts, (b) load and boundary conditions	61
22. Figure 22. Sandwich T-joint CAD model with different configurations. (a) design 1, (b) design 2, (c) design 3 and (d) design 4.	62
23. Figure 23. FEM models (a) design 1, (b) design 2, (c) design 3, (d) design 4.	65
24. Figure 24. Structural analysis layout for composite T-joints	66
25. Figure 25. Mechanical testing of composite structure	66
26. Figure 26. Force vs displacement plot.	67
27. Figure 27. T17 UAVs wing skin optimization layout	70

28. Figure 28. Schematic diagram of multiscale model approach	72
29. Figure 29. Hexagonal unit cells for carbon/epoxy composite.	73
(a) Geometrical model of micro-level unit cell.	
(b) Finite element model of unit cell for UD composite.	
30. Figure 30. Hexagonal unit cells for carbon/epoxy composite Young's Modulus vs Fiber volume fraction	78
31. Figure 31. Hexagonal unit cells for carbon/epoxy composite Shear Modulus vs Fiber volume fraction	79
32. Figure 32. Hexagonal unit cells for carbon/epoxy composite Shear Poisson's ration vs Fiber volume fraction	79
33. Figure 33. Geometrical configuration of composite wing skin with stiffener	81
34. Figure 34. Preliminary design strategy, (a) is case study_1,	83
35. (b) Case study_2 and (c) Case study_3.	
36. Figure 35. Load and boundary conditions for case_1, (a) Compressive load, (b) Shear load	84
37. Figure 36. Load and boundary conditions for case_2 &3, (a) Compressive load, (b) Shear load	86
38. Figure 37. Bio-composite fabrication strategy	89
39. Figure 38. Bio-composites (a) Laminates, (b) Sandwich structures with different configurations and (c) Tested specimens as ASTM standards.	90
40. Figure 39. Compression test setup for bio-composite structure, (a) specimens, (b) compression test setup, (c) tested specimens.	91
41. Figure 40. Force vs displacement plots at various compressive test specimens, (a) Bio-composite specimens plots, (b) Hybrid composite (Jute_75% and Glass_25%) specimens plots, (c) Hybrid composite (Jute_25% and Glass_75%) specimens plots and (d) Synthetic composite specimen plots.	93
42. Figure 41. Tensile test setup for bio-composite structure, (a) specimens, (b) Tensile test setup, (c) tested specimens.	94
43. Figure 42. Force vs displacement plots at various tensile test specimens, (a) Bio-composite specimens plots, (b) Hybrid composite (Jute_75% and Glass_25%) specimens plots, (c) Hybrid composite (Jute_25% and Glass_75%) specimens plots and (d) Synthetic composite specimen plots.	95
44. Figure 43. Three-point bending test setup for bio-composite structure, (a) specimens, (b) Tensile test setup, (c) tested specimens.	95
45. Figure 44. Force vs displacement plots at various three-point bending test specimens, (a) Bio-composite specimens plots, (b) Hybrid composite (Jute_75% and Glass_25%) specimens plots, (c) Hybrid composite (Jute_25% and Glass_75%) specimens plots and (d) Synthetic composite specimen plots.	96
46. Figure 45. Bio-composite surface analysis (a), (b) The fiber pullout each other, (c), (d) Fiber shear splitting and (e), (f) Fiber breaking.	97
47. Figure 46. Maximum stress plots of jute (a-d), Glass (e-h) and Sandwich-Jute (i-l).	100

48. Figure 47. Maximum strain plots of jute (a-d), Glass (e-h) and Sandwich-Jute (i-l)	101
49. Figure 48. Deformation plots of jute (a-d), Glass (e-h) and Sandwich-Jute (i-l)	103
50. Figure 49. Design 8 structural failure, (a) stringer failure, (b) Base plate failure, (c) web connection failure and (d) Bolted joint's location failure	104
51. Figure 50. Optimization methodology for sandwich structure	106
52. Figure 51. (a) Local indentation, (b) to (g) is represent maximum deformation of composite sandwich panel results.	107
53. Figure 52. (a) to (g) maximum displacement vs Time graphs.	108
54. Figure 53. The proposed composite sandwich structure with different core configurations.	109
55. Figure 54. Maximum stress plots of jute (a-e) and E-glass (f-j).	110
56. Figure 55. Maximum strain plots of jute (a-e) and E-glass (f-j)	111
57. Figure 56. Maximum shear stress plots of jute (a-e) and E-glass (f-j).	112
58. Figure 57. Maximum deformations plot of jute (a-e) and E-glass (f-j).	113
59. Figure 58. (a), (b), (c) and (d) is Max. Stress at laminate_1, 2, 3 and 4.	116
60. Figure 59. (e), (f), (g) and (h) is Max. Strain at laminate_1, 2, 3 and 4.	117
61. Figure 60. (i), (j), (k) and (l) is Max. deformation at laminate_1, 2, 3 and 4.	117
62. Figure.61 Buckling analysis results from Case_1, (a-b) Deformation at compressive force, (c-d) deformation at Shear force.	119
63. Figure.62 Structural analysis results from Case_2_1mm, (a-b) Deformation and Inverse reserve factor at compression force (c-d) Deformation and Inverse reserve at Shear force.	120
64. Figure.63 Structural analysis results from Case_2_2mm, (a-b) Deformation and Inverse reserve factor at compression force (c-d) Deformation and Inverse reserve at Shear force.	121
65. Figure.64 Structural analysis results from Case_2_3mm, (a-b) Deformation and Inverse reserve factor at compression force (c-d) Deformation and Inverse reserve at Shear force.	122
66. Figure.65 Structural analysis results from Case_3_0mm, (a-b) Deformation and Inverse reserve factor at compression force (c-d) Deformation and Inverse reserve at Shear force.	123
67. Figure.66 Structural analysis results from Case_3_1mm, (a-b) Deformation and Inverse reserve factor at compression force (c-d) Deformation and Inverse reserve at Shear force.	124
68. Figure.67 Structural analysis results from Case_3_2 mm, (a-b) Deformation and Inverse reserve factor at compression force (c-d) Deformation and Inverse reserve at Shear force.	125
69. Figure.68 Structural analysis results from Case_3_3 mm, (a-b) Deformation and Inverse reserve factor at compression force (c-d) Deformation and Inverse reserve at Shear force.	126
70. Figure 69. Convergence of solutions for (0/0/0/0) laminate	131

composite plate at $b=40$ and 80 mm respectively.	
71. Figure 70. Effect of b/t on non-dimensional buckling load under the simply supported condition.	132
72. Figure 71. Effect of $E1/E2$ on non-dimensional buckling load for (0 deg).	132
73. Figure 72. Buckling load factor vs laminating angle, (a-d) with 'b=40' value, (e-h) with 'b=80' value from 0 deg- 45 deg respectively.	133
74. Figure 73. illustrates the layout for the design and optimization of natural reinforced fiber composites.	134
75. Figure 74. illustrates deformation at $0^\circ/30^\circ/45^\circ$ angles with various configurations (Jute – 2, 3, and 4 mm).	135
76. Figure 75. illustrates stress-strain, (a) Natural fiber, (b) hybrid composite at $0^\circ/30^\circ/45^\circ$ angles with various configurations (Jute – 2, 3, and 4 mm).	135
77. Figure 76. Summarized results (Jute and Hybrid—2–4 mm).	136
78. Figure 77. (a) Loading and boundary conditions, (b) Mechanical testing and (c) specimens	139
79. Figure 78. Optimization strategy (a) Laminate 1, (b) Laminate 2, (c) Laminate 3	140
80. Figure 79. Depicts the results of buckling analysis, illustrating plots of the buckling load factor against laminating angle for various stacking sequences, including (a) Laminate 1, (b) Laminate 2, (c) Laminate 3, and (d) Laminate 4 (the reference laminate).	144
81. Figure 80. illustrates the results of compression tests, displaying force versus displacement plots for different stacking sequences, namely (a) Laminate 1, (b) Laminate 2, (c)Laminate 3, and (d) Laminate 4 (reference laminate).	144
82. Figure 81. SEM images of E-glass fibers (a) fracture surface of E-glass fiber and (b) fracture surface of E-glass fibres.	145
83. Figure 83. Fiber and matrix failure under compression load (a) fibers splitting and (b) fibres shearing pullout.	146
84. Figure 84. Spherulitic failure under compression load (a) fibers spherulitic failure and (b) fibres	146
85. Figure 85. Composite laminates configuration and Identified failure criteria, (a) Plies construction, (b) Ansys setup, (c) Laminate 1, (d) Laminate 2, (e) Laminate 3 and (f) Laminate 4 (reference laminate).	147
86. Figure.86 Bio-Composite sandwich structure fabrication strategy for TS17 UAV wing	154
87. Figure.87 Bio-Composite mechanical testing, (a) Tensile test, (b) Compression test.	155

List of Tables

1.	Table 1. Natural fibers properties	44
2.	Table 2. Mechanical properties of composite materials	64
3.	Table 3. Compression test results	67
4.	Table 4. Material properties of fiber and matrix (Carbon fiber/Epoxy)	74
5.	Table 5. Homogenization analysis results of the micro-level	74
6.	Table 6. Mechanical properties of fiber and matrix.	75
7.	Table 7. Summary of effective properties for different fiber volume fraction by ROM.	78
8.	Table.8 The design parameters of TS17 UAV	80
9.	Table 9. The critical flight parameters of TS 17 UAV	80
10.	Table 10. The modified parameters for TS17 UAV	81
11.	Table 11. FEM meshing details at various case studies	83
12.	Table 12. FEM meshing details at various case studies	83
13.	Table 13. Materials properties of Jute/E-glass woven fibers.	87
14.	Table 14. Compression test results raw data	88
15.	Table 15. Tensile stress results of composite laminates	91
16.	Table 16. Three-point bending test results composite laminates.	93
17.	Table 17. The static structural analysis results at various design configurations	102
18.	Table 18. Sandwich panel optimization geometrical parameters.	106
19.	Table.19. Design experiments analysis results	114
20.	Table 20. Mechanical properties of fiberglass	116
21.	Table 21. Simulation results summary	118
22.	Table 22. Case_1 FEM analysis result	126
23.	Table.23 Case_2 FEM analysis result	129
24.	Table.24 Case_3 FEM analysis result	130
25.	Table 25. Mechanical properties of Jute fiber	131
26.	Table 26. displays the optimal ply-stacking sequence outcomes for different configurations ($0^\circ/\pm 45^\circ/90^\circ$).	141
27.	Table 27. Exhibits the optimal ply-stacking sequence results for various configurations ($90^\circ/\pm 45^\circ/0^\circ$ and $(0^\circ/\pm 30^\circ/\pm 60^\circ/90^\circ)$)	142
28.	Table 28. Compression test result.	143
29.	Table 29. Optimization results at various ply orientations	148

1. Introduction

Composite materials are characterized as substances comprising two or more macroscopically distinct phases. This differs from materials like alloy steel, wherein the alloying components are integrated at the microscopic scale, yielding a material that exhibits macroscopic homogeneity. The preeminent exemplar of a composite material is concrete, wherein particles of sand and gravel are amalgamated with a blend of cement and water, resulting in the composite material [1]. Within this investigation, the term "composite materials" refers specifically to fiber-reinforced polymers (FRPs), which encompass resilient and rigid fibers, including glass, carbon, Kevlar, and other types. These fibers are integrated into a flexible and lightweight matrix, such as epoxy, ensuring that the resulting composite materials demonstrate a harmonious blend of properties. The orientation of the constituent fibers has a significant impact on the mechanical properties of these composite materials [2]. Composite materials have been extensively utilized in aerospace applications to attain elevated levels of strength and stiffness while concurrently reducing weight in comparison to corresponding metallic components. Laminates are manufactured by stacking and curing a few plies Fig.1 illustrates a couple of layered laminate where all plies have the same thickness.

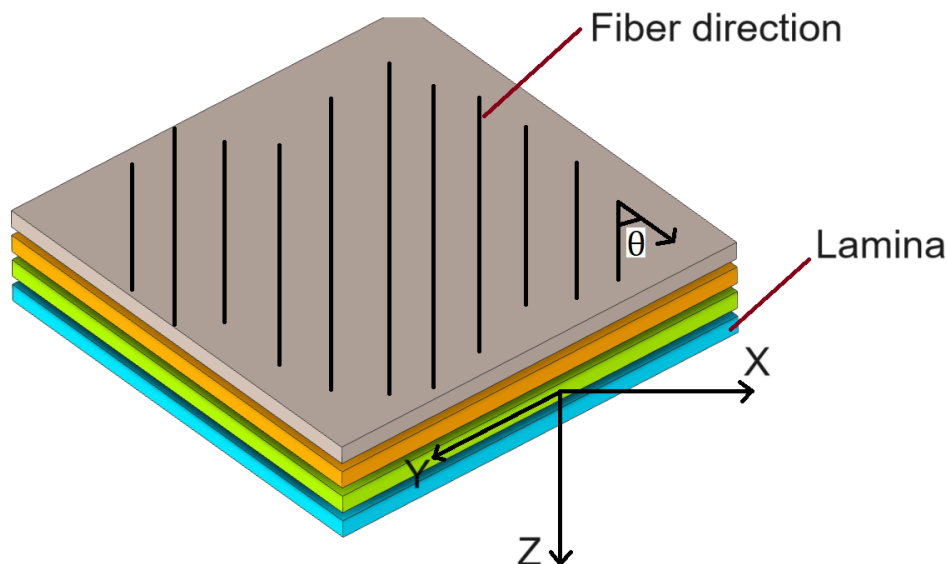


Fig.1. Composite laminate layout

To achieve the required thickness and stiffness, multiple reinforced plies are layered to create composite laminates. Each of these layers is made up of a sheet with many fibers embedded in a matrix material, which could be a polymer or a metal. Usually, the same

matrix material that is present in a single sheet is used to connect the layers. Comprising of multiple sheets oriented in distinct directions, the bidirectional fiber-reinforced sheets are what give composite laminate its name. This arrangement of various orientations is referred to as the lamination scheme or stacking sequence. The stacking sequence, along with the material properties of each individual sheet, grants designers additional flexibility to customize the stiffness and strength of the laminate. I employ classical laminated plate theory to explain the mechanical behaviour of a typical composite laminate [3]. The mechanical characteristics of a laminate result from various factors, such as the material properties of each individual layer, the quantity of layers, the thickness of each layer, and the orientation of the layers. Utilizing laminated composite materials provides significant design flexibility and allows for a high level of customization in the composite structure. By carefully designing and strategically positioning fibers, one can achieve effective structures that possess stiffness meticulously tailored to meet specific operational requirements [4]. Composite materials are frequently employed in high-performance structures because of their superior stiffness and strength-to-weight ratio in comparison to their metallic counterparts [5]. The elevated specific properties facilitate additional weight reduction, leading to decreased fuel consumption in applications such as civilian air transport. Fig.2 illustrates typical uses of laminated composite reinforcements.

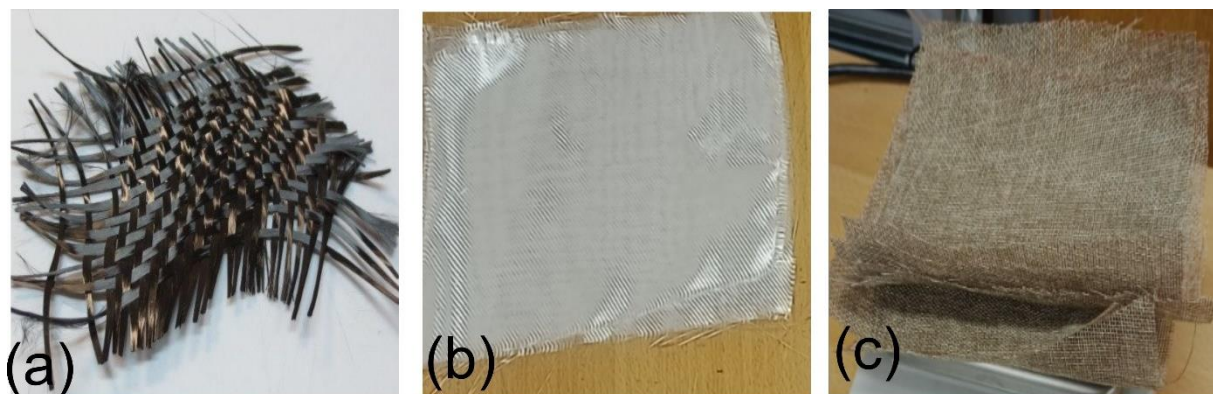


Figure 2. Composite reinforcements, (a) carbon, (b) E-glass and (c) Jute fiber respectively

It is a prevalent characteristic of these structures that their mass significantly impacts their performance, contributing to increased fuel consumption and greater forces transmitted through the structure [6]. The major goal is to use optimization approaches based on classical laminate theory to discover the most effective stacking sequence, resulting in higher

performance metrics while drastically reducing the overall weight of the composite structure. This weight reduction is critical for increasing UAV endurance and fuel efficiency, as lighter structures use less energy during flight. The doctoral dissertation includes two case studies: T-joint structural analysis and sandwich core optimization approaches. During work related to the doctoral thesis, four distinctive T-joint geometrical models were developed and analysed with different material, thickness, and shape, which were included in the doctoral dissertation as one of the case studies. The study involved the fabrication and optimization of a prototype bio-composite material with a focus on environmental sustainability.

1.1 Aim and Thesis

Aim

The aim of the doctoral dissertation is to optimize composite structures for improved load-bearing capacity and stability, particularly in UAV (Unmanned Aerial Vehicle) construction. This research focuses on developing an optimization approach that enhances the performance of natural composite materials while minimizing weight.

Thesis Statement

The doctoral dissertation, titled “**Optimization Method for Ultralight Aerial Composite Structures**”, proposes an innovative optimization approach for natural composite structures, which improves the structural performance and reducing the weight, making it highly suitable for UAV applications. The incorporation of bio-composite materials further enhances sustainability, balancing improved performance with ecological responsibility.

1.2 Scope of the work

The thesis investigates an optimization methodology designed for ultra-lightweight composite constructions. This method requires rigorous control of ply orientation, stacking sequence, and individual lamina thickness. The goal of implementing an optimization technique is to determine the most effective stacking sequence while adhering to classical laminate theory concepts. The outcome of this effort yields highly

refined performance measures, resulting in a significant reduction in the overall weight of the composite structure, thereby improving its lightweight features. Such advances have significant consequences for aircraft endurance and fuel efficiency since reduced weight equates to lower energy consumption during flight operations. Furthermore, the use of a prototype bio-composite material demonstrates a dedication to environmental sustainability. This eco-friendly material not only adds to the composite's structural integrity, but it also aligns with larger programs focused on decreasing the environmental impact of aerospace engineering techniques.

The first chapter contains an introduction to the scientific problem presented in the doctoral dissertation, the current state of art, and the author's publications on which the doctoral dissertation is based.

The second chapter focuses on the literature review state of art and different types of optimization methods, the basics of buckling analysis and bio-composite literature and classical laminated theory was described.

The third chapter addresses the optimization methodology for composite structures, which is the most important part of the dissertation. The detailed optimization method which is the ply orientation methodology and the multi-objective optimization methodology. The scientific article also published related to this chapter.

The fourth chapter deals with case study _1 and case study _2 which is composite t-joints and sandwich core optimization. In this chapter described the case studies in scientific way and one of case study was published in scientific journal.

The fifth chapter containing case study _3, In this chapter the TS17 UAV wing skin design and analysis have been conducted, Different wing skin shapes such as sandwich structure and hat shaped sandwich structure was analysed based on homogenization approach and fiber volume fraction at various stages also analysed.

The sixth chapter consist of the manufacturing and validation of bio-composite at various ply configurations. The experimental validation performed in the laboratory under supervision. The obtained test results can be used for UAV construction.

The seventh chapter contained the obtained results during the research work, the obtained results such as, T-joint optimization results, composite sandwich structure core

optimization results, TS17 UAV wing skin optimization strategy, buckling analysis results, fiber orientation, stacking sequence, structural optimization by GA results.

The eighth chapter is concluded that the final conclusions and future work. The future work can be useful for aerospace industry.

1.3 Scientific Problem

Creating well-designed laminated composite structures is a complex undertaking. The use of composite materials introduces numerous design variables, such as material properties, thickness, orientation, etc., which must be specified for each individual ply throughout the structure. Additionally, the analysis models are often extensive, and various design criteria, including mass, stiffness, and buckling, need to be considered. The conventional design approach involves updating the design based on engineering knowledge and heuristics. However, this method may lead to inefficient and suboptimal designs. There is a need for rational analysis and design methods to assist engineers in the design of laminated composite structures. The application of optimum design procedures brings about an automated and rational analysis and design process where the design is enhanced based on a performance measure describing the quality of the optimized structure. Through continuous analysis and improvement of the design, the optimal structure that meets operational requirements can be achieved.

1.4 Author publications

In this doctoral dissertation, the author primarily relies on six of his publications in scientific journals with a global reach, constituting a series of works related to the development of optimization methods for ultralight aerial composite structures.

1. The review article describes material testing methods crucial for evaluating material strength and identifying potential failure issues [7].
2. The main objective of this research pertains to the optimization of composite structures. In this research article, I analyse comparisons between bio-composite structures, synthetic fibers, and hybrid composites with varying ply stacking sequences, fiber orientations, thicknesses, and weights [8].

3. Continued to the research work, the scientific conference paper addresses the material stability of sandwich structures. The fabricated specimens were tested in the laboratory, leading to conclusions regarding material strength [9].
4. To address the optimization of composite structures, this paper provides a methodology utilizing genetic algorithms. This method primarily focuses on the number of plies, weight, various ply angles, and stacking sequences. By considering all these parameters, the validation or optimization of the structure must compile results, including outcomes such as buckling load factors, deformations, inverse reserve factors, and buckling critical loads [10].
5. The research, in terms of the case study conducted, is addressed in the scientific conference paper, focusing on the failure issues of composite structural T-joints. These T-joints relate to rib-spar and rib-to-skin configurations in wing construction. This paper examines the construction of T-joints with natural composites and evaluates material strength [11].
.
6. To expand the case study research even more, a thorough study of how bio-composites and synthetic composites fail structurally at different geometrical models is carried out." This work also addresses optimization methods regarding geometric shape, weight, and real-world applications. The manuscript was communicated to the engineering failure analysis, Elsevier. [12]

1.5 Acknowledgments

I am extremely grateful to my supervisor, **PhD, DSc, Eng. Wojciech Skarka, Prof. SUT**, for their crucial advice, support, and encouragement throughout the duration of my PhD study. Their competence, compassion, and unshakable faith in my talents have helped shape my academic and personal development.

I am grateful to the **Silesian University of Technology** for providing me with the resources, facilities, and financial support. The grants No. 10/060/BKM21/2021, No. 10/060/BKM22/2022 and 10/060/BKM23/2024. In addition, that the foreign internship has completed at University of Ljubljana, Slovenia. I needed to accomplish my research goals. I am also appreciative to the **Faculty of Mechanical Engineering, Department of Fundamentals of Machinery Design** for creating a challenging academic environment that has piqued my intellectual interest and motivated my desire to learn.

My profound gratitude extends to my family for their constant love, encouragement, and sacrifices throughout this journey. Their constant support has provided me with courage and inspiration during both the successes and tribulations of PhD studies.

I'm also grateful to my brother **Dr. Kishore Kumar Kadimpati** who is working as an assistant Professor at environmental department, SUT Gliwice and **Dr. Miha Brojan** who is working as Professor at University of Ljubljana, Slovenia and coworkers for their support, encouragement, and invaluable ideas. Their connection and camaraderie have made their academic experience more pleasurable and meaningful.

Finally, I'd want to thank everyone who has contributed to this research endeavour, whether directly or indirectly. Your encouragement and support were crucial to the successful completion of this dissertation.

2. Literature Review

2.1 Structural optimization

Shape optimization involves seeking the most favourable configuration of a domain, aiming to minimize or maximize a specified criterion while adhering to a set of constraints. This pursuit has captivated humanity for an extended period, dating back to ancient times, such as the well-known "Problem of Queen Dido." As recounted by the Roman poet Vergil in his renowned epic Aeneid, the Phoenician princess Dido, having fled Tyre (now part of Lebanon), arrived in Africa, where Carthage later emerged. King Jarbas of Numidia permitted Dido and her people to settle under the condition that she could claim only as much land as she could enclose with an ox's skin. Dido ingeniously cut the skin into thin strips, connecting them to form a semi-circle along the coast, thereby securing the largest possible territory [13]. The mathematical expression of the characteristic is articulated through the utilization of isoperimetric inequality: If Ω represents a two-dimensional region with a finite area $|\Omega|$ and perimeter $P(\Omega)$, then,

$$|\Omega| \leq \frac{1}{4\pi} P(\Omega)^2 \quad (1)$$

With equality achieved solely when Ω is a circle, Consequently, we infer that the circle optimizes the area given a constant perimeter. In contemporary industrial design, shape optimization plays a pivotal role, particularly in the field of aeronautics. Significant progress has been made, including optimizing wing profiles to enhance air penetration and lift, constructing quieter aircraft, especially supersonic ones, and conducting research on stealth aircraft. In recent decades, rapid advancements in computing power have transformed the process of structural optimization. What was once reliant on engineers' experience and knowledge has now transitioned to automatic tools employing various mathematical algorithms and techniques. These breakthroughs have facilitated the efficient handling of complex problems, particularly in scenarios where mechanical intuition is limited, such as dynamics and non-linear problems [14]. The evolution of these tools has also contributed to reducing the time and cost associated with extensive trial-and-error design processes.

Given the growing interest in the field, numerous methods have been explored and developed in structural optimization in recent years. For an in-depth exploration, interested readers can consult various sources, including [15] and their respective references. The selection of a geometric representation for a shape influences the categorization of shape optimization problems [16]. Consequently, three primary categories emerge: parametric (or size) optimization, geometric (or shape) optimization, and topology optimization. Each category is briefly described, with a particular emphasis on the last one [17].

2.2 Parametric (size) optimization

Composite materials, due to their high strength-to-weight ratio and customized mechanical properties, have become indispensable in a variety of engineering applications. Composite laminates stand out among numerous configurations due to their structural adaptability and efficiency [18]. Composite laminates provide engineers with a great degree of customization to suit unique performance needs across industries such as aerospace, automotive, marine, and civil engineering. This is accomplished by stacking layers of different materials in precise orientations. Even though composite laminates have many benefits, designing them in the most effective way is still a difficult undertaking. The qualities of the material, the orientation of the plies, the stacking order, and the geometric dimensions all have an impact on how well these structures perform. In addition, the interplay between these elements makes the design process more complicated, and it frequently necessitates the utilization of a substantial amount of computer resources and experimental validation [19].

Parametric optimization approaches provide a systematic solution to the complexity of composite laminate design. One of the goals of parametric optimization is to improve structural performance while simultaneously satisfying design restrictions and objectives. Finding the parameters that have the biggest impact and simultaneously improving them is how to achieve this. Out of all the many optimization procedures, size optimization stands out as a potentially useful method for producing composite laminates that are both lightweight and strong [20]. To enhancing the structural performance of composite laminates, the purpose of parametric optimization, also known as size optimization. The purpose of optimization is to expand the understanding of composite

laminate design optimization and provide practical insights for engineering applications. This will be accomplished through the utilization of numerical simulations, experimental characterization, and optimization techniques.

The shape is predefined using a finite set of parameters. These control variables may include factors like the structure's thickness distribution, the dimensions of structural elements, or the sizes of bars in a truss. Several methods involve parametrizing the structure's boundary with polynomials such as Bezier curves, splines, or NURBS. While widely applied in industrial contexts, this form of optimization provides restricted flexibility for shape variations [21].

2.3 Geometric (shape) optimization

Geometric optimization for composite laminates is the process of refining and improving the shape or geometry of composite materials used in laminated structures. Composite laminates are made up of layers of various materials, such as fibers and resins, that are organized in a certain manner to obtain mechanical qualities. Geometric optimization seeks to increase the overall performance and efficiency of these laminates by modifying their shape and layout. During this process, extensive calculations and simulations are carried out to locate the ideal shape that satisfies predetermined requirements. These criteria may include optimizing strength, lowering weight, or improving structural integrity. Geometric optimization, which is crucial in the design and engineering of contemporary composite structures, makes a significant contribution to the creation of lightweight, durable, and high-performance materials for a variety of applications, including aerospace, automotive, and structural engineering. Shape optimization is significantly influenced across various industries, including, Aircraft wing design such as wings can be accomplished through the application of shape optimization techniques by engineers to achieve the highest possible aerodynamic performance. Through the modification of the wing's curvature, thickness, and profile, they can reduce the amount of drag and increase the amount of lift, which ultimately results in increased fuel efficiency and maneuverability.

Automotive component design such as component design in the automobile industry shape optimization is a technique that is frequently utilized in the automobile industry for the purpose of designing components such as motor vehicle bodywork, chassis, and

suspension systems. Increasing the efficiency of a vehicle's fuel consumption can be accomplished, for instance, by optimizing the geometry of the body panels of the vehicle. Similarly, improving the geometry of the components that make up the suspension can improve the handling of the vehicle as well as the ride comfort. Wind turbine blades are subject to complicated aerodynamic forces that influence energy harvesting and structural integrity. Wind turbine blades are designed to accommodate these forces. Blades can be designed with ideal aerodynamic profiles, twist distributions, and chord lengths through the application of shape optimization techniques. This allows for the maximum amount of energy to be extracted while simultaneously decreasing the amount of material consumed and the fatigue loads. Shape optimization is utilized in the field of biomedical engineering for the purpose of designing implants such as hip replacements, dental prostheses, and orthopedic implants. For example, hip replacements are designed using shape optimization. Engineers can increase implant performance, longevity, and patient comfort by tailoring the shape and topology of implants to match the anatomy and biomechanical requirements of the patient. Bridges, buildings, and dams are all examples of structures that can be designed using shape optimization. This technique is also utilized in the design of civil engineering projects by civil engineers. To improve the structural stability and safety of a building, engineers employ optimization techniques to optimize the shape and layout of structural components. This allows the components to withstand loads more effectively, reduce the amount of material used, and more effectively.

Geometric (shape) optimization involves optimizing the structure by focusing on the structure's boundary as the variable. Unlike predefined families of curves (such as splines or NURBS), the boundary is entirely unrestricted [17, 18, 19,]. It can be represented numerically using a non-structured mesh that undergoes deformation. While the domain has the flexibility to change with the boundary, no alterations in topology are allowed.

2.4 Topology optimization

Topology optimization is a powerful computer method for finding the best way to arrange materials in a design area given a set of loads, boundary conditions, and constraints. The goal is to make the system work as well as possible. Many engineering fields, including biomechanics, aircraft, automotive, and civil engineering, heavily utilize

it to create lightweight and robust structures. It enables the exploration of a more extensive range of shapes, enhancing the likelihood of achieving improved optimal solutions. Various methods for topology optimization are currently documented in the literature, differing mainly in how topological changes occur. The initial attempts to achieve optimal topologies in structural optimization utilized the homogenization method introduced by Murat and Tartar [22-24]. Along with Kohn and Strang [25], Cherkaev, Gibianski, and Lurie [26-28] also made significant contributions. Bendsoe and Kikuchi's article [29] played a crucial role in popularizing this method, leaving a substantial impact on engineers engaged in shape optimization. This method describes shapes through a distribution of intermediate densities ranging from zero to one. In the context of linear elasticity, the relaxed physical properties of the medium are represented by the homogenized elasticity tensors in the space G_θ , depicting "composite" materials formed by mixing a material and void in a specific proportion θ . However, a "composite" structure with graded characteristics generally replaces the idea of a clearly bounded "shape." Unfortunately, for engineering applications, this poses a significant challenge as it hinders the construction of structures through conventional manufacturing methods like machining or molding. Nevertheless, the remarkable recent advancements in additive manufacturing technologies, such as 3D printing, make it feasible to contemplate the production of graded materials in the near future. To achieve a traditional shape from the homogenized optimum, it is common practice to penalize intermediate densities using fictitious interpolation schemes for material properties. This approach tends to result in shapes with values between 0 and 1 .

Except for problems related to compliance and eigenfrequency optimization in elasticity, the homogenization method encounters limitations due to the incomplete knowledge of the set of homogenized elasticity tensors G_θ [13]. Consequently, practitioners must rely on approximations of this set, where global optimality is not guaranteed. The widely used approximation is associated with the SIMP method (Solid Isotropic Material with Penalization) [14]. In this method, G_θ is approximated by elasticity tensors of the form $A_{ijkl}(A) = \theta^p A_{ijkl}$, where A_{ijkl} represents the elasticity tensor of the full material ($A = 1$), and p is the penalization power used to encourage designs with approximate values between 0 and 1 (typically set as $p = 3$). Other approaches, such as RAMP [30] and combinations of penalization techniques with Heaviside projection functions [31], are also noteworthy. The SIMP method, known for its robustness and simplicity, has demonstrated success in

various engineering problems [32]. Additionally, many commercial software tools dedicated to topology optimization, including GENESIS (Vanderplaats), NASTRAN (MSC Software), OPTISTRUCT (Altair), and TOPOL (Samtech), are based on the SIMP method. However, in cases where the interface's position is critical, such as in manufacturing [33], or when pointwise constraints are involved, the SIMP method may not be the most suitable due to the presence of intermediate density zones. For further details, interested readers are referred to [34].

2.5 Parametrization of constitutive mechanical properties

The optimization methodologies used in this study are aimed at improving the structure's inherent properties. Continuous Fiber Angle Optimization (CFAO), Free Material Optimization (FMO), and Discrete Material Optimization (DMO) are the three distinct constitutive parameterizations that are utilized in this process. These parameterizations provide distinct approaches for adjusting the mechanical properties of composite laminates to satisfy certain performance requirements. Understanding and applying these parametrization techniques is critical for engineers and researchers looking to optimize the mechanical performance of composite laminates for a variety of applications.

2.5.1 Continuous Fiber Angle Optimization (CFAO)

Continuous Fiber Angle Optimization (CFAO) is a critical technology in the field of composite laminates, providing a diverse method for tailoring the mechanical properties of these materials to specific applications. Using CFAO, engineers can improve properties such as stiffness, strength, and other crucial performance parameters.

This is accomplished by intentionally altering the orientation of continuous fibers within the laminate structure. CFAO, its underlying concepts, applications, and current breakthroughs in the realm of composite materials are all discussed, which provides an excellent understanding of the material. Kumpati et al. [8] is addressed the mechanical properties in-between the natural composite vs hybrid composite by utilizing the continuous fiber angle optimization and various stacking sequence. The fibers can be described as follows in Fig.3.

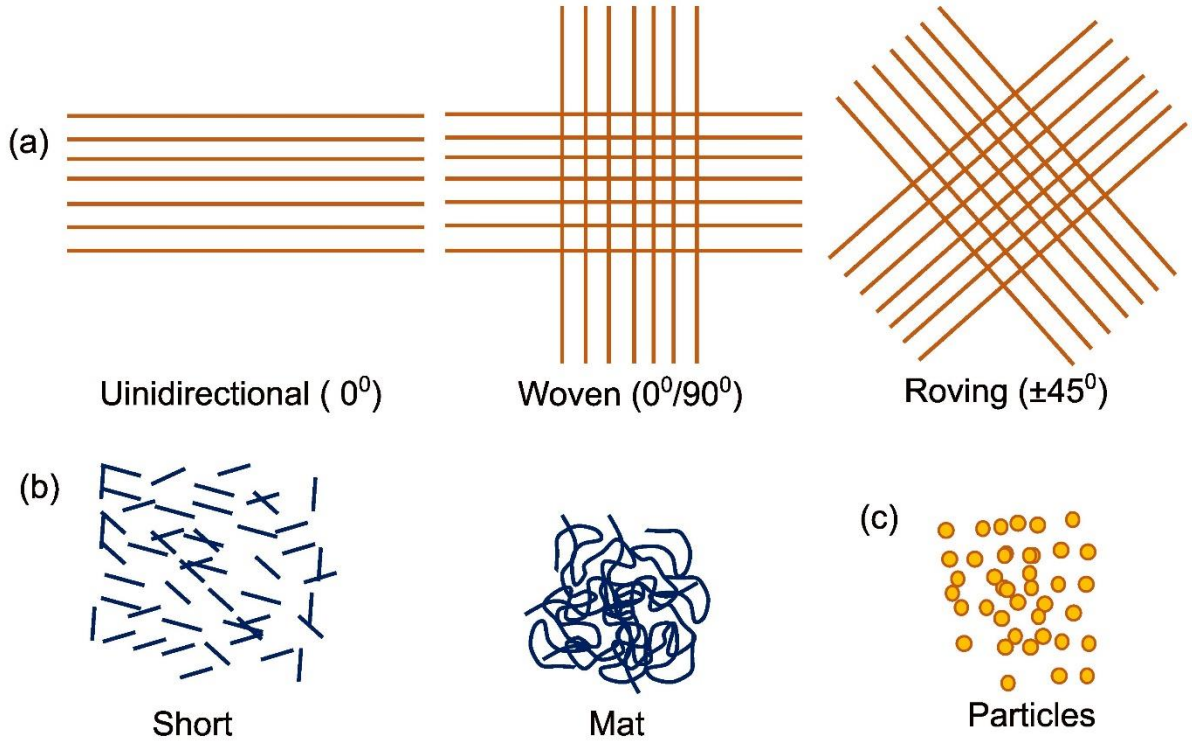


Figure 3. Types of reinforcements, (a) Continuous fibers, (b) Discontinuous fibers, (c) Particles.

The determination of the ideal orientation of an orthotropic material is the primary focus of continuous fiber angle optimization (CFAO). Therefore, in its general formulation, the design variables consist merely of the orientations (θ), which eliminates the possibility of any modification to the topology. Optimal angles are obtained for materials that display high and low shear stiffness in [36], which includes an investigation into the optimization of orthotropic material orientation. Further, [37] provides constraints on the elastic energy of orthotropic materials under the assumption of a continuous strain field. This allows for the elucidation of extremum angles and the nature of the angles that correspond to them (whether they are minimum or maximum).

Because it uses trigonometric functions to find the orientation within the constitutive tensor, CFAO is hard to do because it is not convex, as shown in Equation (2.1). Despite its usefulness, CFAO faces hurdles. Despite this, CFAO can produce designs that are admirable in terms of their performance if appropriate initial angles and a move restriction method are utilized.

$$E_{pl}(\theta_{pl}) = A(\theta_{pl})^{-1} E T(\theta_{pl})^{-T}, \quad \forall p, l$$

$$T(\theta) = \begin{bmatrix} c^2 & s^2 & 2sc \\ s^2 & c^2 & -2sc \\ -sc & sc & c^2 - s^2 \end{bmatrix}, \quad c = \cos(\theta), s = (\sin(\theta)) \quad (2.1)$$

Where, p represents the patch and l indicates the layer. Patches are a collection of pieces that must have the same laminate layup parameters to be considered successful. When using CFAO for optimization, it is of the utmost importance to make certain that the design variable limits are never reached. This is because reaching these limits could influence the other fiber angles. An approximation that is reliable for the bounds on fiber angles is as follows: $\theta_{init} \pm 180.9$ degrees, where θ_{init} is equivalent to the beginning angle.

2.5.2 Free material optimization

Free Material Optimization (FMO) is a ground-breaking methodology in the field of composite laminates, providing a precise mechanism for engineering material properties at the microstructural level. Unlike traditional optimization techniques that focus primarily on structural geometry, FMO investigates the complex manipulation of material distribution inside the laminate, allowing designers to fine-tune mechanical properties to suit a variety of performance objectives. This extensive introduction provides a thorough overview of FMO, clarifying its fundamental concepts, uses, and current advances in the realm of composite materials. Composite laminates, which are made up of layers of various materials such as fibers and matrices, are known for their high strength-to-weight ratio and customized mechanical properties. However, adjusting these qualities to meet specific design requirements remains a significant issue. Traditional optimization techniques frequently concentrate on changing the structural arrangement, ignoring the possible benefits of microstructural changes. In contrast, FMO enables engineers to optimize material distribution within the laminate, giving them unprecedented control over mechanical behaviour.

At the heart of FMO is the notion of material interpolation, in which material properties are interpolated inside each laminate element depending on a set of design parameters. Designers can obtain a variety of desirable qualities, including stiffness, strength, and fatigue resistance, by intentionally changing variables such as fiber volume fractions or material orientations. In addition, FMO lets production limits like fiber steering be built into automated layup processes. This makes sure that optimized designs

can be used in real life. FMO's adaptability spans multiple industries, including aerospace and automotive, renewable energy, and biomedical engineering. In aircraft applications, FMO enables the design of lightweight structures with optimized stiffness distributions to improve fuel efficiency and performance. Similarly, in the automotive industry, FMO enables the development of composite components with improved crashworthiness and energy absorption capacities. Recent developments in computational algorithms and optimization approaches have increased the usefulness of FMO. When engineers use high-fidelity finite element analysis along with advanced optimization methods like genetic algorithms and simulated annealing, they can effectively explore complex design spaces and find the best material distributions. Furthermore, the combination of machine learning and artificial intelligence approaches has the potential to transform FMO by allowing for automated design generation and quick prototyping of composite structures [38]. Finally, Free Material Optimization offers a paradigm leap in composite laminate design and optimization, giving users unparalleled control over material attributes and performance. With its ability to alter mechanical behaviour at the microstructural level, FMO has enormous promise for innovation across multiple industries and is positioned to impact the future of composite materials engineering.

2.5.3 Discrete material optimization

Because of their remarkable strength-to-weight ratio, resistance to corrosion, and design flexibility, composite materials, and laminates in particular, have revolutionized a variety of different industries. When it comes to composite laminate structures, optimizing the distribution and orientation of materials at the microstructural level is necessary to achieve better mechanical characteristics and performance. In composite laminates, discrete material optimization (DMO) is a sophisticated way to change the properties of materials at a localized scale. This improves how the laminate behaves under certain loading conditions. When it comes to composite laminates, discrete material optimization (DMO) is the process of separating the laminate into its individual layers, also known as plies. Each ply is composed of a unique mix of fiber orientation, type, and stacking sequence [39]. Through the manipulation of the properties of each ply, DMO enables engineers to adjust the stiffness, strength, and other mechanical characteristics of the laminate to satisfy performance requirements while simultaneously decreasing the amount of material used and the amount of weight taken up.

When it comes to composite laminates, the process of optimization in DMO normally starts with the definition of a set of design factors. The DMO strategy is presented in Fig.4.

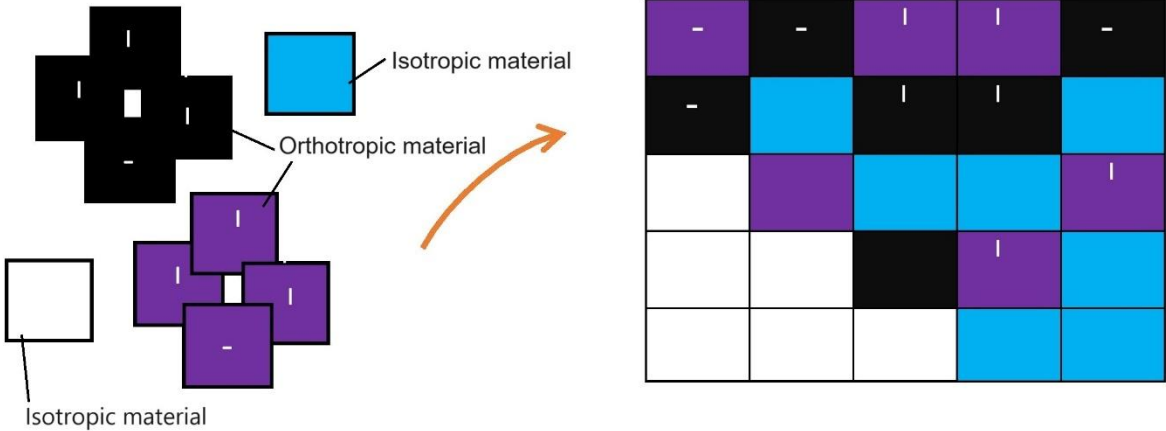


Figure 4. Line diagram of DMO

Figure 4. Line diagram of discrete material optimization approach, each colour represents a different material, where blue and white are isotropic materials or void and black and purple are orthotropic materials have different orientations. A total of ten candidate materials are defined in the figure.

These variables dictate the fiber orientation angles, ply thicknesses, and material types for each layer. After that, these design factors are optimized to maximize performance metrics like stiffness, strength, fatigue resistance, or impact tolerance. However, this optimization process is subject to constraints such as manufacturing limitations, laminate thickness, and structural requirements. In DMO for composite laminates, a wide variety of optimization strategies are utilized. These strategies range from conventional optimization algorithms to more complex computer methods, such as genetic algorithms, finite element analysis (FEA), and topological optimization. With the help of these methodologies, engineers can rapidly explore the wide design space of composite laminates and locate optimal solutions that strike a balance between competing objectives. The application of DMO to composite laminates offers a multitude of advantages. The use of DMO, which entails the customization of material distribution and orientation at the microstructural level, can improve the laminate's overall mechanical performance. This results in better structural efficiency, durability, and reliability. In addition, DMO makes it possible to develop laminates with qualities that are specifically adapted to certain applications. This makes it possible to create customized solutions that can fulfill a wide range of engineering criteria. In composite laminates, DMO has applications in a broad variety of industries, including the aircraft industry, the

automotive industry, the marine industry, the wind energy industry, and the sporting goods industry. Some examples of this include the development of high-performance automotive components for improved fuel efficiency and crashworthiness, the fabrication of long-lasting marine structures that are resistant to harsh environmental conditions, and the design of lightweight aircraft structures that have optimized load-bearing capabilities. In this section, explore the fundamentals, techniques, and applications of discrete material optimization in composite laminates. We also investigate the role that this technique plays in developing the design and manufacturing of lightweight, high-performance structures across a variety of industries. We highlight the potential of DMO for composite laminates to enhance innovation and sustainability in materials engineering by discussing important hurdles, recent developments, and future directions in the field of advanced manufacturing operations (DMO). The DMO issue fundamentally presents a significant combinatorial challenge. However, subsequent works [36, 37] have presented a method of continuous relaxation with penalization to handle the integer problem, given by,

$$E_{pl}(x_{plc}) = \sum_{c=0}^{n_c} w(x_{plc}) E_c, \quad \forall p, l \quad (2.2)$$

$$x_{plc} \in]0, 1[$$

Where, E_{pl} provides the constitutive matrix for a specific patch p and layer l , whereas E_c includes the constitutive properties for a candidate material c , with the total number of candidates marked as n_c . The weight function w is used, and instructions for the penalization strategy are provided in reference [40]. Finally, the design variables x_{plc} are like those used in topology optimization; $x_{plc} = 0$ indicates that the candidate material is not chosen, while $x_{plc} = 1$ signals selection. It's worth noting that just one material can be selected within each design domain, and intermediate values consider the introduction of a synthetic pseudo-material. The weight functions can keep themselves in a state of self-balance during the initial setup, which results in connected design variables. References [41, 42] describe the multiphase SIMP (Solid Isotropic Material with Penalization) and multiphase RAMP (Rational Approximation of Material Properties) methods that were used to solve this coupling problem. These techniques extend the SIMP and RAMP schemes for single isotropic materials, which have been the subject of recent research [43–45]. The following instructions are supplied for the multiphase SIMP formulation:

$$E_{pl}(x_{plc}) = E_0 + \sum_{c=1}^{n^c} x_{plc}^q E_c, q \geq 1, \quad \forall p, l$$

$$x_{plc} \in [0, 1]$$

$$\sum_{c=1}^{n^c} x_{plc} = 1, \quad \forall p, l \quad (2.3)$$

Where, E_0 is a material that guarantees the positive definiteness of the constitutive tensor, and q is a representation of the penalization factor. Since this formulation results in a significant number of sparse linear constraints within the optimization problem, it is necessary to have an optimizer that is capable of effectively managing these constraints. This formulation, along with its equivalent multiphase RAMP formulation, has been utilized to a significant degree over the course of this investigation. Based on the information in references [46, 47], the DMO method has been shown to work well for improving structures that have a lot of criteria functions and configuration variables.

Since the DMO technique generates many design variables, it is necessary to have one for each possible material, layer, and patch. Shape Functions with Penalization (SFP) and Bi-Value Coding Parametrization (BCP) were established in references [48, 49], respectively, to reduce the impact of this big number. It is possible to consider SFP to be a specific instance of BCP. In this case, each candidate material is given a distinct code, which results in the reduction of the number of design variables to a logarithmic scale in relation to the number of candidate materials.

2.6 Buckling analysis

Understanding how thin materials behave when subjected to compressive loads is essential for structural engineers, and one of the fundamental aspects of structural engineering is the analysis of buckling. It is possible for a structural member, such as a column or beam, to reach a critical point when it is subjected to an increasing compressive force. At this point, the member may suddenly distort laterally or buckle rather than undergo the more conventional linear deformation. If this occurrence, which is referred to as buckling, is not adequately accounted for during the design phase, potentially catastrophic structural failure can occur. The example of sandwich structure having a buckling shape, and it is presented in Fig.5.

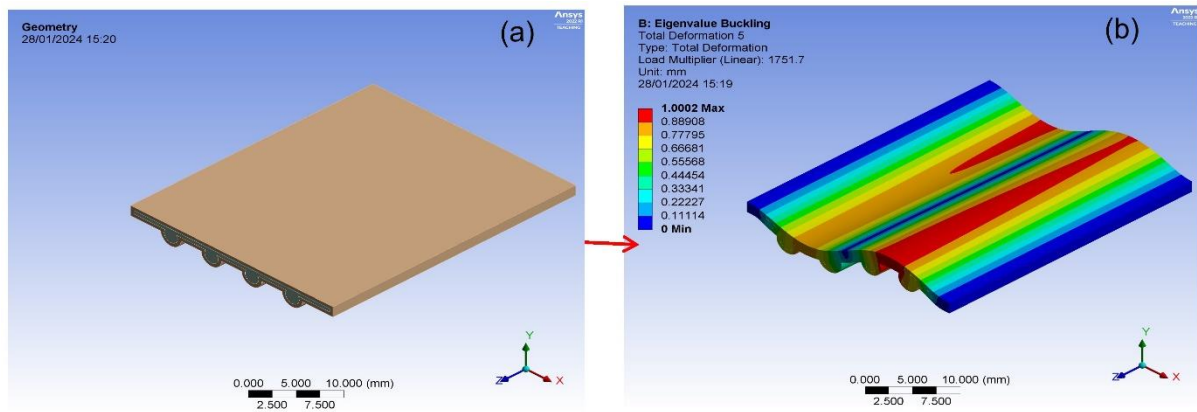


Figure 5. The buckling shape, (a) Geometrical sandwich structure, (b) Buckling mode shape.

Buckling is a topic that has been studied for centuries, with important contributions coming from mathematicians and engineers such as Leonhard Euler in the 18th century. The renowned Euler buckling formula, which predicts the critical buckling load for an idealized column with no flaws, was developed because of Euler's work, which established the groundwork for understanding the stability of thin columns. However, buildings in the real world are rarely perfect, and a wide range of factors can affect how these structures buckle. There are several factors that play a key role in defining the critical buckling load and mode shapes of a structure. These factors include material flaws, geometric irregularities, boundary conditions, and loading conditions. As a result, contemporary methodologies for buckling analysis are designed to take into consideration this complexity to produce reliable forecasts of structural stability.

One method that is frequently utilized in the field of buckling analysis is known as finite element analysis (FEA). This technique involves breaking down a complicated structure into smaller, more manageable components to successfully solve the equations that regulate equilibrium and compatibility by numerical means. With finite element analysis (FEA), engineers can simulate different loading scenarios and boundary conditions. This lets them test how well a structure holds up against buckling in real-world situations.

The idea of bifurcation is another key factor to consider while doing buckling analysis. This refers to the phenomenon in which a structure experiences an abrupt change in its equilibrium state when the load that is being applied increases. This bifurcation point,

which is of utmost significance when it comes to anticipating the behaviour of the structure close to the critical load, indicates the beginning of buckling instability.

Buckling analysis approaches have seen considerable improvements in terms of their accuracy and efficiency in recent years because of developments in computing techniques. These techniques include nonlinear finite element analysis and computational optimization, among others. Engineers can explore a broad variety of design possibilities, optimize structural configurations for buckling resistance, and ensure the safety and reliability of engineering structures with the use of these technologies [50-59].

2.6.1 Linear buckling analysis of structures

Understanding the buckling properties of composite laminates is important for making sure that these complex materials are stable and reliable under a range of loading conditions. Buckling analysis is crucial for forecasting the critical loads and failure modes of composite structures, especially in situations where they experience compressive stresses. Linear buckling analysis, also referred to as eigenvalue buckling analysis, is a fundamental method used to evaluate the stability of structures when subjected to external stress. Within the realm of composite laminates, linear buckling analysis entails forecasting the initiation of buckling instability in the structure through the resolution of the eigenvalue issue linked to the linearized equilibrium equations. The orientation and arrangement of the fiber layers, the constituents' material properties, geometric irregularities, and boundary conditions are just a few of the variables that affect how composite laminates respond to compressive stresses. Linear buckling analysis offers useful insights into the interplay of these factors in influencing the buckling resistance of composite structures. A major difficulty in doing linear buckling analysis of composite laminates is precisely representing the material properties and intricate geometry of the structure. Composite materials possess orthotropic characteristics, indicating that their mechanical properties vary depending on direction, necessitating the use of specialized constitutive models to accurately describe their anisotropic behaviour.

Finite element analysis (FEA) is a robust technique frequently employed to perform linear buckling analysis of composite laminates. By breaking the structure into separate parts and using the right material models, Finite Element Analysis (FEA) lets engineers get a good idea of the critical buckling loads and modes of composite structures.

Recent progress in computer methods and modelling of materials has made it much more accurate to predict the results of linear buckling analysis for composite laminates. By combining multiscale modelling methods with experimental verification, it becomes possible to conduct more accurate simulations of composite behaviour. This technique considers the influence of microstructural factors and material heterogeneity. In the field of engineering, the analysis of linear buckling in composite laminates is extremely important for the design, optimization, and prediction of failure in lightweight and high-performance structures. Engineers can guarantee the safety, dependability, and effectiveness of composite-based systems in different industries by precisely forecasting buckling behaviour.

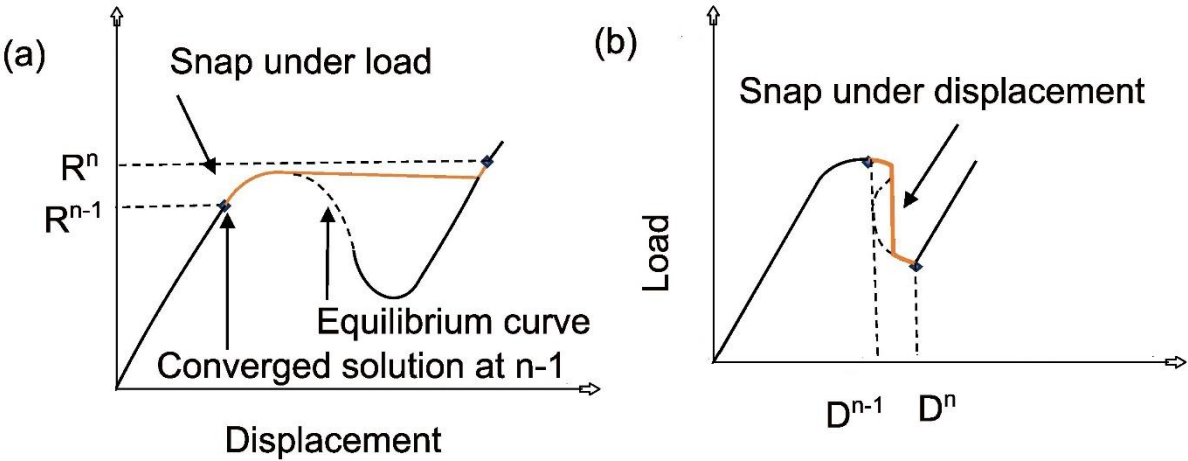


Figure 6. The line diagram of snap distribution, (a) Snap through, (b) snapback

Snap through, illustrated in the Fig.6a left figure, can occur when using a nonlinear solver under load control. In this scenario, surpassing the load limit point leads to finite displacements. Snap back, on the other hand, occurs when the response curve "reverses" itself, exhibiting a turning point known as a displacement limit point. Both snapping occurrences can pose convergence challenges for the solvers.

If the initial response before buckling follows a linear pattern, the displacement stiffness matrix $K_L = 0$. The tangent stiffness matrix is then computed using only the linear stiffness (K_0) and stress stiffness (K_S) matrices. The stress stiffness matrix is made up of stresses from a linear static analysis.

$$(\mathbf{K}_0 + \lambda_j \mathbf{K}_S) \phi_j = 0, j = 1, 2, \dots \dots \tag{2.4}$$

The eigenvalues (λ_j) are believed to be arranged by magnitude, with λ_1 being the lowest. Linear buckling analysis only identifies bifurcation buckling; limit point buckling is caused by nonlinearities in the basic equilibrium curve. Furthermore, the analyst cannot predict if linear buckling analysis is adequate to capture a structure's buckling reaction, so it should be utilized with caution.

When compared to linear buckling analysis, nonlinear buckling analysis takes pre-buckling displacements into account. If these displacements are too large to ignore, the complete tangent stiffness matrix, as shown in Equation (2.3), must be employed, even though linear analysis treats them as insignificant. Following is an explanation of the methodology used for nonlinear buckling analysis in this work, which is based on prior research [60-65].

In nonlinear buckling analysis, the load factor, represented as γ , is closely monitored while a geometrically nonlinear analysis is carried out. Instabilities at the limit point and at the bifurcation can be identified using this methodology. A bifurcation point can be found using tangent stiffness data, and a limit point can be found when the load factor decreases between two equilibrium points. If the load doesn't go down at successive equilibrium points, a bifurcation point will be found at the critical point. This is where the tangent stiffness matrix becomes singular, and Equation (2.4) is reached. Following the one-point method outlined in the critical point can be more easily determined. If a critical point is about to be reached or has already been exceeded, this method can tell you about it. If there are small changes in displacement between the current configuration (n) and the critical configuration (c), the critical point can be estimated using the tangent stiffness matrix at the current load step, as long as $K^{n_L} \approx K^{c_L}$. Furthermore, according to the description in [66], it is assumed that the stress stiffness matrix grows linearly with the load until reaching the critical point, $K^{c_S} \approx \lambda K^{n_S}$. After that, this data is plugged into Equation (2.4), hereby obtaining.

$$(\mathbf{K}_0 + \mathbf{K}_L^n + \lambda_j \mathbf{K}_L^n) \phi_j = 0 \quad (2.5)$$

From the nonlinear stability equation, the scaling between the current and critical load factor may be calculated as

$$\gamma_j^c = \lambda_j \gamma^n \quad (2.6)$$

It may be observed that $\lambda_1 > 1$ indicates the impending arrival of a critical point, whereas $\lambda_1 < 1$ signifies the passing of a critical point. The convergence of this technique is demonstrated at the critical load limit [67]. While linear buckling analysis is computationally inexpensive, nonlinear buckling analysis is more accurate; however, it becomes costly when the analysis required to find the critical point becomes nonlinear, necessitating an iterative method to trace the equilibrium curve.

2.6.2 Non-linear analysis of structures

Engineering uses nonlinear buckling analysis as a crucial method to understand how structures respond to compressive stresses. Nonlinear buckling analysis differs from linear buckling analysis in that it considers massive displacements and material nonlinearities rather than assuming tiny deformations. This technology allows engineers to forecast the precise moment when a structure reaches a state of instability, resulting in buckling. This capability is crucial for guaranteeing the safety and soundness of diverse mechanical and civil engineering designs.

Engineers commonly perform geometrically nonlinear analysis. During this analysis, they track the load factor (represented as γ) at every stage of the process. GNL buckling analysis may effectively detect both bifurcation and limit point instabilities. A drop in the load factor between two equilibrium points identifies a limit point, while the tangent stiffness identifies a bifurcation point.

2.7 Natural fibers

Presently, because of advancements in material and manufacturing techniques, there is a growing demand to employ cutting-edge manufacturing processes and materials, while also assessing their mechanical properties in extreme operating conditions [68, 69]. In recent decades, natural fibers have become increasingly prevalent in our everyday product. There has been a noticeable rise in the desire to manufacture biodegradable composite materials for numerous automotive components instead of the commonly utilized glass, carbon, Kevlar, and other synthetic reinforcements that pose challenges in recycling. [70, 71]. Bio-composites have assumed a pivotal role in the automotive industry, contributing significantly to factors such as passenger comfort, noise reduction, and vibration control within the vehicle, lightweight, flexibility recyclability and cost advantages. This, in turn, enhances the perceived value of the

vehicle for customers and ultimately delivers considerable advantages to manufacturers [72,73]. In recent studies, there has been a directed towards the synthesis of polymer composites using natural fibers, with a particular emphasis on substituting conventional synthetic reinforcements, as indicated by research [74]. Hossain et al. [75] conducted a study on the tensile characteristics of jute epoxy-based composites. The researchers examined various orientations of jute fibers while maintaining a constant overall volume percentage of 25%. The composite laminates were created using the Resin Transfer Molding (RTM) process. The composite exhibited greater tensile strength when the fibers were oriented at 0-0° compared to the orientations at 0-45° and 0-90°, respectively. However, in the transverse direction, the 0-0° fiber orientation displayed lower bending and tensile strength, primarily attributed to the inferior performance of jute fiber when subjected to forces perpendicular to its alignment (transverse direction). In their study, Shah and Lakad [76] examined the mechanical characteristics of unidirectional jute-polyester and jute-epoxy composites, along with their hybrid counterparts incorporating glass fibers. The investigation into the mechanical properties of polyester composite laminates reinforced with PALF (Pineapple leaf fiber) -glass and sisal-glass fibers revealed that a small quantity of glass fibers was added to the PALF (Pineapple leaf fiber) material. The study observed significant enhancements in the flexural, tensile, and impact properties of sisal-reinforced polyester composites, indicating a favourable hybrid effect. Zewdie A et al. [77] and Ramesh et al. [78] carried out an experimental investigation to examine the mechanical characteristics of hybrid composites such as jute-glass and sisal-glass reinforced epoxy fibers. The flexural tests were conducted following the guidelines specified in ASTM D790. The outcomes of the study indicated that the sisal-glass composite displayed higher tensile strength in comparison to the jute-glass composite. Additionally, the results concluded that under flexural loading, the jute-glass hybrid composites exhibited higher load capacities than the sisal-glass hybrid composites. Braga et al. [79] A study was conducted on jute-glass hybrid composites with varying weight percentages of jute-glass fibers. The authors discovered that the hybrid composites laminate, which incorporated the greatest proportion of glass fibers, exhibited significant flexural strength. Ajith et al. [80] The authors conducted a characterization of mechanical properties using various resins while keeping the fiber volume and resin ratio constant. The results indicated that the jute-reinforced epoxy composite exhibited superior mechanical properties in comparison to the jute-polyester composite. The fiber volume

percentage is also one of the major key factors in composites. With a fiber volume of 60% in the composite configuration, these combinations of laminates revealed the highest tensile strength (90.52 ± 8.83). The jute fibers possess a consistent cross-sectional shape, featuring multicellular microfibrils in their structure. Nonetheless, the physical and mechanical properties of jute vary significantly and primarily rely on factors such as the geographic origin, climatic conditions during growth, and the techniques employed during processing. Gowda et al. [81] the researchers assessed a range of fundamental mechanical properties of jute-polyester composites, including compressive strength, flexural strength, tensile strength, impact strength, in-plane shear strength, inter-laminar shear strength, and hardness. The authors showcased the versatility of jute, a sustainable natural fiber, for various consumer products, based on their research findings. Verma et al. [82] and Mohan et al. [83] conducted research on the mechanical characteristics of jute-glass hybrid composites in both polyester resin and epoxy resin. In their study, Zhang et al. [84] examined the flexural response of a hybrid composite made from carbon and glass fibers, investigating various stacking sequences. The findings of this study revealed that the flexural strength was influenced by the arrangement of plies, with higher strength observed when carbon layers were positioned on the outermost surface. In another study, Ashraf et al. [85] performed an evaluation using Ansys software to analyze the impact of ply orientation, stacking sequence, and laminate thickness on the mechanical properties of the material. The study focused on material deformation and strength, and the findings indicated that the strength of the material is influenced by ply orientation among other factors. In their research, Ahmed and Vijayarangan [86] examined the mechanical characteristics of a composite material made from untreated woven jute fabric embedded in an isothalic polyester matrix. The study explored the response of the composite under various loading conditions, including tension, compression, in-plane shear, inter-laminar shear, and impact. The impact strength of natural fiber composites is also a significant concern. Elbadry et al. [87] conducted a drop weight test on hybrid composites made from various weight percentages of jute fibers. Their findings revealed that the impact strength of the hybrid composite improved as the proportion of jute fibers increased. Khondker et al. [88] The authors also conducted a drop weight test on a woven jute fabric composite and determined that these composites, which are based on natural fibers, exhibited superior impact strength compared to composites reinforced with synthetic fibers.

Achieving optimal adhesion between epoxy and natural fibers remains a challenge due to the contrasting characteristics of these two components. In their research, Yang et al. [89] investigated the impact of alkali treatments on a composite composed of short jute fibers and polylactic acid (PLA). The short jute fibers underwent treatment with different concentrations of NaOH and H₂O₂, and composite samples were fabricated with varying ratios of treated and untreated jute fibers. The study revealed that the highest tensile strength was observed in the composites treated with 10% NaOH and 20% H₂O₂ bleaching. Ullah et al. [90] studied a 3-D finite element model (FEM) to examine the behaviour of fiber-metal laminates (FMLs) under high-velocity impact. The ABAQUS/explicit platform was employed for this investigation. Numerical and experimental methods were employed to analyze the flexural response of glass-reinforced epoxy composites without fillers. Specimens were prepared using the vacuum bagging technique and subjected to testing following ASTM D790 standards. The results indicated an approximate error of 10%. Another research study aimed to investigate the damage occurring in woven glass reinforced epoxy composites when subjected to higher deflections during three-point bending. A minor discrepancy was observed when comparing the experimental and numerical outcomes [91]. Additionally, a numerical analysis was conducted to predict the flexural strength of thick-walled carbon fiber reinforced composites (CFRP), utilizing engineering constants obtained from tensile tests on thin-walled CFRP composites [92]. It was found that the error for unidirectional composites was approximately 10%, while woven composites exhibited an error exceeding 10%. Finite element analysis (FEA) simulations were performed on both on-axis and off-axis specimens to determine the flexural strength under these two loading orientations. The analysis revealed that on-axis loading exhibited fiber dominations, while off-axis loading showcased matrix domination [93]. Polymer matrix composites offer a superior option for producing sports equipment and various other products due to their high strength-to-weight ratio, ease of preparation, and durability. The jute-glass hybrid composite is specifically utilized in load-bearing applications like automobile bumpers and seat backings [94]. Currently, skateboards are manufactured using glass and jute fibers through hand layup techniques [95]. Upon visual examination, it was found that the hand layup procedures proved reliable in creating an optimal skateboard. Test results indicated that the jute-glass fiber-based polymer skateboard exhibited sustainable strength compared to Canadian hard rock maple wood, making it suitable for constructing

sportswear components such as skateboards. Cost analysis revealed that utilizing this skateboard can result in cost savings exceeding 20%. A majority of the existing studies have focused on experimental assessments of the mechanical properties of composites reinforced with either natural or synthetic fibers. However, numerical simulation tools present an opportunity to analyze the material's response under various loading conditions. Current researchers have developed an accurate numerical model that can be used to evaluate the mechanical behaviour of fiber-reinforced composites, reducing the need for extensive experimental testing. This not only leads to cost savings but also enables researchers to assess the properties of potential materials. Additionally, it is worth noting that the hand layup method is commonly employed in the manufacturing of these fiber-reinforced composites, but it is recognized for producing lower-quality composites [96].

Therefore, there is a need to explore new and environmentally friendly materials (Bio-composites) for industrial applications, utilizing an efficient and reliable manufacturing process to keep up with advancements in material science. Finally, there are limited studies on mechanical strength, characterization of natural fiber like jute (with synthetic glass fiber) reinforced hybrid composites through various mechanical tests. The purpose of this study is to fill these research gaps and bio-composite can be used as structure in UAV.

2.8 Classical laminated plate theory

A laminate consists of arranged layers of composite plies, each with fibers aligned in a single direction rather than a woven pattern. The orientation of these plies defines the overall structure of the stack. Drawing from the principles of classical lamination theory [97–100], the analysis of composite laminates involves considering a symmetric stiffness matrix that connects forces per unit width (N) = (N_{xx} , N_{yy} , N_{xy}), moment resultants per unit width of the laminate (M) = (M_{xx} , M_{yy} , M_{xy}), as well as mid-surface strains (ε) = (ε_{xx}° , ε_{yy}° , γ_{xy}°), and curvatures (k) = (k_{xx}° , k_{yy}° , k_{xy}°).

$$\begin{pmatrix} N \\ M \end{pmatrix} = \begin{pmatrix} A & B \\ B & D \end{pmatrix} \begin{pmatrix} \varepsilon^\circ \\ k^\circ \end{pmatrix} \quad (2.7)$$

The elements within a submatrix A , denoted as A_{ij} , signify the degree of stiffness exhibited by the matrix under stretching. In engineering notation, i and j range from 1 to 2 to 6,

where 1 represents the direction of reinforcement (fiber), 2 indicates the transverse in-plane direction, and 6 signifies the in-plane shear direction. These values vary based on both ply orientation and total thickness. The coefficients D_{ij} represent the matrix's bending stiffness, influenced by ply orientation, ply thickness, and stacking sequence. The coefficients B_{ij} denote the stiffness related to bending and extensional coupling, and their calculation method is as follows,

$$\begin{aligned} A &= \sum_{k=1}^N (z_k - z_{k-1}) Q^{(k)} \\ B &= \frac{1}{2} \sum_{k=1}^N (z_k^2 - z_{k-1}^2) Q^{(k)} \\ D &= \frac{1}{3} \sum_{k=1}^N (z_k^3 - z_{k-1}^3) Q^{(k)} \end{aligned} \quad (2.8)$$

The z_k and z_{k-1} represent the vertical positions of the upper and lower surfaces in the direction perpendicular to the laminate plane for the k -th ply, which is oriented at an angle θ_k . In Figure 7a, a composite plate is depicted under a typical loading scenario, with l , w , and h denoting its length, width, and thickness respectively. Meanwhile, figure 7b illustrates the arrangement of the laminate stacking sequence.

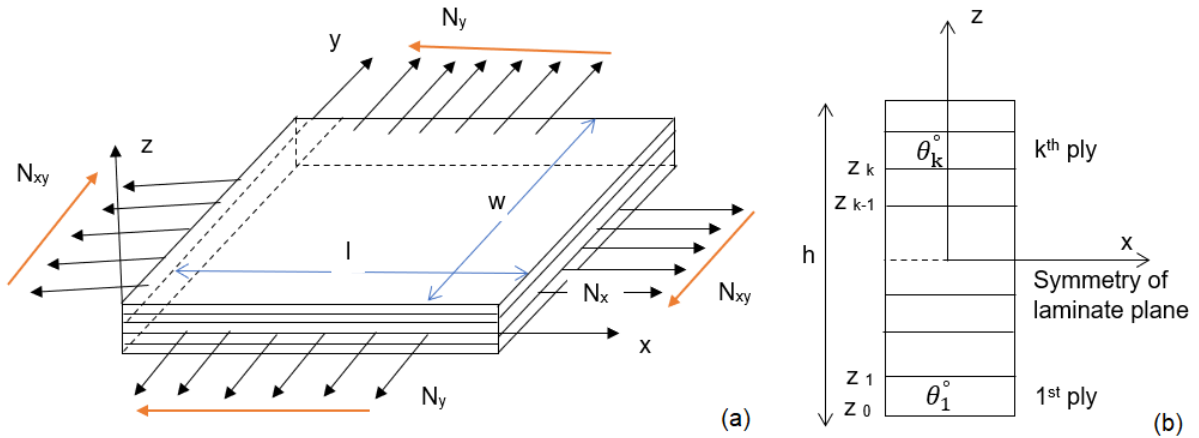


Figure 7. (a) Composite laminate general loading configuration. (b) Laminate stacking sequence layout.

In the component material coordinate system attached to the k -th ply, stresses and strains are related as

$$\begin{pmatrix} \delta_1 \\ \delta_2 \\ \tau_{12} \end{pmatrix} = \begin{pmatrix} \bar{Q}_{11} & \bar{Q}_{12} & 0 \\ \bar{Q}_{12} & \bar{Q}_{22} & 0 \\ 0 & 0 & \bar{Q}_{66} \end{pmatrix} \begin{pmatrix} \varepsilon_1 \\ \varepsilon_2 \\ \gamma_{12} \end{pmatrix} \quad (2.9)$$

Where,

$$\bar{Q}_{11} = \frac{E_1}{1-\nu_{12}\nu_{21}} \quad \bar{Q}_{22} = \frac{E_2}{1-\nu_{12}\nu_{21}} \quad \bar{Q}_{12} = \frac{\nu_{12}E_2}{1-\nu_{12}\nu_{21}} \quad \text{and} \quad \bar{Q}_{66} = G_{12} \quad (2.10)$$

Equation (2.10) involves parameters E_1 , E_2 , ν_{12} , ν_{21} , and G_{12} , representing material properties such as Young's modulus, Poisson's ratio, and shear modulus in the ply direction, as seen in a unidirectional ply. The composite material is treated as anisotropic. Due to the symmetry of the stiffness matrix, the elastic behaviour of the laminate can be described using 18 material stiffness moduli (6 terms for each 3×3 matrix A, B, and D). These moduli are interdependent as they vary with the ply directions $[\theta_k-1, \dots, N]$. However, the subsequent six linear relationships collectively reduce the number of moduli to 12 for any standard composite laminate.

$$\begin{aligned} A_{66} &= \frac{1}{2}(A_{11} + A_{22}) + h\left(\frac{1}{2}(\bar{Q}_{11} + \bar{Q}_{12}) + \bar{Q}_{16}\right) \\ A_{12} &= A_{66} + h(\bar{Q}_{12} + \bar{Q}_{66}) \quad , \quad B_{66} = \frac{1}{2}(B_{11} + B_{22}), \quad B_{12} = B_{66} \\ D_{66} &= \frac{1}{2}(D_{11} + D_{22}) + \frac{h^3}{12}\left(\frac{1}{2}(\bar{Q}_{11} + \bar{Q}_{22}) + \bar{Q}_{16}\right) \\ D_{12} &= D_{66} + \frac{h^3}{12}(\bar{Q}_{12} - \bar{Q}_{66}) \end{aligned} \quad (2.11)$$

The laminate will be represented as orthotropic, with D_{16} and D_{26} set to zero. This assumes that it can buckle into m and n half-waves in the x - and y -directions respectively when the load amplitude factor reaches a value λ_{wb} , as defined by the equation provided in reference [101]. The compression test buckling formula follows.

$$\frac{\lambda_{wb}}{\pi^2} = \frac{D_{11}(m/l)^4 + 2(D_{12} + 2D_{66})(m/l)^2(n/w)^2 + D_{22}(n/w)^4}{N_x(m/l)^2 + N_y(n/w)^2 + N_{xy}(mn/lw)} \quad (2.12)$$

λ_{wb} represents the critical buckling amplitude factor, influenced by factors such as (m, n) configurations, dimensions of the laminate, and the specific loading scenario. The buckling phenomenon at a defined margin M_b can be explained through the following relationship.

$$M_b = (\lambda_{wcb} - 1) \times 100\%, \quad \text{with} \quad \lambda_{wcb} = \min_{m,n}(\lambda_{wb}) \quad (2.13)$$

Utilizing a multi-criteria technique similar to the Hasin method [97], our approach integrates enhanced failure criteria, enabling the distinction between fiber failure (*FF*) and laminate matrix failure (*MF*) in both tension and compression modes for each individual layer [102-104, 10].

$$\text{Fiber failure (FF):} \begin{cases} f_1^+ = \left(\frac{\delta_{11}}{x_t}\right)^2 = 1, \text{ if } \delta_{11} \geq 0 \\ f_1^- = \left(\frac{\delta_{11}}{x_c}\right)^2, = 1, \text{ if } \delta_{11} < 0 \end{cases} \quad (2.14)$$

$$\text{Matrix failure (MF):} \begin{cases} f_2^+ = \left(\frac{\delta_{22}}{Y_t}\right)^2 + \left(\frac{\tau_{12}}{S_c(1-p\delta_{22})}\right)^2 = 1, \text{ if } \delta_{22} \geq 0 \\ f_2^- = \left(\frac{\delta_{22}}{Y_c}\right)^2 + \left(\frac{\tau_{12}}{S_c(1-p\delta_{22})}\right)^2, = 1, \text{ if } \delta_{22} < 0 \end{cases} \quad (2.15)$$

The parameter '*p*' facilitates a precise depiction of the reinforcement witnessed in experimental settings, particularly regarding transverse compression and in-plane shear. In this context, X_t , X_c , Y_t , Y_c , and S_c denote the strengths in longitudinal tension and compression, transverse tension and compression, and in-plane shear strength, respectively [105-110].

$$M_f = \left(1 / \min_{k, mode} (f_{mode}^{(k)}) - 1\right) \times 100\% \quad (2.16)$$

3. Methodology

This chapter discusses the design methodology and optimization methods in detail. The composite structure's optimization considers the form of the ply configuration, stacking sequence, and laminate thickness. The scientific articles were published the basis of optimization such as ply orientation methodology (variable thickness approach), while the second focuses on the multi-objective optimization methodology, which uses genetic algorithms [8, 10]. Designing laminated composite structures is an extremely complex process due to the multiple factors involved, including material qualities, thickness, and ply orientation, all of which must be precisely defined for each layer. These structures' analysis models are frequently comprehensive and must account for a variety of design requirements, such as mass, stiffness, and buckling behaviour. Traditionally, engineers update designs using experience and heuristic approaches, however this approach can lead to inefficiencies and unsatisfactory results. There is an obvious need for more rational and systematic design approaches. By using optimization approaches, the design process can be automated and driven by performance metrics that assess the structure's quality. This iterative technique enables continual refining, resulting in an ideal design that meets all operational criteria. To address such a problem in composite wing structures the doctoral dissertation included optimization methodology for TS17 UAVs wing. There are three stages to the doctoral dissertation. Fig. 8a and 8b presents the overall idea of the thesis.

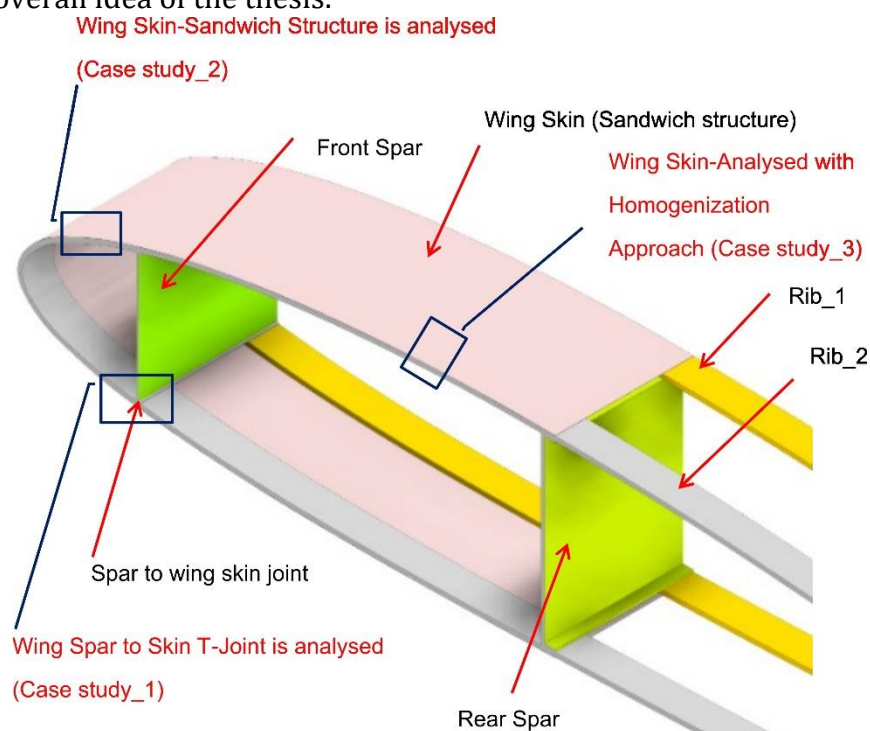


Figure 8a. The overview of the research work

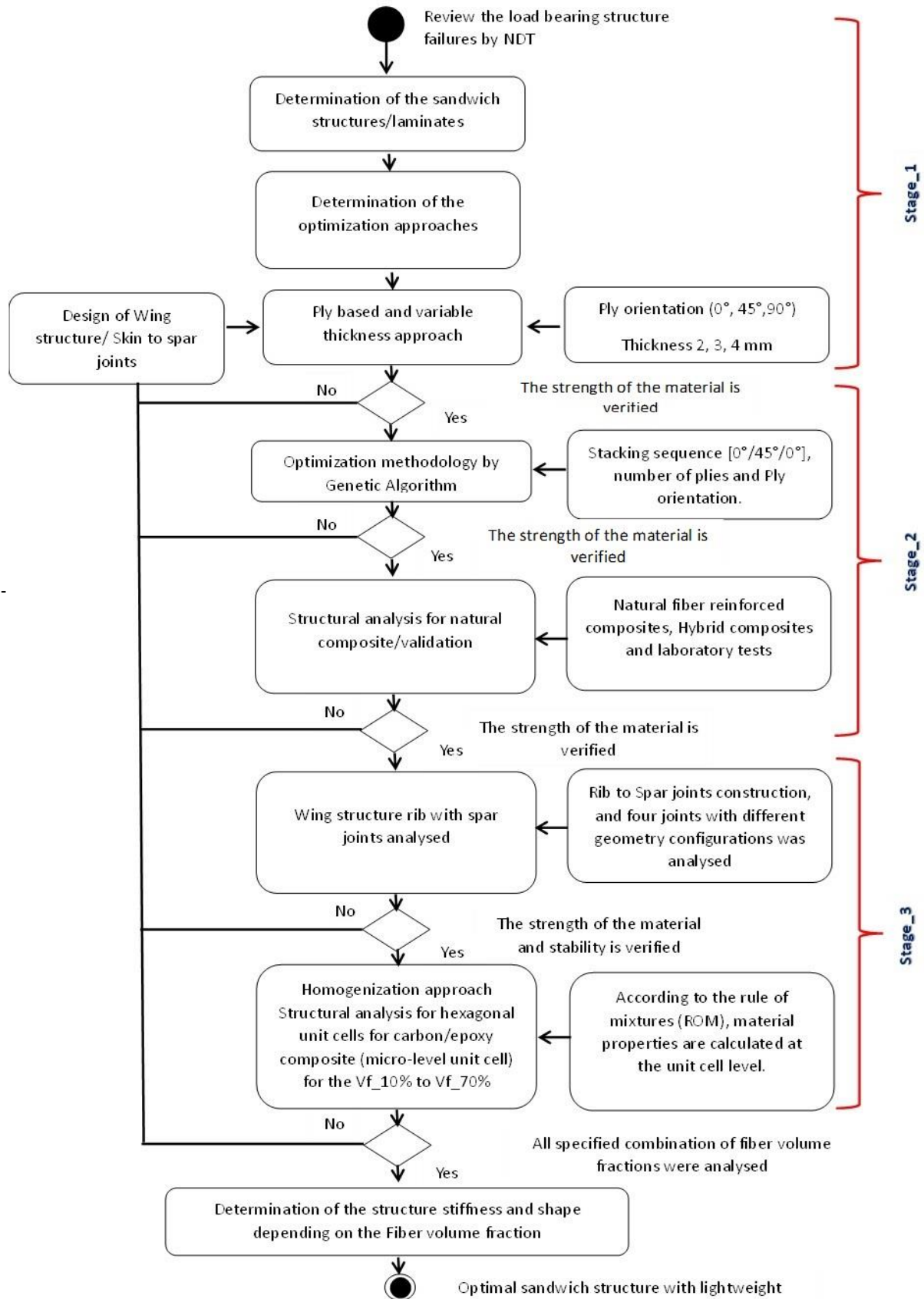


Figure 8b. The process flow chart for TS17 UAVs wing.

Stage_1

- NDT examined mechanical failures in composite structures.
- Developed an optimization approach for composite structures.

Stage_2

- GA developed the second optimization approach for composite structures.
- Analyzed composite structure by ANSYS
- Identified structural failures at various configurations

Stage_3

- Carried out a numerical simulation to determine the stability of the structure.
- Optimization approaches solve technological issues.
- In this research designed a new biomaterial for TS17 UAVs wing construction.

3.1 Material selection

The automobile and aerospace industries have been using natural fibers since the early 1990s. The automotive sector shows great promise and encouragement in utilizing Natural Fiber Reinforced Composites (NFRC) due to their significant potential and wide range of applications. The material selection is categorized and illustrated in Figure 8c.

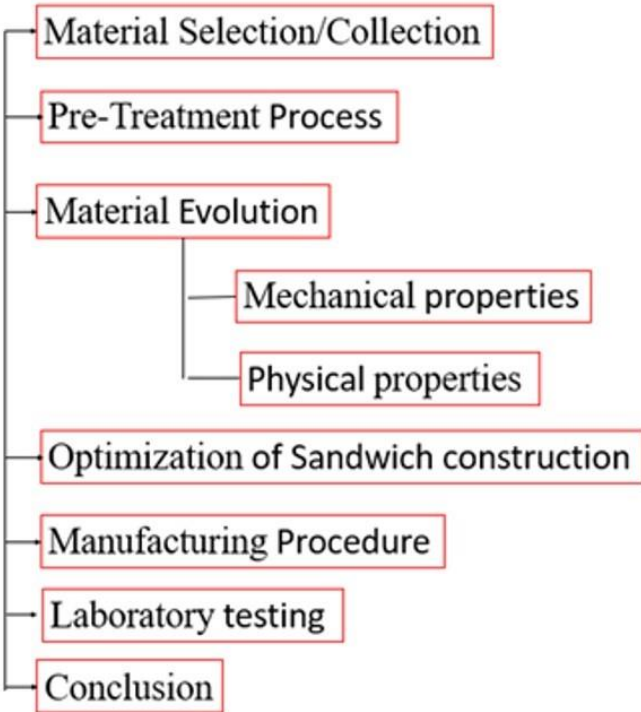


Figure 8c. The material selection layout

Contemporary car and aircraft manufacturers have integrated diverse NFRC components. The optimal design methodology by natural fiber material for UAVs by evaluating its mechanical qualities, lightweight nature, superior strength, and adaptability. This research specifically examines the properties and features of natural fibers, including jute fiber, glass fiber, and an epoxy resin. The natural fibers properties are presented in Table 1.

Table 1. Natural fibers properties [10]

Natural fibers types	Dia. (μm)	Tensile strength (MPa)	Young's modulus (GPa)	Elongation at break (%)
Natural Jute fiber	26–201	201, 394, 773–1110	13.1–25.2, 26.1, 25.5	0.7, 1.16–1.5
Natural Flax fiber	11–41	111, 344, 600–2000	12.1, 30.1, 60.1, 85.10–120.10	0.7, 1, 1.16, 1.5, 2.1–4
Natural Sisal fiber	51–201	469–641	09.4–22.0	3–7
Natural Cotton fiber	–	284–801	05.5–12.6	7–8
Natural Coir fiber	101–451	132–176	4.1–6.1	15.1–40.10
Natural raw date palm fiber (DPF)	101–1001	59–204	2.1–7.6	5–10

3.2 *E-glass reinforcement*

E-glass fiber was also used for comparison between natural composites and hybrid composites. The E-glass fiber is an ultra-lightweight with notable strength and durability. While equated to metals, it has superior material strength, stiffness, and weight properties. Randomly oriented E-glass fiber reinforced with epoxy resin. E-glass fiber has mechanical qualities such as 3445 MPa tensile strength, 1080 MPa material compressive strength, 73 GPa elastic modulus, 2.58 g/cm³ density, and 0.22 Poisson's ratio [112].

3.3 *Type of Adhesive*

Epoxy resins, also known as thermosetting resins, are excellent bonding agents that come in both liquid and solid forms. Today's market offers a wide variety of resins, such as epoxy resins, vinyl ester resins, or polyester resins. We combine the resin with a hardener at various ratios to improve mechanical qualities.

3.4 Optimization procedure

A primary analysis was conducted to determine the material mass and cross-sectional area for optimizing by using CAD designed components. This research primarily focused on assessing material strength across different geometrical configurations, performed in Ansys. The optimization process considered natural-fiber-reinforced composites (NFRC), integrating CAD geometrical models into Ansys for ply orientation. These CAD models were used to illustrate the technical configuration of composite materials. The second methodology involved hybrid natural reinforced composites (HNRC) to enhance the properties. The design methodology is depicted in Figure 9.

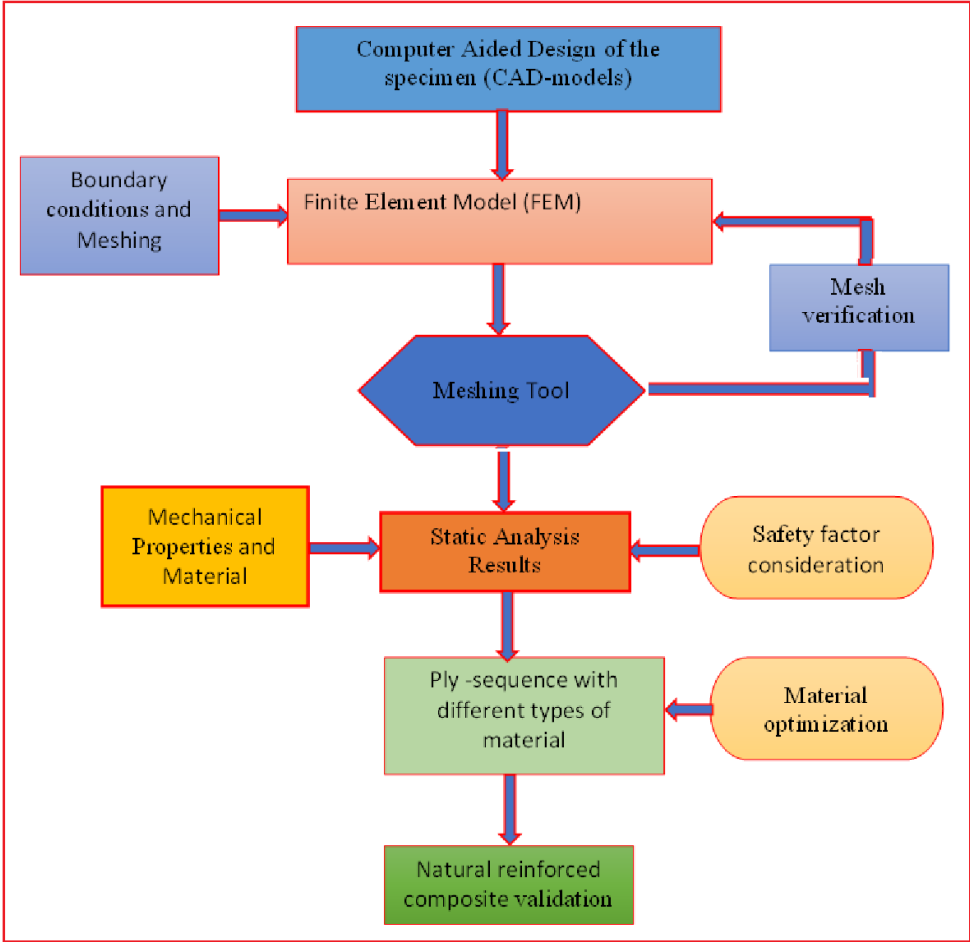


Figure 9. NFRC optimization layout.

3.5 Research methodology

The research focused on the material optimization, for analysis the designs categorized into six cases. Each case optimized the configuration and verified material

properties and behaviour. In Case 1, The thickness of the laminate was 2 mm and the lamina orientations such as $\{0^\circ\}$, $\{30^\circ\}$, and $\{45^\circ\}$. In the 2nd and 3rd Cases, the thickness is 3 mm and 4 mm, respectively, with material strength oriented in the parallel to the x-axis fiber direction. Similarly, Cases 4th, 5th, and 6th involved testing HNRC instead of NFRC. The thickness differences in Cases 1st, 2nd, and 3rd resulted from extra bio fiber layers without E-glass fiber. In contrast, Cases 4th, 5th, and 6th had internal core layers made with E-glass fiber, by increased thickness due to additional natural fiber layers. The design methodology is illustrated in Figure 10.

- ✚ Case 1: NFRC with 2 mm thickness.
- ✚ Case 2: NFRC with 3 mm thickness.
- ✚ Case 3: NFRC with 4 mm thickness.
- ✚ Case 4: HNRC with 2 mm thickness.
- ✚ Case 5: HNRC with 3 mm thickness.
- ✚ Case 6: HNRC with 4 mm thickness.

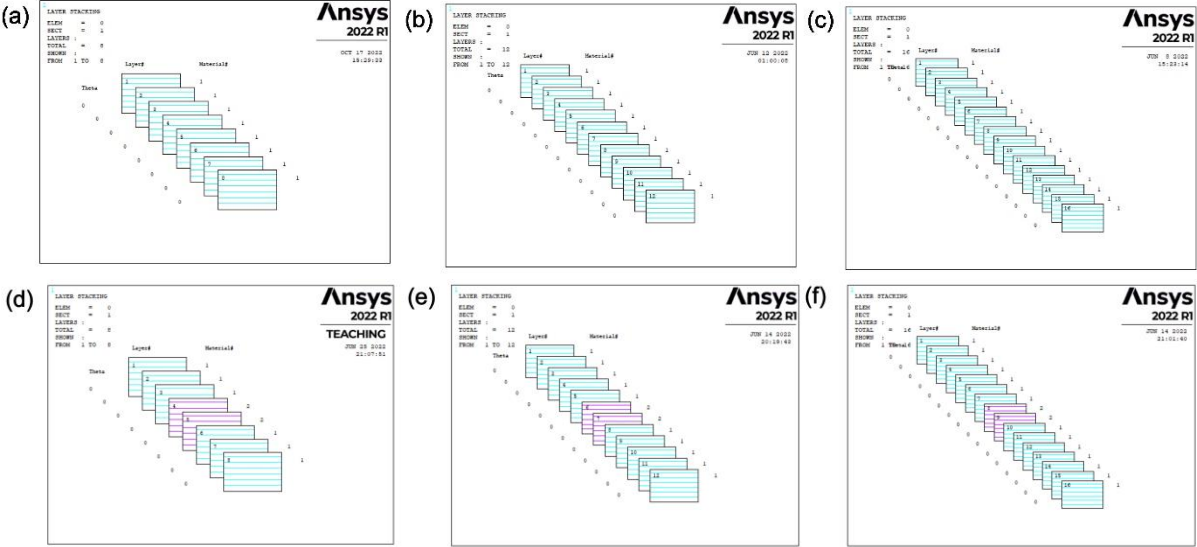


Figure 10. Configuration of ply-orientation for NFRC laminates, (a), (b), (c) Ply-orientation with 2, 3 and 4mm, HNRC laminates (d), (e), (f) Ply-orientation with 2, 3 and 4mm at 0°

3.6 Geometrical modelling procedure

The NFRC consists of a variety of ply orientations and requires a precise ply sequence to optimize the composite material strength and minimize the structure's total weight. In Case 1, the ply orientations are $\{0^\circ\}$, $\{30^\circ\}$, and $\{45^\circ\}$ (balanced laminate), with an $[0^\circ]_8$. The second ply stacking sequence, at 30° , is an angle-symmetric laminate with a

sequence of $[0^\circ/30^\circ/0^\circ/-30^\circ]_8$. The 3rd ply stacking sequence is $[0^\circ/45^\circ/0^\circ/-45^\circ]_8$. The laminates thickness such as 2, 3, 4 mm respectively and epoxy resin is considered. NFRC-woven sheets have dimensions such as 300x50 mm, with fiber thickness ranging from 0.25 to 0.33 mm. These laminas are thin and make natural fiber-reinforced composite structures. The geometrical configuration at various laminates is shown in Fig.11.

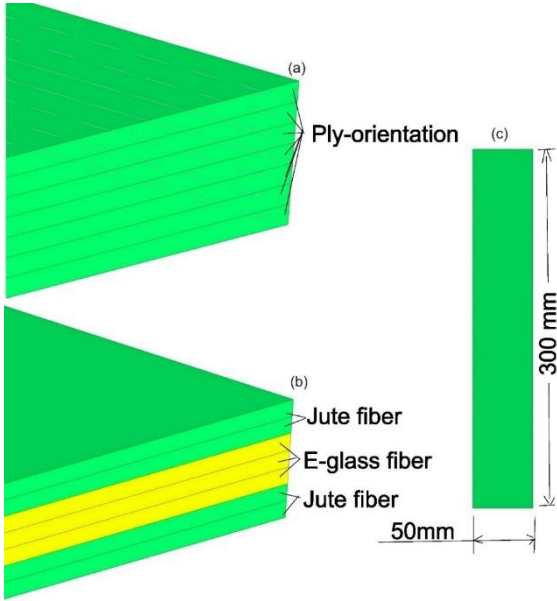


Figure 11. The geometrical configuration of various composite laminates, (a) NFRC, (b) HNRC and (c) Geometrical dimensions.

3.7 Load and boundary strategy

The applied load is longitudinally, with the fiber orientation considered in a unidirectional manner. A boundary condition (Dof-0) is applied at one end, while a static tension load of 2500 N is applied at the other end. The NRFC model is discretized into small elements through meshing. Selecting the appropriate mesh type is crucial as it consists of elements containing nodes. A sweep mesh is used for this research, with a meshing element size of 2 mm, comprising 3926 nodes and 3750 elements of shell 181 type. The geometrical shape of the specimen and boundary conditions are presented in Fig.12.

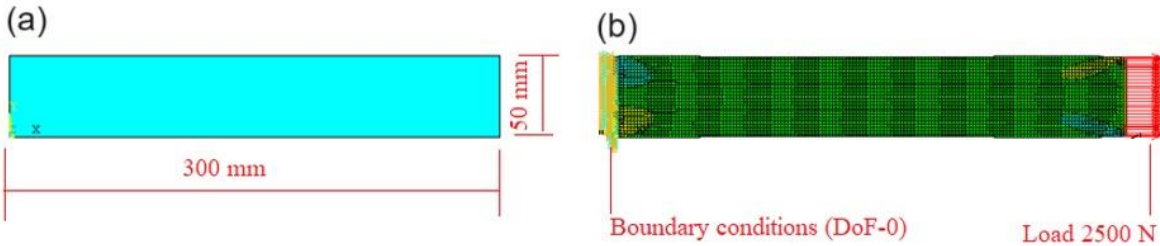


Figure.12. (a) Geometrical dimensions of laminate, (b) Boundary conditions

3.8 Multi-objective optimization methodology by GA

The second optimization approach for composite structures, focusing on the utilization of genetic algorithms. The research work included the optimizing stacking sequences in lightweight composite structures that employs multi-objective evolutionary algorithms. In the optimization framework, were successfully incorporated engineering design standards applicable to stacking sequence design as constraints or supplementary targets. Additionally, were created a new initiation technique based on the real applications to improve the optimization process. The optimization procedure is illustrated in Fig.13. [113]

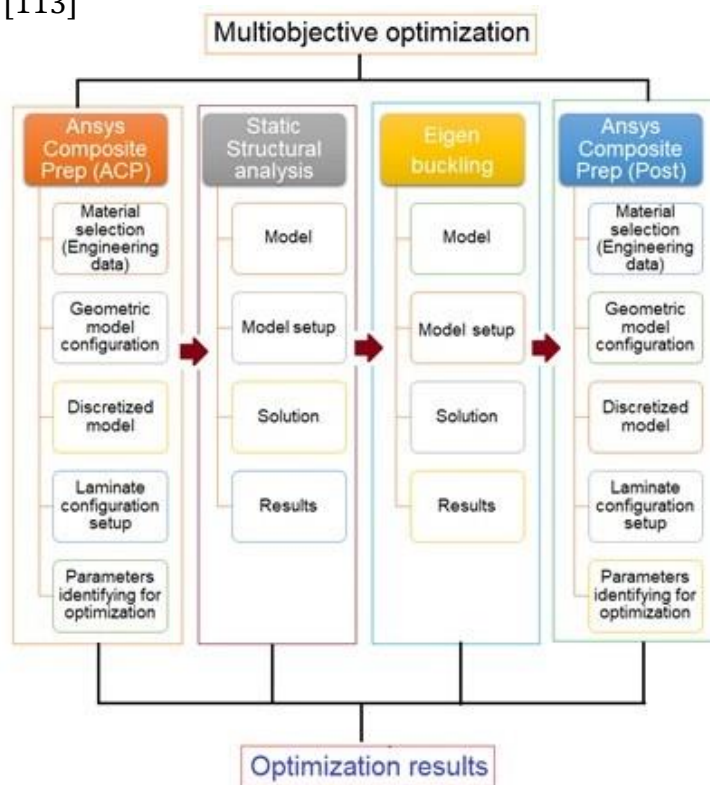


Figure 13. Multi- objective optimization strategy

3.8.1 Optimization statement

To improve the design of the LSS, it's essential to consider various specimen boundary conditions, such as compression and tensile loads. The optimization problem can be outlined as follows:

- ✚ Design variables: The orientation of laminas denoted as $(\theta_k=1, \dots, N)$.
- ✚ Objectives: Minimization of the total number of laminas (N), total weight of the laminate, inverse reserve factor, and total deformation load multiplier.
- ✚ Constraints: The $IRF < 1$ and total deformation load multiplier ($DLM > 1$).

- ✚ Fixed parameters: composite material, specimen geometrical dimensions, boundary conditions, and lamina angle discretization at $\{0^\circ, 30^\circ, 45^\circ, 60^\circ, \text{ and } 90^\circ\}$.

3.8.2 Optimization methodology

Multi-objective genetic algorithms (MOGAs) are material optimization approaches based on Darwinian evolutionary concepts. They are used to resolve the material optimization difficulties with several, seemingly competing aims. MOGAs, which mimic natural selection, crossover, and mutation processes, yield a collection of optimal solutions known as the Pareto front, which depicts the trade-offs between various objectives. ANSYS Workbench provides tools and interfaces for integrating MOGAs into the optimization process. These tools enable users to establish objectives, constraints, and design variables. MOGAs are then used to explore the design space and determine the Pareto front, which represents the best trade-off solutions. The benefits of using this optimization approach (MOGAs in ANSYS Workbench) include the ability to quickly explore many design options and identify the best trade-off solutions. MOGAs allow engineers to explore a variety of solutions that reflect the trade-offs between numerous objectives. MOGAs provide a Pareto front, which affords engineers with a thorough understanding of design trade-offs, allowing them to make more informed decisions.

3.8.3 Design recommendations

The optimizing the LSS using a multi-objective genetic algorithm approach. Several key guidelines were followed for the initial LSS design, based on earlier laboratory tests and analyses. Prior research has emphasized the need for a balanced stacking sequence, including an equivalent number of $+\theta$ and $-\theta$ plies and ensuring laminate symmetry about the midplane to avoid shear-extension coupling ($A_{16} = A_{26} = 0$) and extension-bending coupling ($B_{ij} = 0$). To minimize laminate matrix propagation (contiguity constraint), laminas with the same direction and thickness should be avoided. Additionally, successive lamina directions should not vary by more than $\{45^\circ\}$ to avoid edge delamination (disorientation constraint). For designs where material strength is crucial, a homogeneous LSS is recommended. When using lamina with angles such as $+\theta$ and $-\theta$, they should be placed close together to reduce bending-twisting coupling effects, precisely D_{16} and D_{26} . Detailed LSS guidelines are provided in [114]. Following these LSS

design rules, the elastic features of a symmetrical and balanced laminate is defined by 6 stiffness parameters A_{11} , A_{22} , D_{22} , D_{66} , D_{26} , and D_{16} should be minimized.

3.8.4 Analysis setup

The dimensions of the composite laminate used were 140 mm length, 12 mm in width, and 0.15 mm in thickness, following ASTM standards. The load and boundary conditions are illustrated in Fig.14.

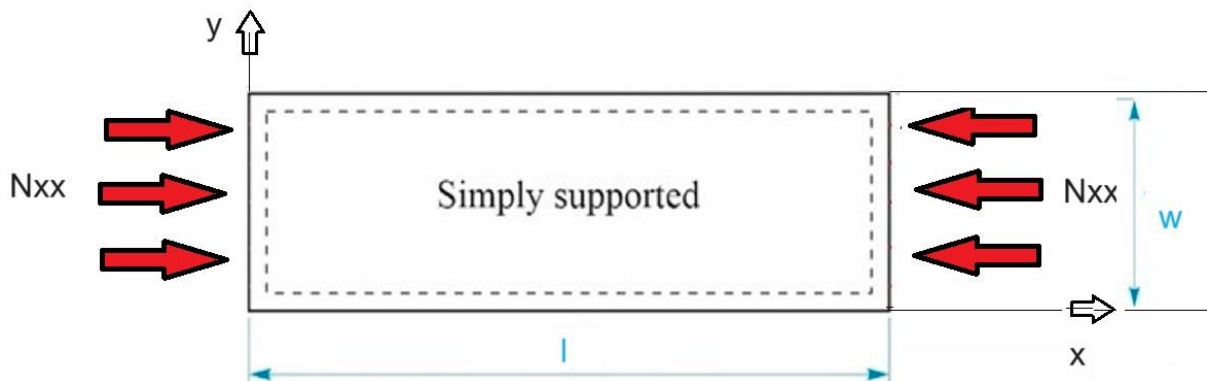


Figure 14. Loading and boundary conditions.

The composite plate was simply supported at all edges, with a unidirectional load of $N_{xx} = 250$ N applied. Shell elements were used for the simulations, and the number of elements and nodes was determined using a sweep mesh. Due to the thinness of the bidirectional fabric (0.15 mm), the laminate thickness is 2 mm. The contiguity constraint obligatory at minimum two adjacent layers to have the same direction. The reference LSS design consisted of 16 plies, arranged as $[\pm 45_2/90_2/0_3/90_2/0_3/90_2/\pm 45_2]$. The mechanical properties of bio-composite such as, $E_1=45$ GPa, $E_2=10$ GPa, $\nu_{12}=0.3$, $G_{12}= 5$ GPa, $X_t=780$ MPa, $X_c= 480$ MPa, $Y_t= 31$ MPa, $Y_c=10$ MPa and $Sc=MPa$.

3.8.5 Fabrication of composite laminate

The laminates were fabricated based on optimal LSS results, using various configurations available bidirectional woven E-glass fiber. This fiber had a thread count of 16×15 (16 yarns in the warp direction and 15 in the weft direction per centimetre, labeled as (GF-22-100-100) and was reinforced with LB2 epoxy bio-resin (EP-LB_10). The E-glass fiber featured an area density of 100 g in a 2×2 twill woven pattern and had a

material thickness is 0.15 mm. The epoxy resin and hardener were mixed with a ratio of 100:27. The composite optimization strategy is illustrated in Figure 15.

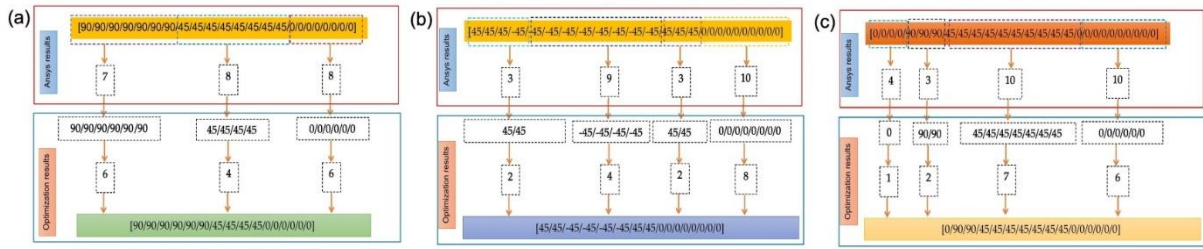


Figure 15. Optimization strategy (a) Laminate 1, (b) Laminate 2, (c) Laminate 3.

Composite laminates were produced using the hand-layup method with a vacuum bagging process, incorporating various lamina orientations in the LSS. The LSS design was categorized based on Ansys analysis results, which yielded stacking sequences of 24 laminas as $\{90_7/45_8/0_8\}$, 25 laminas as $\{45_3/-45_9/45_3/0_{10}\}$, and 27 laminas as $\{0_4/90_3/45_{10}/0_{10}\}$. Following the Ansys results, the number of laminas was systematically reduced to attain the specified thickness for mechanical testing, adhering to ASTM testing recommendations. For Laminate 1, the design methodology involved transitioning from $[90]_7$ to $[90]_6$, $[45]_8$ to $[45]_4$, and $[0]_8$ to $[0]_6$. This same methodology was applied consistently to Laminate 2 and Laminate 3. The optimized stacking sequences were,

- Laminate_1 $\{90_6/45_4/0_6\}$
- Laminate_2 $\{45_2/-45_4/45_2/0_8\}$
- Laminate_3 $\{0/90_2/45_7/0_6\}$
- Laminate_4 $\{45/-45/90_2/0_3/90_2/0_3/90_2/-45/45\}$ - reference laminate.

The optimized LSS results were compared with the reference stacking sequences, which served as the basis for the initial optimization in this research.

3.9 Sandwich structure design and analysis

This study aims to design and analyze composite sandwich structures with the goal of optimizing material weight while enhancing material strength to reduce aerodynamic loads. The research involves analyzing material stability and mechanical properties to develop thin-walled composite materials. Since material failure modes occur during operational loads, including debonding at core-facing interfaces, indentation failure under concentrated loads, core material failures, compression wrinkling above the core

face, and global buckling, it is crucial to address these issues. To do so, core materials are analyzed alongside skin materials using scale models, followed by the creation of CAD models with various geometric parameters analyzed in ANSYS. Simulation results are compared with results from multiple models and mechanical properties to determine the most effective approach for ensuring material stability. A novel corrugated material is proposed as the core material, with layers formed by Epoxy Carbon fibers UD and glass-epoxy fibers planned for the skin. This combination of materials in different proportions aims to resolve the aforementioned issues and achieve lightweight, high-strength material preparation.

3.9.1 Material design methodology

In this research, the materials used for constructing thin-walled composite sandwich CAD models feature a corrugated core. The face layers (skin) comprise epoxy Carbon fibers, while the core material consists of epoxy carbon (UD) fibers. Common parameters considered in this study include the composite panel aspect ratio, mechanical properties of the core and skins, the thickness of the core and skins, and boundary conditions. The novel proposed sandwich structure is presented in Fig.16.

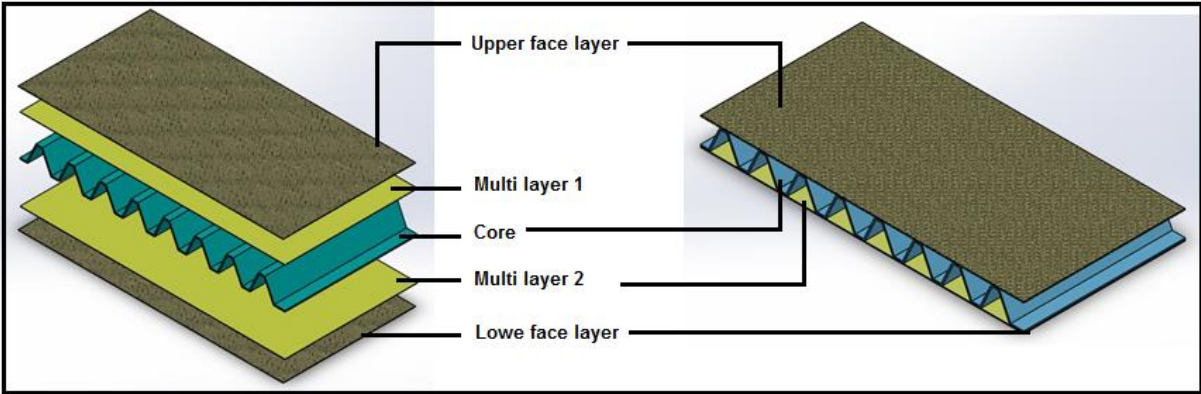


Figure 16. Novel sandwich structure schematic diagram.

3.9.2 Design constraints

The material stiffness formulas are derived using a combination of micromechanics methodology and laminate theory to determine the equivalent properties of a corrugated (z)-cored structure. This approach facilitates the determination of equivalent in-plane and bending stiffnesses, as well as longitudinal and transverse shear stiffnesses, which are all considered in the present study. Additionally, the assumptions of laminate theory are taken into account in this research.

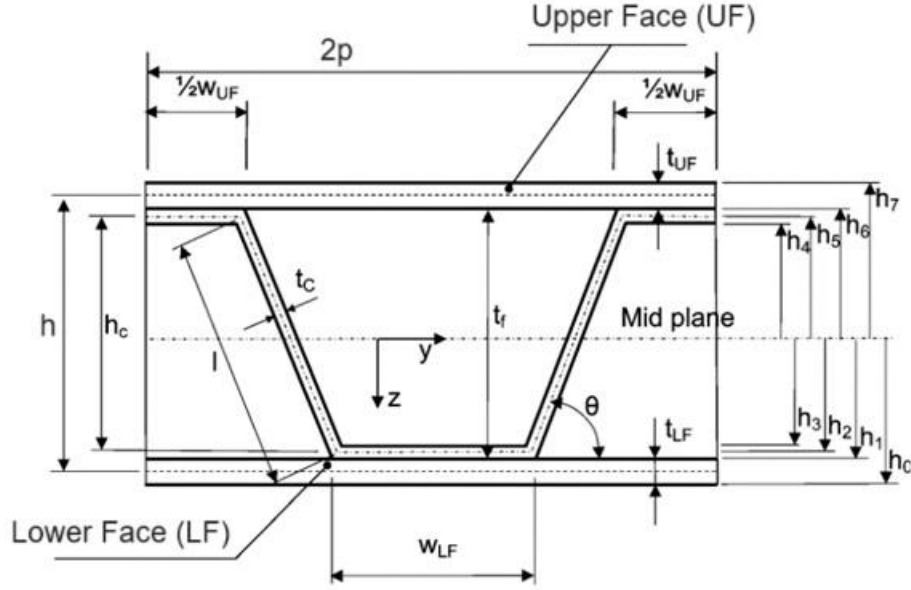


Figure 17. The geometrical parameters with corrugated (z) -core sandwich panel

3.9.3 Stiffness terms since laminate theory

The subsequent model considers the sandwich panel membrane, the membrane with bending coupling, and finally the bending stiffness conditions for single corrugated z-core sandwich panels [115].

$$(A_{ij}, -2B_{ij}, 3D_{ij}) = \sum_{k=1}^{\eta} \frac{((h_{k-1})^m - (h_k)^m)}{2p} \cdot (\bar{Q}_{ij})_k \cdot \left[w_k \text{ or } \frac{t_k}{\sin \theta} \right] \quad (3.1)$$

Where, A is the composite structure extensional stiffness matrix, B is the composite structure membrane bending coupling stiffness matrix, D is the composite structure bending stiffness matrix, Q is the composite structure transformed reduced layered elasticities of the laminae, p is the corrugation pitch of sandwich panel, k is the identification subscript of layer or stiffening element, h is the height of the layer from the midplane of the sandwich panel (i.e. the reference plane), m is the subscript for A , B , and D stiffness components (equal to 1,2 or 3) and w , t , θ are the width, thickness, and angle of the stiffening element, respectively. The corrugation panel (core) is oriented at an angle to the reference plane, rendering the panel structure heterogeneous. This can be represented by dividing its thickness by the sine of the inclination angle, allowing for the

consideration of each panel segment and its shape. However, it is important to note that the limitations of this approach mirror those found in lamination theory.

Equation (3.1) above represents the calculation of the fundamental stiffness. The formula for longitudinal stiffness can be expressed as:

$$\begin{aligned}
(A_{1,1}, -2B_{1,1}, 3D_{1,1}) = & (\bar{Q}_{LF})_{1,1} \cdot (h_1^m - h_0^m) + \frac{(\bar{Q}_C)_{1,1} \cdot (h_3^m - h_1^m)}{2p} w_{LF} \\
& + \frac{(\bar{Q}_C)_{1,1} \cdot (h_6^m - h_4^m)}{2p} w_{UF} + \frac{(\bar{Q}_C)_{1,1} \cdot (h_5^m - h_2^m)}{p} \frac{t}{\sin \theta} \\
& + \frac{(\bar{Q}_F)_{1,1} \cdot (h_5^m - h_2^m)}{2p} (w_{UF} + w_{LF}) + (\bar{Q}_{UF})_{1,1} \cdot (h_7^m - h_5^m)
\end{aligned} \quad (3.2)$$

In this context, the subscript "C" denotes the corrugation, "F" denotes the foam material, and "LF" and "UF" denote the lower and upper faces, respectively. When considering stiffness perpendicular to the corrugation direction (i.e., along the *z*-axis) and the 12 coupling stiffness terms, it is assumed that the contribution of the corrugation is restricted to the segments lying within the plane of the panel. This is because the "accordion" shape of the corrugation makes it highly compliant in the transverse direction.

$$\begin{aligned}
(A_{i,j}, -2B_{i,j}, 3D_{i,j}) = & (\bar{Q}_{LF})_{i,j} \cdot (h_1^m - h_0^m) + \frac{(\bar{Q}_C)_{i,j} \cdot (h_3^m - h_1^m)}{2p} w_{LF} \\
& + \frac{(\bar{Q}_C)_{i,j} \cdot (h_6^m - h_4^m)}{2p} w_{UF} \\
& + \frac{(\bar{Q}_F)_{i,j} \cdot (h_5^m - h_2^m)}{2p} (w_{UF} + w_{LF}) + (\bar{Q}_{UF})_{i,j} \cdot (h_7^m - h_5^m)
\end{aligned} \quad (3.3)$$

3.9.4 In-Plane Constants

Equation (3.1) presents the stiffness terms of the panel, computed by summing the contributions of all layers or stiffening elements. For a laminated composite plate, the equivalent engineering constants can be determined as follows [116].

$$E_x = \frac{1}{h \cdot a_{11}}; \quad E_y = \frac{1}{h \cdot a_{22}}; \quad G_{xy} = \frac{1}{h \cdot a_{33}} \quad (3.4)$$

the Poisson's ratios follow,

$$v_{xy} = -\frac{a_{12}}{a_{11}}; v_{yx} = -\frac{a_{12}}{a_{22}} \quad (3.5)$$

where, h is the distance between the centerline of the upper and lower skin and the a_{ij} terms are the components of the compliance matrix.

3.9.5 Extensional Stiffnesses matrix of sandwich panel

For symmetrical composite sandwiches, an alternative to the equation can be derived from the correlation between force and deformation in both the longitudinal and transverse directions, as depicted in Fig.18.

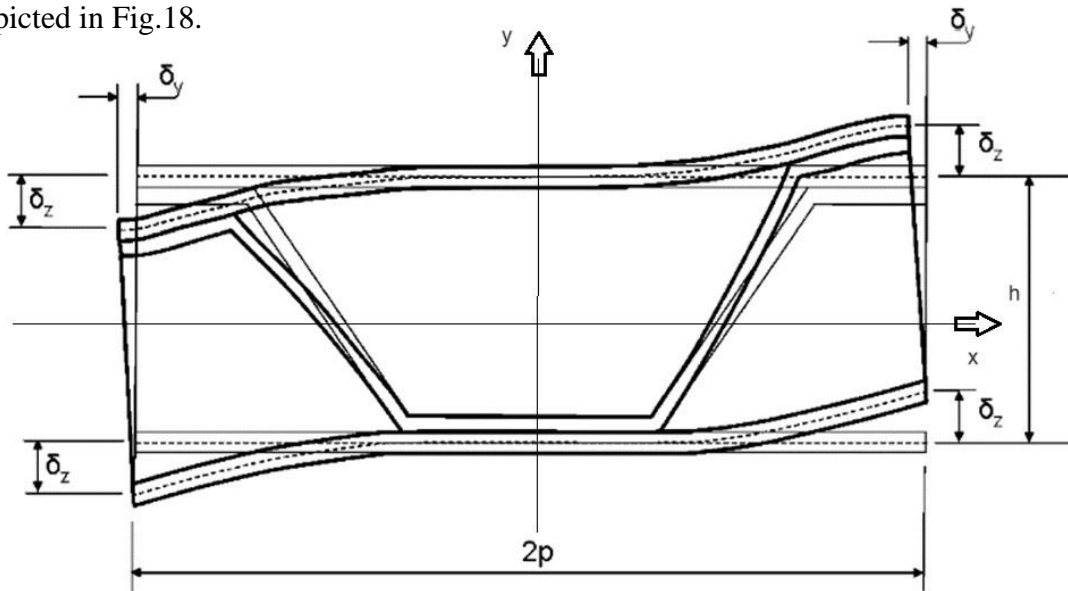


Figure 18. Deformation of a corrugated (z)-core sandwich panel subjected to transverse shear in planes perpendicular to the corrugation.

$$E_x = \overline{EA}_x$$

$$E_y = \frac{\overline{EA}_y}{1 - v_1^2 \cdot \left(1 - \frac{\overline{EA}_y}{\overline{EA}_x}\right)} \quad (3.6)$$

where,

$$\frac{\overline{EA}_x}{\overline{EA}_y} = \frac{E_C \overline{A}_C + 2 \cdot E_1 \cdot t_1}{2 \cdot E_1 \cdot t_1}$$

The EC modulus of elasticity of core material, AC area, per unit width, of corrugation cross section perpendicular to corrugation axis, $E1$ modulus of elasticity of the upper and lower skin $t1$ skin thickness, $\nu1$ Poisson's ratio of the skin material, The Poisson's ratios associated with expansion are given,

$$\nu_{xy} = \nu_1; \text{ and } \nu_{yx} = \nu_{xy} \cdot \frac{E_y}{E_x} \quad (3.7)$$

3.9.6 Bending Stiffness of sandwich structure

The bending stiffnesses follows [109-110],

$$D_x = \overline{EI}_x \quad (3.8)$$

$$D_y = \frac{\overline{EI}_y}{1 - \nu_1^2 \cdot \left(1 - \frac{\overline{EI}_y}{\overline{EI}_x}\right)} \quad (3.9)$$

Where,

$$\frac{\overline{EI}_x}{\overline{EI}_y} = \frac{E_C \bar{I}_C + \frac{1}{2} \cdot E_1 \cdot t \cdot h^2 + \frac{1}{2} \cdot E_C \cdot t_C \cdot h_C^2 \cdot \left(\frac{w_{UF} + w_{LF}}{2p}\right)}{\frac{1}{2} \cdot E_1 \cdot t \cdot h^2}$$

I_C is the moment of inertia, per unit width, of corrugation cross section area about the mid-plane and t is the skin thickness (assumed to be the same for both skins in this case).

3.9.7 Transverse shear stiffness of sandwich structure

When deriving the transverse shear stiffness in planes parallel to the corrugation, we must consider an element of the z -core sandwich with a length, dx , and width, $2p$, subjected to a transverse shear, D_x . The transverse shear is balanced by the variation of bending moment, DM , along the element. Assuming that the only source of flexibility in the element is the corrugation in shear, the transverse shear stiffness can then be expressed as

$$D_{Q_x} = \frac{Q_x}{\gamma_x} = G_C \cdot t_c \cdot \frac{I \cdot h}{p \cdot \int_0^l Q ds} \quad (3.10)$$

Where, Q_x the angle representing the average shear strain, equal to $\delta x/h$; I is the moment of inertia of width $2p$ of cross section parallel to yz -plane; p is the corrugation pitch; l is the length of one corrugation leg measured along the center line; Q is the static moment about the middle plane of the sandwich.

$$D_{Q_x} = G_C \cdot t_c \cdot \frac{\frac{h^2 \cdot t}{p \cdot 2d \cdot t_c} + \frac{1}{6} \cdot \left(\frac{h_c}{p}\right)^2}{\frac{t}{t_c} + \frac{2d \cdot h_c}{3ph}} \quad (3.11)$$

This can be further simplified by solely considering the skin contribution to bending stiffness, resulting in a constant shear flow in the corrugation. This simplification leads to the following calculation.

$$D_{Q_x} = \frac{G_C \cdot t_c^2}{A_c} \cdot \left(\frac{h}{p}\right)^2 \quad (3.12)$$

Where, A_c represents the cross-sectional area of the corrugation per unit width, and t_c denotes the thickness of the corrugation.

3.10 Light aircraft wing skin as a carrier for photovoltaic cells

The solar collection system integrated onto the surface of UAV wings is an efficient energy solution harnessing solar power. Recognized as renewable energy, it caters to the power needs of UAVs operating at both high and low altitudes with extended endurance. UAVs, renowned for their lightweight design, demonstrate remarkable performance across diverse applications.

This research endeavors to develop an ultra-lightweight photovoltaic composite structure (UPCS) tailored to the geometrical specifications of TS17 UAVs. To enhance the flexibility of solar cells, the innovative approach involves embedding solar panels within the wing structure and designing a lighter wing to accommodate photovoltaic panels. Material properties are investigated across various skin (laminate) and core thicknesses using Finite Element Method (FEM) software. The simulation analysis best results will be used for the UAV wings [117-125].

3.10.1 Wing construction methodology

The design concept involves embedding solar cells into the composite wing structure. We fabricated small-scale samples, each containing a single solar cell, using various lamination processes to assess the impact on solar performance and durability resulting from this embedding. We then evaluated these samples at various testing stages. We used this approach to test solar cells on a small scale, gaining insights that we could apply to larger arrays embedded into actual wings. We tested four distinct laminate conditions for embedding photovoltaic cells into composites. Fig.19 presents the information about these conditions.

- ✚ No laminate (L1): cells would remain exposed on the wing's surface.
- ✚ Fiberglass (L2): A layer of fiberglass on the wing's surface would embed cells.
- ✚ Polyurethane Film (L3): The wing's surface would embed cells beneath an abrasion-resistant polyurethane film.
- ✚ Polyurethane Film with fiberglass (L4): For more stiffness the additional glass fiber layer added.

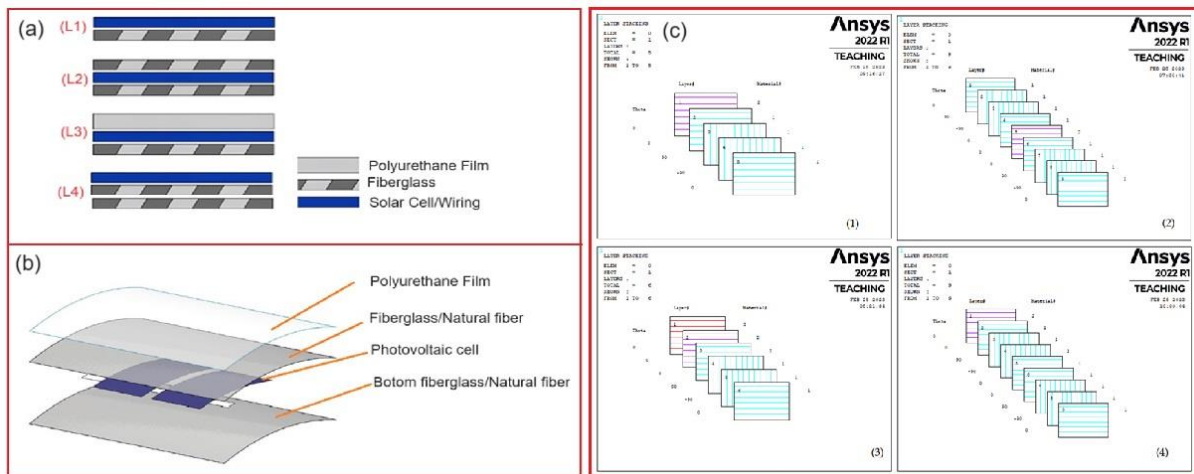


Figure 19. (a) Design concept of the photovoltaic cell embedded into the wing, (b) Exploded view of the photovoltaic cell and (c) Ply orientation configuration for laminate_1, 2, 3 and 4.

4. Case study_1&2

4.1 *Design of composite sandwich T-joint*

This chapter discusses the case study (doctoral dissertation), in detailed optimization and design methodology is addressed in detail. Airframe structures consist of fundamental components that are interconnected to form a channel for the transmission of loads. The joints serve as potential areas of vulnerability and play a pivotal role in determining the overall efficiency of the composite structure. The importance of T-joints in aircraft wings made of composite materials resides in their complex geometry and their crucial function in sustaining the overall structural integrity. These joints repeatedly fail because of transverse normal and shear stresses. This is mostly attributable to the lack of reinforced fibers oriented perpendicular to the laminate plane. Therefore, resin predominates, resulting in diminished interlaminar strength qualities. Therefore, the strength of the single laminates greatly restricts the strength of T-joints in the out-of-plane direction. When a force is applied in a direction perpendicular to the plane, it results in many types of stresses, including interlaminar normal stress (σ_z), interlaminar shear stresses (τ_{yz} and τ_{xz}), and in-plane stress (σ_y). The failure of T-joints is a result of all these elements.

According to reports, transverse normal loads are the primary cause of composite T-joint failure, particularly near the interface of the web and skin. To achieve more accurate failure predictions, we must develop a method to precisely estimate the magnitude of these transverse normal stress components at the web/skin juncture. Only a three-dimensional method can achieve this level of accuracy in determining the transverse stress components [126]. The weak interlaminar strength properties make it possible to look at and predict possible failures in areas with a lot of stress. Transverse normal stresses play a critical role at the web/skin interface as they can induce failure, particularly in static loading scenarios [127]. Researchers have managed wide examines on the failure causes of both bonded and bonded/bolted single-lap joints [128]. However, most of the research on T-joints has concentrated on adhesively bonded lap joints. Interestingly, there has been a lack of investigation into T-joints bonded to natural fiber composites. The design of T-joints varies depending on their intended applications [129-130]. The conventional T-joint design for sandwiches typically involves incorporating elements such as a base core drop-off and merging the upper and lower composite surfaces to form a cohesive laminate at the joint area. However, this manufacturing method is complex and costly. Fibers like carbon, glass, and Kevlar, which can be expensive, often reinforce composite

materials. Conversely, there are natural fibers, such as those discussed by Ganesan et al. [131], which are cost-effective, biodegradable, and simpler to work with. These natural fibers find widespread use in aerospace, automotive, and various other sectors due to their eco-friendliness and biodegradability. The doctoral dissertation is addressed the optimized methodology for construction of TS 17 UAVs wing. The process flow chart provided in Fig.20.

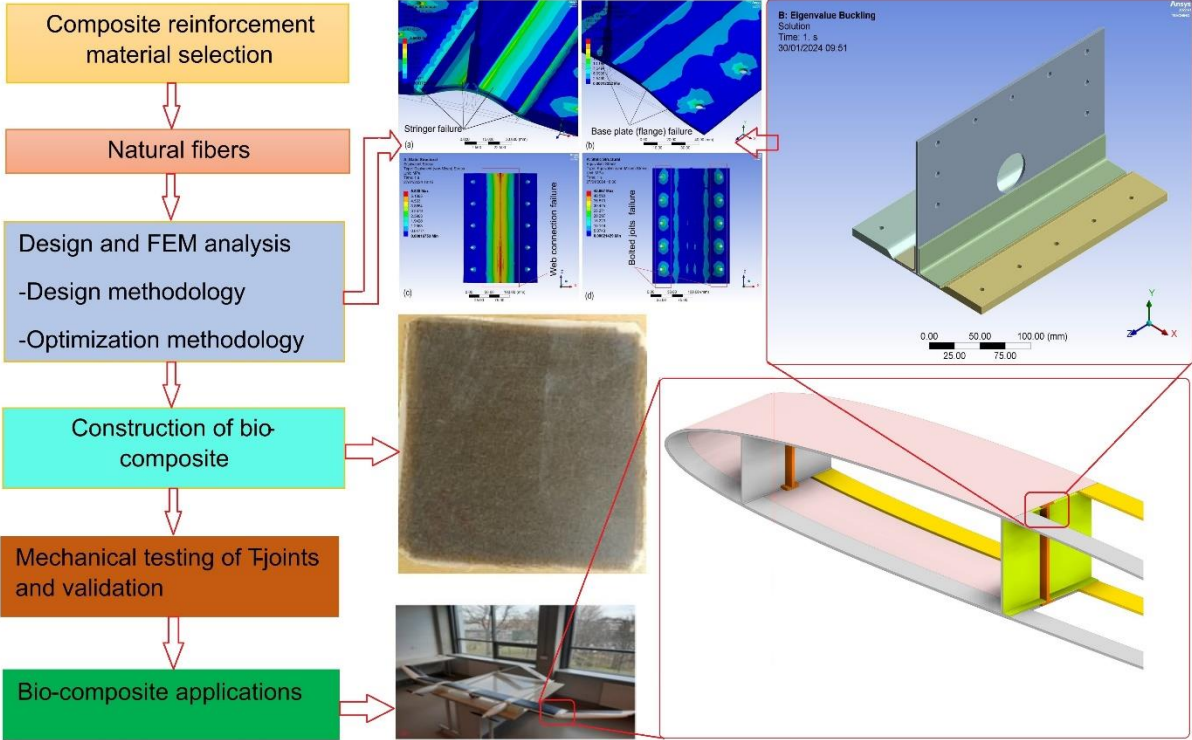


Figure 20. Process flow layout for Sandwich T-joint.

This study expands upon the investigation of composite-bonded T-joint structures with different geometric configurations. We conducted the structural analysis using Ansys software. Experimental testing includes compressive, tensile, and flexural tests to evaluate the failure characteristics and strength of the bio-composites.

4.2 Design methodology

Two flat panels, one serving as a base and the other as a web, were configured into a T-shape and connected at a right angle using two L-shaped stringers. The dimensions of the base panel, measuring 180 mm wide by 260 mm long, and the web panel, measuring 150 mm high by 260 mm long, are depicted in Fig.21.

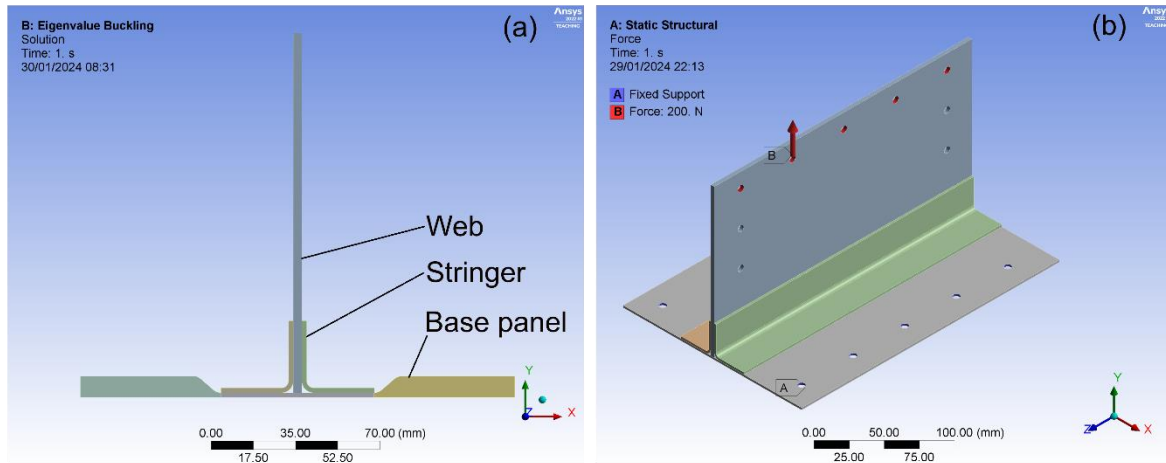


Figure 21. Sandwich T-joint, (a) CAD model parts, (b) load and boundary conditions

The web panel comprised a 3.5 mm-thick composite laminate surface consisting of 10 layers of 0.35 mm-thick jute-epoxy woven fabric symmetrically oriented at $[\pm 45]$ degrees. Each composite face on the base was constructed using ten layers of the same jute-epoxy woven fabric, symmetrically arranged, with a ply thickness of 0.35 mm. A monolithic laminate was adhered to the laminate base in the joint area where the composite faces merged seamlessly. To connect the two panels, two L-shaped stringers, made of 2 mm-thick jute-epoxy woven fabric, were affixed to the web and base panel surfaces. Epoxy glue was used to fill the triangular space between the web, base panel, and stringers in the joint region.

In this study, we created four distinct geometric patterns, each showcasing a variety of forms. Design 1 comprises a web, a flange, and two L-shaped stringers. The entire model incorporates jute fiber material to evaluate both the failure region and material strength. Design 2 mirrors the geometric shape of Design 1 but introduces a hole in the web section. Designs 3 and 4 diverge entirely from the preceding designs. Although Designs 3 and 4 share a similar geometric structure, the design 4 incorporates a hole in the web section. Fig.22 illustrates the geometric designs.

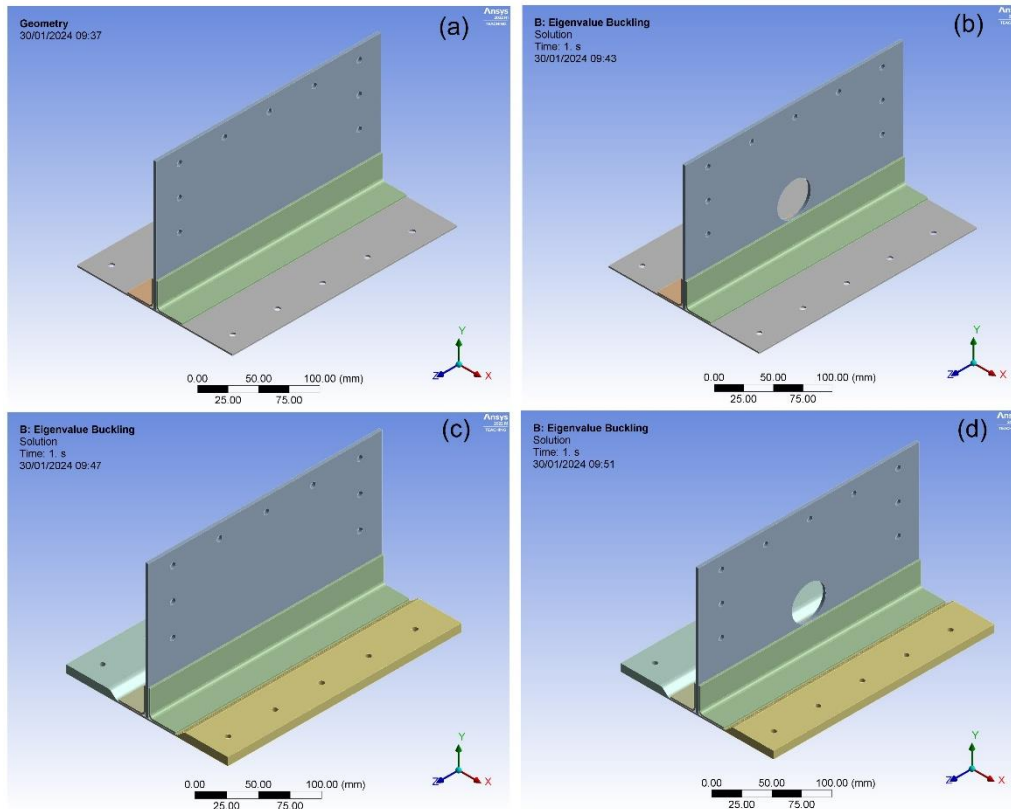


Figure 22. Sandwich T-joint CAD model with different configurations. (a) design 1, (b) design 2, (c) design 3 and (d) design 4.

4.3 Structural failure of the laminates

Composite materials are renowned for their blend of lightweight properties and high strength, surpassing the mechanical qualities of alternative materials like aluminium. These attributes exhibit variability in both transverse and longitudinal orientations. However, under certain extreme conditions, composites may encounter stability issues or induce structural damage. Kumpati et al. [7],[132] discussed methods for characterizing these materials, noting that composites are particularly vulnerable to damage in two specific scenarios: when material impairment begins with a minor crack (arising possibly from the manufacturing process), leading to the propagation of damage. These challenges often emerge prior to the actual material damage. The criteria for failure in composite laminates are expressed mathematically, as detailed by equations from Goumgh et al. [133], Alawar et al. [134-137], and Kumpati et al. [10].

Bio- composite tension/shear

$$\left(\frac{E_1(\varepsilon_1)}{X_{1T}}\right)^2 + \left(\frac{G_{31}(\varepsilon_{31})}{S_{FS}}\right)^2 = r_7^2 \quad (4.1)$$

Natural composite structure at compression

$$\left(\frac{E_1(\varepsilon_1)}{X_{1c}}\right)^2 = r_8^2 \varepsilon_1 = -\varepsilon_1 - (\varepsilon_3) \frac{E_3}{E_1} \quad (4.2)$$

Natural composite structure tension/shear

$$\left(\frac{E_2(\varepsilon_2)}{X_{2T}}\right)^2 + \left(\frac{G_{23}(\varepsilon_{23})}{S_{FS}}\right)^2 = r_9^2 \quad (4.3)$$

Natural composite structure compression

$$\left(\frac{E_2(\varepsilon_2)}{X_{2c}}\right)^2 = r_{10}^2 \varepsilon_2 = -\varepsilon_2 - (\varepsilon_3) \frac{E_3}{E_1} \quad (4.4)$$

Natural composite structure damage

$$\left(\frac{E_3(\varepsilon_2)}{S_{Fc}}\right)^2 = r_{11}^2 \quad (4.5)$$

Natural composite structure shear failure

$$\left(\frac{G_{12}(\varepsilon_{12})}{S_{12}}\right)^2 = r_{12}^2 \quad (4.6)$$

Natural composite structure shear failure

$$S^2 \left(\frac{E(\varepsilon_3)}{S_{3T}}\right) + \left(\frac{G_{23}(\varepsilon_{23})}{S_{23}}\right) + \left(\frac{G_{31}(\varepsilon_{31})}{S_{31}}\right)^2 = r_{13}^2 \quad (4.7)$$

In Equation (4.1-4.7), the variables X_{1T} , X_{1c} , X_{2T} , and X_{2c} signify the longitudinal tensile and compressive strengths in direction_1, as well as the transverse tensile and compressive strengths in direction_2, respectively. S_{Fc} , S_{FS} and S_{3T} represent the natural fiber damage strength under shear, tension (in direction_2), and material tensile strength. Similarly, S_{12} , S_{23} , and S_{31} denote the shear strength of the natural fiber composite matrix in modes 12, 23, and 31.

The symbol S in the equation denotes the material delamination scaling factor, while r_{7-13} indicates the material damage thresholds. Additionally, G_{12} , G_{23} , and G_{31} correspond to the shear modulus of the natural fiber composite matrix in directions 12, 23, and 31. Finally, E_1 , E_2 , and E_3 represent Young's modulus of the natural fiber composite matrix in different directions.

4.4 Optimization methodology

Utilizing a straightforward sandwich T-joint design without removing the core foundation could achieve both cost efficiency and simplicity in manufacturing. This alteration could also improve the bending stiffness of the base panel. To evaluate this novel approach, four different designs with various base core materials were simulated and examined.

For optimizing the composite T-joint structure, we utilized three different reinforcement materials: jute fiber, E-glass, and PVC foam, with epoxy resin as the adhesive. We conducted the entire investigation using Ansys Workbench, establishing three analysis cases. In the first case (Case 1), the analysis covers the entire set of designs (Designs 1 to 4) using epoxy jute fiber. In the second case (Case 2), E-glass material is employed throughout designs 5 to 8. The third case (Case 3) involves a sandwich configuration, where the web is constructed of PVC foam, the stringers are made of jute fibers, and the flange is composed of PVC foam; this setup is applied to Designs 9 to 12. The mechanical properties are summarized in Table 2.

Table 2. Mechanical properties of composite materials [12]

Material type	E_1 (GPa)	E_2 (GPa)	X_t (MPa)	X_c (MPa)	Y_t (MPa)	Y_c (MPa)	ν_{12}	τ_{12} (MPa)
Epoxy Jute	4.89	0.489	6.4	-7.05	0.642	-0.705	0.25	20.10
E-glass	4.5	1.0	1.1	-6.75	3.5	-1.2	0.3	80
PVC foam core	0.07	-	-	-	-	-	0.3	26.9

4.5 Analytical information of composite bonded T-joints

The static analysis covered all design cases, from 1 to 3. The term "static" refers to the condition where applied forces remain constant over time, or any time variation is considered insignificant and can be disregarded safely. This type of analysis assesses the effects of consistent loading conditions on a structure, excluding inertia and damping effects resulting from time-varying loads. It may involve steady inertia loads such as gravity and rotational speed, as well as time-varying loads that are essentially equivalent to static loads.

Static analysis aims to determine displacements, stresses, strains, and forces in structures or components subjected to loads that do not induce significant inertia and damping effects. It assumes steady loading and response conditions, implying that both the loads and the structure's response change slowly with respect to time. Examples of loading applicable in static analysis include externally applied pressures, steady-state inertia

forces (e.g., gravity or rotational velocity), imposed displacements, and temperatures (for thermal strains). The static analysis equation is expressed as follows:

$$\{k\} \{u\} = \{f\} \tag{4.8}$$

Here, considering the geometry and properties, 'K' represents the system stiffness matrix automatically generated by ANSYS for Windows. 'f' signifies the vector of applied forces specified by the user, while 'u' is the vector of displacements computed by ANSYS. After calculating displacements, ANSYS employs this information to determine element forces, stresses, reaction forces, and strains.

The geometrical model was constructed in Inventor with boundary conditions applied at the base plate, functioning as a flange, where bolted joints include circular holes on the surface with all degrees of freedom set to zero (DOF-0). Nodal displacements (*UX*, *UY*, *UZ*, *ROTX*, *ROTY*, and *ROTZ*) are constrained. Simultaneously, a static tension load of 200 N is applied to the web panel, where the bolted joints are located, featuring circular holes. The load and boundary conditions are depicted in Figure 23b. The designed models undergo discretization into small elements during the meshing process. The meshed model is shown in Fig.23.

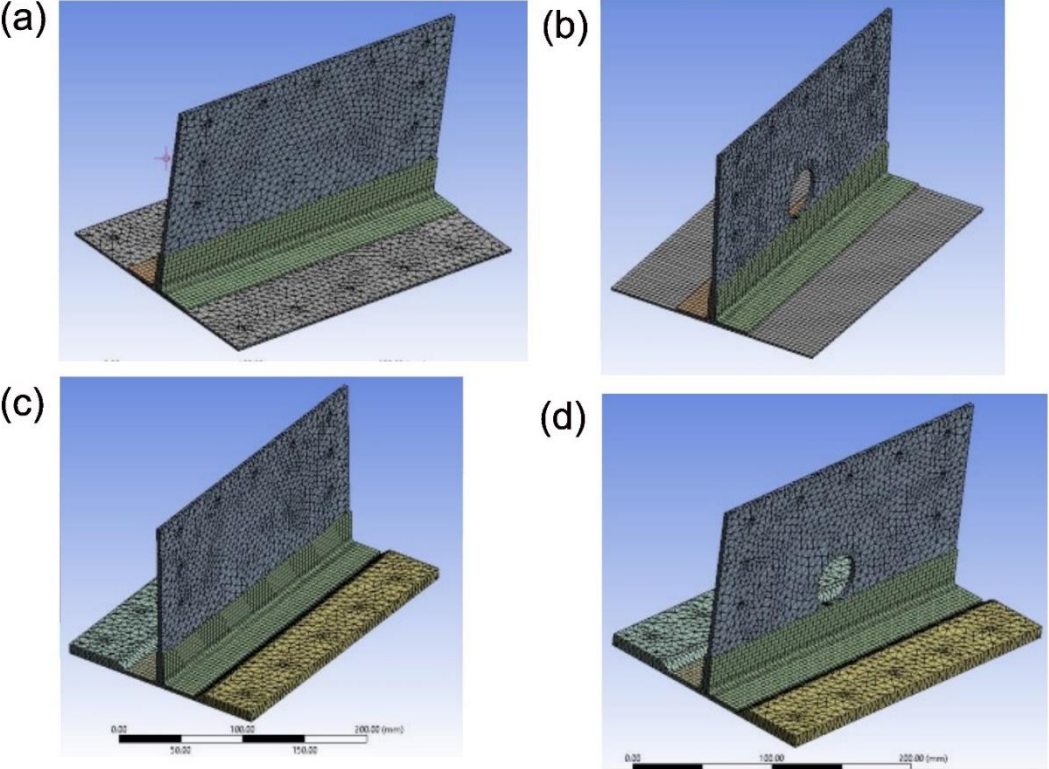


Figure 23. FEM models (a) design 1, (b) design 2, (c) design 3, (d) design 4.

The choice of mesh type is crucial, as it determines the elements that contain nodes. This study employs a combination of sweep and mapped mesh techniques, setting the meshing element size to 4 mm and employing shell elements. Design 1 consists of 61,787 nodes and 23,227 elements; the design 2 includes 60,170 nodes and 22,404 elements; the design 3 involves 64,684 nodes and 23,087 elements; and the design 4 encompasses 63,067 nodes and 22,264 elements. Fig.24 depicts the structural analysis process flowchart.

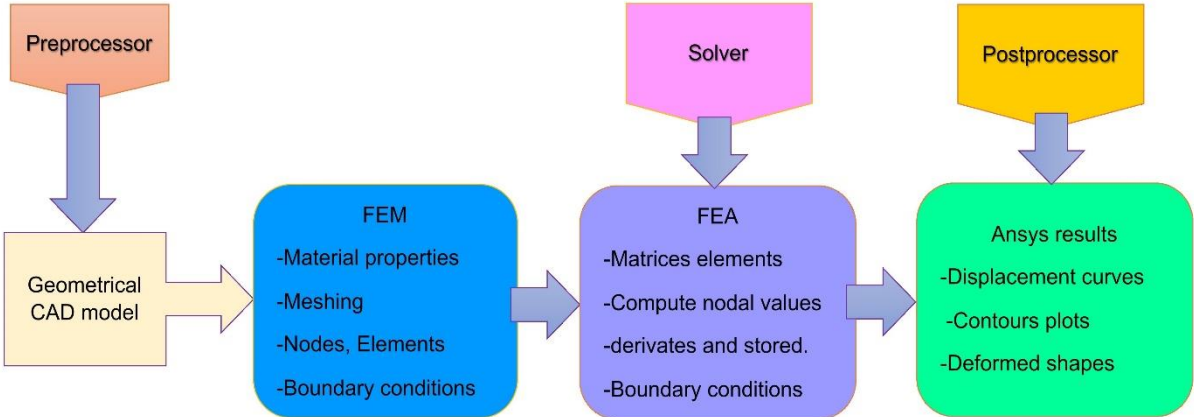


Figure 24. Structural analysis layout for composite T-joints

4.6 *Bio-composite validation*

This case study focuses on validating the bio-composite structure, which incorporates jute fiber as the reinforcement material and PVC foam as the core material, specifically for T-joints. The compression test setup is illustrated in Fig.25, and the corresponding results are outlined in Table 3.

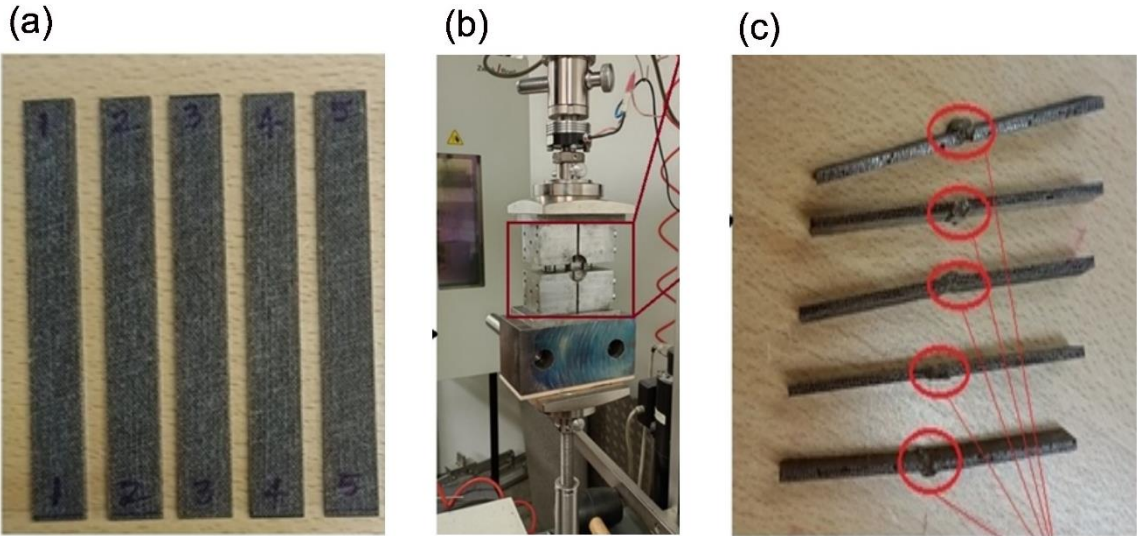


Figure 25. Mechanical testing of composite structure

The mechanical compression test was conducted following ASTM standards, and the resulting data, including the force versus displacement plot, is depicted in Fig. 17.

Table 3. Compression test results [12]

Specimens description	F_{max} (N)	dL max (F_{max} -mm)	Thickness (t- mm)	Width (b- mm)	Area (mm ²)	Compressive strength (MPa)
SP1	1666.1	1.252	2.57	12.2	31.40	53.05
SP2	1735.7	0.929	2.42	12.1	29.40	59.03
SP3	2032.0	0.834	2.64	12.1	32.18	63.14
SP4	1361.8	0.843	2.51	12.1	30.57	44.54
SP5	1901.1	0.821	2.57	12.1	31.19	60.93

The Figure 26 displays the setup for the mechanical compression test. This examination offers significant understanding of how the material behaves when subjected to compressive forces, which is especially relevant in situations involving axial loads or compressive stresses. The compressive strength measures at 63.14 MPa, the tensile strength at 113.75 MPa, and the flexural strength at 63.67 MPa.

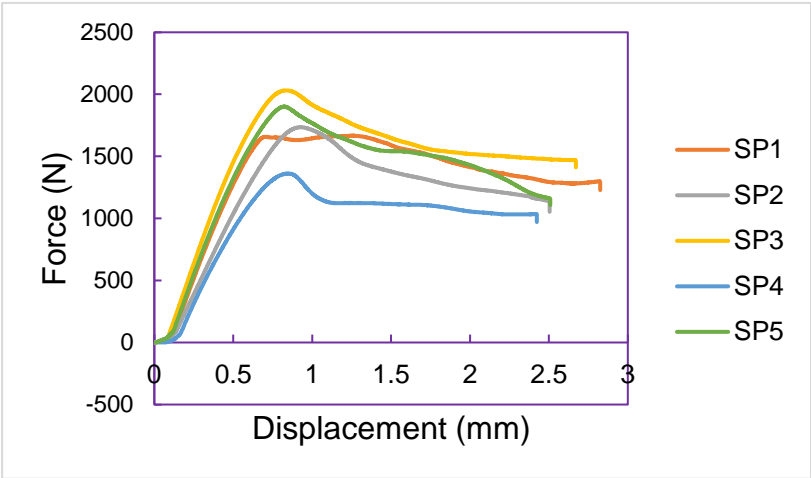


Figure 26. Force vs displacement plot.

4.7 *Highlights of case study*

The performance of epoxy-jute composite, epoxy-glass composite, and sandwich structures was evaluated through design examples involving deformation and stress analysis.

- ✚ The epoxy-jute composite exhibited moderate deformation and stress values across all design scenarios. Although it generally performs adequately, further

adjustments may be necessary to enhance its mechanical properties for specific applications.

- ✚ In contrast, the epoxy-glass composite displayed reduced deformation and stress levels, indicating superior structural integrity and load-bearing capacity. These findings highlight its suitability for applications requiring increased strength and durability.
- ✚ The sandwich structure demonstrated a balanced distribution of deformation and stress, leveraging the advantages of its composite composition. With its enhanced stiffness-to-weight ratio and resistance to bending and buckling, it presents an attractive option for lightweight structural systems.

5. Case Study_3

5.1 *Design of composite wing for TS-17 UAV*

In smaller companies that develop and produce single series of modern ultra-light unmanned aerial vehicles (UAVs), the design process typically starts with hand calculations. Although these calculations are supported by standards and guidelines, often the aircraft being designed do not conform to these specifications. Additionally, the unpredictable aerodynamic forces acting on the wings and the use of sandwich-structured composites that deform nonlinearly complicate the design process. This makes the introduction of the Finite Element Method combined with an optimization scheme particularly beneficial. This is especially crucial for ultra-light structures like the High-Altitude Long Endurance Unmanned Aerial Vehicle Twin Stratos (HALE UAV TS) family, which includes the TS12 and TS17, developed by a scientific and technical consortium [138]. The TS is a double-hull UAV with an A-type tail, powered by electric motors and a hybrid system combining photovoltaic cells and a lithium-ion buffer battery. Key characteristics include its large size and low weight, necessitating a specialized design approach that incorporates energy optimization via Model-Based Design and the use of ultra-light materials. The design methodologies employed have been tested by consortium members in aviation [139, 140], in automotive [141] and robotic [142] applications. For thin-walled structures, generative design [143] was used. Structural optimization poses a significant challenge.

The composites' structure involves the material selection, determining the material content, and configuring the internal construction of the FRP composites. The manufacturing process of composites is complex and plays a vital role in certifying that the final performance of the composites meets the designed specifications. Analytical methods were initially the primary approaches for expecting the macro properties of simple composites, such as laminated plates. However, these methods fall short in explaining the mechanical behaviour at the micro- or meso-scale due to the difficult inner structure of composites. At the micro scale, a fiber tow comprises hundreds of unidirectional fibers arranged randomly and bonded with polymer resin. The optimization mythology was represented in Fig. 27.

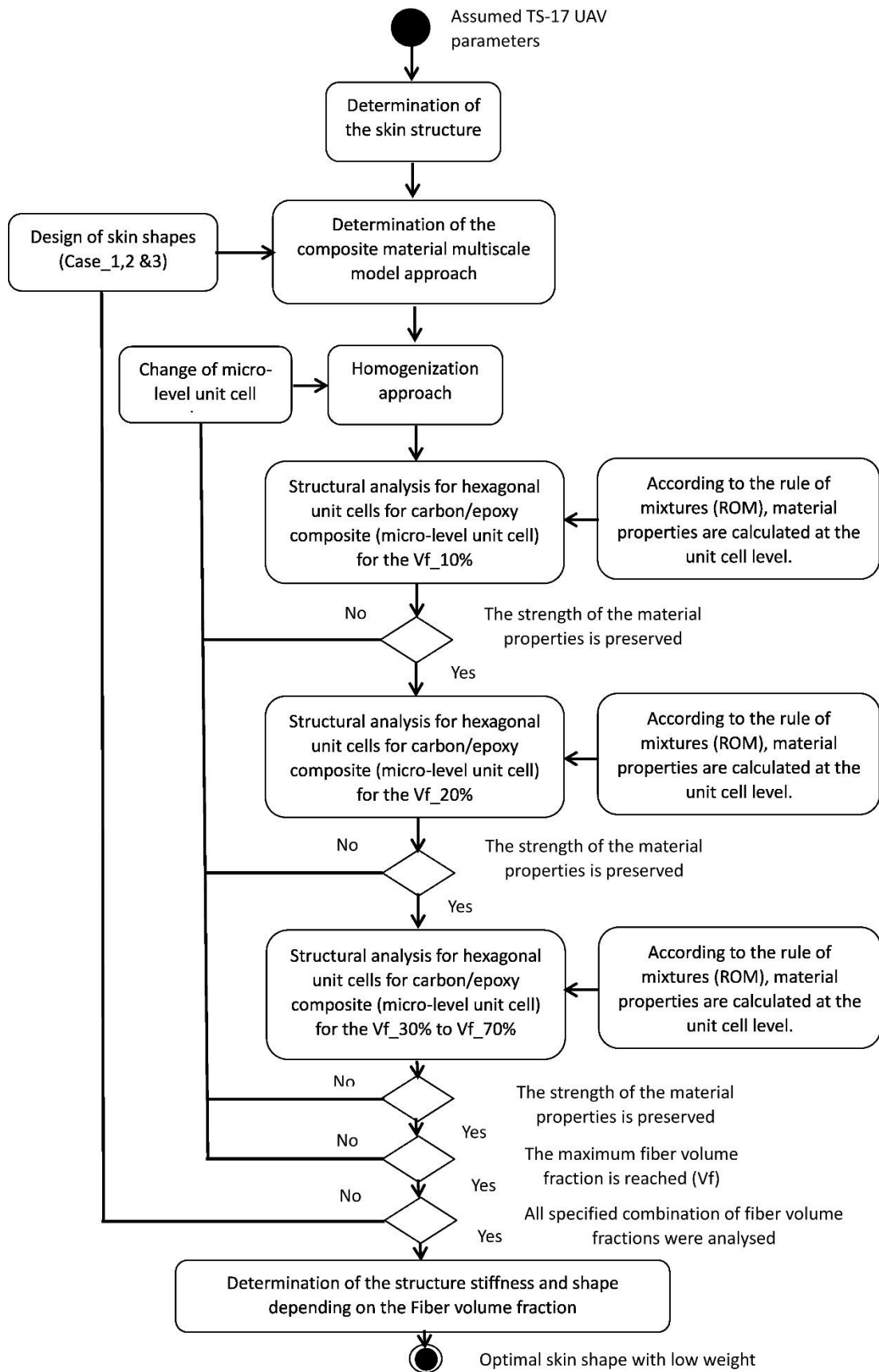


Figure 27. T17 UAVs wing skin optimization layout

The initial approach for expecting the properties of composites was the macro-scale method, which primarily describes the overall mechanical behaviour of a composite. The optimization methodology is illustrated in Fig. 28. This method is largely based on phenomenological theory, experimental data, and classical finite element analysis. It is widely known that multiple meso- or micro-damages in composite materials, such as yarn or fiber breakage and matrix cracking, can result in macroscopic structural failure. For an FRP composite structure, its mechanical properties at the structural level are closely linked to the meso-structure of the yarns. The behavior of the yarns depends on the arrangement and interaction of fibers at the fiber level, with the relative motion of fibers within a yarn being a key factor in changes to the yarn's cross-sectional shape (Miao et al., 2008). Recently, researchers have also employed the molecular dynamics (MD) method to study the interface properties between fibers and resin at the nanoscale (Sun et al., 2018; Sun et al., 2021). This suggests that single-scale methods are inadequate for predicting the composite properties, especially failure process from initial defects to structural damage. Additionally, as fiber-reinforced composites become more widely used in aerospace, the size of components is increasing, and the need for precise analysis is growing. Therefore, research on predicting the mechanical properties of composites has evolved from traditional single-scale methods to multi-scale methods.

The construction of composite structures employing carbon fabric composites requires very reliable mechanical properties. The homogenization approach is a numerical procedure that converts a heterogeneous elastic medium into a comparable model that retains energetic equivalence to the original medium. This approach for fiber-reinforced composites presumes that composite materials possess a periodic microstructure, as depicted in Figure 27, and simplifies it to a unit cell problem. The homogenization method is utilized to evaluate the mechanical properties of composite materials through the examination of their components and microstructure. Babu et al. developed four representative volume elements (RVEs) with different fiber orientations in unidirectional (UD) composites and predicted the effective properties using the random sequential adsorption (RSA) algorithm, as opposed to the Halpin-Tsai and Mori-Tanaka homogenization techniques. Qi et al. created representative volume elements (RVEs) by considering fiber orientation and ply angle in carbon fiber reinforced plastics (CFRPs),

projected effective properties through cross-scale simulations, and corroborated these predictions with tensile test outcomes. Gao et al. advocated the use of the Integrated Computational Material Engineering framework, employing the rule of mixtures (ROM) to create a unidirectional CFRP laminated structure, and compared the simulation results with tensile and three-point bending tests.

These studies introduced multiple RVE models to forecast the effective characteristics at the fiber level. Nonetheless, these models include limitations since they fail to consider the uncertainty in mechanical properties arising from the structural characteristics of fiber-matrix composites and intrinsic flaws. Lee et al. established a linear link between the effective and material parameters by employing Monte Carlo simulations (MCS) to address these uncertainties. Kamiński and Kazimierczak analysed material properties based on deviations using square RVEs with single cylindrical fibers. However, these studies mainly focused on the fiber levels of UD composites, which have considerably simpler internal structures than fabric composites.

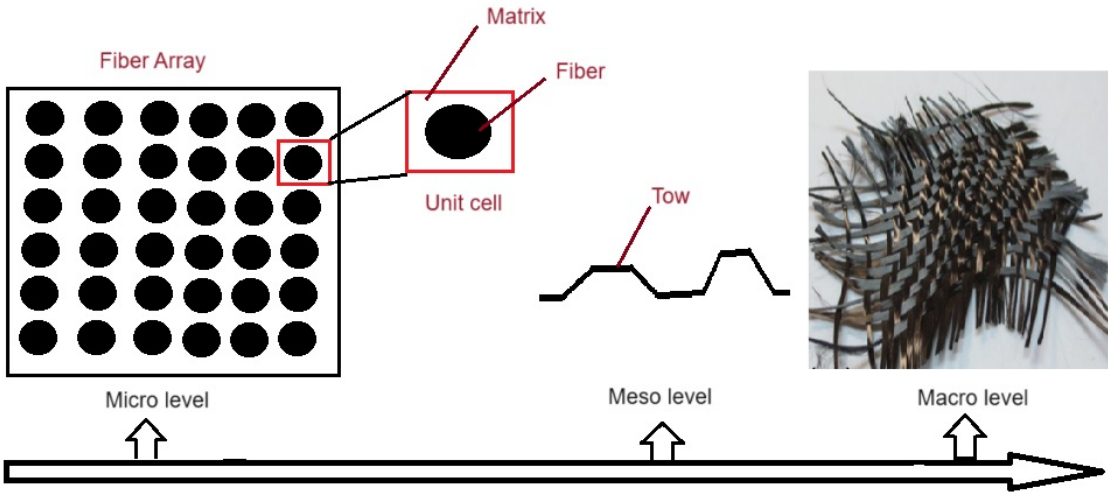


Figure 28. Schematic diagram of multiscale model approach

The tests aimed at predicting the composites with carbon fibers, as outlined in the preceding section, exhibit considerable limitations regarding cost and time efficiency. Consequently, an analytical approach is required for forecasting the characteristics of composites. Nonetheless, it is unfeasible to study each fiber array individually by modeling them in a random sequence. The homogenization technique is utilized to estimate effective attributes by using a representative volume element (RVE) model to

handle this issue. The RVE model delineates a unit cell through a repeated arrangement of carbon fiber and matrix, commonly employing square and hexagonal configurations.

5.2 Homogenization approach

The unit cells of unidirectional composites with carbon/epoxy at the microscale were modelled as square arrays to forecast the effective properties utilizing the homogenization technique, as seen in Figure 29. The total volume of each unit cell was presumed to equal one. Unit cells were simulated for carbon fiber volume fractions between 10% and 70% to forecast the mechanical properties of composites with differing volume fractions utilizing Ansys Workbench.

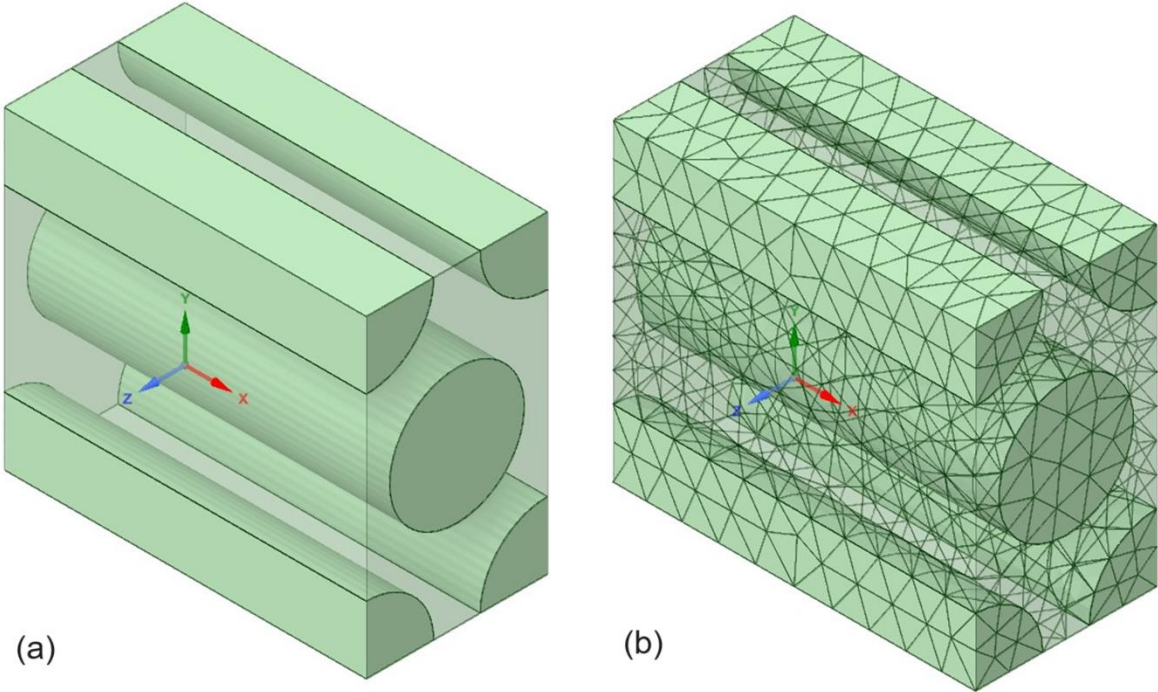


Figure 29. Hexagonal unit cells for carbon/epoxy composite; (a) Geometrical model of micro-level unit cell; (b) Finite element model of unit cell for UD composite.

The number of nodes and elements is 4169 and 2231 respectively. The Mori-Tanaka theory [144,145] was employed to determine the mechanical properties of the homogenization process. This theory predicts the interactions between each phase by assuming each element is embedded in an infinite matrix and is subjected to remote loading due to the average strain or stress of the medium. The mechanical properties are presented in Table 4.

Table 4. Material properties of fiber and matrix (Carbon fiber/Epoxy)

	Carbon fiber	Epoxy
Young's Modulus (GPa)	230	3.78
Shear Modulus (GPa)	9	1.4
Poisson's Ratio	0.2	0.35

5.3 Homogenization Analysis

Table 5 provides the optimal properties from the homogenization analysis based on varying volume fractions. To validate the homogenization technique employed in this study, the effective properties were calculated using the rule of mixture [146-148] and then compared to the results obtained from the homogenization analysis.

Table 5. Homogenization analysis results of the micro-level

	Vf_10%	Vf_20%	Vf_30%	Vf_40%	Vf_50%	Vf_60%	Vf_70%
	(GPa)	(GPa)	(GPa)	(GPa)	(GPa)	(GPa)	(GPa)
E1	26.410	49.039	71.664	94.287	116.91	139.53	162.15
E2	4.747	5.413	6.184	7.130	8.326	9.870	11.859
E3	4.747	5.413	6.184	7.130	8.326	9.872	11.856
G12	1.621	1.879	2.187	2.558	3.015	3.596	4.364
G23	1.585	1.803	2.069	2.403	2.833	3.401	4.132
G31	1.621	1.879	2.187	2.557	3.015	3.596	4.364
v12	0.332	0.315	0.298	0.282	0.267	0.253	0.238
v 13	0.332	0.315	0.298	0.282	0.267	0.253	0.238
v 23	0.497	0.500	0.494	0.483	0.469	0.452	0.436
Weight	1.224E-09	1.288E-09	1.352E-09	1.416E-09	1.48E-09	1.544E-09	1.608E-09

5.4 Rule of Mixture for Composite material

The mechanical features of composites are influenced by the volume fractions of both the reinforcement and the matrix materials. Fundamental properties can be estimated using the rule of mixtures, based on certain assumptions. The nature of the fiber reinforcement such as fiber, whisker and particle and its orientation are significantly affecting the strength of the composites. In fiber-reinforced composites, fibers aligned at specific angles exhibit greater strength in the direction of the fibers compared to other directions. For particle-reinforced composites, the even distribution of particles throughout the

component is essential for ensuring consistent material properties. The reinforcement properties are listed in Table.6

Table 6. Mechanical properties of fiber and matrix.

	Carbon Fiber Units (GPa)	Epoxy resin Units (GPa)
E1	230	3.78
E2	23	3.78
E3	23	3.78
G12	9	1.4
G23	8.21	1.4
G31	9	1.4
v12	0.2	0.3
v 13	0.4	0.3
v 23	0.2	0.3
Tensile yield strength		0.054

The volume fraction formulas are presented below,

Fiber volume fraction $V_f = \text{Volume of fiber} / \text{Volume of composite}$

$$\text{Volume of composite} \quad V_c = V_f + V_m \quad (1)$$

$$\text{For unit volume of composite} \quad 1 = V_f + V_m \quad (2)$$

$$\text{Volume fraction of matrix} \quad V_m = 1 - V_f \quad (3)$$

The notations used in the composite rule of mixtures are as follows: c , f , and m represent composite, fiber, and matrix, respectively, V denotes the volume fraction, P represents the load capacity, A stands for the cross-sectional area, E is the elastic modulus, σ is the stress, ε is the strain, ν refers to the Poisson's ratio and ρ denotes the density.

When a fiber-oriented composite is loaded in the longitudinal direction of fiber alignment, the strain in the fiber, matrix, and composite are equal (iso-strain condition).

$$\text{In the composite iso-strain state,} \quad \varepsilon_c = \varepsilon_f = \varepsilon_m \quad (4)$$

$$\text{Load withstand by composite,} \quad P_c = P_f + P_m \quad (5)$$

$$\text{Withstand the load written as,} \quad \sigma_c A_c = \sigma_f A_f + \sigma_m A_m \quad (6)$$

$$\text{Composite stress for longitudinal load, } \sigma_c = \sigma_f V_f + \sigma_m V_m \quad (7)$$

$$\text{Elastic Modulus at longitudinal, } E_{1c} = V_f E_{1f} + V_m E_{1m} \quad (8)$$

$$\text{Poisson ratio, } \nu_{12} = V_f \nu_f + V_m \nu_m \quad (9)$$

$$\text{Composite material density, } \rho_c = \rho_f V_f + \rho_m V_m \quad (10)$$

When a fiber-oriented composite is subjected to loading perpendicular to the direction of fiber alignment, the stress experienced by the fiber, matrix, and composite is identical (iso stress).

$$\text{For iso-stress conditions, } \sigma_c = \sigma_f = \sigma_m \quad (11)$$

$$\text{Composite Strain, } \varepsilon_c = \varepsilon_f V_f + \varepsilon_m V_m \quad (12)$$

$$\text{Transverse elastic modulus of composite, } \frac{1}{E_{cT}} = \frac{V_f}{E_f} + \frac{V_m}{E_m} \quad (13)$$

According to the ROM, material properties are calculated at the unit cell level. The engineering data for these calculations is sourced from Table 3.

Volume Fiber Fraction is $V_f=0.10$,

$$\begin{aligned} \text{Matrix Volume Fraction, } V_m &= 1 - V_f \\ &= 1 - 0.10 \\ V_m &= 0.90 \end{aligned}$$

Effective Moduli Calculations

Longitudinal Modulus (E_1)

$$\begin{aligned} E_{1c} &= V_f E_{1f} + V_m E_{1m} \\ E_{1c} &= 0.10 * 230 + 0.90 * 3.78 \\ E_{1c} &= \mathbf{26.002 \text{ GPa}} \end{aligned}$$

Transverse Moduli (E_2 and E_3)

For transverse properties, the Halpin-Tsai equations or similar micromechanics models can be used. For simplicity the rule of mixtures for calculations,

$$\frac{1}{E_{cT}} = \frac{V_f}{E_f} + \frac{V_m}{E_m}$$

$$\frac{1}{E_{2c}} = \frac{V_f}{E_{2f}} + \frac{V_m}{E_{2m}}$$

$$\frac{1}{E_{2c}} = \frac{0.10}{23} + \frac{0.90}{3.78}$$

$$\mathbf{E_{2c} = 4.44 \text{ GPa}}$$

Assuming $E_{2c} = E_{3c}$

Shear Moduli (G_{12} , G_{23} , G_{31})

$$\frac{1}{G_{12c}} = \frac{V_f}{G_{12f}} + \frac{V_m}{G_{12m}}$$

$$\frac{1}{G_{12c}} = \frac{0.10}{9} + \frac{0.90}{1.4}$$

$$\mathbf{G_{12c} = 2.0 \text{ GPa}}$$

$$\frac{1}{G_{23c}} = \frac{V_f}{G_{23f}} + \frac{V_m}{G_{23m}}$$

$$\frac{1}{G_{23c}} = \frac{0.10}{8.21} + \frac{0.90}{1.4}$$

$$\mathbf{G_{23c} = 1.56 \text{ GPa}}$$

$$\frac{1}{G_{31c}} = \frac{V_f}{G_{31f}} + \frac{V_m}{G_{31m}}$$

$$\frac{1}{G_{31c}} = \frac{0.10}{9} + \frac{0.90}{1.4}$$

$$\mathbf{G_{31c} = 2.0 \text{ GPa}}$$

Poisson's Ratios (ν_{12} , ν_{13} , ν_{23})

$$\nu_{12c} = V_f \nu_{12f} + V_m \nu_{12m}$$

$$\nu_{12c} = 0.10 * 0.2 + 0.90 * 0.3$$

$$\mathbf{\nu_{12} = 0.29}$$

$$\nu_{13c} = V_f \nu_{13f} + V_m \nu_{13m}$$

$$\nu_{13c} = 0.10 * 0.4 + 0.90 * 0.3$$

$$\nu_{13} = 0.31$$

$$\nu_{23c} = V_f \nu_{23f} + V_m \nu_{23m}$$

$$\nu_{23c} = 0.10 * 0.2 + 0.90 * 0.3$$

$$\nu_{23c} = 0.29$$

Using the rule of mixture, the mechanical properties have been calculated for V_f values of 10%, 20%, 30%, 40%, 50%, 60%, and 70%. The calculated properties are outlined in Table 7.

Table 7. Summary of effective properties for different fiber volume fraction by ROM.

	Vf_10%	Vf_20%	Vf_30%	Vf_40%	Vf_50%	Vf_60%	Vf_70%
	(GPa)	(GPa)	(GPa)	(GPa)	(GPa)	(GPa)	(GPa)
E _{1c}	26.902	49.256	72.51	95.76	119.89	144.0	168.11
E _{2c}	4.58	5.33	6.43	7.61	8.85	10.17	11.57
E _{3c}	4.58	5.33	6.43	7.61	8.85	10.17	11.57
G _{12c}	2.23	2.61	3.29	4.09	5.04	6.19	7.64
G _{23c}	1.62	1.75	1.97	2.23	2.53	2.86	3.22
G _{31c}	2.23	2.61	3.29	4.09	5.04	6.19	7.64
ν _{12c}	0.29	0.28	0.27	0.26	0.25	0.24	0.23
ν _{13c}	0.31	0.32	0.33	0.34	0.35	0.36	0.37
ν _{23c}	0.29	0.28	0.27	0.26	0.25	0.24	0.23

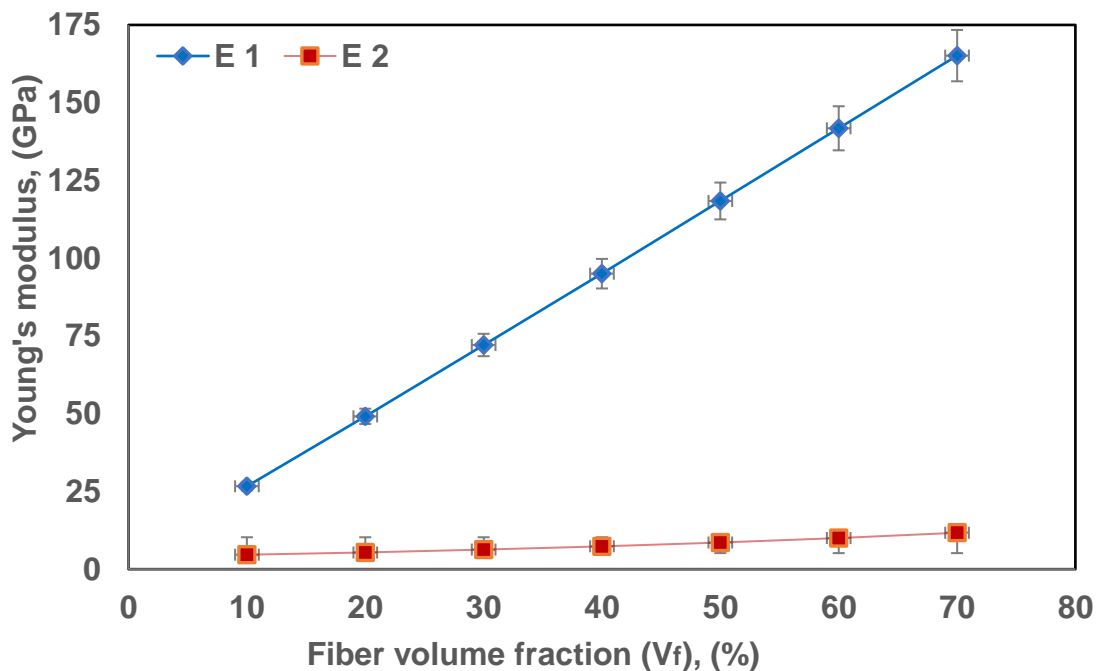


Figure 30. Hexagonal unit cells for carbon/epoxy composite Young's Modulus vs Fiber volume fraction

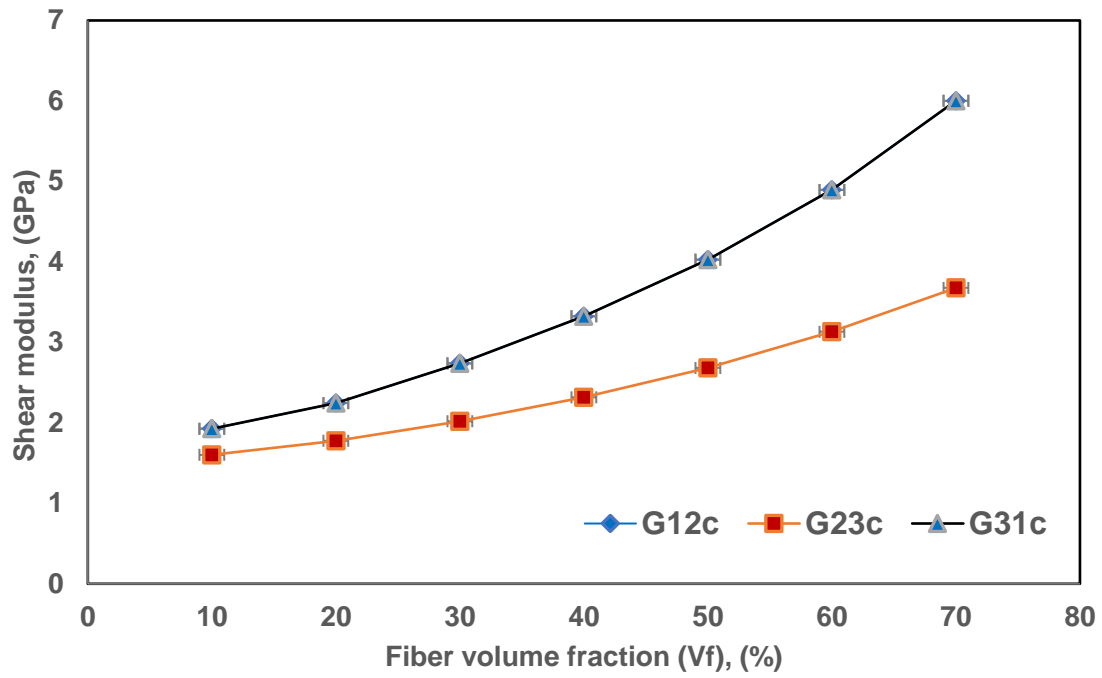


Figure 31. Hexagonal unit cells for carbon/epoxy composite Shear Modulus vs Fiber volume fraction

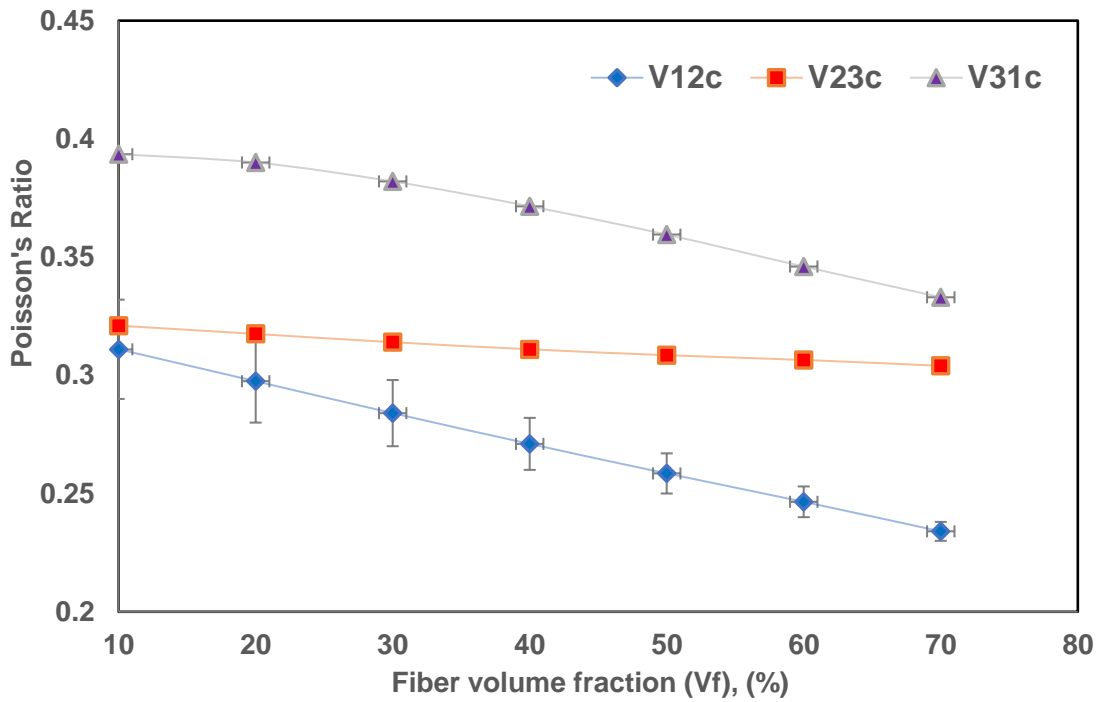


Figure 32. Hexagonal unit cells for carbon/epoxy composite Shear Poisson's ratio vs Fiber volume fraction

Figure 32 is showing the $E1c$ of a composite material increases as the volume fiber fraction (V_f) from 0.10 to 0.70. However, this relationship is addressed by the ROM, which predicts that the overall stiffness of the composite is a weighted average of the stiffnesses of the fiber and matrix materials.

For less volume fiber fractions ($V_f=0.10$), the Young's modulus ($E1c$) is closer to that of the matrix due to the matrix's dominant presence. As V_f increases, the contribution of the stiffer reinforced fiber material becomes more significant, leading to a higher $E1c$. At $V_f=0.70$, the young's modulus is much closer to the fiber's modulus, indicating that the fibers predominantly influence the composite's mechanical behaviour.

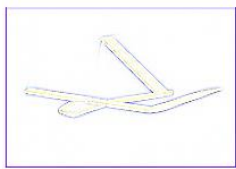
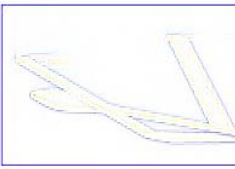
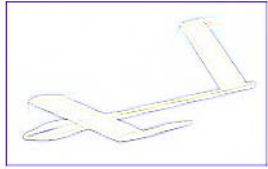
This trend demonstrates that the effectiveness of fiber reinforcement in enhancing the parallel axis stiffness of the composite, highlighting the importance of optimizing volume fiber fraction in composite design to achieve the desired mechanical properties and this optimization is significant changes in the UAV structures. Furthermore, $V_f=0.50$ is consider for further analysis of UAV skin.

The case study extended to more detailed in the wing skin, the assumptions of the parameters were considered from TS17. The detailed parameters are listed in Table 8, Table 9 and Table 10. The geometrical proposed CAD model is presented in Figure 33.

Table.8 The design parameters of TS17 UAV [138]

Scale	1:8	1:7	Unit
Take off mass	7,1	9,8	[kg]
Aspect Ratio (AR)	16,91	14,46	[-]
Wing area	0,55	0,70	[m ²]
Maximum ceiling	5000	5000	[m]
Maximum flight duration	12	24	[h]
Payload	2,5	2,5	[kg]
Middle chord	0,20	0,28	[m]
Wing Span [A]	3,0	3,6	[m]
Tail unit area	0,21	0,25	[m ²]
Lenght of aeroplane [C]	1,4	1,8	[m]
Hight of tail unit [B]	0,24	0,29	[m]
Assumed motors power	150	300	[W]

Table 9. The critical flight parameters of TS 17 UAV [138]

Name	I critical flight condition	II critical flight condition	III critical flight condition
Results view			
AoA	0 [°]	14,25 [°]	-5 [°]
Horizontal speed	35 [m/s]	19[m/s]	22[m/s]

Air pressure [atm]	1	1	1
Air temperature [°C]	25	25	25
Lift Force	245,8 [N]	272,01 [N]	-42,44 [N]
Drag Force	22,4 [N]	46,83 [N]	10,16 [N]

Table 10. The modified parameters for TS17 UAV

Material	Layer thickness	The number of layers	Direction relative to the span
Wing skin			
Epoxy Carbon UD	0.10 [mm]	1	45°
Epoxy Carbon UD	0.10 [mm]	1	-45°
PVC Foam	2 [mm]	1	0°
Epoxy Carbon UD	0.10 [mm]	1	45°
Epoxy Carbon UD	0.10 [mm]	1	-45°

Geometrical construction

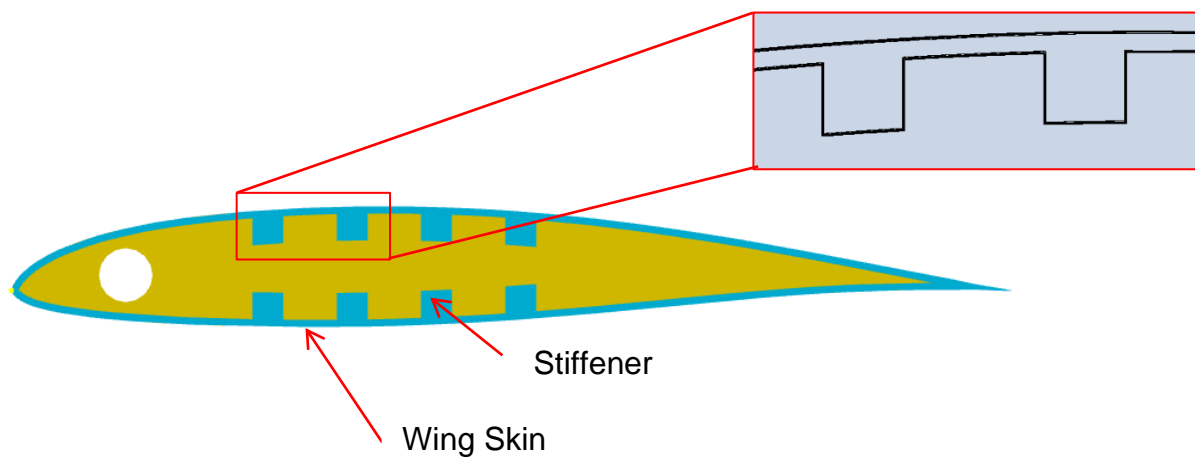


Figure 33. Geometrical configuration of composite wing skin with stiffener

5.5 Preliminary Design Methodology

This research aimed to optimize the weight and stiffness of the wing skin through a series of case studies conducted at different stages. A key innovation explored in this study is the integration of stiffeners with the wing skin. The stiffeners are affixed to the skin using fasteners, which plays a crucial role in enhancing the wing's structural integrity. The addition of these stiffeners significantly impacts the overall wing structure, as they are designed to provide secondary loads.

The preliminary design cases are as follows:

- **Case 1:** This case utilizes four layers of unidirectional (UD) carbon fiber, each with a thickness of 0.10 mm, arranged in a lamina orientation of [45/-45/45/-45].

- **Case 2:** This case features a sandwich structure with two layers of UD carbon fiber on both the top and bottom skins. The PVC foam core varies in thickness, with options of 1 mm, 2 mm, and 3 mm. The stacking sequence is [45/-45/PVC foam/45/-45].
- **Case 3:** This case features a sandwich structure with the top and bottom layers consisting of two layers of UD carbon fiber, each 0.10 mm thick. The core is designed with a hat-shaped PVC foam that varies in thickness from 0 to 3 mm. The stacking sequence is [45/-45/PVC foam/45/-45].

The preliminary design strategy is presented in Fig.34. Each configuration demonstrates different structural designs used to optimize the weight and stiffness in composite materials, particularly in applications like UAV wing skins.

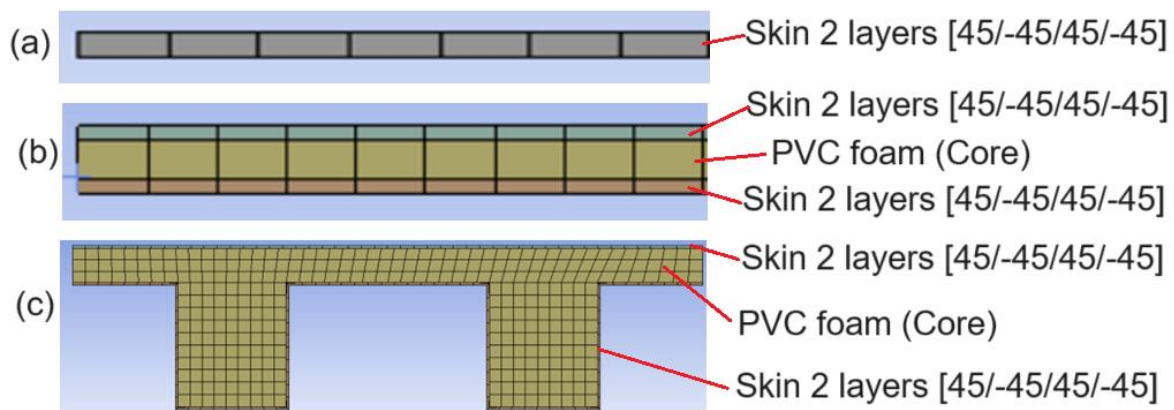


Figure 34. Preliminary design strategy, (a) is case study_1, (b) Case study_2 and (c) Case study_3.

5.6 FEA of UAV wing skin Stiffeners

The FEA was conducted on various case studies for the wing skin, focusing on weight and stiffness as the primary parameters. To evaluate the structural stability of the wing skin, the FEA incorporated load boundary conditions, including shear and compressive loads, applied to the model with simply supported boundary conditions. The mesh element size used was 1 mm and individual cases models with elements, nodes are presented in the Table 11.

Table 11. FEM meshing details at various case studies

	Thickness	Elements	Nodes
	(mm)		
Case_1	0.4	4608	4753
Case_2	1	13680	42046
	2	18240	60717
	3	22800	79388
Case_3	0	30115	93572
	1	34770	121332
	2	39425	140386
	3	44080	159440

For analysis the mechanical properties are considered from homogenization results ($V_f=50$) is considered. The material properties are presented in Table 12.

Table 12. FEM meshing details at various case studies

Material	Density [$\frac{kg}{m^3}$]	Young's Modulus			Shear Modulus		
		Ex [Gpa]	Ey [Gpa]	Ez [Gpa]	XY [MPa]	YZ [MPa]	XZ [MPa]
Epoxy Carbon UD	1.48E-09	119.89	8.85	8.85	5.04	2.53	5.04
PVC Foam	60	0,07	0,07	0,07	27	27	27

Load and Boundary conditions

For the analysis, load and boundary conditions were applied to the model. Two different loads were applied. To address wing skin failures such as buckling or wrinkling, preliminary analysis was carried out with compression and shear loads. The load and boundary conditions are presented in Fig. 35 and Fig. 36.

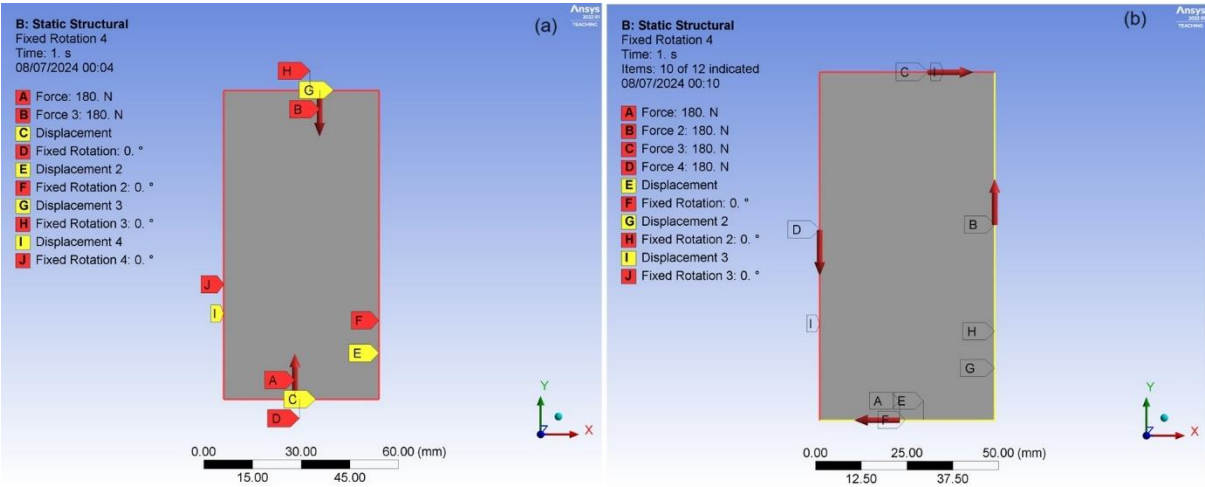


Figure 35. Load and boundary conditions for case_1, (a) Compressive load, (b) Shear load

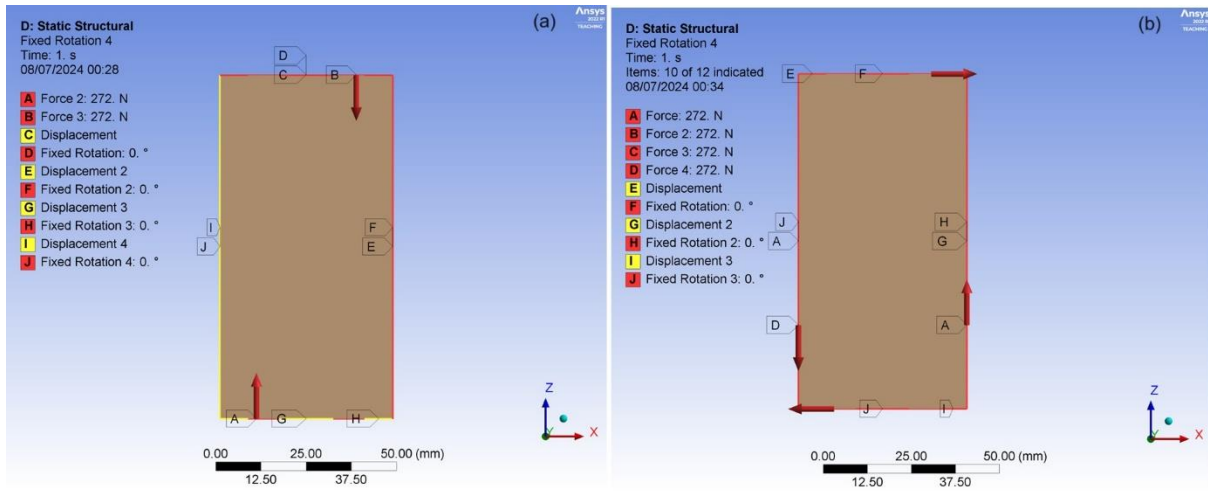


Figure 36. Load and boundary conditions for case_2 &3, (a) Compressive load, (b) Shear load

6. Manufacturing of bio-composite and validation

The current study focuses on conducting a variety of experiments to evaluate the mechanical properties of bio-composite and hybrid materials. A novel composite laminate and sandwich material structure is introduced, comprising Bio-Epoxy resin combined with various reinforcements including plain-woven E-glass, plain-woven jute fibers, and PVC foam. These reinforcements are utilized in the form of fabrics and mats, specifically woven jute (90 g/m²), woven E-glass (100 g/m²), and PVC foam (75 g/m³), as depicted in table 13.

6.1 *Composite laminate fabrication strategy*

The current research focuses on conducting various tests to assess the mechanical properties of bio-composite and hybrid composites. The study involves fabricating different configurations of composite laminates and sandwich structures. The process of fabricating composite laminates begins by using a 600x600x10 mm square wood plate as a mould. In this research, the vacuum bagging technique was utilized for the fabrication of composite structures. Vacuum bagging techniques are widely employed in the fabrication of composite structures due to their ability to enhance mechanical properties and prevent structural defects. Initially, the mould is cleaned, and a layer of wax is applied as a mould release agent. After the application of wax, the mould is left for 30 minutes to allow the wet surface to dry. The reinforcements are trimmed according to ASTM standards, and a thin layer of resin, mixed with 100:27% hardener (bio-resin), is applied to the mould using a flat brush. The weight of the bio-resin is determined based on the weight of the fibers, which is measured using a calibrated digital scale. Next, the successive layers of reinforcement are impregnated with the bio-resin using a brush with a roller. This process helps compact the layers and remove any air bubbles. Once the plies are laid based on the stacking sequence and ply orientation, a peel ply is applied to the combined laminate surfaces. A thin layer of release film is then placed to ensure the uniform flow of bio-resin throughout the reinforcement. A breather cloth is applied as the next layer, followed by sealing the vacuum bagging film with vacuum bagging sealant. The mould is then connected to a vacuum pump, which runs for approximately 8 hours to cure

the laminates. Finally, after a post-curing period of 24 hours, the laminate is demoulded. The bio-composite fabrication methodology was presented in Fig. 36.

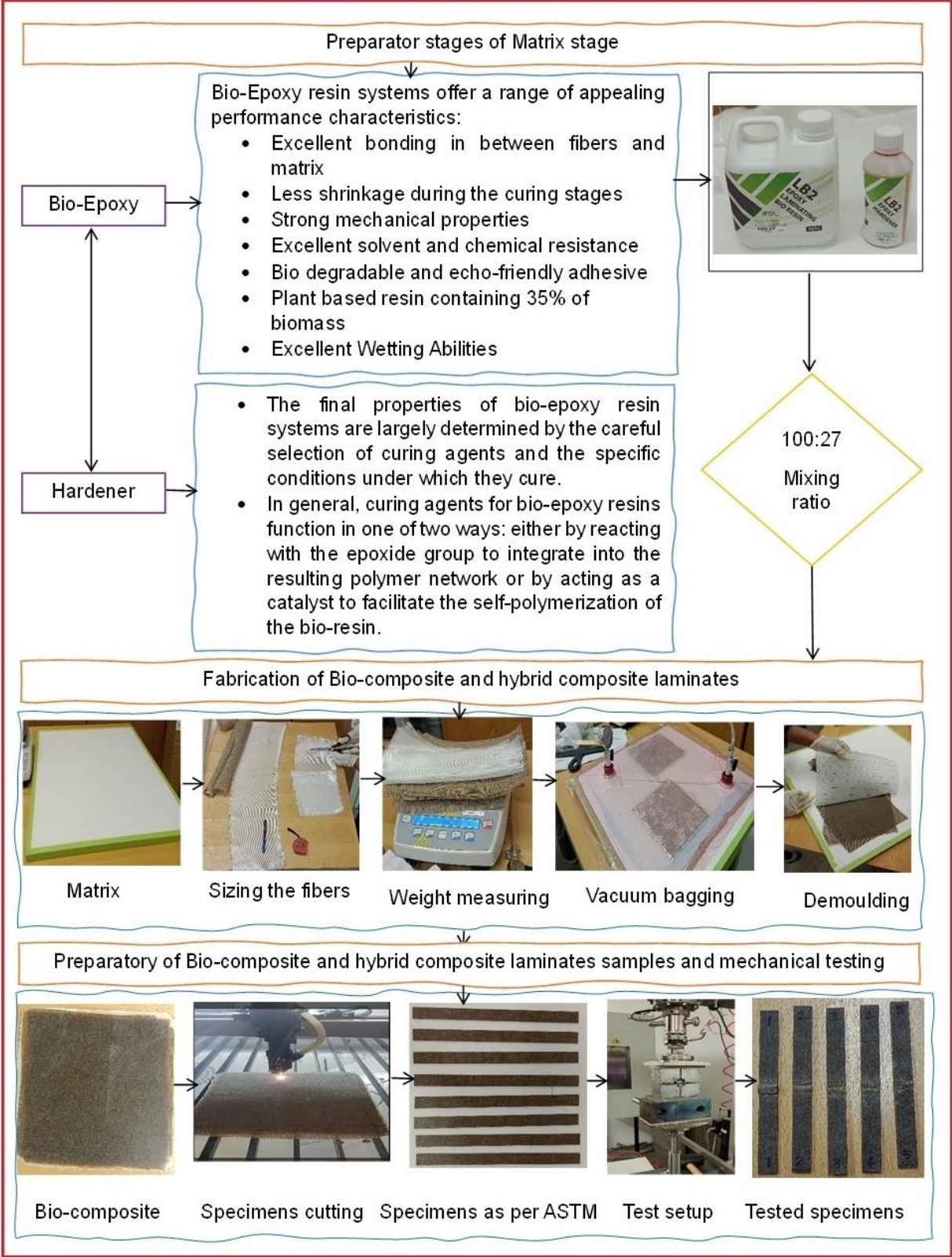


Figure 37. Bio-composite fabrication strategy

Table 13. Materials properties of Jute/E-glass woven fibers.

Fabric Type	Ply Thickness (mm)	Density	Elongation (%)	Poisson Ratio	Tensile Modulus (MPa)
Jute	0.15	90 (g/m ²)	1.5-1.7	0.3	65
E-glass	0.30	100 (g/m ²)	2.2-2.6	0.32	586
PVC foam	3	75 (g/m ³)			1.89
Bio-resin	-	1.16 (g/cm ³)	4.3		3230

Stage 1 and 2 consist of laminate 1 (Bio-composite) consists of bio-resin with six layers of natural fibers, such as pure biodegradable fabric. The specimens were labelled on the specimens as per standards. Laminate 2 (Hybrid composite) is composed of bio-resin with 25% volume fiber from two layers of E-glass and 75% volume fiber from six layers of jute. Laminate 3 (Hybrid composite) is fabricated using bio-resin with 75% volume fiber from six layers of E-glass and 25% volume fiber from two layers of jute. Laminate 4 (Synthetic composite) consists of bio-resin with ten layers of E-glass fiber and pure synthetic fiber. Stage 3 contains laminate 5 (Bio-composite) consists of bio-resin with eight layers of natural fibers, such as pure biodegradable fabric. Laminate 6 (Hybrid composite) is composed of bio-resin with 25% volume fiber from two layers of E-glass and 75% volume fiber from eight layers of jute. Laminate 7 (Hybrid composite) is fabricated using bio-resin with 75% volume fiber from fifteen layers of E-glass and 25% volume fiber from three layers of jute. Laminate 8 (Synthetic composite) consists of bio-resin with fourteen layers of E-glass fiber and pure synthetic fiber. Stage 4 having laminate 9 (Bio-composite) consists of bio-resin, PVC foam thickness of 3 mm with two layers of natural fibers. Laminate 10 (Hybrid composite) is composed of bio-resin, PVC foam thickness of 3 mm with 25% volume fiber from two layers of E-glass and 75% volume fiber from three layers of jute. Laminate 11 (Hybrid composite) is fabricated using bio-resin, PVC foam thickness of 3 mm with 75% volume fiber from four layers of E-glass and 25% volume fiber from two layers of jute. Laminate 12 (Synthetic composite) consists of bio-resin PVC foam thickness of 3 mm with ten layers of E-glass fiber and pure synthetic fiber. Finally, stage 5 contain laminate 13 (Bio-composite) consists of bio-resin, PVC foam thickness of 3 mm with two layers of natural fibers. Laminate 14 (Hybrid composite) is composed of bio-resin, PVC foam thickness of 3 mm with 25% volume fiber from two layers of E-glass and 75% volume fiber from three layers of jute. Laminate 113 (Hybrid composite) is

fabricated using bio-resin, PVC foam thickness of 3 mm with 75% volume fiber from four layers of E-glass and 25% volume fiber from two layers of jute. Laminate 16 (Synthetic composite) consists of bio-resin PVC foam thickness of 3 mm with ten layers of E-glass fiber and pure synthetic fiber. The design optimization strategy is presented in Table 14.

Table 14. Description of the current research design methodology for laminate

Types of tests	Types of laminate	Number of plies	Stacking sequence	Designation
Compression test	Bio-composite	6	[0-90°/0-90°/±45/±45/0-90°/0-90°]S	J/J/J/J/J/J
	Hybrid (Jute-75%)	8	[0-90°/0-90°/0-90°/±45/±45/0-90°/0-90°/0-90°]S	G/J/J/J/J/J/J/G
	Hybrid (Jute-25%)	8	[0-90°/0-90°/0-90°/±45/±45/0-90°/0-90°/0-90°]S	G/G/G/J/J/G/G/G
	Synthatic composite	10	[0-90°/0-90°/0-90°/±45/±45/±45/±45/0-90°/0-90°/0-90°]S	G/G/G/G/G/G/G/G/G/G/G
Tensile test	Bio-composite	6	[0-90°/0-90°/±45/±45/0-90°/0-90°]S	J/J/J/J/J/J
	Hybrid (Jute-75%)	8	[0-90°/0-90°/0-90°/±45/±45/0-90°/0-90°/0-90°]S	G/J/J/J/J/J/J/G
	Hybrid (Jute-25%)	8	[0-90°/0-90°/0-90°/±45/±45/0-90°/0-90°/0-90°]S	G/G/G/J/J/G/G/G
	Synthatic composite	10	[0-90°/0-90°/0-90°/±45/±45/±45/±45/0-90°/0-90°/0-90°]S	G/G/G/G/G/G/G/G/G/G/G
Flexural test	Bio-composite	8	[0-90°/0-90°/±45/±45/±45/±45/0-90°/0-90°]S	J/J/J/J/J/J/J/J
	Hybrid (Jute-75%)	10	[0-90°/0-90°/0-90°/±45/±45/±45/±45/0-90°/0-90°/0-90°]S	G/J/J/J/J/J/J/J/J/G
	Hybrid (Jute-25%)	18	[0-90°/0-90°/0-90°/0-90°/0-90°/±45/±45/±45/±45/±45/±45/±45/±45/±45/±45/0-90°/0-90°/0-90°/0-90°/0-90°]S	G/G/G/G/G/G/G/J/J/J/G/G/G/G/G/G/G/G/G
	Synthatic composite	14	[0-90°/0-90°/0-90°/0-90°/±45/±45/±45/±45/±45/±45/±45/±45/0-90°/0-90°/0-90°/0-90°]S	G/G/G/G/G/G/G/G/G/G/G/G/G/G/G/G

The fabrication and tested of bio-composite structures are presented in Fig.37.

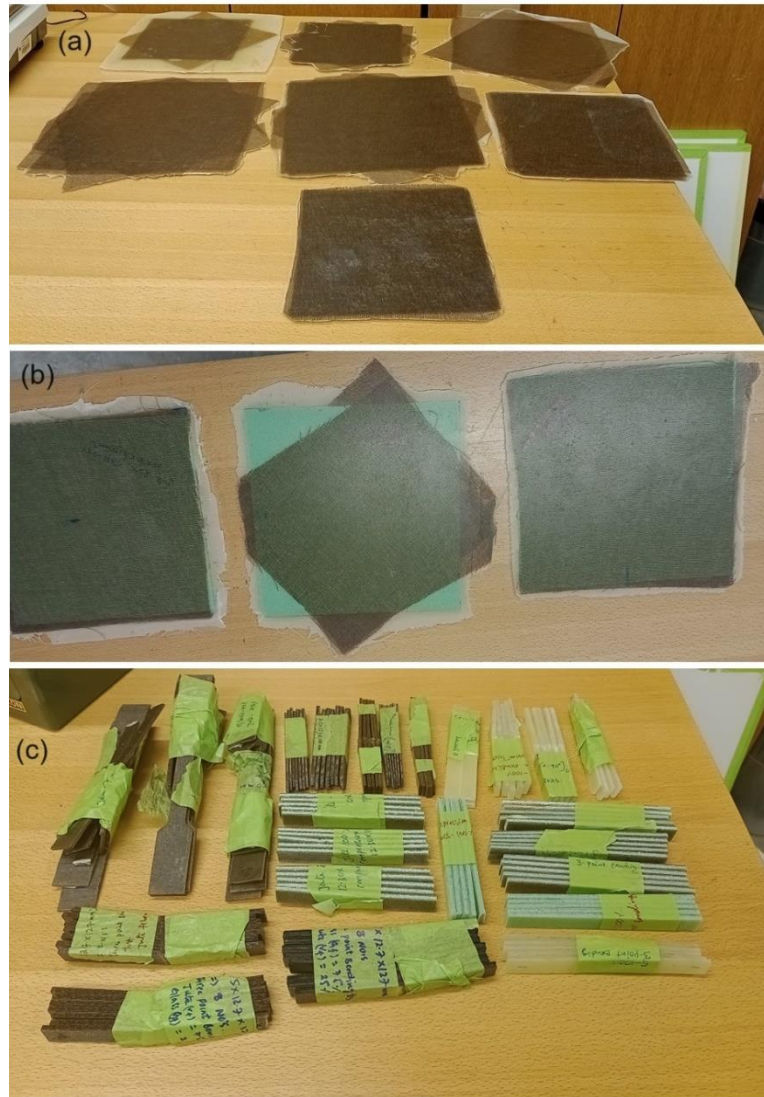


Figure 38. Bio-composites (a) Laminates, (b) Sandwich structures with different configurations and (c) Tested specimens as ASTM standards.

6.2 Mechanical characterization of composite materials

After successfully curing the bio-composite, the hybrid laminates and sandwich structures were trimmed to the desired shape and size in accordance with ASTM standards using a CNC automated laser cutting machine. Initially, compression tests, tensile tests, and flexural tests were performed on laminates, while flat compression tests and 3-point bending tests were conducted on sandwich structures, following the ASTM standards.

6.3 Compression test

The compression test was carried out on four different laminate configurations with each configuration having five specimens, all of them had a thickness ranging from 1.8 mm to

3.2 mm, with a tolerance of ± 0.3 mm. The load scale ranged from 0 to 5000N, and the dimensions and shape of the specimens were selected in accordance with the ASTM D 3410-03 standards. The specimens had dimensions of length 12.5 mm, width 110 mm, and a thickness ranging from 1.8 mm to 3.2 mm. The gauge length 10 mm-maintained room temperature and constant head-speed is 1.5 mm/min. Compression test specimen is setup shown in Fig.39.

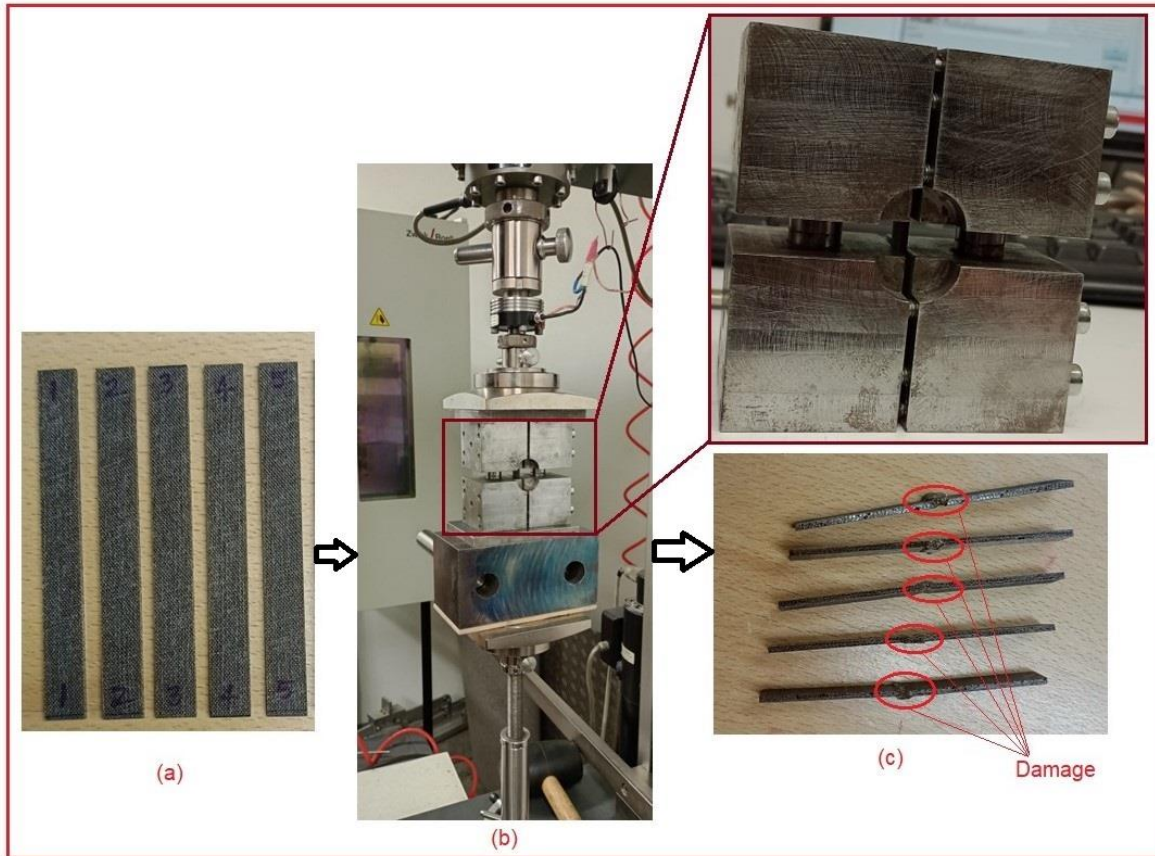


Figure 39. Compression test setup for bio-composite structure, (a) specimens, (b) compression test setup, (c) tested specimens.

The maximum compressive stress/Ultimate compressive strength is calculated by using Equ.1 and 2.

$$F^{cu} = P^{max} / A \quad (5.1)$$

$$\sigma_i^c = P_i / A \quad (5.2)$$

Where, F_{cu} = compressive strength, [MPa], P_{max} = maximum force before failure, [N], P_i = force at *ith* data point, [N], A = cross-sectional area of the specimen, [mm²], σ_i^c = compressive stress as the *ith* data point, [MPa]. The test results presented in Table 15.

Table 15. Compression test results raw data

Description	Specimens	F_{max} N	$dL(F_{max})$ mm	a_0 mm	b_0 mm	h_0 mm	A mm ²	σ_i MPa
Bio-composite (Jute_100%)	Sp 1	2288.321	1.035366	2.65	12.24	110	32.436	70.54879
	Sp 2	2106.138	0.883968	2.63	12.21	110	32.1123	65.58663
	Sp 3	2244.286	0.811597	2.6	12.24	110	31.824	70.5218
	Sp 4	2178.46	0.926029	2.63	12.26	110	32.2438	67.56213
	Sp 5	1910.658	1.090765	2.53	12.15	110	30.7395	62.15643
Hybrid composite (Jute_75%)	Sp 6	3233.172	1.350195	3.25	12.2	110	39.65	81.5428
	Sp 7	3254.908	1.397478	3.25	12.2	110	39.65	82.09101
	Sp 8	3705.789	1.469338	3.24	12.34	110	39.9816	92.68735
	Sp 9	3210.813	1.427533	3.2	12.1	110	38.72	82.92389
	Sp 10	3261.687	1.31561	3.2	12.2	110	39.04	83.54731
Hybrid composite (Jute_25%)	Sp 11	3288.168	1.302477	1.8	12.3	110	22.14	148.5171
	Sp 12	3335.531	1.331456	1.74	12.32	110	21.4368	155.5984
	Sp 13	2904.818	1.180288	1.73	12.36	110	21.3828	135.8484
	Sp 14	3664.738	1.424947	1.8	12.3	110	22.14	165.5257
	Sp 15	3130.133	1.266176	1.8	12.24	110	22.032	142.0721
Synthetic composite (Glass_100%)	Sp 16	3492.226	1.290112	2.33	12.21	110	28.4493	122.7526
	Sp 17	5802.306	1.811302	2.05	12.21	110	25.0305	231.8094
	Sp 18	5306.431	1.57696	2.02	12.22	110	24.6844	214.971
	Sp 19	3833.96	1.347635	1.96	12.2	110	23.912	160.3362
	Sp 20	2520.883	1.305242	1.56	12.23	110	19.0788	132.1301

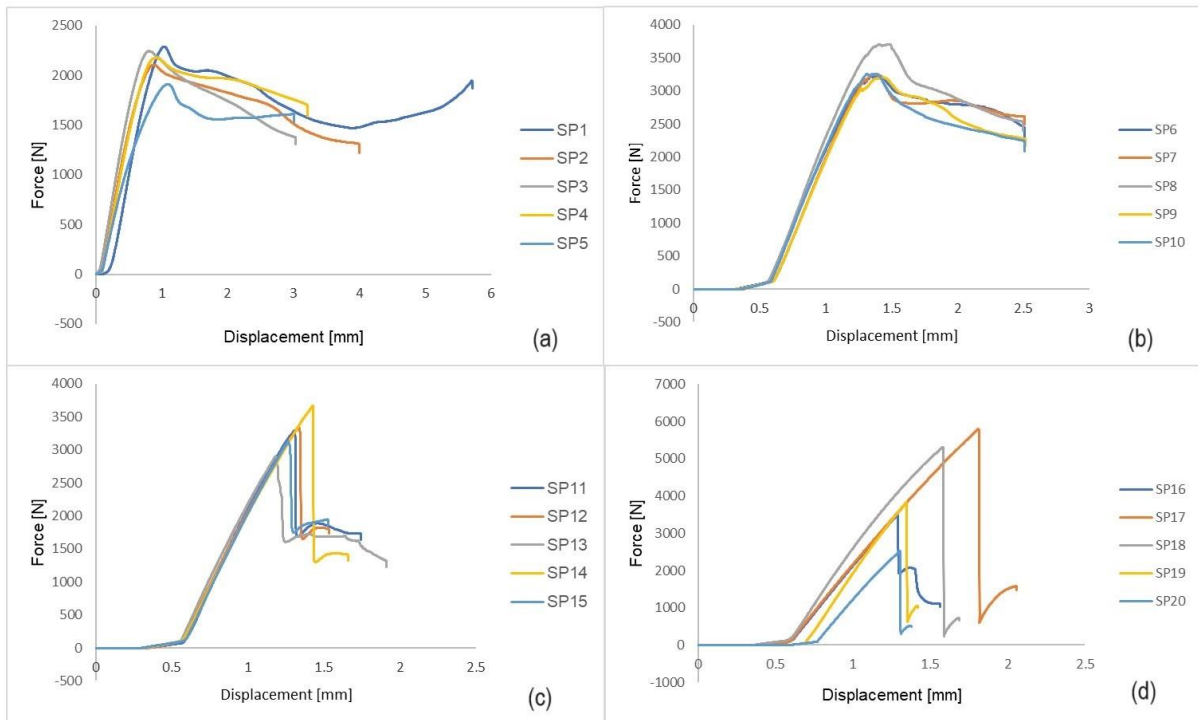


Figure 40. Force vs displacement plots at various compressive test specimens, (a) Bio-composite specimens plots, (b) Hybrid composite (Jute_75% and Glass_25%) specimens plots, (c) Hybrid composite (Jute_25% and Glass_75%) specimens plots and (d) Synthetic composite specimen plots.

6.4 Tensile test

After the successful preparation, the samples were cut using the laser cutting machine in accordance with ASTM D 3039. Four different types of laminates, including bio-laminate, hybrid composites with two configurations, and synthetic composites, were subjected to testing, as detailed in Table 2. The tensile test was conducted following the guidelines of ASTM D 3039, considering the specified load and environmental conditions for such tests. The test was performed at a constant head-speed of 2 mm/min, with an extensometer length of 10 mm. The specimens had dimensions of length 250 mm, width 25 mm, and a thickness ranging from 1.8 mm to 2.90 mm, and each specimen was prepared in the dog bone shape.

$$F^{tu} = P^{max} / A \quad (5.3)$$

$$\sigma_i = P_i / A \quad (5.4)$$

Where, F_{tu} = ultimate tensile strength, [MPa], P_{max} = maximum load before failure, [N], P_i = load at i_{th} data point, [N], A = cross-sectional area of the specimen, [mm²], σ_i = tensile stress as the i_{th} data point, [MPa]. The calculation of tensile strain, or ultimate tensile strain, involves determining the material response using an extensometer. The Equation. 5.5 is then used to determine the value of tensile strain. Five specimens were tested for the tensile test, the tensile test can be observed in Fig.41.

$$\epsilon_i = \delta_i / L_g \quad (5.5)$$

Where, ϵ_i = tensile strain at i_{th} data point, $\mu\epsilon$; δ_i = extensometer displacement at i_{th} data point, [mm] and L_g = extensometer gage length, [mm]. The obtained tensile results are presented in Table 16.

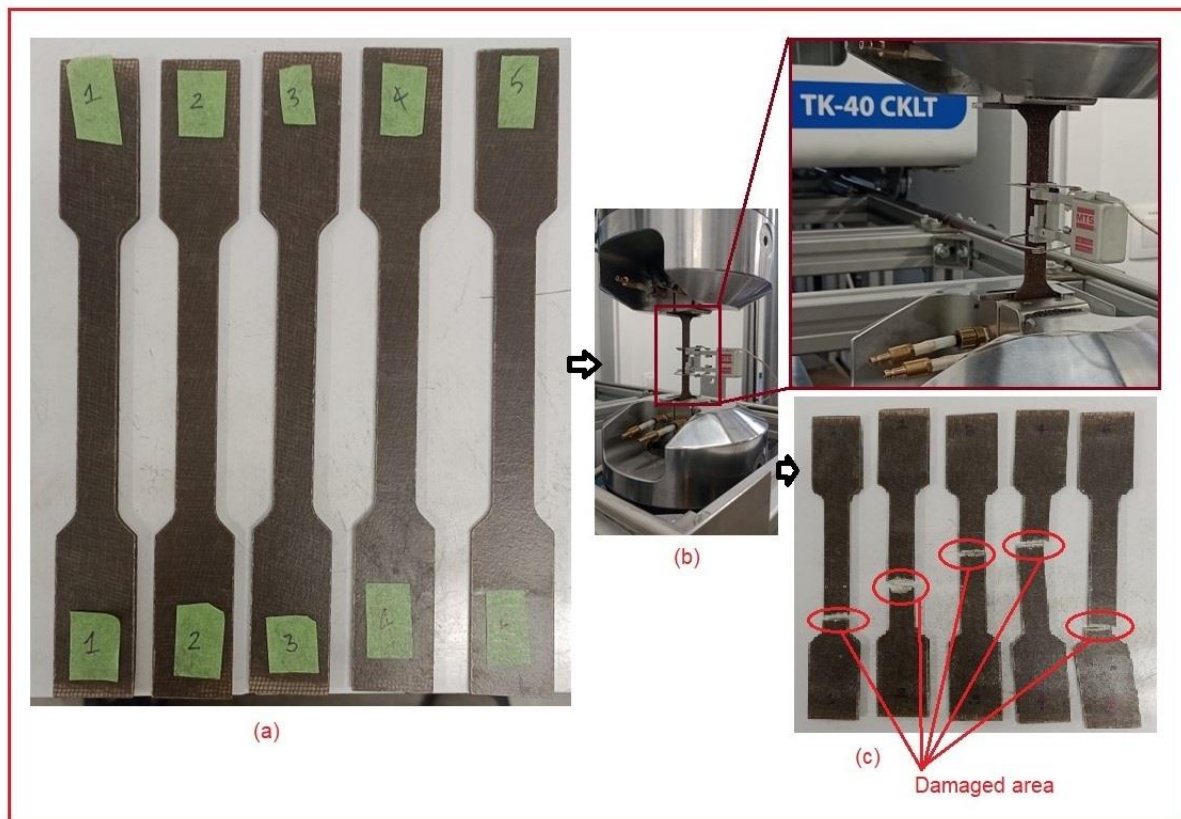


Figure 41. Tensile test setup for bio-composite structure, (a) specimens, (b) Tensile test setup, (c) tested specimens.

Table 16. Tensile stress results of composite laminates

Description	Specimens	Peak Load N	Break Load N	Width (b) mm	Thickness (t) mm	Area mm ²	Peak Stress MPa	Break Stress MPa	Modulus MPa
Bio-composite (Jute_100 %)	Sp1	1745.4847	1737.9153	12.65	2.43	30.7395	56.78312	56.53688	4897.6403
	Sp 2	1896.5873	1896.5873	12.6	2.3	28.98	65.4447	65.4447	5069.6129
	Sp 3	1783.6334	1783.6334	12..62	2.31	29.1522	61.18349	61.18349	5256.493
	Sp 4	1817.2844	1817.2844	12.56	2.34	29.3904	61.83259	61.83259	5247.7863
	Sp 5	1763.5501	1763.5501	12.62	2.4	30.288	58.22603	58.22603	5074.4083
Hybrid composite (Jute_75%)	Sp 6	2399.9214	2399.9214	12.43	3.2	39.776	60.33592	60.33592	4708.4048
	Sp 7	2306.9707	2251.6416	12.48	3.21	40.0608	57.58674	56.20561	4855.2475
	Sp 8	2352.5825	2349.115	12.42	3.26	40.4892	58.10395	58.01831	4718.3047
	Sp 9	2430.0623	2430.0623	12.45	3.25	40.4625	60.05715	60.05715	4748.4218
	Sp 10	2400.3669	2393.8855	12.5	3.26	40.75	58.90471	58.74566	4735.3931
Hybrid composite (Jute_25%)	Sp 11	2400.0547	2400.0547	12.5	1.8	22.5	106.6691	106.6691	8511.1058
	Sp 12	2559.4004	2559.4004	12.5	1.8	22.5	113.75113	113.75113	7861.69772
	Sp 13	2499.8547	2499.8547	12.56	1.8	22.608	110.5739	110.5739	7971.91335
	Sp 14	2429.0552	2429.0552	12.5	1.8	22.5	107.95801	107.95801	8023.46205
	Sp 15	2597.8777	2597.8777	12.58	1.82	22.8956	113.46624	113.46624	7711.96932

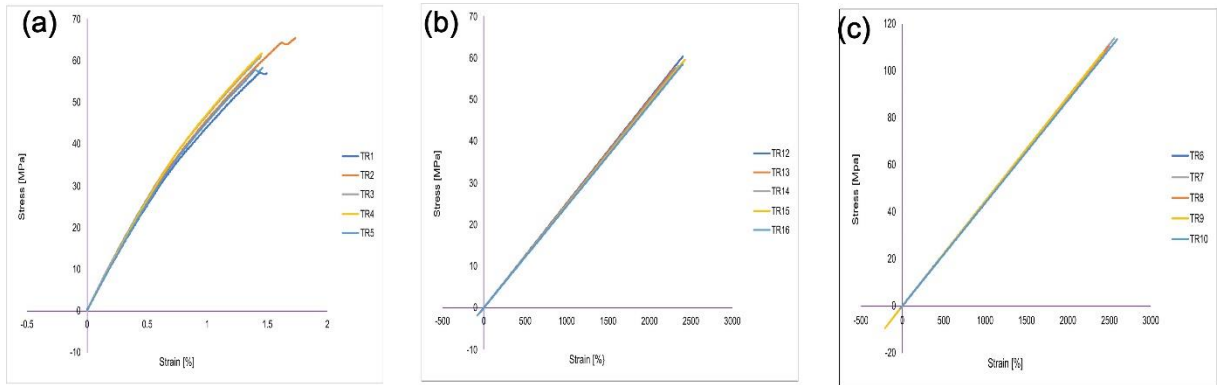


Figure 42. Force vs displacement plots at various tensile test specimens, (a) Bio-composite specimens plots, (b) Hybrid composite (Jute_75% and Glass_25%) specimens plots, (c) Hybrid composite (Jute_25% and Glass_75%) specimens plots and (d) Synthetic composite specimen plots.

6.5 Three-point bending test

Once the new composite was produced, a three-point bending test was conducted at room temperature using a universal machine (Zwick/Z050, guided by Test Xpert V.12.0) with a cross-head speed of 2 mm/min. This machine has the capability to perform traction, compression, and bending tests effortlessly, allowing for easy assembly and disassembly of jaws. Additionally, it features a load cell with a capacity of 5 kN and offers a range of loading speeds from 1 to 400 mm/min, which are automatically regulated. Fig.43 shows the three-point bending tests using different specimens. Table 16 presents the results of the mechanical properties for five specimens of different configurations of composite laminates. To ensure greater uniformity in presenting the outcomes, we have employed the provided equations derived from beam theory.

$$\sigma = \frac{3Pl}{2bh^2} \quad (5.6)$$

$$\varepsilon = \frac{6hY}{l^2} \quad (5.7)$$

where, ε is the maximum strain at maximum force, h is the thickness, l is the distance between the supports and Y is the displacement.

$$E = \frac{l^3}{4bh^3} \cdot \frac{\Delta P}{\Delta Y} \quad (5.8)$$

In this context, the symbols used have specific meanings: σ represents normal stress, ϵ represents relative strain, b represents width, h represents thickness, P represents applied load or force, Y represents displacement, l represents the distance between supports, and E represents Young's modulus. The Force-displacement curve is represented in Fig.42.

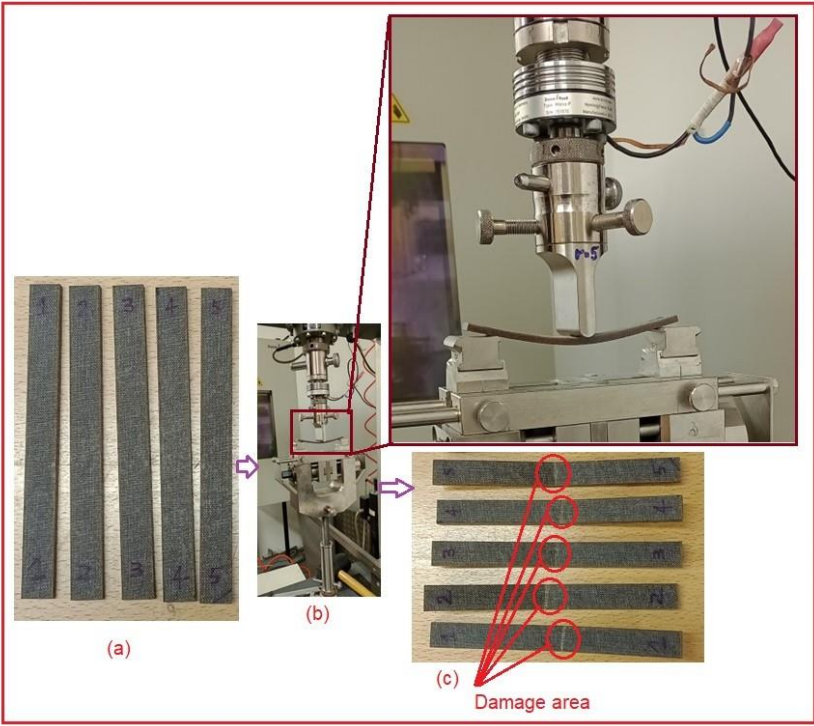


Figure 43. Three-point bending test setup for bio-composite structure, (a) specimens, (b) Tensile test setup, (c) tested specimens.

Table 17. Three-point bending test results composite laminates.

Description	Specimens	Thickness mm	width mm	weight mm	dL at F_{max} mm	F_{max} N	Flexural strength MPa
Bio-composite (Jute_100%)	SP 1	4.15	12.6	7.77	8.996403	92.11636	63.67387866
	SP 2	4.2	12.7	7.91	12.24399	94.70345	63.4095647
	SP 3	4.2	12.8	7.98	7.829504	88.68158	58.91367692
	SP 4	4.1	12.8	7.66	10.33464	81.84861	57.05909563
	SP 5	4.18	12.7	7.56	8.736538	82.22053	55.57957661
Hybrid composite (Jute_75%)	SP 6	3.9	12.7	6.87	14.86341	74.07	57.51758841
	SP 7	3.8	12.7	6.81	16.00617	72.2	59.05511811
	SP 8	3.8	12.7	6.8	16.19745	71.56	58.53163784
	SP 9	3.8	12.6	6.76	11.24549	65.57	54.05784197
	SP 10	3.8	12.7	6.7	14.29757	67.42	55.14537483
Hybrid composite (Jute_25%)	SP11	4.96	12.59	9.74	9.765504	453.44	219.5947761
	SP 12	5.08	12.6	9.8	10.16082	470.2	216.9081719
	SP 13	5.09	12.58	9.74	9.550131	456.43	210.0628411

SP 14	5.01	12.51	9.63	10.62717	465	222.1321655
SP 15	4.89	12.61	9.61	11.09965	465.25	231.4434189

In Figure 43, we observed that both the bio-composite laminate and hybrid laminates exhibited linear elastic behaviour initially but experienced failure once they reached the maximum stress. This type of failure can occur because of either complete fiber failure or matrix failure. Notably, the obtained plots showed a high degree of similarity (homogeneity) in both the elastic and plastic regions.

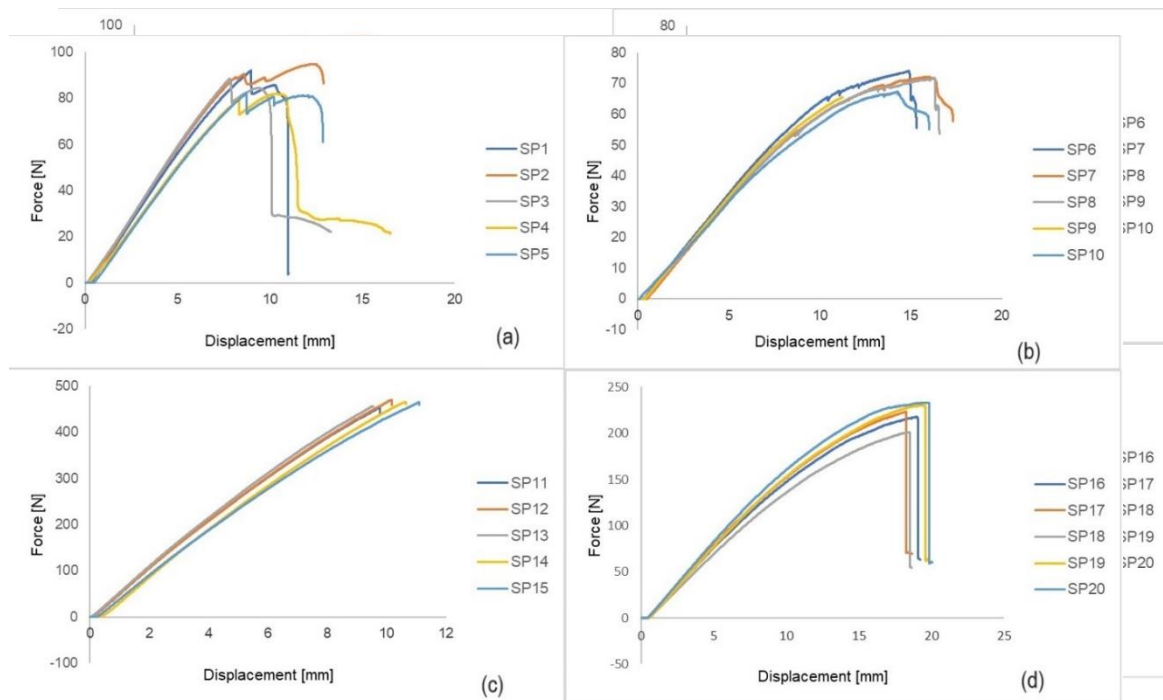


Figure 44. Force vs displacement plots at various three-point bending test specimens, (a) Bio-composite specimens plots, (b) Hybrid composite (Jute_75% and Glass_25%) specimens plots, (c) Hybrid composite (Jute_25% and Glass_75%) specimens plots and (d) Synthetic composite specimen plots.

6.6 Microscopic surface assessment

A study was carried out on (machine name) to examine the failure modes of fractured specimens in various stacking sequences through fractographic analysis.

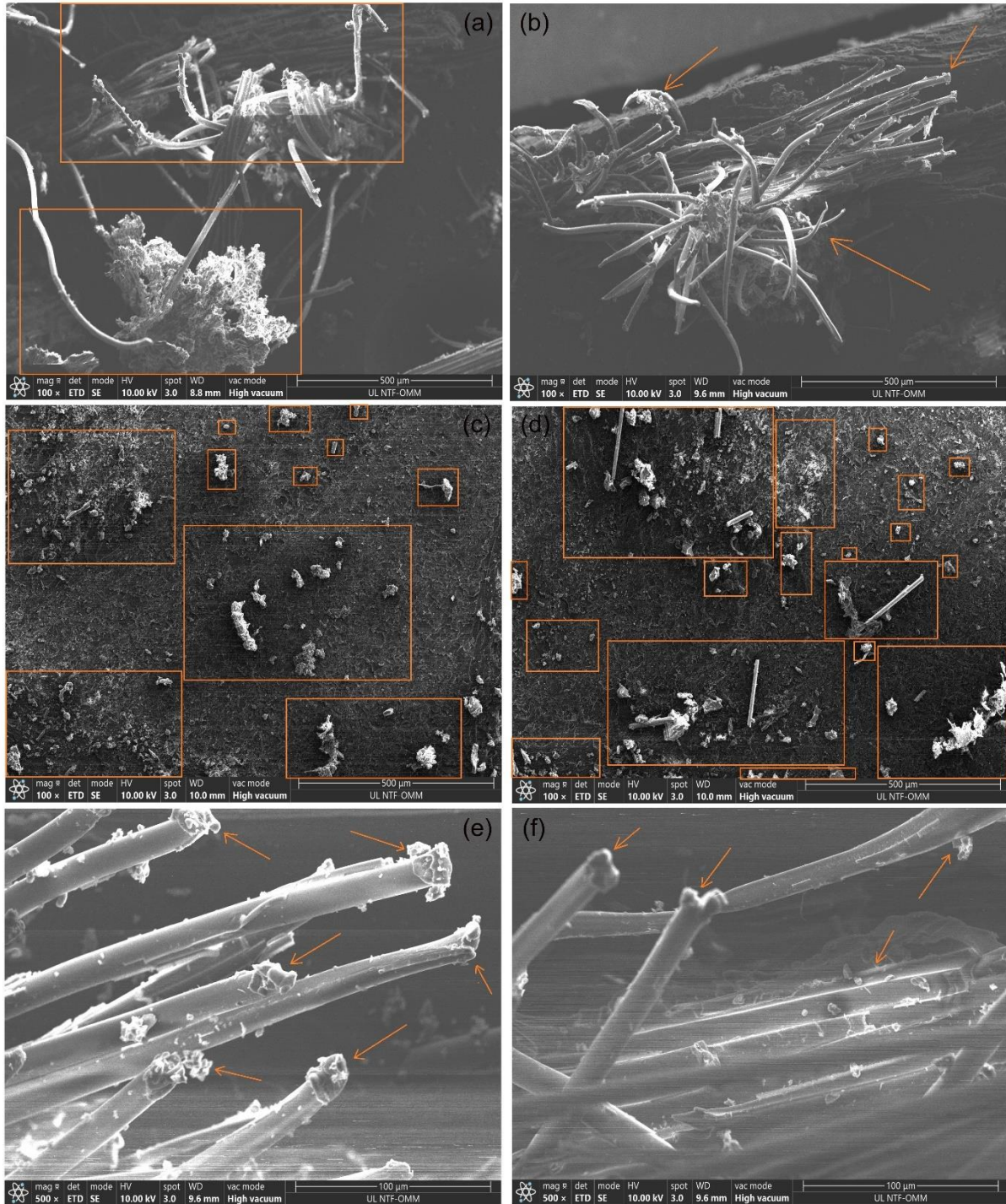


Figure 45. Bio-composite surface analysis (a), (b) The fiber pullout each other, (c), (d) Fiber shear splitting and (e), (f) Fiber breaking.

Fig. 45 shows the typical fracture surface, demonstrating how compression loads impact composite laminates. The failure of these laminates involved the shearing and splitting of matrix fibers, along with some instances of fiber pullout at the $\pm 45^\circ$ direction. Notably, significant matrix cracks, resulting from shearing, clearly indicate failure in bio-composite laminates under compression loads. These cracks are highlighted within rectangles in Figure 45a, b, c, and d. Fig. 45e and 45f demonstrates spherulitic failure. In Figure 45b, 45e the occurrence of spherulitic matrix failure (MF) suggests the focal point of compressive force around the fiber, as indicated by the arrow. This compressed region is prone to brittleness compared to the adjacent matrix material. Figure 44f exhibits the likelihood of matrix cracking and fiber fracture (FF) under compressive load, as shown by the arrow.

7. Results and Discussion

7.1 Case study_1 analysis result for T-joints

The structural analysis was effectively carried out for different scenarios, encompassing Case 1, Case 2, and Case 3. The outcomes, featuring maximum material stress, strain, displacement, shear stress, and deformed modes, are depicted in Figures 45, 46, and 47 below. Within the subplots a–d of the Von Mises stress graphs for jute, the values range from 45.667 MPa to 5.811 MPa. Von Mises stress indicates the degree of stress in the material under loading conditions. Higher values suggest potential failure or yielding points in the jute structure, while lower values indicate areas under comparatively less stress.

The Von Mises stress plots for glass (subplots e–h) display values ranging from 42.038 MPa to 5.569 MPa. Glass, being brittle with poor ductility and high rigidity, responds differently under applied stresses. Regions with high Von Mises stress in glass may indicate weaker areas prone to breakage or failure, whereas lower stress regions suggest areas less susceptible to damage. In the case of the sandwich-jute arrangement (subplots i–l), Von Mises stress values range from 57.754 MPa to 5.828 MPa. Sandwich structures typically comprise layers of different materials bonded together to meet performance objectives. These stress values demonstrate how the combination of jute and other materials influences stress distribution within the structure. Lower stress regions indicate areas where the configuration is better suited to withstand applied loads, while higher stress regions may raise concerns regarding potential failure or structural integrity issues. The maximum stress plots with various configurations are presented in Fig. 46.

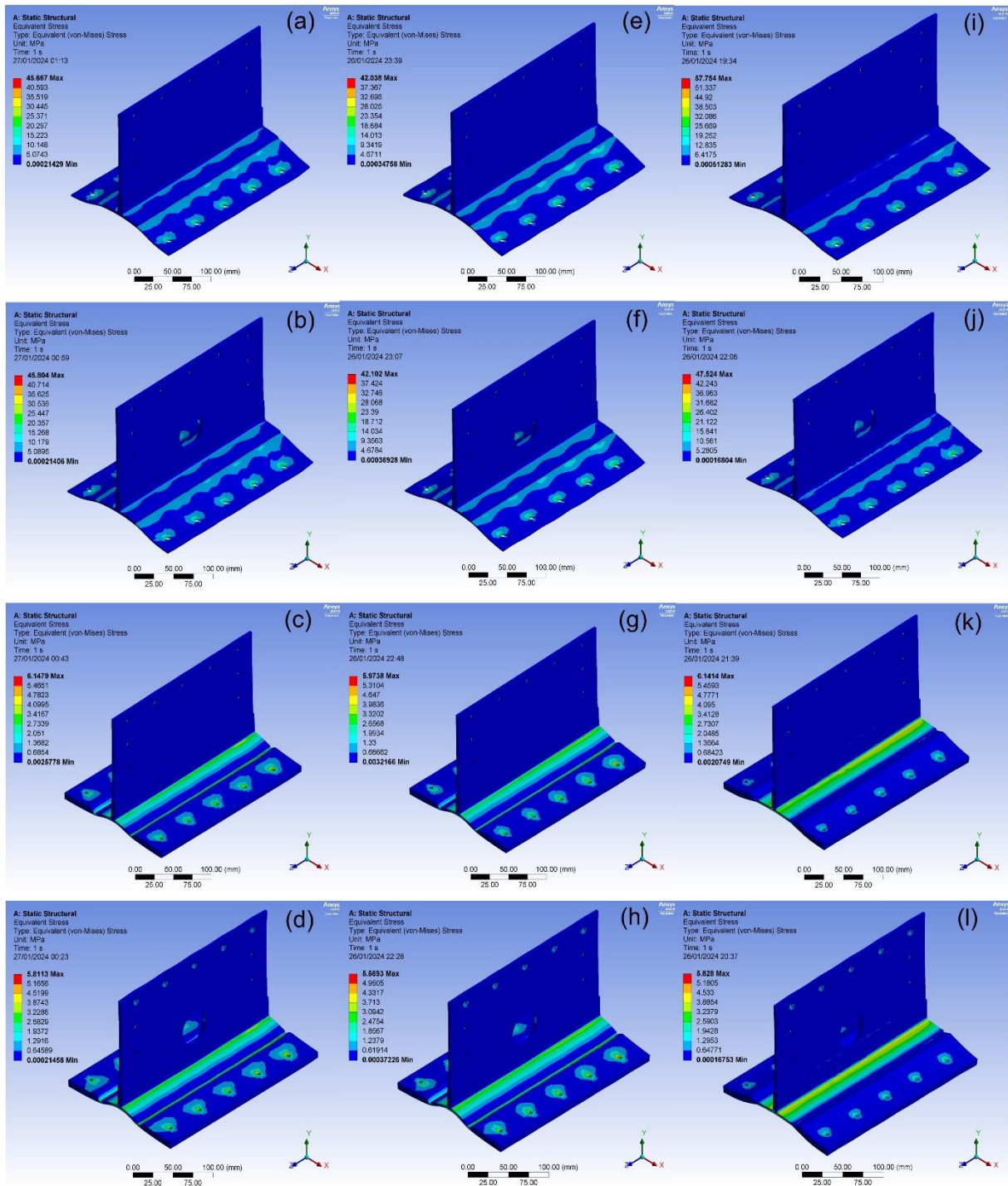


Figure 46. Maximum stress plots of jute (a-d), Glass (e-h) and Sandwich-Jute (i-l).

The values in the maximum strain plots for jute (subplots a-d) range from 0.0093 to 0.0001. Strain, indicating the deformation caused by applied loads, reflects the relative change in size or shape of a material. For the maximum strain plots of glass (subplots e-h), values range from 0.0013 to 0.0001. Glass, being brittle, typically experiences sudden failure without significant deformation. In the maximum strain plots for the sandwich-jute configuration (subplots i-l), values range from 0.013 to 0.042. The combination of

jute and other materials in a sandwich configuration influences the overall strain distribution within the structure. The maximum strain plots with various configurations are depicted in Fig. 47.

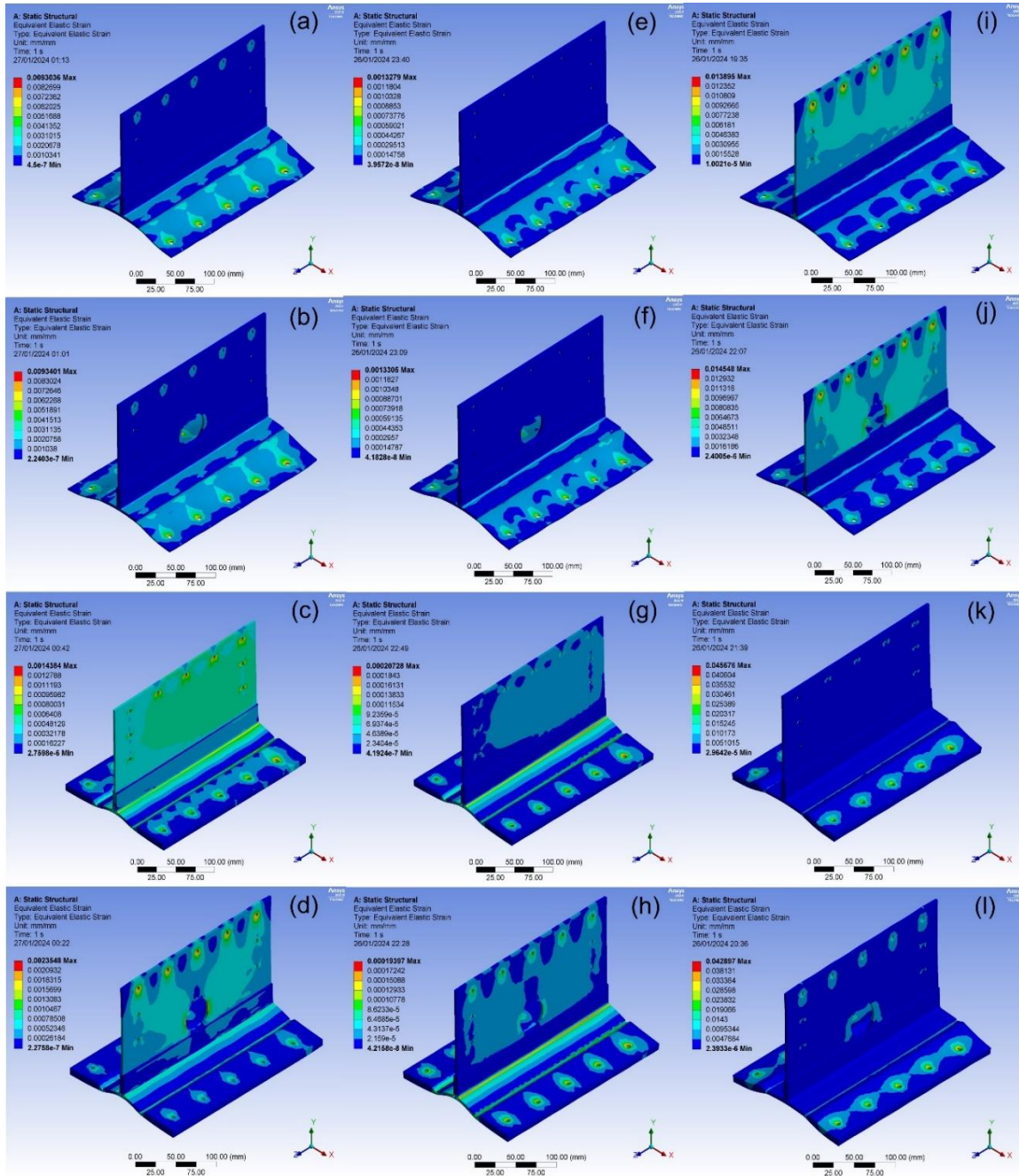


Figure 47. Maximum strain plots of jute (a-d), Glass (e-h) and Sandwich-Jute (i-l).

The jute maximum shear stress plots (subplots a-d) exhibit values ranging from 22.948 MPa to 2.929 MPa. Shear stress, occurring parallel to a surface, is a type of stress. Lower values indicate regions with relatively lower shear stresses, while higher values signify areas where the material is more susceptible to shear failure. For glass (subplots e-h), the

maximum shear stress plots range from 21.325 MPa to 2.855 MPa. Shear forces can lead to material fracture or failure. In the case of the sandwich-jute arrangement (subplots i–l), the maximum shear stress graphs display values ranging from 28.889 to 2.953 MPa. These values indicate the distribution of shear stresses within the structure.

The Fig.47 illustrate the deformation plots for jute (subplots a–d) exhibit values ranging from 1.441 mm to 0.022 mm. Higher values indicate areas where the material undergoes greater displacement. In contrast, deformation plots for glass (subplots e–h) range from 0.171 mm to 0.022 mm. Glass, known for its rigidity and low ductility, typically yields lower values compared to jute, reflecting its brittle nature. For the sandwich-jute structure (subplots i–l), deformation graphs display values ranging from 2.038 mm to 2.125 mm. These values demonstrate the extent of deformation within the structure. The Ansys results obtained are presented in Table 17.

Table. 17 The static structural analysis results at various design configurations.

Description	Epoxy -Jute composite - Design cases 1				Epoxy-Glass composite- Design cases 2				Sandwich structure- Design cases 3			
	D1	D2	D3	D4	D5	D6	D7	D8	D9	D10	D11	D12
Force (N)	200	200	200	200	200	200	200	200	200	200	200	200
Deformation (mm)	1.441	1.443	0.24	0.225	0.171	0.171	0.025	0.022	2.038	1.984	2.302	2.125
Von Mises stress (MPa)	45.667	45.804	6.147	5.811	42.038	42.102	5.973	5.569	57.754	47.524	6.141	5.828
Max. Strain	0.0093	0.0093	0.0014	0.0023	0.0013	0.0013	0.0001	0.0001	0.013	0.014	0.045	0.042
failure index	0.2283	0.229	0.0307	0.0291	0.2102	0.2105	0.0299	0.0278	0.2888	0.2376	0.0307	0.0291
Max.shear stress (MPa)	22.948	23.016	3.099	2.929	21.325	21.358	3.063	2.855	28.889	23.88	3.116	2.953
Buckling load factor	8.135	8.129	8.063	9.287	10.8	9.384	8.926	9.543	1.237	1.251	1.109	1.258
Buckling critical load (N)	1627	1625.8	1612.6	1857.4	2160	1876.8	1785.2	1908.6	161.68	159.87	180.34	158.98
Strength ratio (R)	4.3795	4.3664	32.536	34.417	4.7576	4.7504	33.484	35.913	3.463	4.2084	32.568	34.317
Temperature (C°)	40	40	40	40	40	40	40	40	40	40	40	40

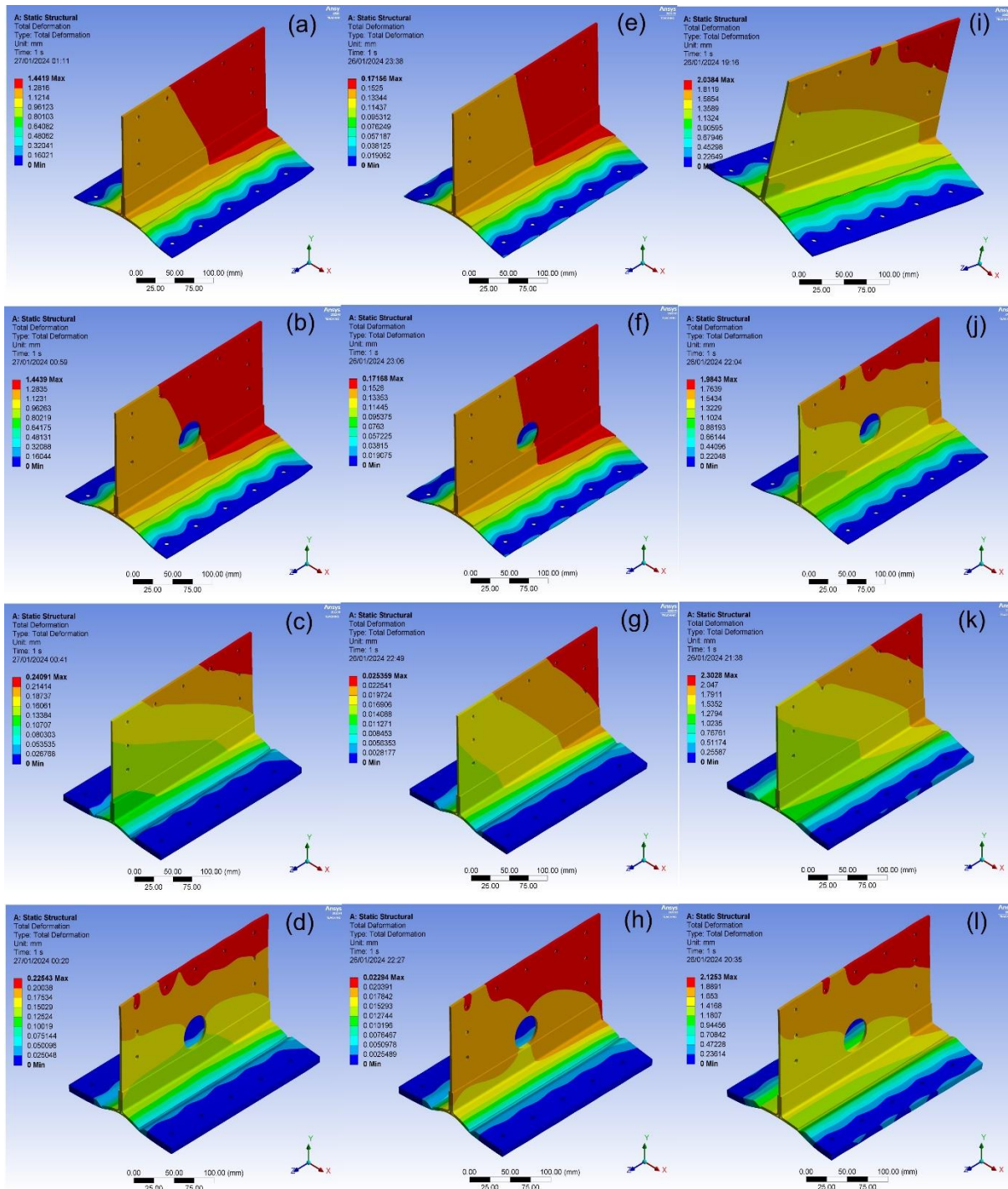


Figure 48. Deformation plots of jute (a-d), Glass (e-h) and Sandwich-Jute (i-l).

The investigation examined the mechanical behaviour of three distinct composite structures within the specified design scenarios. These comprised an epoxy-jute composite (Design Case 1), an epoxy-glass composite (Design Case 2), and a sandwich structure (Design Case 3). Each configuration was subjected to a 200 N force, and various mechanical attributes were measured to evaluate its performance under loading conditions.

Epoxy-Jute Composite (Design Case 1): The epoxy-jute composite exhibited significant deformation, ranging from 0.022 mm to 2.038 mm across different design instances. Von Mises stress values varied from 5.569 MPa to 57.754 MPa, indicating fluctuating stress levels within the material. Maximum strain values ranged from 0.0001 to 0.014, signifying localized strain within the composite. The failure index values were relatively low, suggesting minimal likelihood of failure under the applied load. The buckling load factor was high, indicating resistance to buckling. Strength ratio results were moderate, indicating a balanced strength-to-weight ratio for the composite. The structural failure of T-joints is presented in Fig.48.

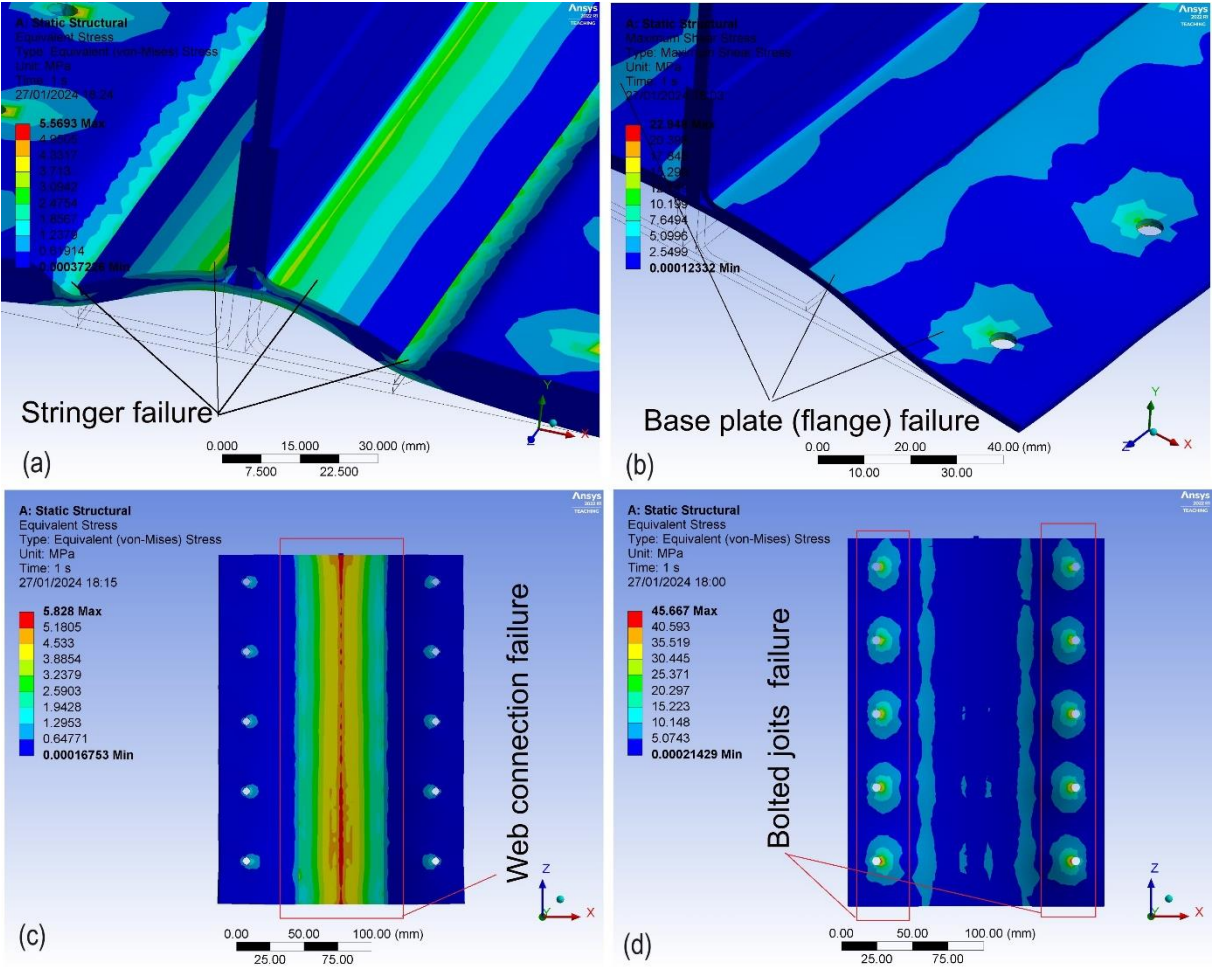


Figure 49. Design 8 structural failure, (a) stringer failure, (b) Base plate failure, (c) web connection failure and (d) Bolted joint’s location failure.

Epoxy-Glass Composite (Design Case 2): The epoxy-glass composite exhibited lower levels of deformation compared to the epoxy-jute composite, with values ranging from 0.022 mm to 2.302 mm. Von Mises stress values ranged from 5.569 MPa to 47.524 MPa,

similar to those of the epoxy-jute composite. Maximum strain values varied from 0.0001 to 0.045, with higher strain values compared to the epoxy-jute composite.

The failure index values remained low, indicating minimal likelihood of failure. The buckling load factor remained high, indicating resistance to buckling. Strength ratio values were moderate, suggesting a similar strength-to-weight ratio to the epoxy-jute composite.

Sandwich Structure (Design Case 3): The sandwich structure exhibited the highest deformation among the three designs, with values ranging from 1.984 mm to 2.302 mm. Von Mises stress values ranged from 5.828 MPa to 57.754 MPa, indicating varying stress concentrations.

The maximum strain values ranged from 0.013 to 0.045, surpassing those observed in the two composite designs. Low failure index values indicated a minimal likelihood of failure. However, the buckling load factor was low, suggesting lesser resistance to buckling compared to composite constructions. Strength ratios were moderate, indicating a balanced strength-to-weight ratio. The current study can be compared to prior research conducted by S. Guo and R. Morishima [119]. The failure location was identified at various points, as illustrated in Fig. 48. It is crucial to extend research efforts to explore alterations in geometric shapes, fiber orientations, and ply stacking sequences to mitigate structural failures in T-joints, particularly at the interfaces of the stringer, base plate, and web.

7.2 Case study_2

7.2.1 Sandwich structure design and analysis (approach_1)

To enhance the density of the material (achieving lightweight yet high strength) as explored in this study, the critical design parameters of the corrugated sandwich panel were optimized. These parameters include the core height (h_c), corrugated angle (θ), and core thickness (t_c).

Seven numerical models were devised and are outlined in Table 4 of the research. Among them, three models maintained the same core height but varied in corrugated angle, with consistent thickness. Similarly, another three models kept the corrugated height constant while altering the corrugated angle, with thickness remaining consistent. Additionally, one model was developed with varying core height, angle, and thickness. The geometrical

aspects were crafted using CATIA V5, with detailed model specifications provided subsequently.

Table 18 . Sandwich panel optimization geometrical parameters.

S.No	Core	Dimensions (mm)	h _c (mm)	θ	t _c (mm)
1	C1	240x78x10.5	16	25°	0.5
2	C2	240x92x12.6	20	25°	1.0
3	C3	240x 70.8x 16.6	18	45°	0.75
4	C4	240x 46.8x 18.2	16	65°	0.5
5	C5	240x64.8x 15	16	45°	0.5
6	C6	240x 53.8x 22.3	20	65°	1.0
7	C7	240x 76.4x 18.3	20	45°	1.0

Fig. 50 illustrates the alteration in corrugated core material properties resulting from optimizing the sandwich panel's overall structure, with a focus on reducing weight. Various modifications, including adjusting thickness and angles, were made to the corrugated core, and these changes were implemented in the final CAD models analysed using ANSYS. The mechanical properties of epoxy carbon such as E1=1.21E+005 MPa, E2=8600 MPa, Poisson’s ratio=0.27, and G1=4700 MPa.

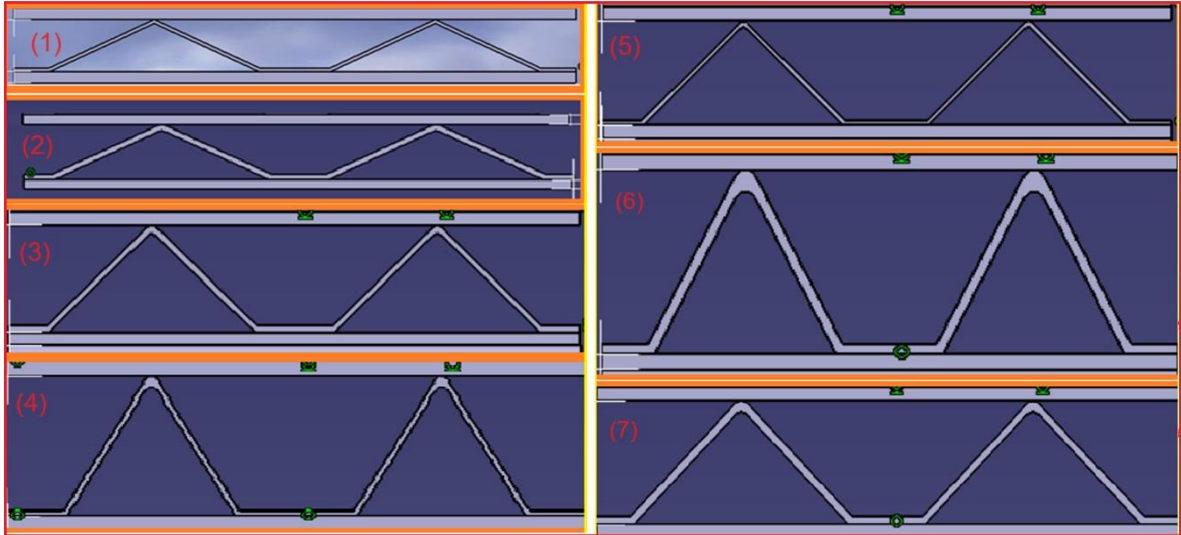


Figure 50. Optimization methodology for sandwich structure

Numerical analyses were conducted in ANSYS to validate the stiffness terms. While the

linear portion of the force-displacement curve is primarily of interest for validation, understanding the behavior in the nonlinear region is also important for optimal panel configuration with a corrugated core. A finite element (FE) model was utilized, analyzing a total of 7 panels with varying geometrical configurations. ANSYS library elements SHELL91 and SOLID95 were employed, with SHELL91 offering six degrees of freedom at each node: translations in the nodal x, y, and z directions, and rotations about the nodal x, y, and z axes. The FE analysis of the 3-point bending test (quasi-static) was performed, and the results for corrugated core sandwich panels A1 to A7 are presented in Fig.51

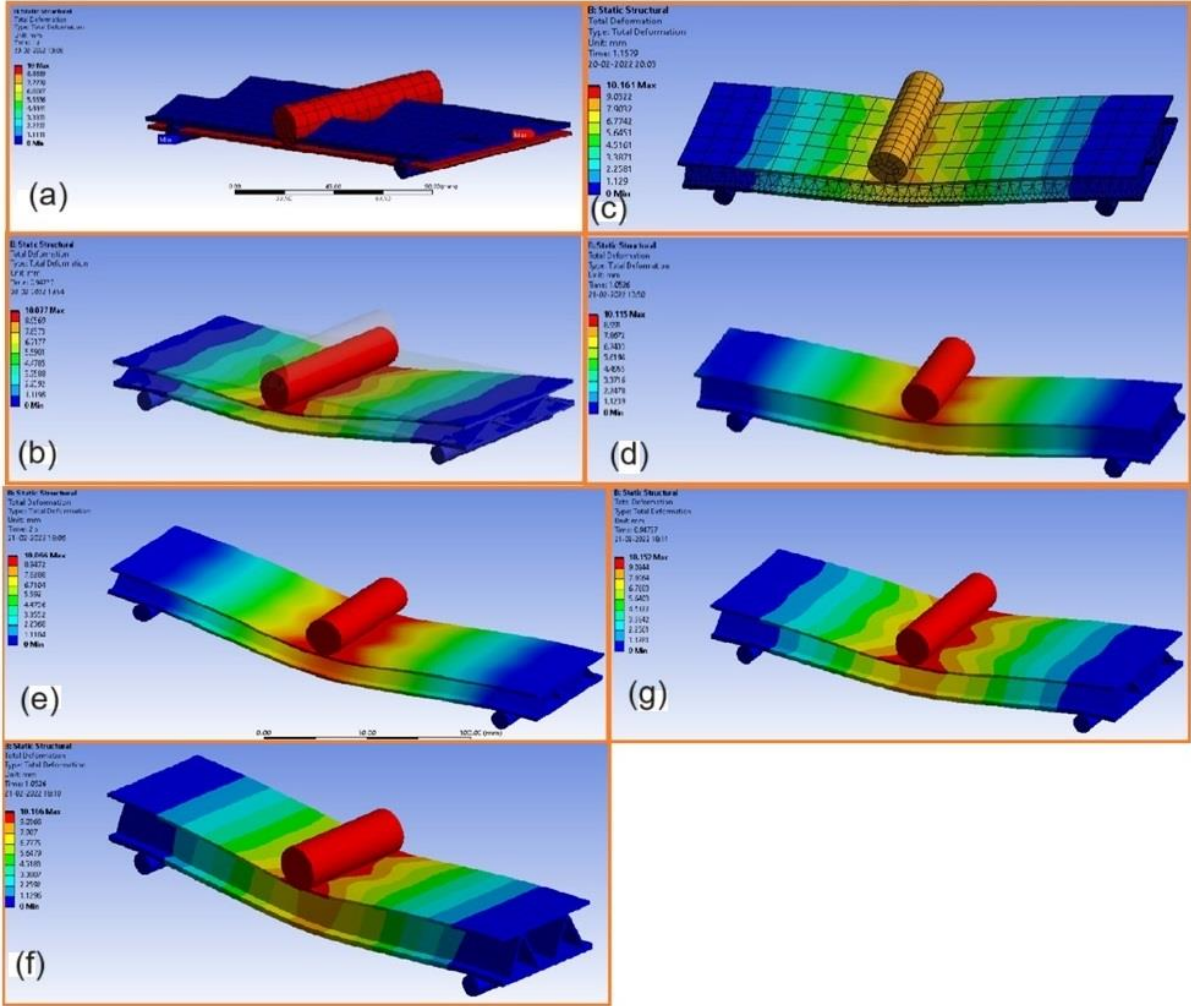


Figure 51. (a) Local indentation, (b) to (g) is represent maximum deformation of composite sandwich panel results.

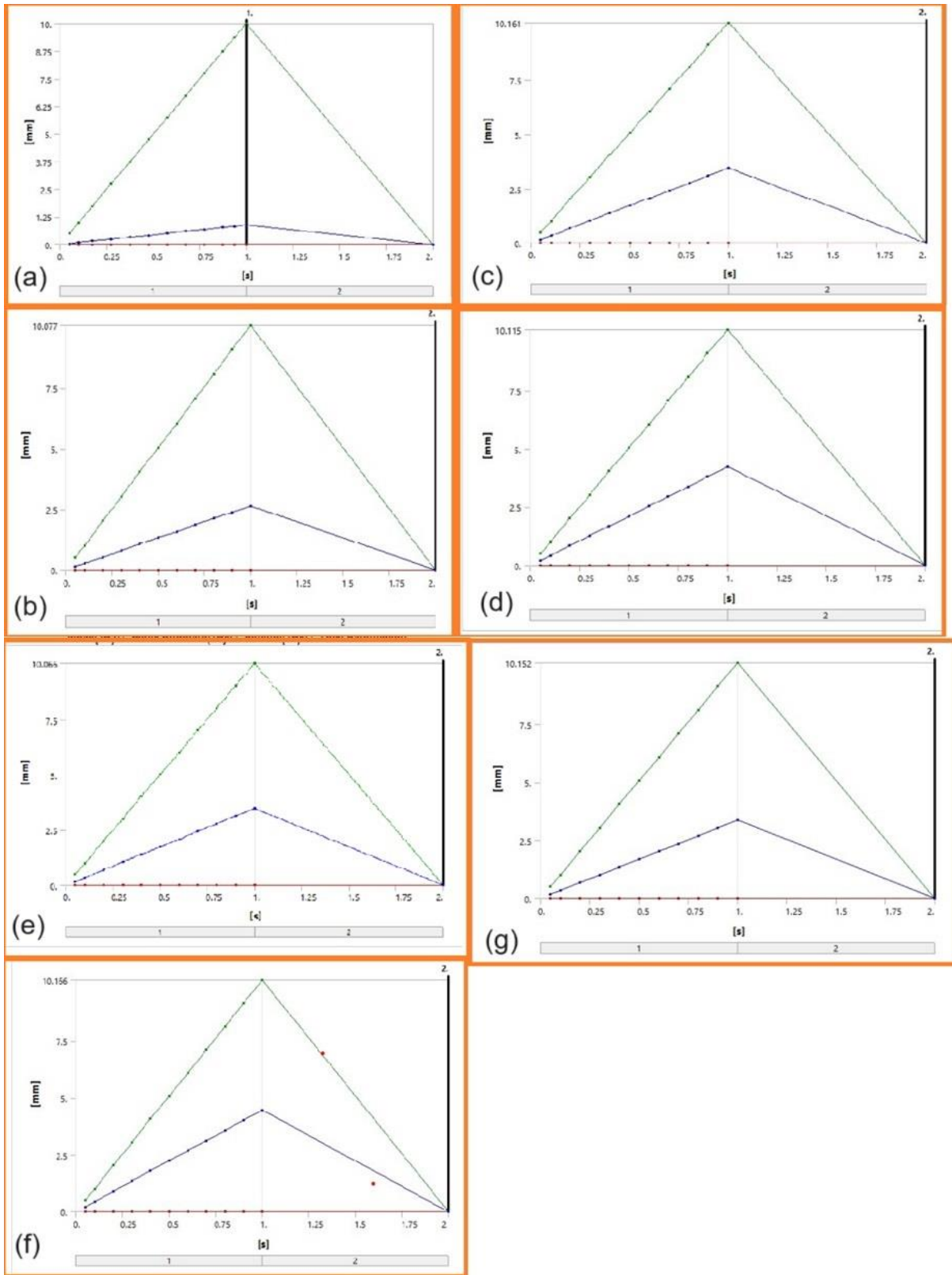


Figure 52. (a) to (g) maximum displacement vs Time graphs.

The FEM analysis of composite corrugated sandwich panels was conducted using ANSYS software, considering parameters such as corrugated core thickness, angle, and height for optimization purposes. This study primarily emphasizes both material strength and

structural stability. Subsequently, a comparison of specific energy absorption is performed to assess the performance of the sandwich panels. The deformation-time curves of all seven sandwich panels during local indentation exhibit a similar trend: initially, force increases linearly, reaches a peak, and then gradually decreases. Finally, summarizing all simulated 3-point bending test results, the most favourable outcome (with minimal deformation and indentation observed on corrugated core composite sandwich panel (C2) is identified for future research, following ASTM C 393-94 standards.

7.2.2 Sandwich structure design and analysis (approach_2)

In this research manly focused on the sandwich structures core optimization methodology core shape and other parameter also studied in terms material. Five different geometrical shape is considered for analysis along with two different material such as, Natural fiber and E-glass fibers as reinforcement were consider and core materials such as PVC foam. The structural analysis is carried out in the ANSYS. The element type SOLID95 were used from the ANSYS library. The FEA static analysis was carried out, the maximum stress, deformation, strain, and shear stress plots are shown in Fig.52. The mechanical properties are considered from engineering data and experimental data. (Jute fiber/E-glass). Jute fiber properties such as, $E1=4.89\text{GPa}$, $E2=0.489\text{GPa}$, $\nu1=0.25$ and $G_{xy}= 2.03\text{GPa}$.

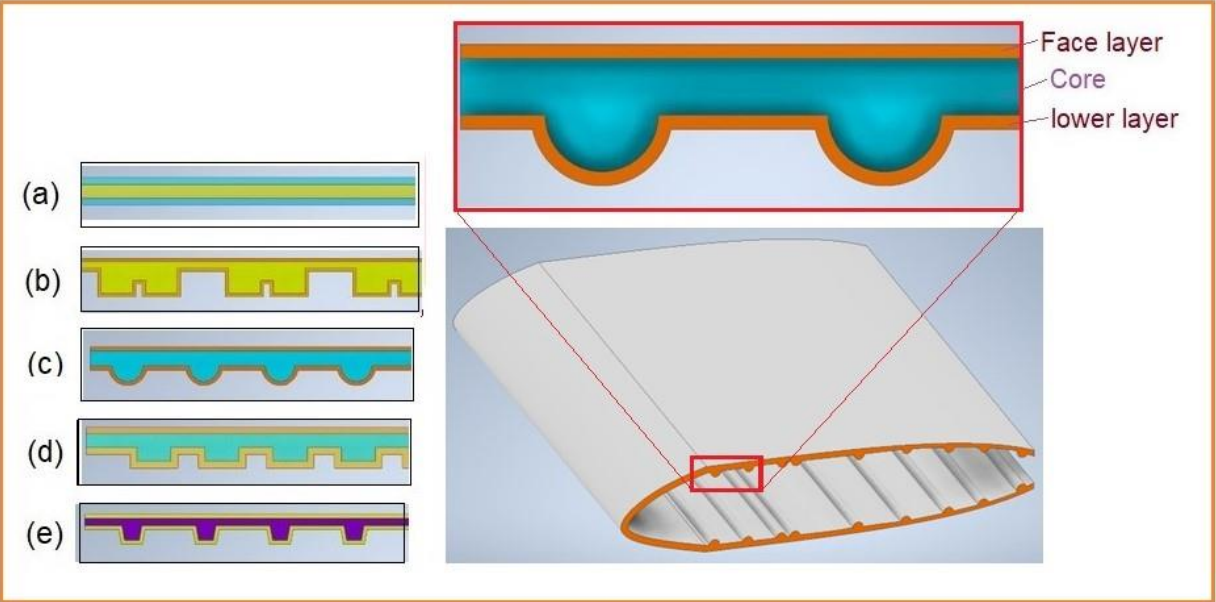


Figure 53. The proposed composite sandwich structure with different core configurations.

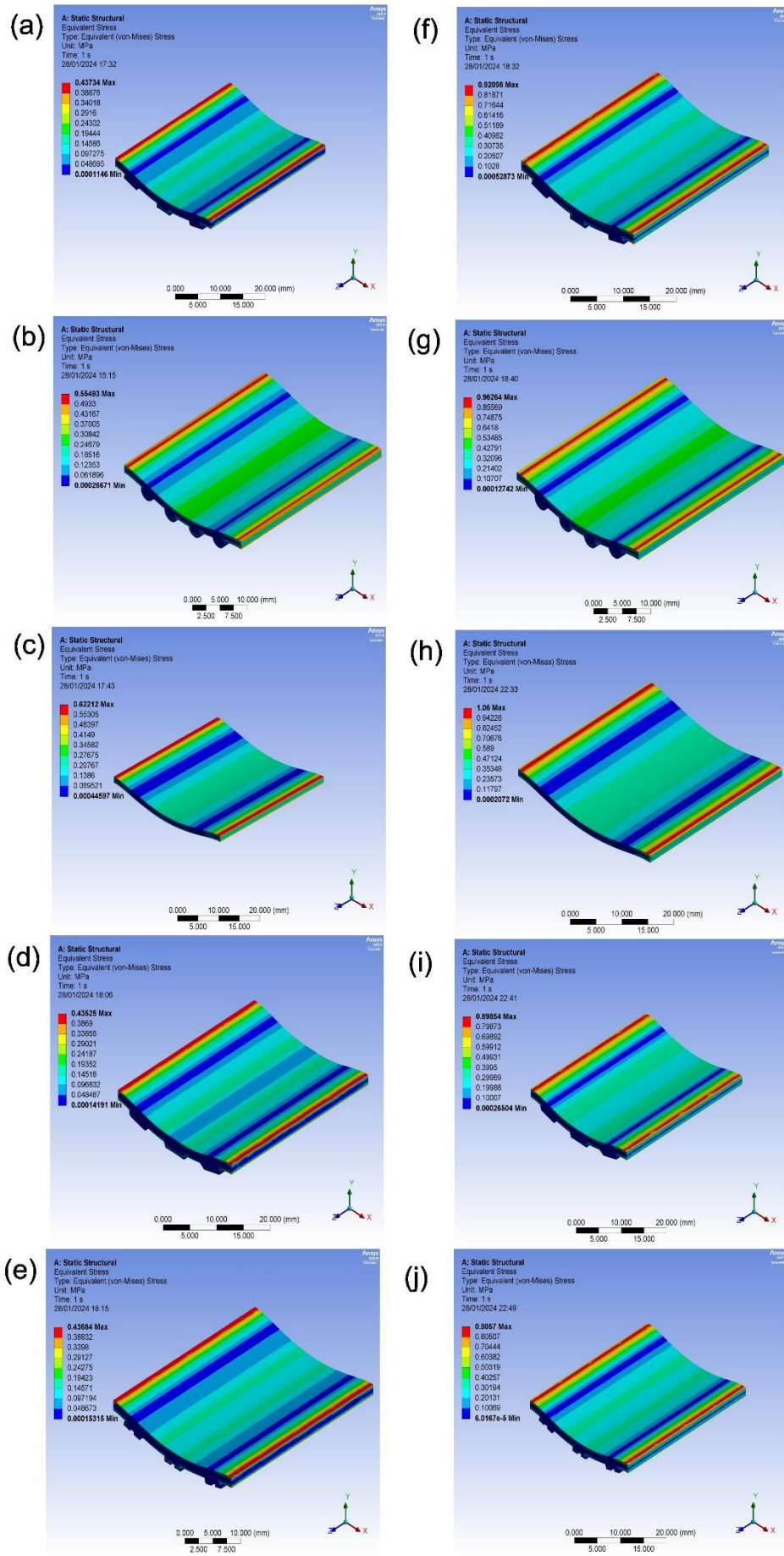


Figure 54. Maximum stress plots of jute (a-e) and E-glass (f-j).

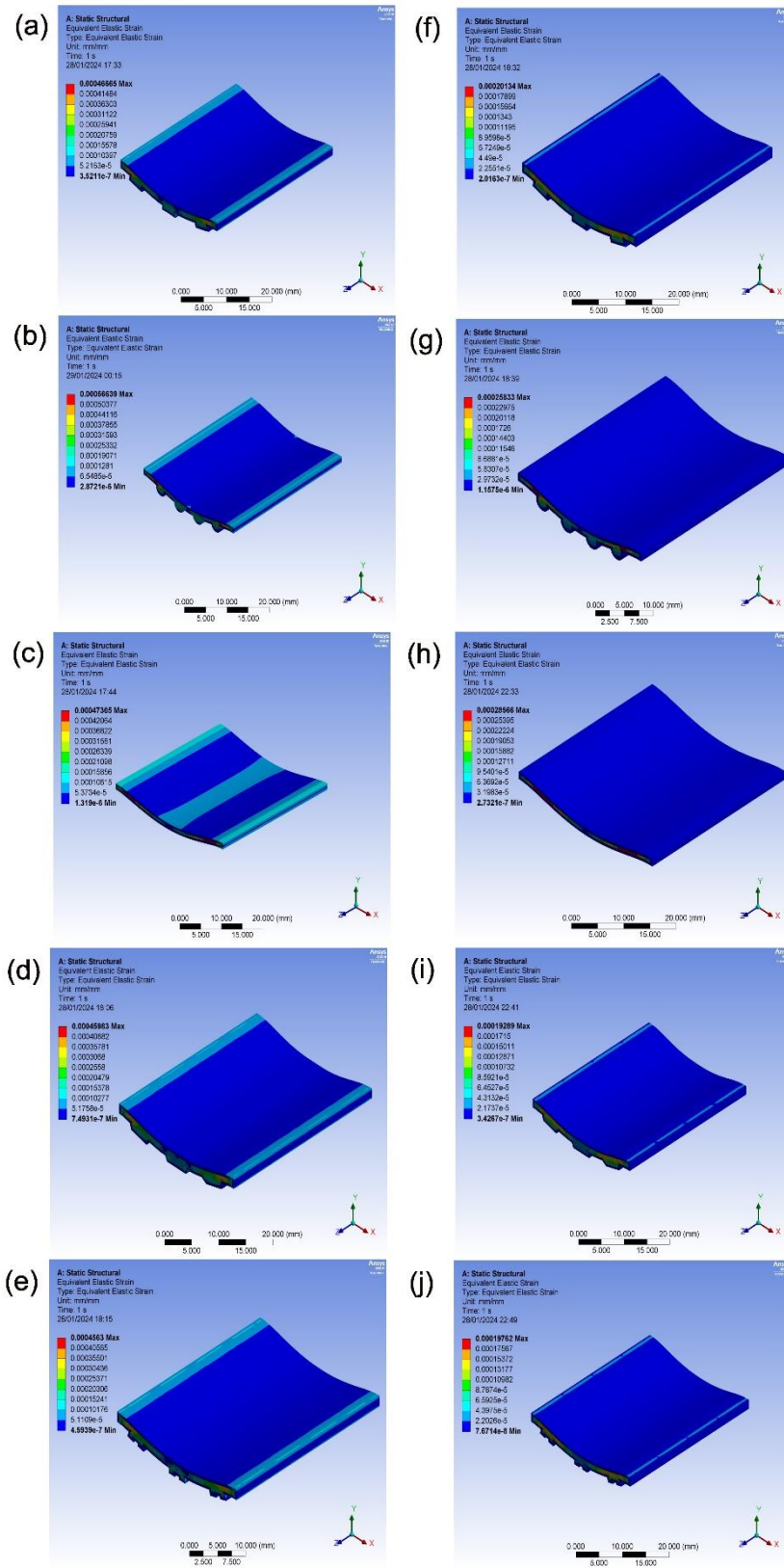


Figure 55. Maximum strain plots of jute (a-e) and E-glass (f-j)

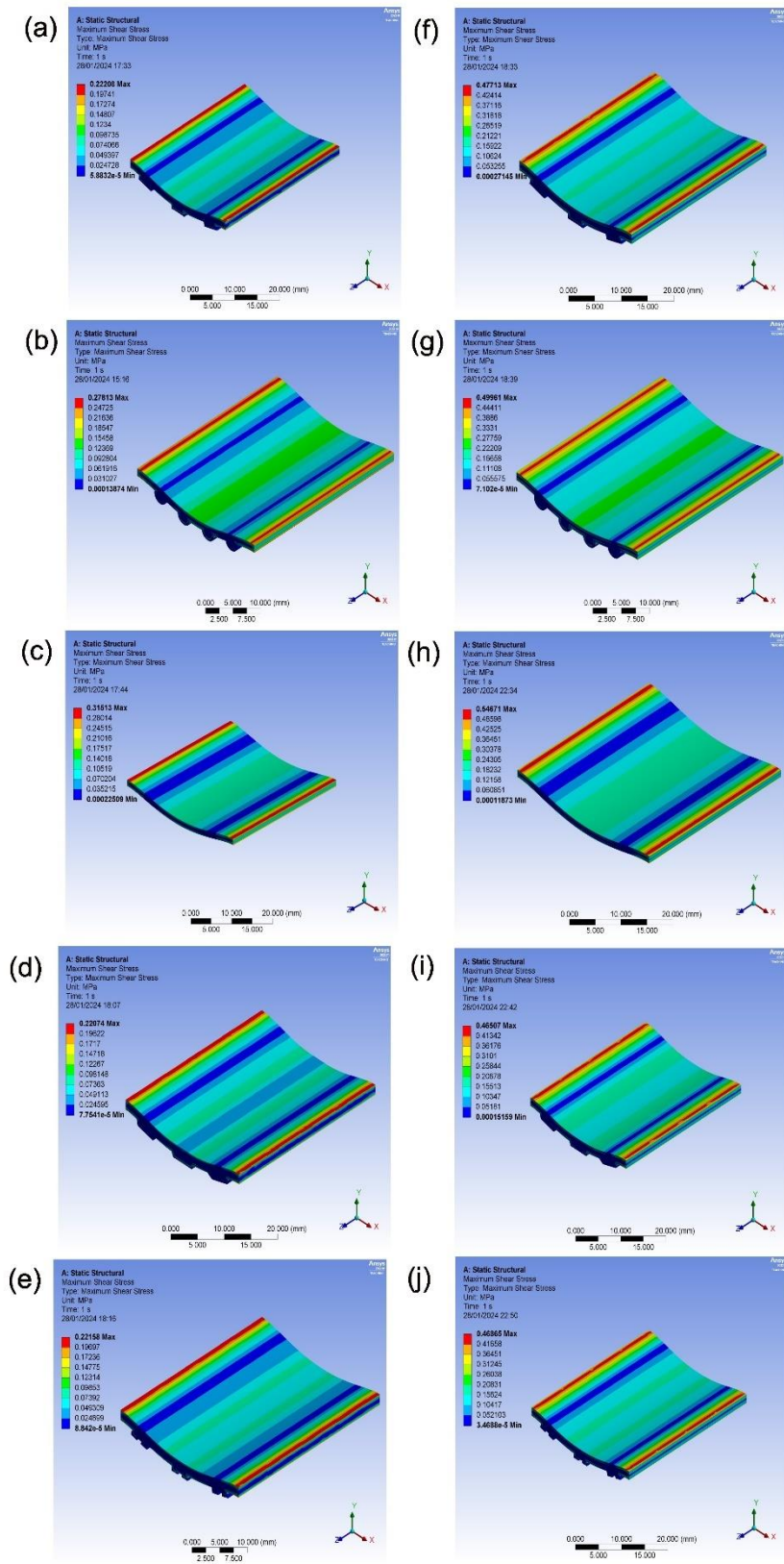


Figure 56. Maximum shear stress plots of jute (a-e) and E-glass (f-j).

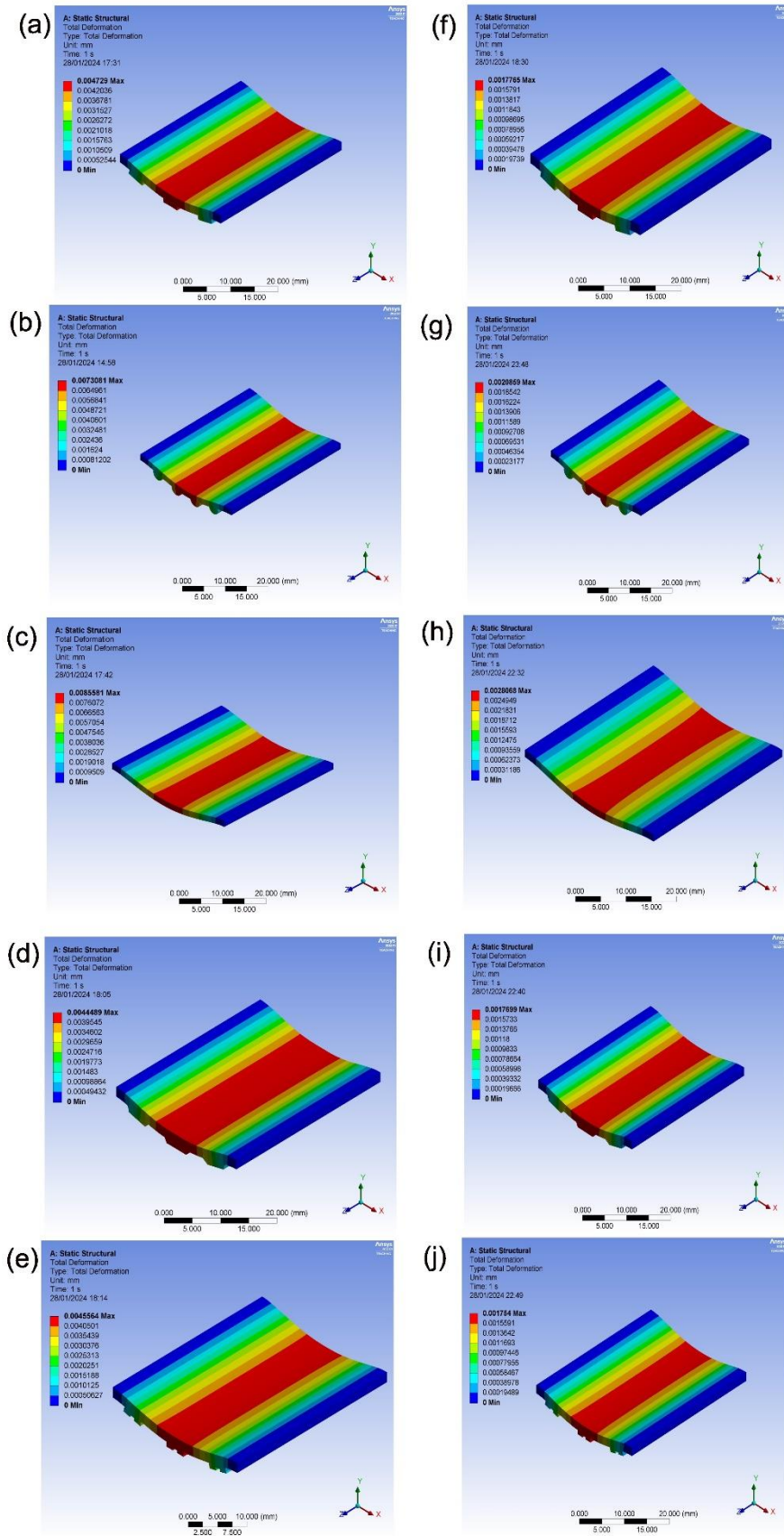


Figure 57. Maximum deformations plots of jute (a-e) and E-glass (f-j).

The experiment aimed to explore the mechanical characteristics of composite materials made up of jute fiber reinforced with PVC foam and E-glass fiber reinforced with PVC foam. The measured parameters encompassed stress, strain, shear stress, deformation, and critical buckling load. Details of the experimental design are presented in Table 19.

Table.19. Design experiments analysis results.

Experiments	Skin	core	Stress (MPa)	Strain	Shear stress (MPa)	Deformation (mm)	Critical buckling load (N)
D1	Jute fiber	PVC foam	0.437	0.0004	0.222	0.004	4518
D2	Jute fiber	PVC foam	0.554	0.0005	0.278	0.007	2712
D3	Jute fiber	PVC foam	0.622	0.0004	0.315	0.008	Error
D4	Jute fiber	PVC foam	0.435	0.0004	0.220	0.004	4765
D5	Jute fiber	PVC foam	0.436	0.0004	0.221	0.004	4718
D6	E-glass fiber	PVC foam	0.920	0.0002	0.477	0.007	9737
D7	E-glass fiber	PVC foam	0.962	0.0002	0.499	0.002	6912
D8	E-glass fiber	PVC foam	1.06	0.0002	0.546	0.002	Error
D9	E-glass fiber	PVC foam	0.898	0.0001	0.465	0.001	10316
D10	E-glass fiber	PVC foam	0.905	0.0001	0.468	0.001	10256

In the case of jute fiber reinforced PVC foam composites, it's evident from the data that there is a variation in stress and strain among different samples (D1 to D5). The stress values ranged from 0.435 MPa to 0.622 MPa, while the strain values ranged from 0.0004 to 0.0005. Similarly, shear stress varied between 0.220 MPa to 0.278 MPa. However, the deformation was relatively consistent across samples, indicating a stable behaviour in terms of material response to external forces. Notably, the critical buckling load for jute fiber reinforced composites ranged from 2712 N to 4765 N.

For E-glass fiber reinforced PVC foam composites (D6 to D10), a different trend is observed. The stress values are notably higher compared to the jute fiber composites, ranging from 0.898 MPa to 1.06 MPa. Similarly, shear stress values are elevated, ranging from 0.465 MPa to 0.546 MPa. Despite the higher stress levels, the strain values are relatively lower, ranging from 0.0001 to 0.0002. This suggests that the E-glass fiber composites exhibit greater stiffness compared to jute fiber composites. The critical buckling load for E-glass fiber composites is notably higher, ranging from 6912 N to 10316 N, indicating their superior load-bearing capacity compared to jute fiber composites.

In conclusion, the experimental results demonstrate that both jute fiber and E-glass fiber reinforced PVC foam composites exhibit promising mechanical properties suitable for various applications. However, each composite offers distinct advantages.

- ✚ Jute fiber reinforced composites exhibit moderate stress and strain characteristics along with consistent deformation behavior. While they may not offer the highest mechanical strength, they provide a balance between strength and flexibility, making them suitable for applications where resilience to deformation is crucial.
- ✚ On the other hand, E-glass fiber reinforced composites demonstrate significantly higher stress levels and critical buckling loads, indicating superior mechanical strength and load-bearing capacity. These composites are well-suited for applications requiring high structural integrity and resistance to heavy loads.

7.2.3 *Light aircraft wing skin as a carrier for photovoltaic cells results*

The aim of this research's structural testing was to assess and contrast the structural durability of individual cell samples once they were characterized and assessed for solar efficiency. Out-of-plane static testing was chosen as it effectively represents the types of loads that could potentially lead to failure of embedded solar cells or arrays, rather than tensile testing. Common sources of damage for UAV wings during assembly, disassembly, or landing include impacts with objects, drops, or mishandling. Out-of-plane stress testing primarily aims to replicate these impact failures under static conditions. Composite UAV wings are often over-engineered during fabrication, meaning that, unless subjected to notably high loads during normal flight, the skin and structure of a wing are typically much stronger than required by flight loads alone. This is due to the perceived stressfulness of wing handling, which is considered a more probable source of damage to the wing's skin and structure than aerodynamic forces, thus posing a higher risk of accidents. Consequently, the tensile or shear loads experienced by an aircraft's wing skin during regular operation are usually minimal compared to the structural capabilities of the wing itself. Tensile testing simulates static loads most akin to distributed aerodynamic forces in this scenario, and tensile failure is less probable compared to impact, which is more likely to cause damage to the solar cells. The analysis involves evaluating three laminates, along with the solar cell, using different materials and configurations, conducted with ANSYS. The photovoltaic cell configuration measures 76.2 x 91.44 mm in dimensions. The composite photovoltaic cell wing static analysis is carried out in Ansys,

the total node is 825 and elements is 768. The element type is Shall 188 and meshing element size is 2mm.The dimensions of the solar cell is 70x 90 mm and the thickness of the total specimen is 2.2 mm and thickness are varying each configuration. The mechanical properties are presented in Table 19 and simulation results are presented Table 20. The analysis results are shown in Fig. 57, Fig. 58

Table 20. Mechanical properties of fiberglass

S.No	Description	Youngs modulus (GPa)	Yield strength (GPa)	Tensile strength (MPa)	Density (kg/m ³)	Refence
1	Polyurethane	0.002- 0.030	25 - 51	25 - 51	1,000 - 1,300	[120]
2	Solar cell /Silicone	0.005- 0.022	2.4 - 5.5	2.4 - 5.5	1,300 - 1,800	[120]
3	GFRP, epoxy matrix (isotropic)	15 - 28	110 - 190	140 -240	1,800 – 2,000	[120]

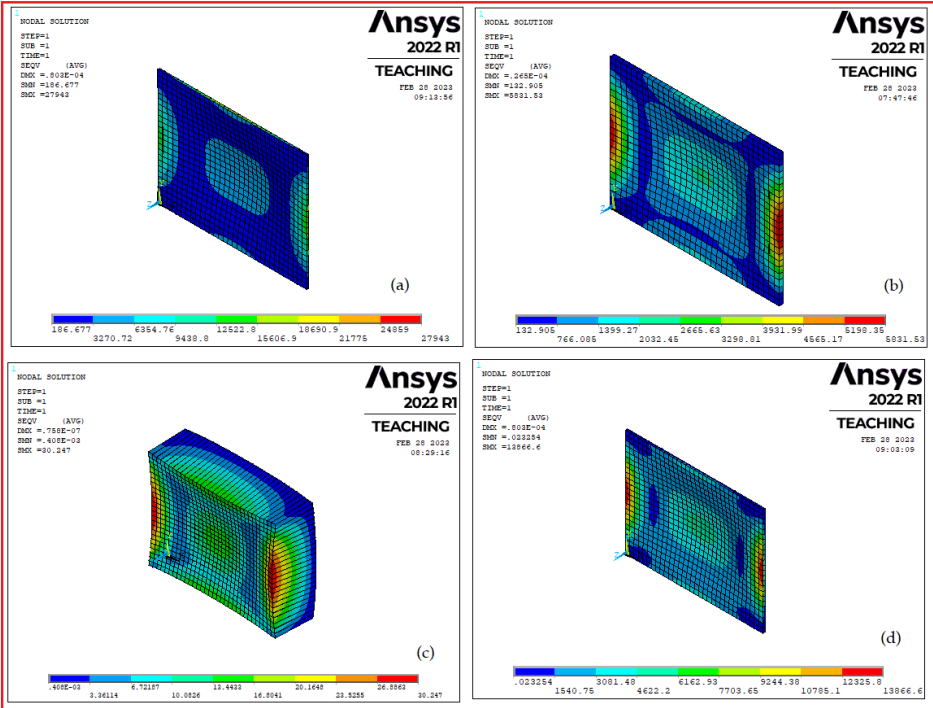


Figure 58. (a), (b), (c) and (d) is Max. Stress at laminate_1, 2, 3 and 4.

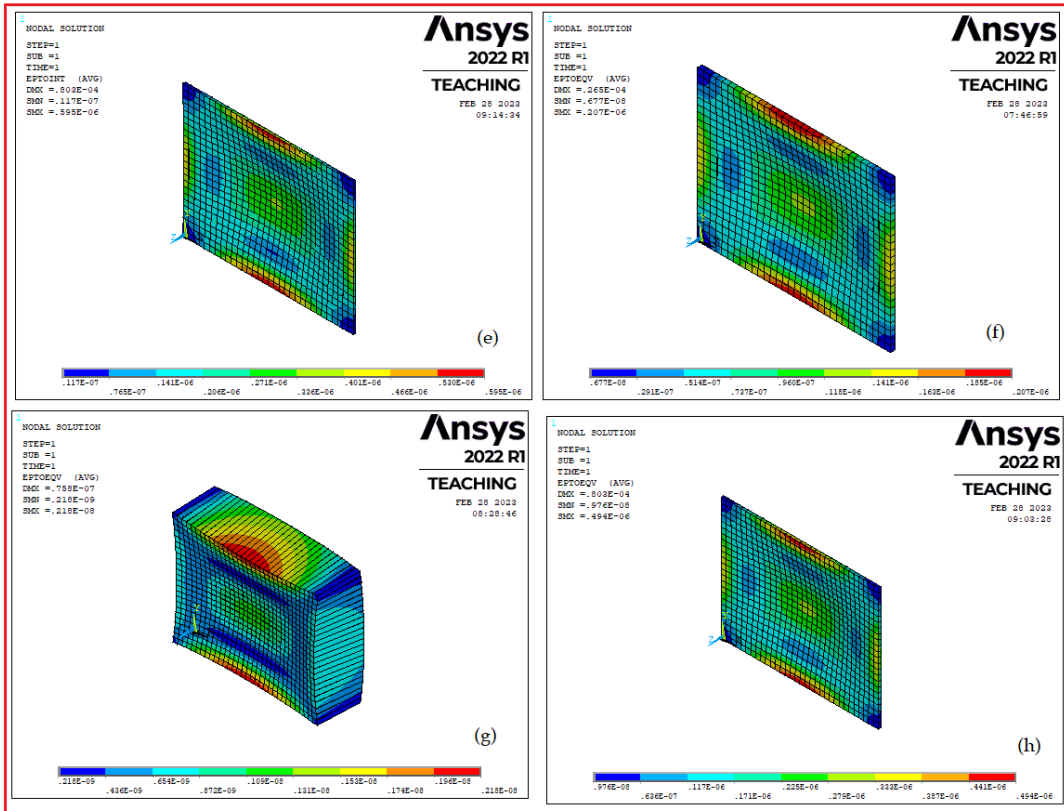


Figure 59. (e), (f), (g) and (h) is Max. Strain at laminate_1, 2, 3 and 4.

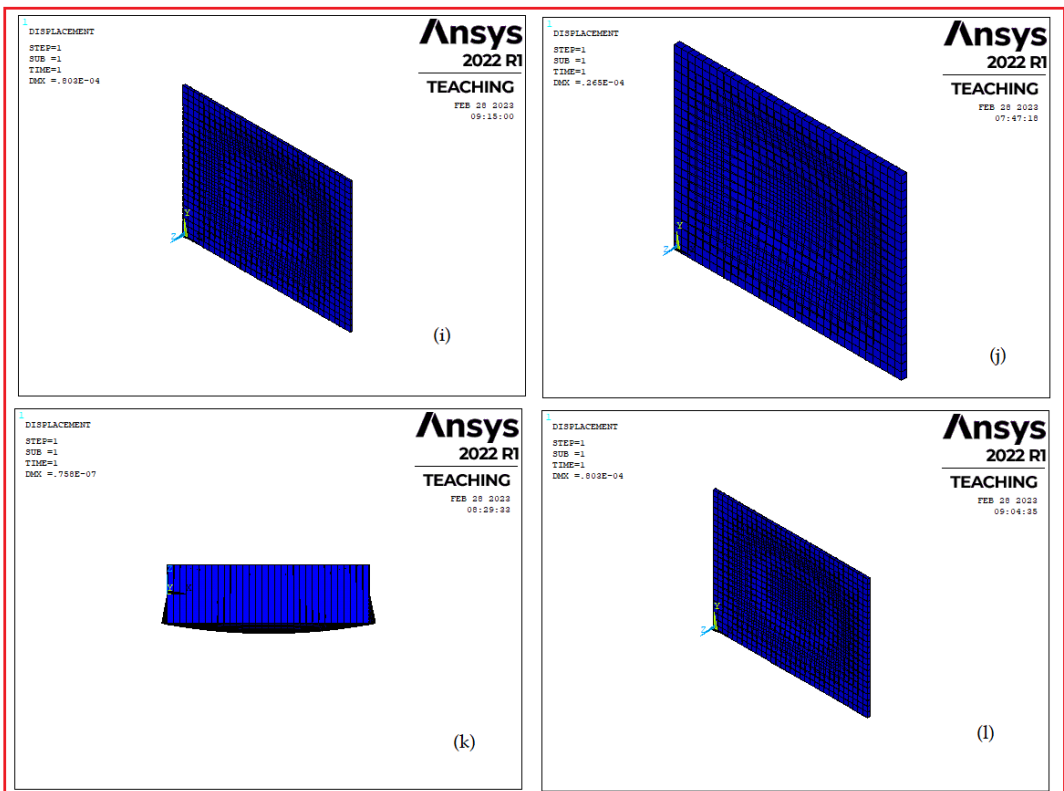


Figure 60. (i), (j), (k) and (l) is Max. deformation at laminate_1, 2, 3 and 4.

Table 21. Simulation results summary

S.No	Description	Material arrangement	Ply-Orientation	Max. Stress (Pa)	Max. Strain	Deformation
1	Laminate_1	Solar cell/Glass fiber	0/+90/-90/0	27941.5	0.595E-06	0.803E-04
2	Laminate_2	Glass fiber/Solar cell/Glass fiber	0/+90/-90/0	5831.53	0.207E-06	0.265E-04
3	Laminate_3	Polyurethane/Solar cell/Glass fiber	0/+90/-90/0	30.241	0.218E-08	0.758E-07
4	Laminate_4	Solar cell/Glass fiber/Glass fiber	0/+90/-90/0	10045.5	0.172E-06	0.143E-04

The objective of the structural testing in this study was to assess the integrity of individual cell samples following characterization and evaluation for solar performance. Static testing was chosen as a suitable method to represent the types of loads that could lead to failure of embedded solar cells or arrays, as opposed to flexural testing. Common sources of damage for UAV wings during assembly, disassembly, or landing include impacts with objects, drops, or mishandling. Out-of-plane stress testing was primarily aimed at simulating these impact failures under static conditions. The structural static tests were conducted using Ansys, and four laminates with different configurations were analyzed in this research. The highest stress was observed in laminate_1, while the minimum deformation was noted in laminate_4. Laminate_2 demonstrated the best results when compared to all evaluated laminates. These simulation results hold promise for future applications in UAV wing design.

7.3 Case study_3

Case_1 result

FEA is successfully carried out at various cases with different load conditions, the obtained results are presented in below. Buckling analysis results presented in Fig.60 for Case_1.

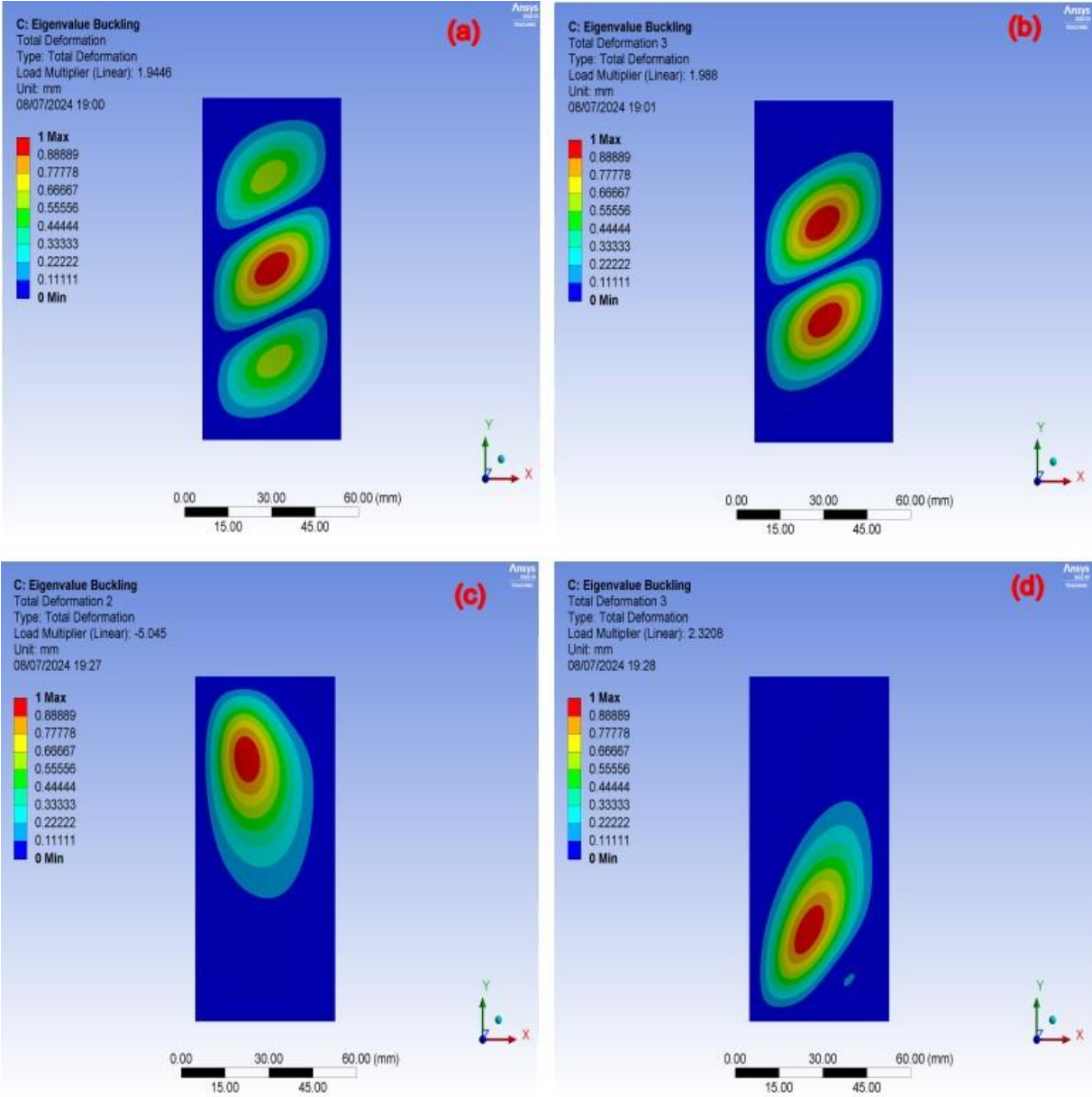


Figure.61 Buckling analysis results from Case_1, (a-b) Deformation at compressive force, (c-d) deformation at Shear force.

Case_2 results

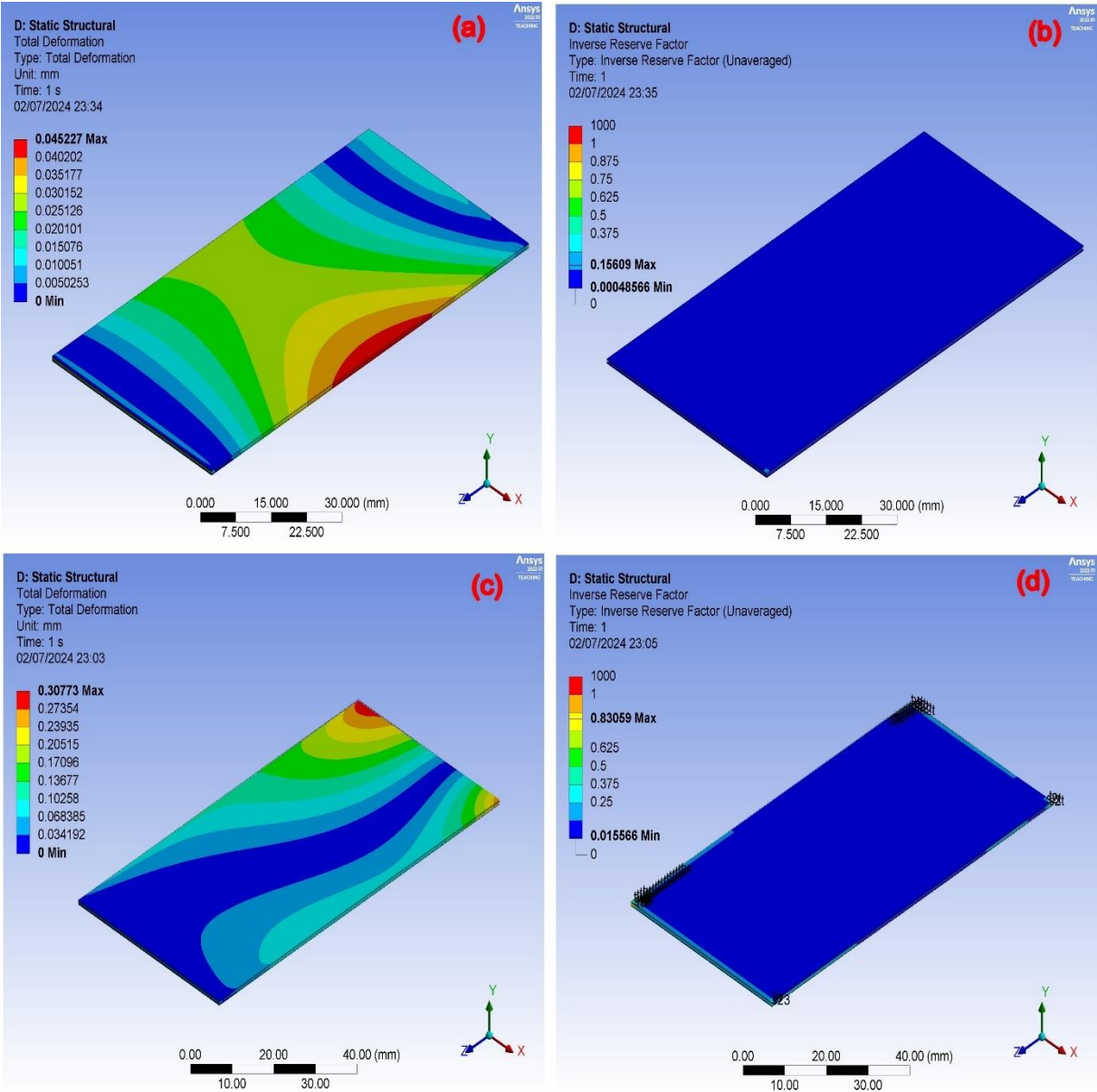


Figure.62 Structural analysis results from Case_2_1mm, (a-b) Deformation and Inverse reserve factor at compression force (c-d) Deformation and Inverse reserve at Shear force.

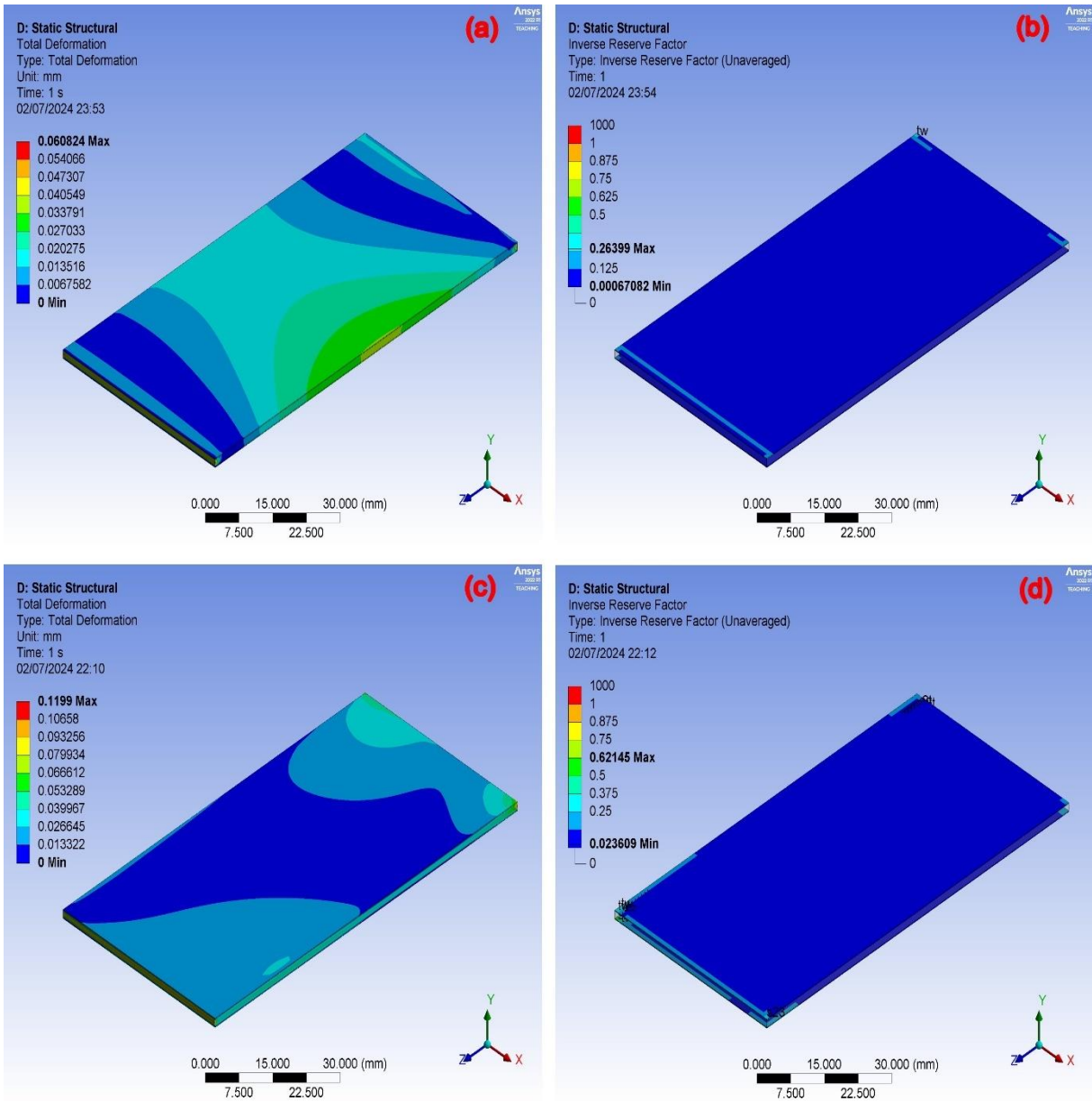


Figure.63 Structural analysis results from Case_2_2mm, (a-b) Deformation and Inverse reserve factor at compression force (c-d) Deformation and Inverse reserve at Shear force.

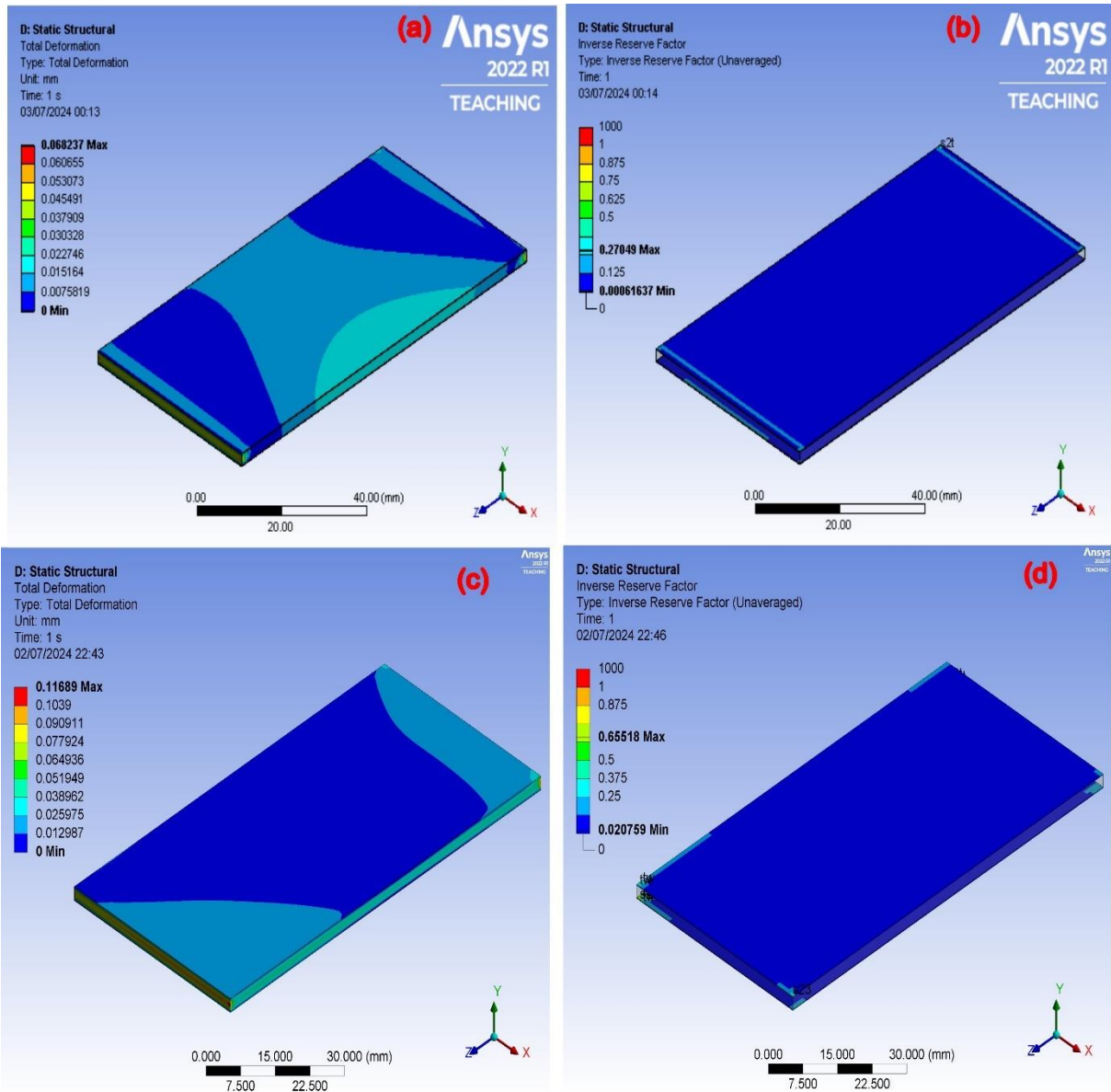


Figure.64 Structural analysis results from Case_2_3mm, (a-b) Deformation and Inverse reserve factor at compression force (c-d) Deformation and Inverse reserve at Shear force.

Case_3 results

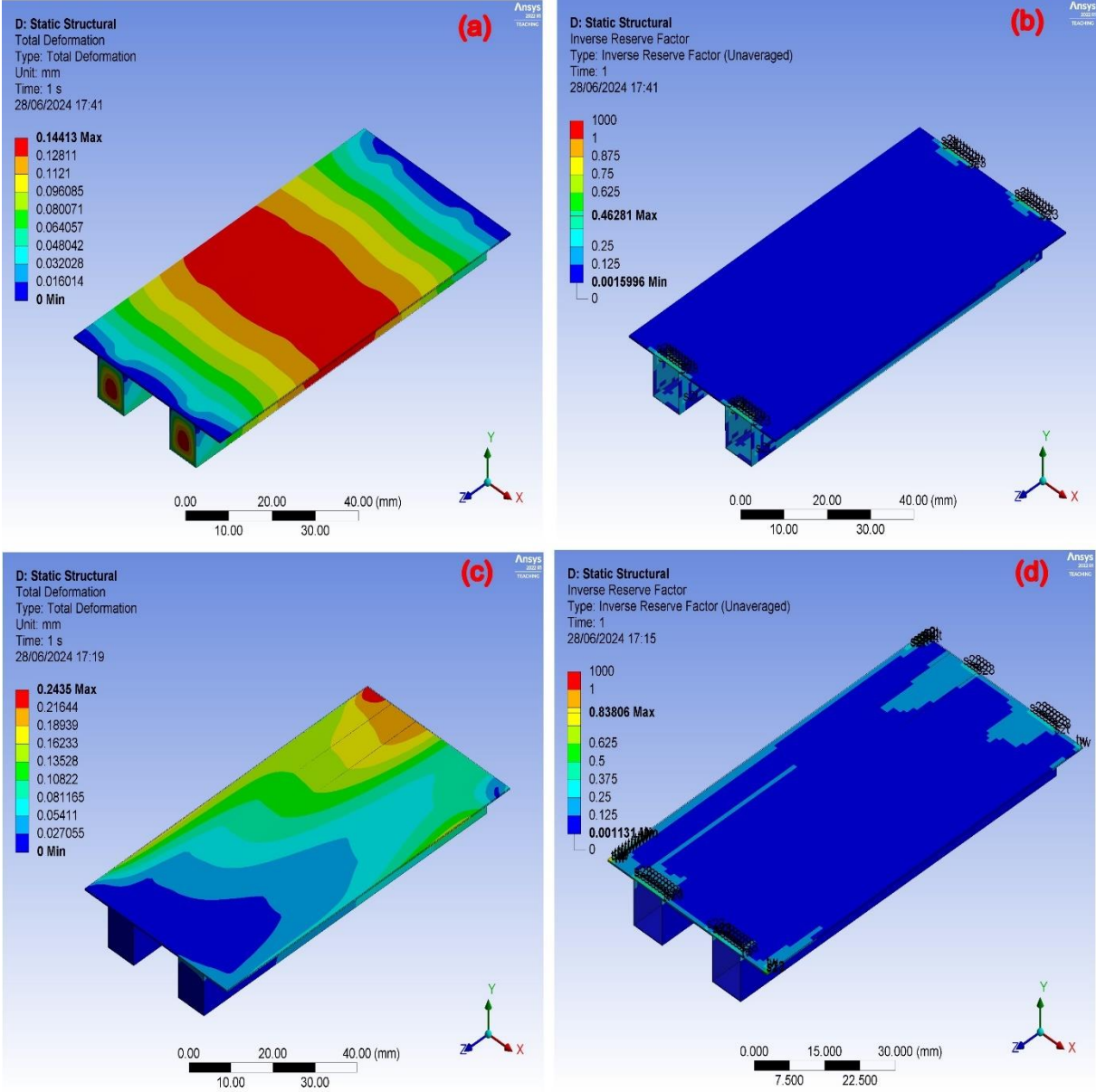


Figure.65 Structural analysis results from Case_3_0mm, (a-b) Deformation and Inverse reserve factor at compression force (c-d) Deformation and Inverse reserve at Shear force.

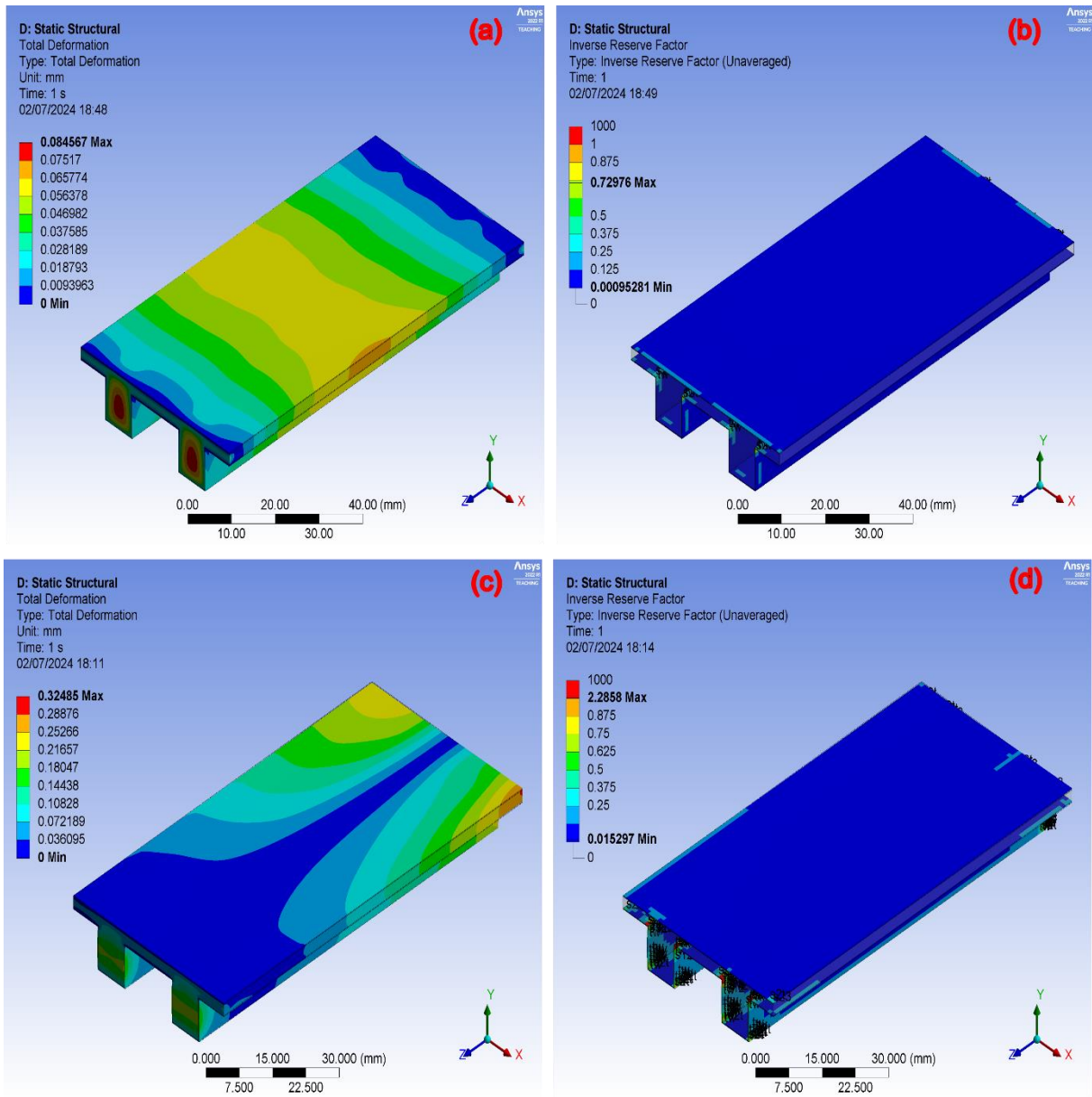


Figure.66 Structural analysis results from Case_3_1mm, (a-b) Deformation and Inverse reserve factor at compression force (c-d) Deformation and Inverse reserve at Shear force.

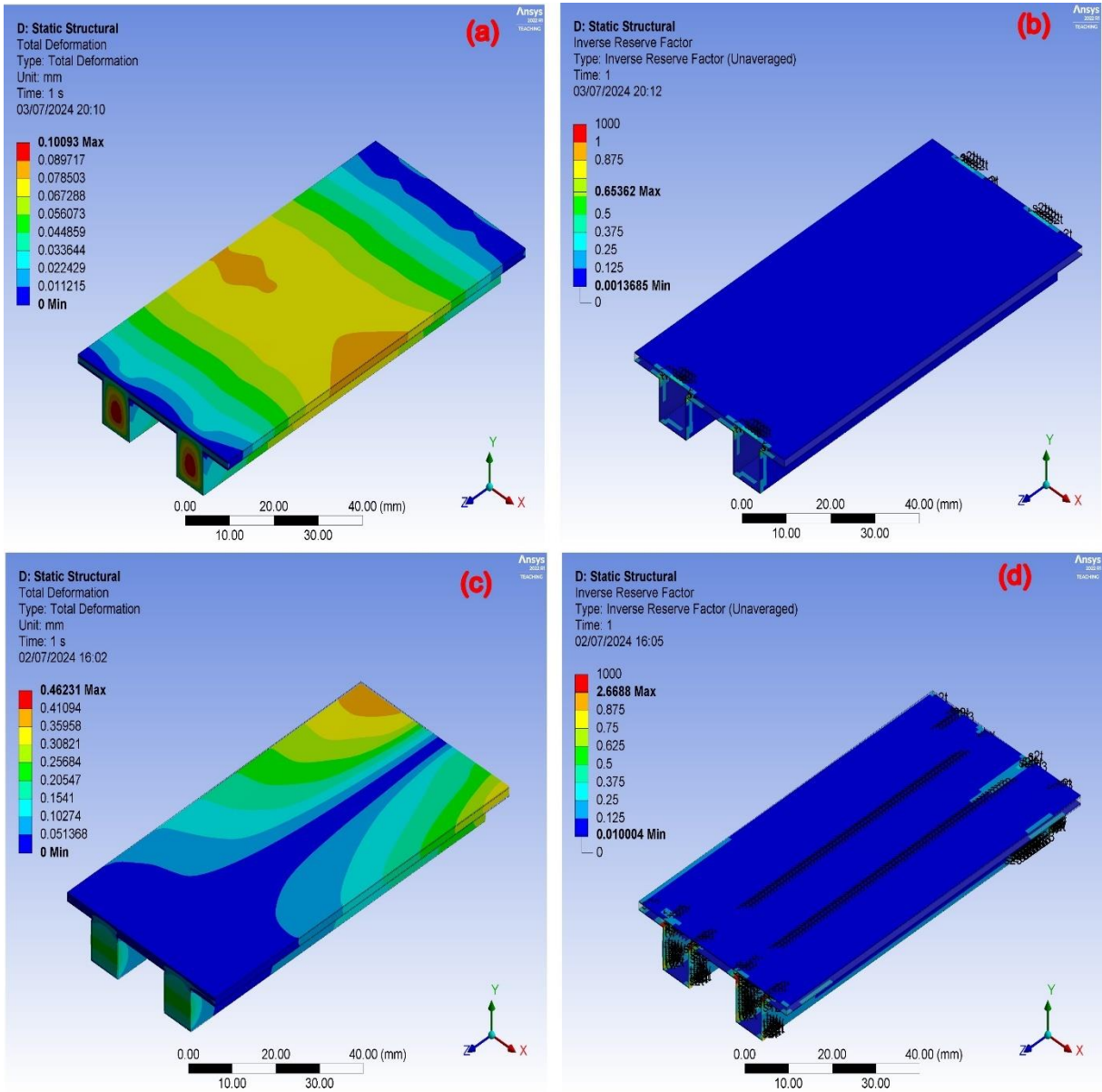


Figure.67 Structural analysis results from Case_3_2 mm, (a-b) Deformation and Inverse reserve factor at compression force (c-d) Deformation and Inverse reserve at Shear force.

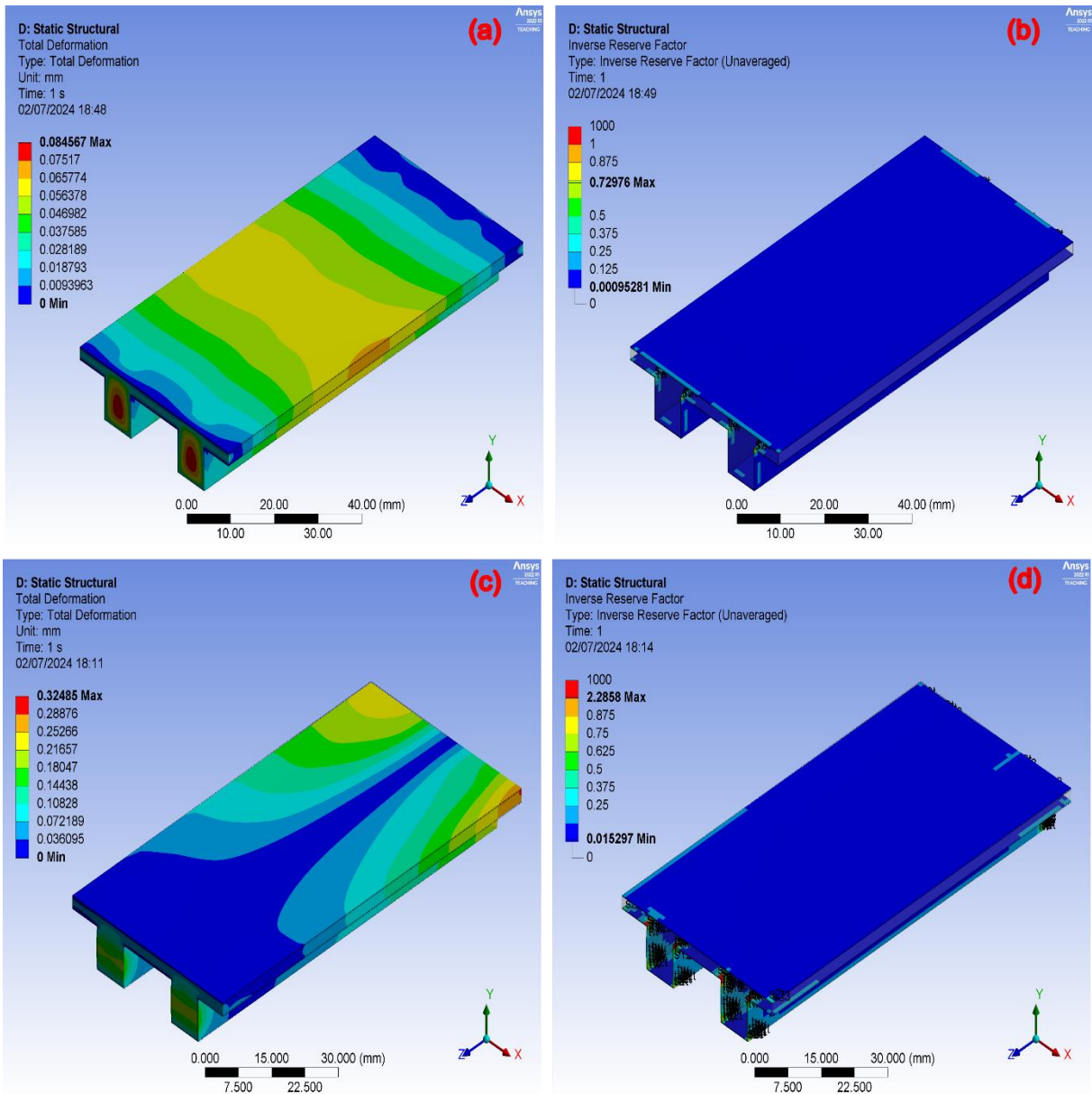


Figure.68 Structural analysis results from Case_3_3 mm, (a-b) Deformation and Inverse reserve factor at compression force (c-d) Deformation and Inverse reserve at Shear force.

Table 22. Case_1 FEM analysis result

Case_1_Results	Thickness	IRF	Deformation	Stress	Strain	Compressive stress_X	Compressive stress_Y	Compressive stress_Z	Weight
Compression load	0.4	0.058	0.054	11.709	0	-4.41E-08	-9.414	0	6.89E-03
	Thickness	IRF	Deformation	Stress	Strain	Shear_XY	Shear_XZ	Shear_YZ	
Shear load	0.4	0.423	0.081	98.53	0.005	20.969	4.91E-26	1.85E-15	6.89E-03

In the Table 10, the FEM analysis results are presented, based on the load conditions and obtained results are discussed by individual load conditions.

Case 1: Compression Load

In this study, the material's response to a compression load was analyzed with a focus on several key parameters: thickness, Inverse Reserve Factor (IRF), deformation, stress, strain, and compressive stresses along the X, Y, and Z axes.

1. **Thickness:** The sample maintained a consistent thickness of 0.4 units under the applied compression load. This constancy suggests that the material's structural integrity in terms of thickness is preserved despite the applied load, indicating robust behavior under compression.
2. **Inverse Reserve Factor (IRF):** The IRF was measured at 0.058. The IRF is an indicator of the material's reserve capacity before failure; a lower IRF implies that the material is closer to its failure point. In this context, the low IRF indicates that the material has a limited reserve capacity under the given compression load.
3. **Deformation:** The recorded deformation was 0.054 units. This small deformation value suggests that the material exhibits minor physical changes when subjected to compression, demonstrating good resistance to compressive forces.
4. **Stress:** The stress experienced by the material under compression was 11.709 units. This stress value reflects the internal resistance offered by the material against the applied load, which is significant and should be compared against the material's yield and ultimate strengths for safety assessments.
5. **Strain:** The strain was recorded as 0, indicating no relative deformation per unit length. This suggests that the material is highly rigid under compression and does not exhibit elongation or contraction, which could be beneficial in applications requiring minimal deformation.
6. **Compressive Stress Components:**
 - **Compressive Stress_X:** $-4.41\text{E}-08$ units, essentially zero, indicating negligible compressive stress along the X direction.

- **Compressive Stress_Y:** -9.414 units, indicating significant compressive stress along the Y-axis. This value suggests substantial internal forces acting in the Y direction.
- **Compressive Stress_Z:** 0 units, indicating no compressive stress along the Z direction.

Case 1: Shear Load

The response to shear load was also analyzed, focusing on thickness, IRF, deformation, stress, strain, and shear stresses in the XY, XZ, and YZ planes.

1. **Thickness:** Under shear load, the thickness remained constant at 0.4 units, indicating stability in the material's dimensions and suggesting resilience under shear forces.
2. **IRF:** The IRF was significantly higher at 0.423 compared to the compression load. This higher IRF suggests that the material has a greater reserve capacity before failure under shear load, indicating better resistance to shear forces.
3. **Deformation:** The deformation recorded under shear load was 0.081 units, higher than the deformation under compression. This higher deformation suggests that the material undergoes more significant physical changes when subjected to shear, indicating different mechanical behavior compared to compression.
4. **Stress:** The stress value under shear load was 98.53 units, significantly higher than the stress experienced under compression. This high stress indicates substantial internal forces within the material when subjected to shear, highlighting the material's differing response to shear versus compressive loads.
5. **Strain:** The strain was measured at 0.005 units, a non-zero value, indicating that the material undergoes some degree of relative deformation under shear load. This contrasts with the zero-strain observed under compression, suggesting different deformation mechanisms.
6. **Shear Stress Components:**

- **Shear_XY:** 20.969 units, indicating a significant shear stress component in the XY plane. This suggests notable internal shear forces when the material is loaded in this direction.
- **Shear_XZ:** 4.91E-26 units, effectively zero, indicating negligible shear stress in the XZ plane.
- **Shear_YZ:** 1.85E-15 units, effectively zero, indicating negligible shear stress in the YZ plane.

Summary of the Case_1

The material exhibits distinct mechanical responses under compression and shear loads. Under compression, it maintains its thickness and shows negligible deformation and strain, with significant compressive stress along the Y-axis. Conversely, under shear load, the material demonstrates greater deformation and strain, with substantial shear stress in the XY plane. These observations indicate that the material has anisotropic mechanical properties, reacting differently based on the type of applied load. Understanding these responses is crucial for designing applications where the material will be subjected to various loading conditions, ensuring structural integrity and performance under different mechanical stresses.

Table 23. Case_2 FEM analysis result

Case_2_Results	Thickness	IRF	Deformation	Stress	Strain	Compressive stress_X	Compressive stress_Y	Compressive stress_Z	Weight
Compression load	1	0.156	0.0452	18.85 4	0.175	11.757	0.446	11.757	1.40E-02
	2	0.263	0.06	41.28 7	0.087 4	17.633	1.119	20.481	1.42E-02
	3	0.27	0.068	41.31 8	0.057	16.768	1.642	20.876	1.45E-02
	Thickness	IRF	Deformation	Stress	Strain	Shear_XY	Shear_XZ	Shear_YZ	
Shear load	1	0.83	0.307	296.1 6	0.236	8.678	134.67	4.538	1.40E-02
	2	0.621	0.119	215.7 5	0.132	5.176	97.917	2.572	1.42E-02
	3	0.655	0.116	200.3 5	0.1	3.805	90.958	1.899	1.45E-02

Summary of the Case_2

In the Table 11, the obtained FEA result shows, under a constant load of 272 N, the material exhibits distinct behaviours based on its thickness. In compression, thicker samples show higher stress and deformation but lower strain, indicating greater internal resistance and stiffness. In shear, thicker samples show reduced deformation and strain, with decreased shear stresses, particularly in the XZ plane, indicating improved resistance to shear forces. These observations underscore the material's anisotropic properties, where mechanical responses vary significantly with thickness, crucial for designing applications involving different loading conditions.

Table.24 Case_3 FEM analysis result

Case_3 _Results	Thickness	IRF	Deformation	Stress	Strain	Compressive stress_X	Compressive stress_Y	Compressive stress_Z	Weight
Compression load	0	0.462	0.144	79.479	0.053	35.312	20.921	62.967	2.02E-02
	1	0.495	0.125	59.391	0.044	32.938	22.216	53.515	2.03E-02
	2	0.653	0.1	59.902	0.046	30.941	20.563	57.009	2.06E-02
	3	0.729	0.084	72.339	0.046	29.437	28.914	62.653	2.09E-02
Shear load	0	0.838	0.243	289.29	0.01	0.365	130.88	29.565	2.02E-02
	1	3.368	0.543	756.62	0.103	3.87	131.61	343.84	2.03E-02
	2	2.668	0.462	694.75	0.087	2.793	121.14	314.53	2.06E-02
	3	2.285	0.324	639.35	0.087	2.408	110.45	289.52	2.09E-02

In the Table 12, the obtained FEA result shows, under both compression and shear loads, the material exhibits varied responses depending on its thickness. Compression tests show varying stress and deformation levels with increasing thickness, indicating different levels of internal resistance and stiffness. Similarly, shear tests reveal varying shear stress and deformation levels, indicating different levels of material displacement and internal forces in thicker samples. These results highlight the material's complex mechanical behaviour under different loading conditions, emphasizing the importance of considering thickness variations in applications requiring specific mechanical properties.

7.4 Stability analysis of composite laminate results

In analysing the buckling of composite laminated plates, classical thin plate theory is primarily utilized for its analytical simplicity, neglecting the out-of-plane shear deformation. When subjected to compressive in-plane loads, composites experience buckling. Therefore, it's vital to examine and understand the buckling traits of laminated

composites while considering the impact of material properties. The mechanical characteristics of a lamina employed in the examination were the following in the Table 25. $E_1=4.89E+09$, $E_2=4.89E+08$, $G_{12}=0.5E2$, $\nu_{12}=0.25$, $G_{13}=0.5E2$, $G_{23}=0.3E2$, $b=40/80$ mm, $a/b=1$, $a/h=20$, $a=40/80$ mm, $h=2/4$ mm and number of layers 4.

Table 25. Mechanical properties of Jute fiber

E1/E2	E1	E2	E3	G12	G23	G13
10	4.89E+09	4.89E+08	4.89E+08	2.45E+08	1.47E+08	2.45E+08
20	9.78E+09	4.89E+08	4.89E+08	2.45E+08	1.47E+08	2.45E+08
40	1.96E+10	4.89E+08	4.89E+08	2.45E+08	1.47E+08	2.45E+08
60	2.93E+10	4.89E+08	4.89E+08	2.45E+08	1.47E+08	2.45E+08
80	3.91E+10	4.89E+08	4.89E+08	2.45E+08	1.47E+08	2.45E+08
100	4.89E+10	4.89E+08	4.89E+08	2.45E+08	1.47E+08	2.45E+08

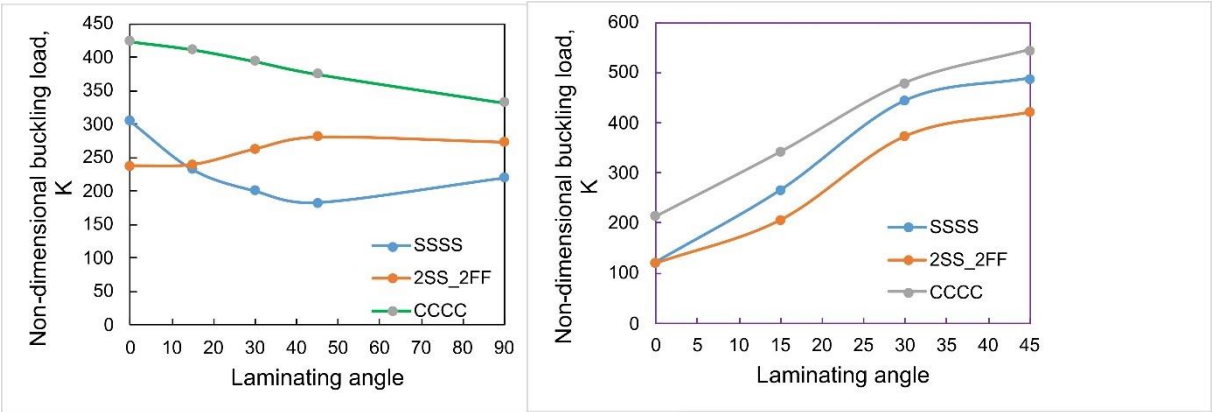


Figure 69. Convergence of solutions for (0/0/0/0) laminate composite plate at b=40 and 80 mm respectively.

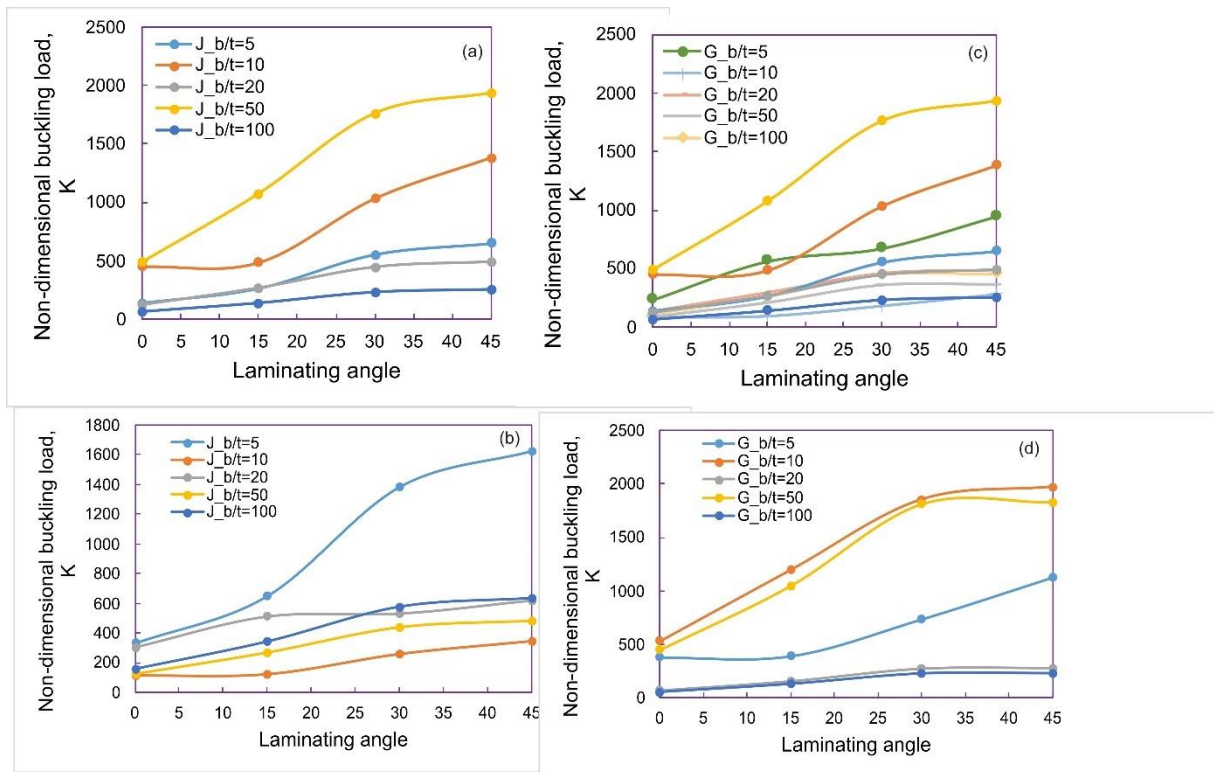


Figure 70. Effect of b/t on non-dimensional buckling load under the simply supported condition.

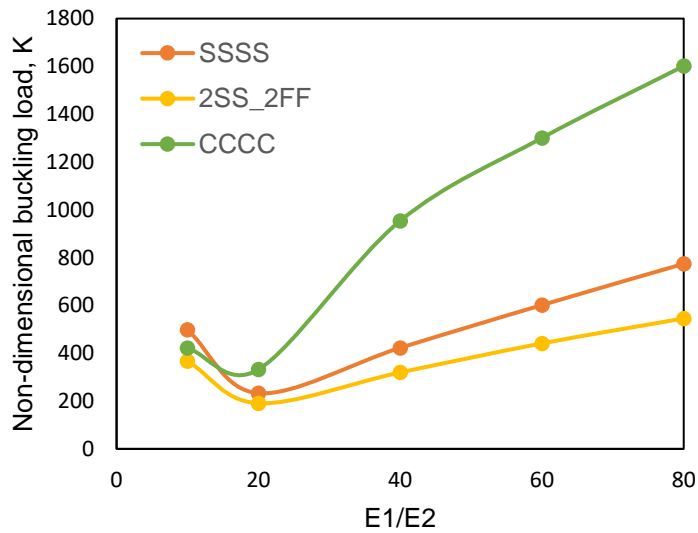


Figure 71. Effect of $E1/E2$ on non-dimensional buckling load for (0 deg).

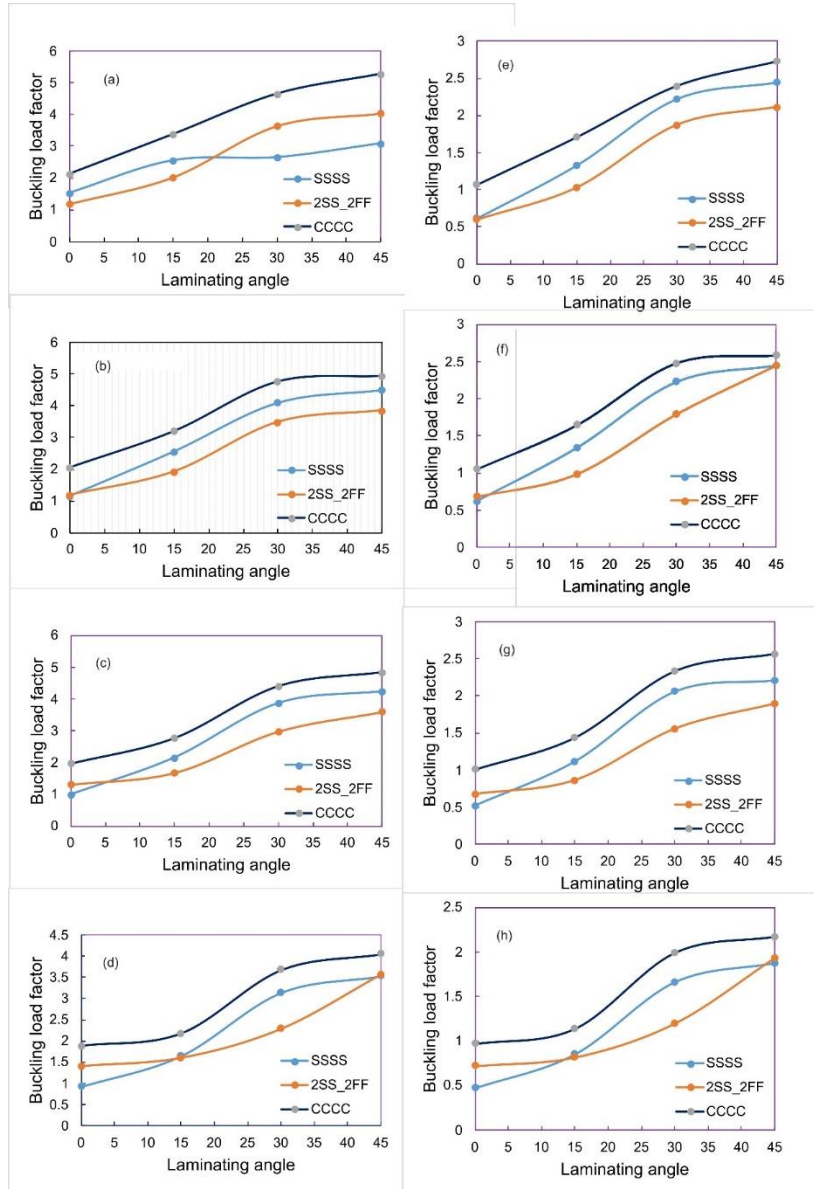


Figure 72. Buckling load factor vs laminating angle, (a-d) with 'b=40' value, (e-h) with 'b=80' value from 0 deg- 45 deg respectively.

7.5 Fiber orientation and stacking sequence results

The initial assessment involved determining material density and cross-sectional area to optimize material weight using 3D CAD models. This study primarily focused on exploring material strength across various geometric configurations, conducted through Ansys. Optimization of natural-fiber-reinforced composites (NFRC) was a key consideration. In this optimization process, 3D CAD geometric models were incorporated into Ansys for ply orientation, providing insights into the technical configuration of composite materials. The subsequent step involved hybrid natural reinforced composites (HNRC), aimed at enhancing material strength and other mechanical properties while promoting

sustainability. A design for the natural reinforced fiber composite was developed, and the optimization process is illustrated in Fig.73.

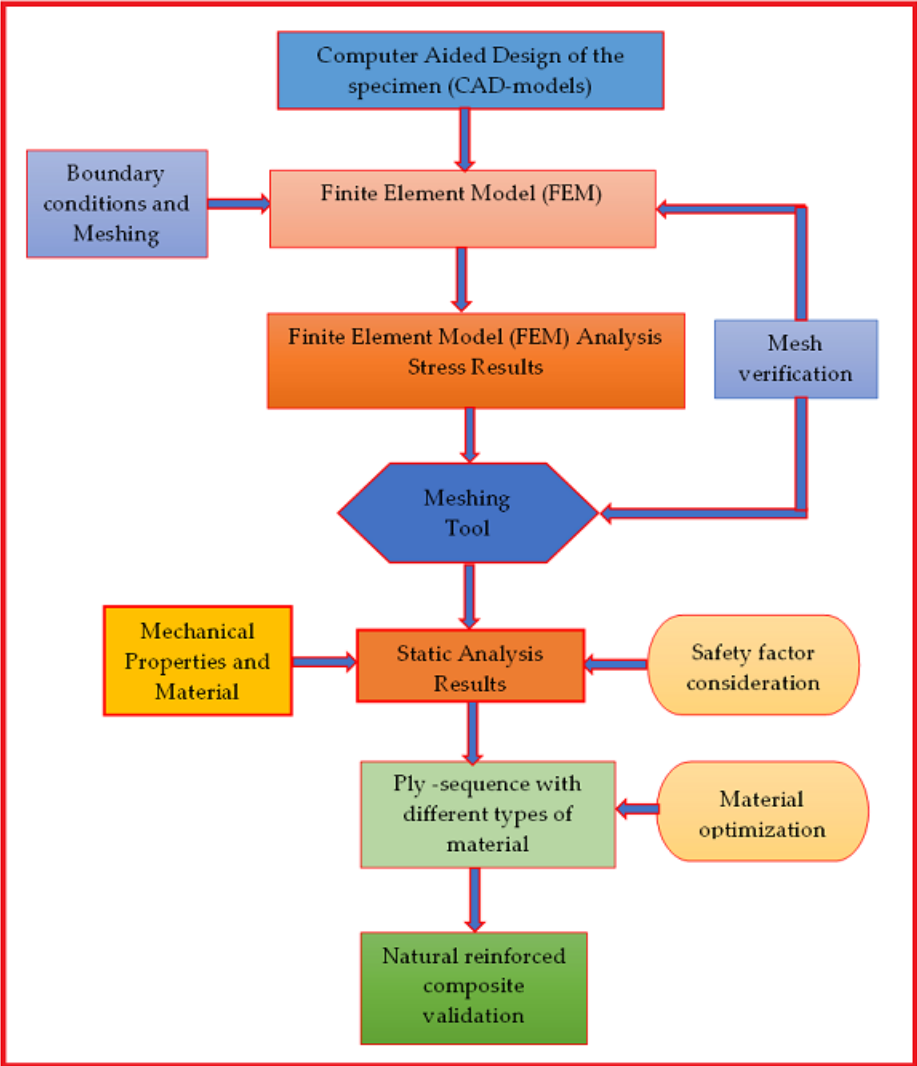


Figure 73. illustrates the layout for the design and optimization of natural reinforced fiber composites.

The study focused on material optimization and analysis of lightweight structural strength, categorized into six distinct cases. Each case involved configuring and verifying mechanical properties and behaviour. Case_1 entailed a total thickness of 2 mm for the Natural fiber reinforced composite, with ply orientation aimed at enhancing material strength along the longitudinal fiber direction. Various ply sequences were considered, including 0°, 30°, and 45°. In Case_2, Case_3, Case_4, Case_5, and Case_6, the ply orientation remained the same, but the total laminate thickness differed, with the addition of E-glass fiber. The thicknesses were 2 mm, 3 mm, and 4 mm, respectively. The classification of design cases is presented in Figure 3 as follows: Case 1: Optimization of

NFRC with 2 mm thickness, Case 2: Optimization of NFRC with 3 mm thickness, Case 3: Optimization of NFRC with 4 mm thickness, Case 4: Optimization of HNRC with 2 mm thickness, Case 5: Optimization of HNRC with 3 mm thickness and Case 6: Optimization of HNRC with 4 mm thickness. The examination proceeded in two phases, as previously outlined. The initial phase focused on analyzing natural reinforced fiber composite laminates with varying ply orientations. Fig. 73. depict the total deformation. The highest deformation value (0.950 mm) was observed at 30° with a 2 mm thickness, while the lowest deformation (0.105 mm) occurred at 45° with the same thickness.

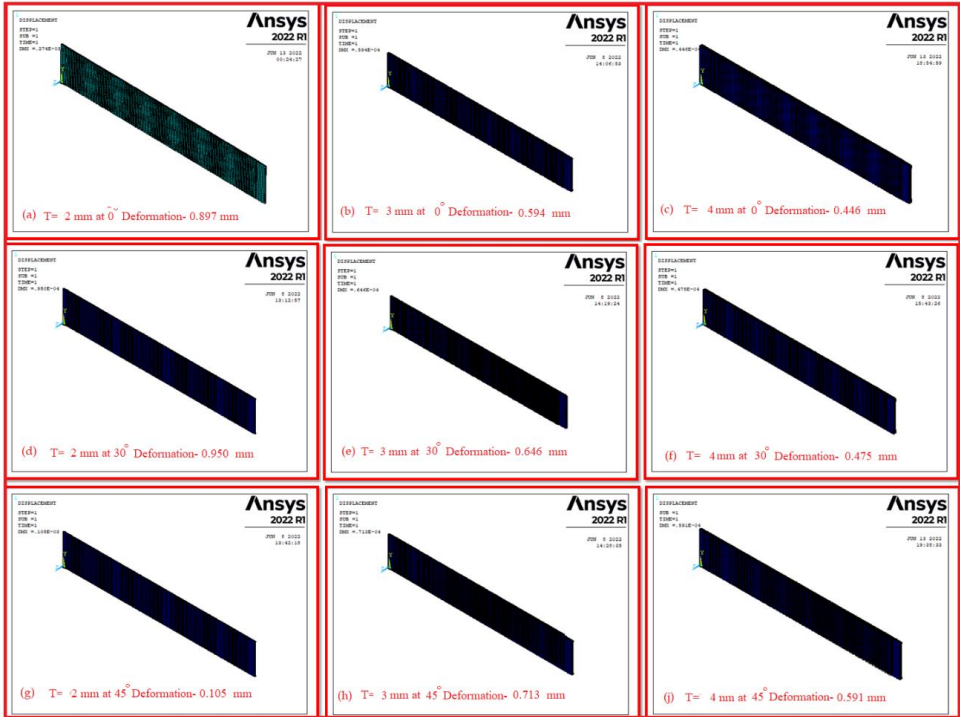


Figure 74. illustrates deformation at 0°/30°/45° angles with various configurations (Jute – 2, 3, and 4 mm).

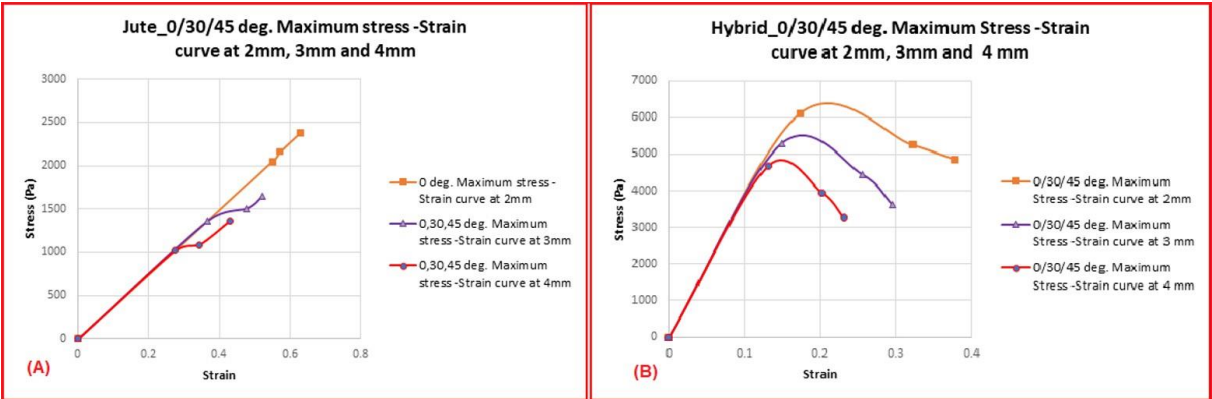


Figure 75. illustrates stress-strain, (a) Natural fiber, (b) hybrid composite at 0°/30°/45° angles with various configurations (Jute – 2, 3, and 4 mm).

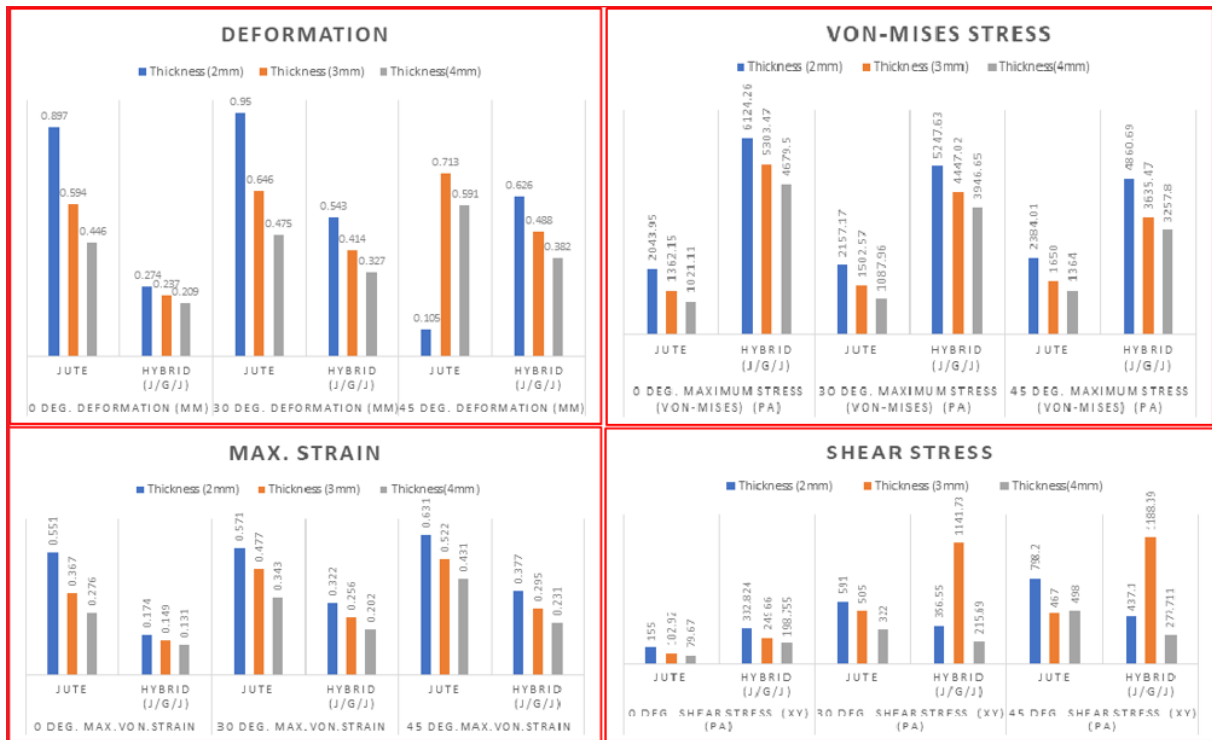


Figure 76. Summarized results (Jute and Hybrid—2–4 mm).

In this study, research was conducted on materials with varying strengths and different ply sequences, considering thickness. Maximum stress, strain, deformation, and shear stress were evaluated for different ply configurations using Ansys. Specifically, natural reinforced fiber composite (Jute) was analyzed as a laminate with 2 mm thickness and eight total plies, each with different sequences. The simulation revealed that mechanical properties, such as maximum stress values, were highest in the longitudinal direction with various fiber orientations. For HFRC laminates, the 0° ply orientation showed notable results, with values of 0.274, 0.237, and 0.209 mm for thicknesses ranging from 2 to 4 mm. Other orientations and ply sequences did not yield significant improvements. However, at a 45° ply orientation and 3 mm thickness, tensile strength and deformation were noted as 1188 GPa and 0.237, respectively. Hybrid natural-fiber-reinforced composites exhibited superior mechanical properties compared to natural fibers, particularly at different configurations. The combination of jute and glass fiber with epoxy resin composite showed promising results, especially at 3 mm thickness with a 45° ply orientation. These hybrid composites hold potential for use in UAV wing construction, including sub-parts such as spars, ribs, and skin components.

The study highlighted a significant increase in material yield strength when natural fibers were combined with synthetic fibers. Despite less deformation in natural fibers, the

material exhibited linear elastic behaviour, with strength influenced by fiber orientation. However, laboratory testing of specimens is essential to validate these findings. Ultimately, it was concluded that natural hybrid composites are suitable for prototype UAV structure fabrication based on simulation results. Recommendations were made for future work, including fabricating test specimens according to ASTM standards and conducting further analyses based on laboratory tests. If confirmed through testing, this material holds promise for UAV manufacturing applications.

7.6 Structural optimization method results

This study presents the application of multi-objective evolutionary algorithms to improve the layer arrangement in lightweight composite constructions. The focus is on adhering to engineering design principles that are particular to layer arrangement. These guidelines are incorporated into the optimization process either as restrictions or additional targets. An innovative initialization technique, grounded in mechanical principles, is suggested to enhance the optimization procedure. The method is utilized to optimize a composite laminate by considering weight, inverse reserve factor, and buckling load factor. The mechanical properties of three distinct laminates are examined, with a focus on the influence of design and material composition. The study demonstrates that utilizing a novel stacking sequence $[90_6/45_4/0_6]$ results in superior optimal designs when compared to the conventional sequence of plies positioned at 0° , 45° , and 90° angles. The findings indicate that the identified stacking sequence is optimal, which is especially relevant for future applications in unmanned aerial vehicle (UAV) structures.

To enhance the design of the LSS, it's essential to consider various specimen boundary conditions, such as compression and tensile loads. The optimization problem can be outlined as follows:

- ✚ Design variables: The orientation of plies denoted as $(\theta_{k=1,\dots, N})$.
- ✚ Objectives: Minimization of the total number of plies (N), total weight of the laminate, inverse reserve factor, and total deformation load multiplier.
- ✚ Constraints: The inverse reserve factor ($IRF < 1$) and total deformation load multiplier ($DLM > 1$).
- ✚ Fixed parameters: Material, specimen dimensions, boundary conditions, and ply angle discretization at 0° , 30° , 45° , 60° , and 90° .

The inverse reserve factor measures the safety margin in a design, calculated by the ratio of applied load to ultimate load capacity. It indicates how much the applied load surpasses the structure's strength. If the inverse reserve factor exceeds 1, the laminate fails. With the total DLM, designers can estimate the overall deformation or strain in the composite laminate, ensuring it remains within acceptable limits to prevent structural failure or performance issues.

Multi-objective genetic algorithms (MOGAs) are optimization approaches based on Darwinian evolutionary concepts. They are used to solve optimization problems with several, seemingly competing aims. MOGAs, which mimic natural selection, crossover, and mutation processes, yield a collection of optimal solutions known as the Pareto front, which depicts the trade-offs between various objectives. ANSYS Workbench provides tools and interfaces for integrating MOGAs into the optimization process. These tools enable users to establish objectives, constraints, and design variables. MOGAs are then used to explore the design space and determine the Pareto front, which represents the best trade-off solutions. The benefits of using this optimization approach (MOGAs in ANSYS Workbench) include the ability to quickly explore many design options and identify the best trade-off solutions. MOGAs enable engineers to explore a variety of solutions that reflect the trade-offs between numerous objectives. MOGAs provide a Pareto front, which provides engineers with a thorough understanding of design trade-offs, allowing them to make more informed decisions.

Geometric models are mathematical representations of geometric shapes and structures, used to study and analyze various geometric properties. The parameters of the composite laminate used followed ASTM requirements. The length (l) was 140 mm, the width (w) was 12 mm, and the thickness (h) was 0.15 mm. The graphical representation is presented in Fig.77.

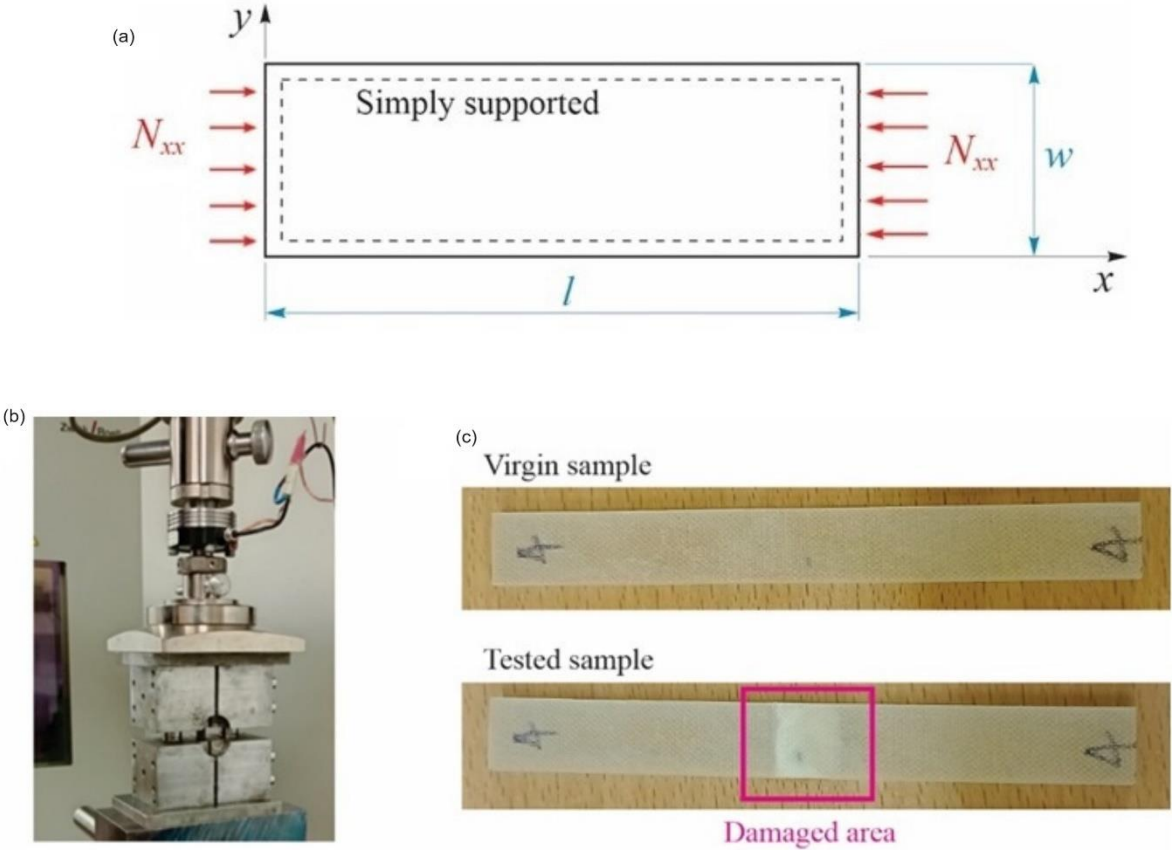


Figure 77. (a) Loading and boundary conditions, (b) Mechanical testing and (c) specimens

The MOGAs method, a variation of the widely used NSGA-II (Non-dominated Sorted Genetic Algorithm-II), incorporates controlled elitism concepts. It accommodates multiple objectives and constraints, aiming to discover the global optimum by initially generating 200 samples, followed by 50 samples per iteration, and ultimately identifying three candidates. These outcomes can be further refined to offer the designer a well-organized array of solutions.

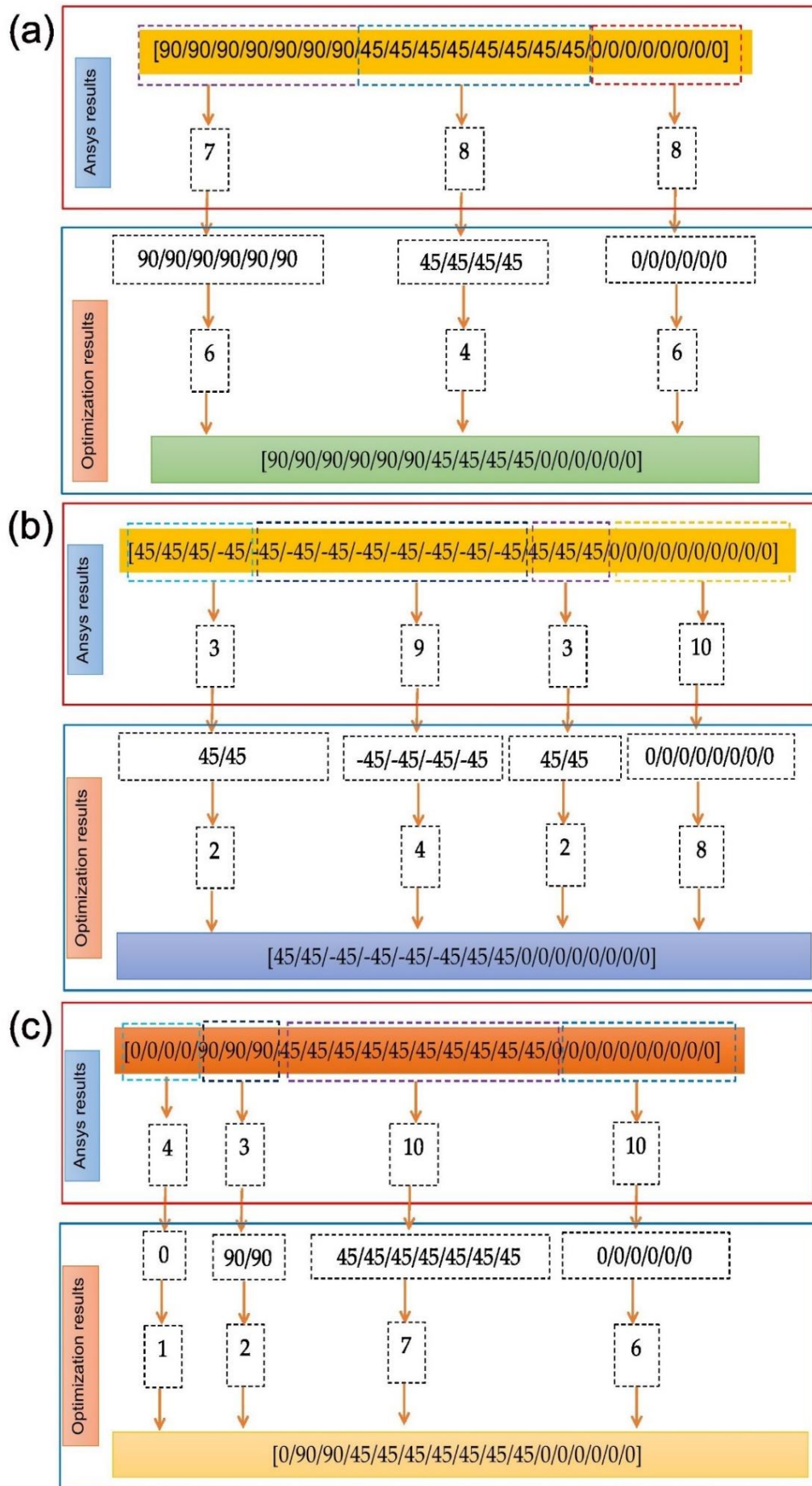


Figure 78. Optimization strategy (a) Laminate 1, (b) Laminate 2, (c) Laminate 3

Optimal solutions are arranged based on criteria such as minimum buckling margins, including the inverse reserve factor, maximizing the total weight of the laminate, and minimizing the buckling load factor. Tables 26 and 27 present selected results from the optimal solutions generated by the optimization algorithm following a single run, comprising 200 evaluations for various combinations of plies and ply angle constraints. The stacking sequences of plies were considered for the laminate. Table 27, specifically, addresses the homogeneity constraints, aiming to mitigate bending and twisting issues.

Table 26. displays the optimal ply-stacking sequence outcomes for different configurations ($0^\circ/\pm 45^\circ/90^\circ$)

Description	Plies quantity	Ply stacking sequence	Inverse reserve factor (IRF)	Buckling factor/ Load Multiplier	Weight of the laminate
stacking sequence $\{0^\circ, \pm 45^\circ, 90^\circ\}$	24	[90 ₇ /45 ₈ /0 ₈]	0.1044	2.3960	5.73E-06
	25	[45 ₃ /-45 ₉ /45 ₃ /0 ₁₀]	0.1115	2.5453	5.73E-06
	27	[0 ₄ /90 ₃ /45 ₁₀ /0 ₁₀]	0.04075	4.6152	5.75E-06
Stacking sequence $\{0^\circ, \pm 45^\circ, 0^\circ\}$	30	[-45 ₈ /90/45/ 45 ₆ /45 ₁₁ /0 ₃]	0.0901	5.5743	5.88E-06
	34	[0 ₂ /-45 ₅ /90 ₂ /-45 ₈ /45 ₁₄ /0 ₃]	0.0582	6.4597	5.91E-06
	45	[0 ₆ /45 ₉ /-45 ₉ /45 ₁₅ /0 ₆]	0.0305	15.5221	5.83E-06
stacking sequence $\{\pm 45^\circ, 0^\circ, 90^\circ\}$	45	[45/90 ₂ /0 ₁₁ /45 ₈ /0 ₄ /90 ₁₉]	0.0818	10.4888	6.64E-06
	57	[-45 ₉ /45 ₃₂ /0 ₆ /90 ₁₀]	0.0719	14.7583	6.61E-06
	47	[90 ₃ /45 ₁₈ /-45 ₁₀ /0 ₆ /90 ₁₀]	0.1236	10.0268	6.73E-06

The results displayed in Tables 26 and 27 were achieved by implementing balance and symmetric constraints. In both tables, the optimization process involved utilizing ply orientations such as $\{0^\circ, \pm 45^\circ, 90^\circ\}$, $\{0^\circ, \pm 45^\circ, 0^\circ\}$, $\{90^\circ, \pm 45^\circ, 0^\circ\}$, $\{\pm 45^\circ, 0^\circ, 90^\circ\}$, and $\{0^\circ, \pm 30^\circ, \pm 45^\circ, \pm 60^\circ, 90^\circ\}$. However, in Table 2, the range of ply orientations extended to $\{0^\circ, \pm 30^\circ, \pm 60^\circ, \text{ and } 90^\circ\}$, resulting in varied numbers of plies noted as 24, 25, 27, 30, 34, 45, 45, 57, and 47. The obtained results in Table 9 indicated the lowest number of plies among all results, reflecting efforts to minimize the LSS, which is a current constraint of the design guidelines. Despite achieving a maximum inverse reserve factor value of 0.090, the number of plies decreased to 24 compared to Table 26, albeit with a slight increase in the total weight of the laminate. The contrast between Tables 26 and 27 highlights the potential benefits of incorporating new ply orientations compared to the traditional $\{0^\circ,$

$\pm 45^\circ$, 90° arrangement, particularly evident with the inclusion of disorientation and homogeneity constraints.

Table 27. Exhibits the optimal ply-stacking sequence results for various configurations ($90^\circ/\pm 45^\circ/0^\circ$ and $(0^\circ/\pm 30^\circ/\pm 60^\circ/90^\circ)$)

Description	Plies quantity	Ply stacking sequence with symmetric and unbalanced constraints and homogeneity constraints	Inverse reserve factor (IRF)	Buckling factor/ Load Multiplier	Weight of the laminate
Stacking sequence $\{90^\circ, \pm 45^\circ, 0^\circ\}$	52	$[0_{11}/-45_{11}/0_3/-45_{16}/45_{11}]$	0.0479	17.7556	6.12E-06
	45	$[-45_5/0_6/-45/0_4/90_{10}/-45_{14}/45_5]$	0.0698	12.1819	6.17E-06
	36	$[90_7/45_7/90_2/0_3/-45_{12}/45_5]$	0.0783	7.9316	6.17E-06
Stacking sequence $\{0^\circ, \pm 30^\circ \pm 60^\circ, 90^\circ\}$	26	$[-60_8/-30_5/30_7/0_6]$	0.1009	2.5155	5.73E-06
	25	$[-20_2/60_9/30_7/0_7]$	0.0889	2.6258	5.70E-06
	27	$[30_4/90_4/-30_7/30_{12}]$	0.0639	3.579	5.75E-06
Stacking sequence $\{0^\circ, \pm 30^\circ \pm 60^\circ\}$	26	$[0_6/30_{14}/0_6]_s$	0.0333	4.6113	5.67E-06
	25	$[30_2/60_9/30_7/0_7]$	0.0889	2.6258	5.73E-06
	37	$[60_2/0_5/60_7/0_7/-30_7/30_7/0_2]$	0.0607	7.1319	5.78E-06

Moreover, the mechanical properties of four different composite laminates with different ply orientations (Laminate 1, Laminate 2, Laminate 3, and a reference Laminate 4) were investigated. The compression test results, outlined in Table 28, included parameters such as maximum force (Fmax), displacement at Fmax (dL), thickness, width, cross-sectional area (Area), and ultimate compressive strength (σ_c). For instance, laminate 1 displayed an Fmax of 8370.988 N with a corresponding displacement of 1.528346 mm, a thickness of 4.2 mm, a width of 12.16 mm, an area of 51.072 mm², and an ultimate compressive strength of 163.9056 MPa. Similarly, laminate 2 exhibited an Fmax of 5777.181 N, a displacement of 1.457818 mm, a thickness of 3.2 mm, a width of 12.1 mm, an area of 38.72 mm², and an ultimate compressive strength of 149.204 MPa. Laminate 3 and the reference Laminate 4 also demonstrated distinct mechanical properties, providing further insights into their performance under compression testing conditions.

Table 28. Compression test result.

		F_{max}	$dL(F_{max})$	Thickness	width	Area	σ_c
Description		N	mm	mm	mm	mm ²	MPa
Laminate 1	SP 1	8370.988	1.528346	4.2	12.16	51.072	163.9056
	SP 2	8074.094	1.665818	4.1	12.1	49.61	162.7513
	SP 3	6448.679	1.296282	4.15	12.12	50.298	128.2094
	SP 4	8430.247	1.685427	4.2	12.1	50.82	165.8844
	SP 5	8500.917	1.414758	4.3	12.12	52.116	163.1153
Laminate 2	SP 6	5777.181	1.457818	3.2	12.1	38.72	149.204
	SP 7	7716.452	1.647232	2.85	12.2	34.77	221.9284
	SP 8	8095.023	1.660723	3.15	12.5	39.375	205.5879
	SP 9	6228.349	1.396224	3.38	12.32	41.6416	149.5704
	SP 10	6576.884	1.312205	3.3	12.27	40.491	162.4283
Laminate 3	SP 11	5167.207	1.311693	3.55	12.25	43.4875	118.8205
	SP 12	8106.793	1.792589	4.35	11.93	51.8955	156.2138
	SP 13	7709.107	1.501875	4.42	11.88	52.5096	146.8133
	SP 14	7708.057	1.421926	4.33	12.28	53.1724	144.9635
	SP 15	5532.686	1.176934	4.33	12.29	53.2157	103.9672
Laminate 4 (Reference laminate)	SP 16	7868.818	1.75447	4.15	12.21	50.6715	155.2908
	SP 17	7907.699	2.141184	4.14	12.12	50.1768	157.5967
	SP 18	6915.887	1.883853	4.31	12.19	52.5389	131.6337
	SP 19	7360.653	2.130509	3.94	12.18	47.9892	153.3814
	SP 20	4275.142	1.881446	3.87	12.08	46.7496	91.44767

Figure 78 presents data on the relationship between the buckling load factor and laminating angle, offering significant insights into the buckling characteristics of the composite laminate. Recognizing the variations in the buckling load factor concerning the laminating angle is essential for enhancing the stability and resilience against buckling failure in laminate design.

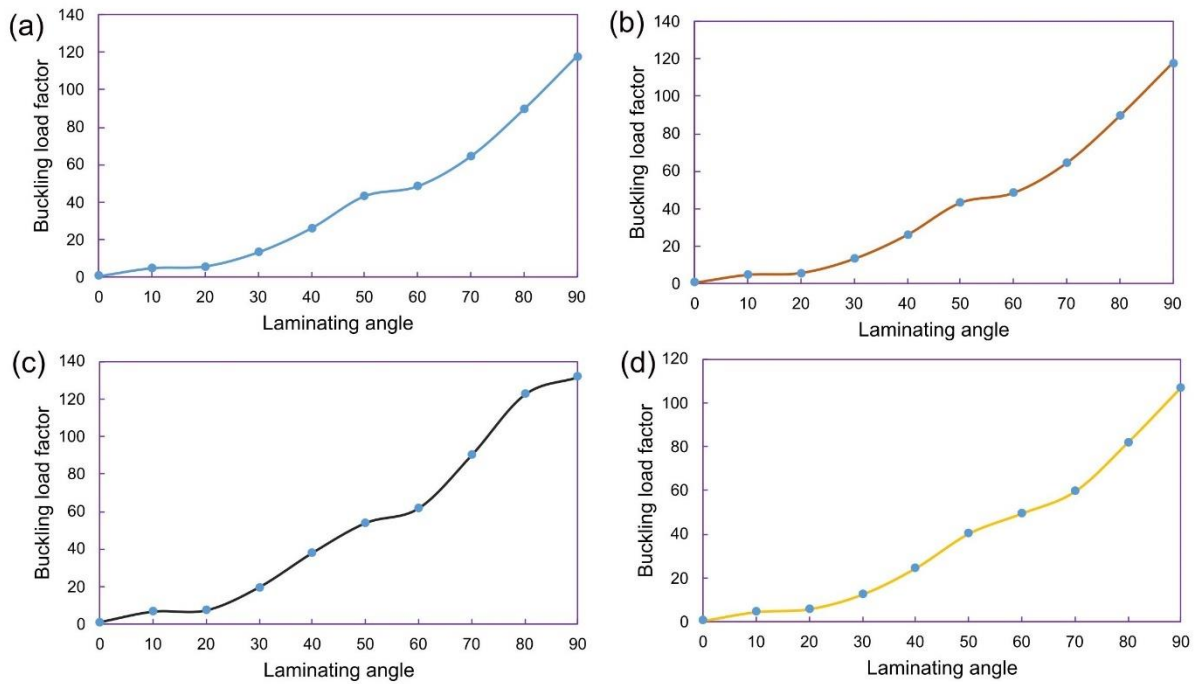


Figure 79. Depicts the results of buckling analysis, illustrating plots of the buckling load factor against laminating angle for various stacking sequences, including (a) Laminate 1, (b) Laminate 2, (c) Laminate 3, and (d) Laminate 4 (the reference laminate).

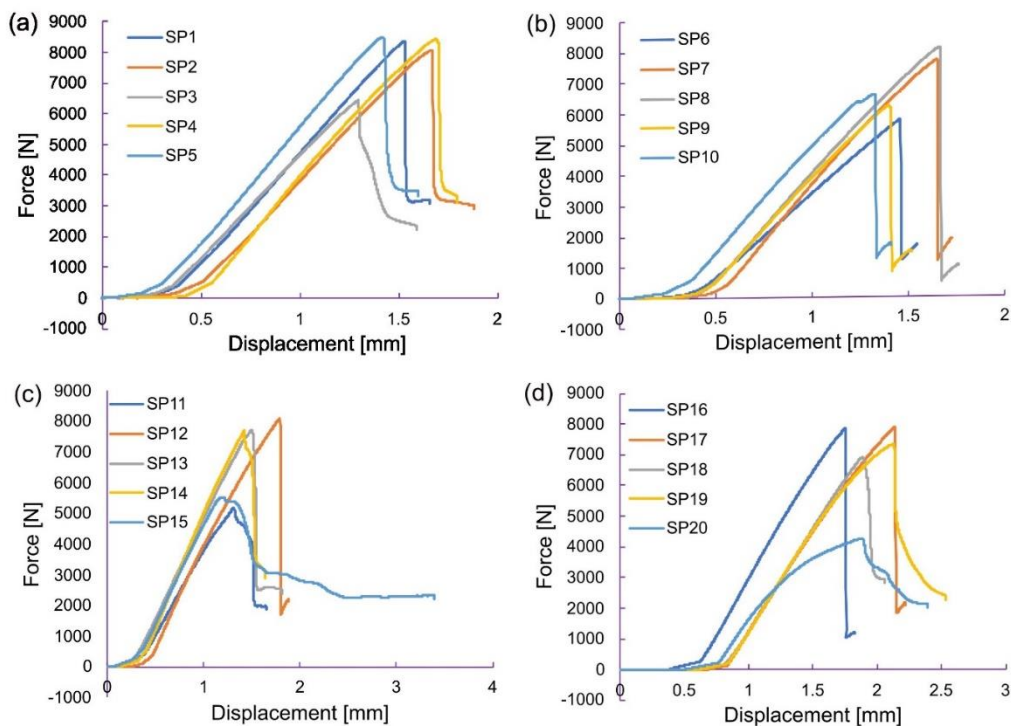


Figure 80. illustrates the results of compression tests, displaying force versus displacement plots for different stacking sequences, namely (a) Laminate 1, (b) Laminate 2, (c) Laminate 3, and (d) Laminate 4 (reference laminate).

The laminate 4, the reference laminate, had a thickness of 4.15 mm, a width of 12.21 mm, and an area of 50.6715 mm². Figure 48 showcases the force and displacement plots for Laminates 1 to 4. To evaluate the adhesion between the fiber matrix and the composites, E-glass fibers were examined using a Thermo Scientific scanning electron microscope (SEM, Thermo Fisher scientific, Ljubljana, Slovenia), Quattro S with ULTIM MAX. The SEM samples underwent carbon coating via sputter coating technique, utilizing high-purity carbon fiber thread (grade CT4) with a diameter of 0.8 mm and a weight of 0.4 g/m. Furthermore, specimens of Laminate 2 and 3 were scrutinized, and the fracture surfaces resulting from compression tests were analyzed using SEM.

The Fig.81 illustrates the fracture surfaces of E-glass fiber composite Laminates 2 and 3, where the fiber showed debonding from the matrix, with fibers splitting and being pulled towards $\pm 45^\circ$. These SEM findings are depicted in Fig. 80a, and 80b.

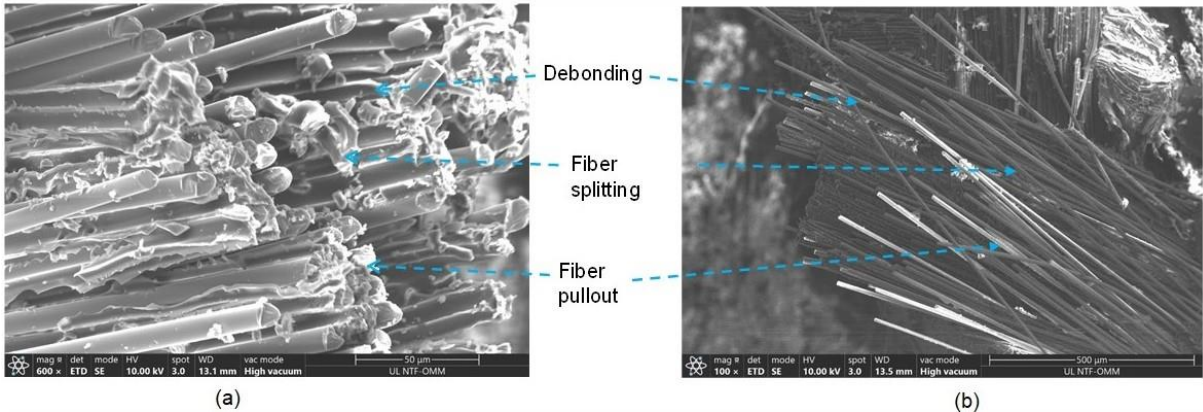


Figure 81. SEM images of E-glass fibers (a) fracture surface of E-glass fiber and (b) fracture surface of E-glass fibres.

Fig. 81 depicts the conventional fracture surface, illustrating the effects of compression loads on Laminates 2 and 3. Their failure was characterized by the shearing and splitting of the matrix fibers, along with instances of fiber pullout in the $\pm 45^\circ$ direction. Notably, the presence of substantial matrix cracks, stemming from the shearing effect, serves as a clear indicator of failure in E-glass bio-epoxy composite laminates subjected to compression loads. These cracks are delineated by the rectangles in Figure 50a and b.

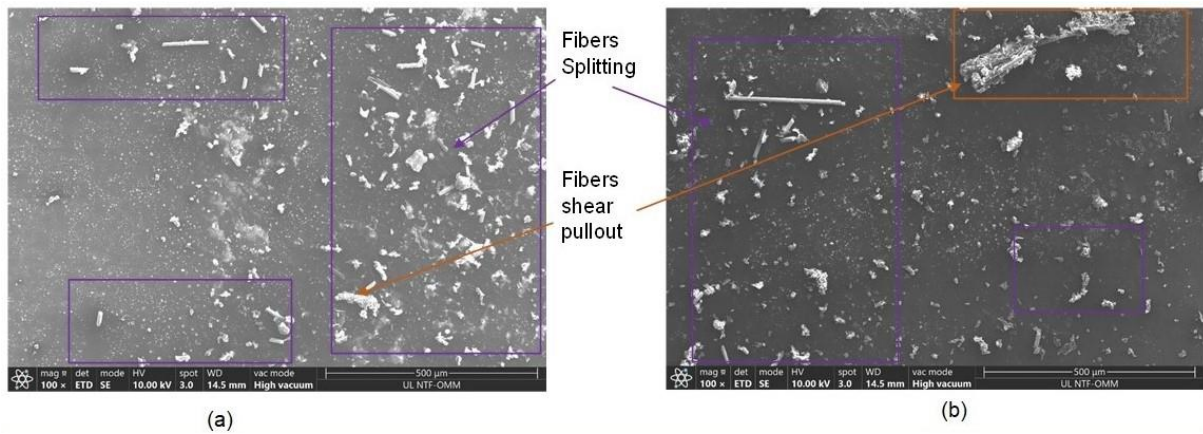


Figure 83. Fiber and matrix failure under compression load (a) fibers splitting and (b) fibres shearing pullout.

Figure 83 illustrates spherulitic failure. In Figure 83a, the presence of spherulitic matrix failure (MF) indicates the concentration of compressive force around the fiber, highlighted by the arrow. This area of compression is more susceptible to brittleness than the surrounding matrix material. Figure 83b shows the propensity for matrix cracking and fiber fracture (FF) under compressive load, as depicted by the arrow.

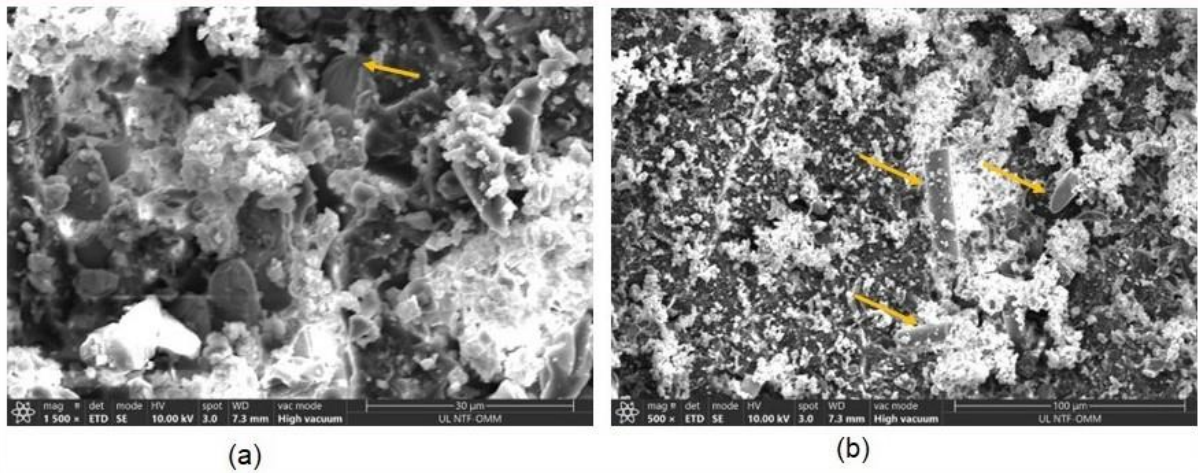


Figure 84. Spherulitic failure under compression load (a) fibers spherulitic failure and (b) fibres

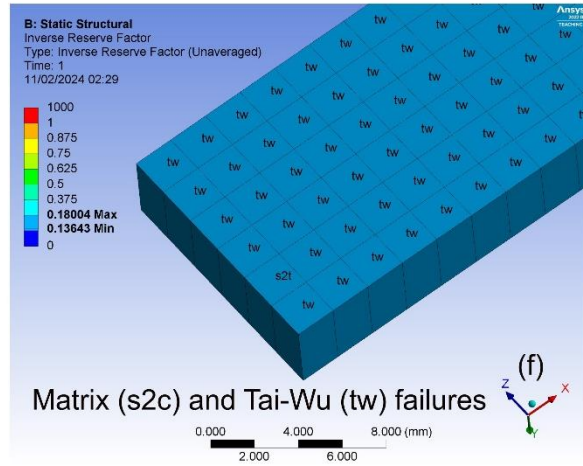
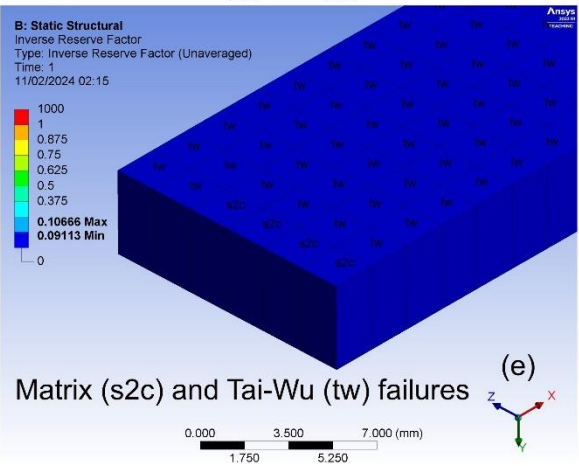
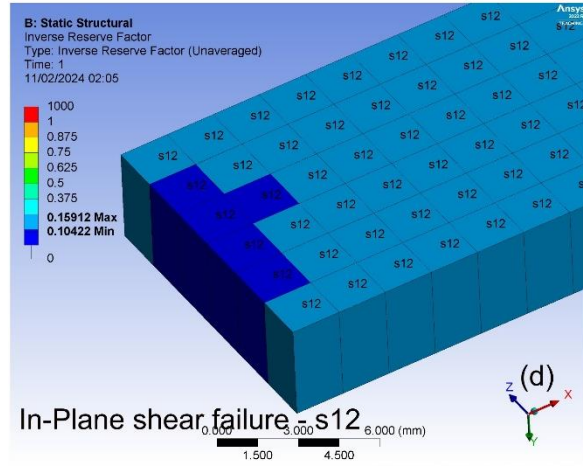
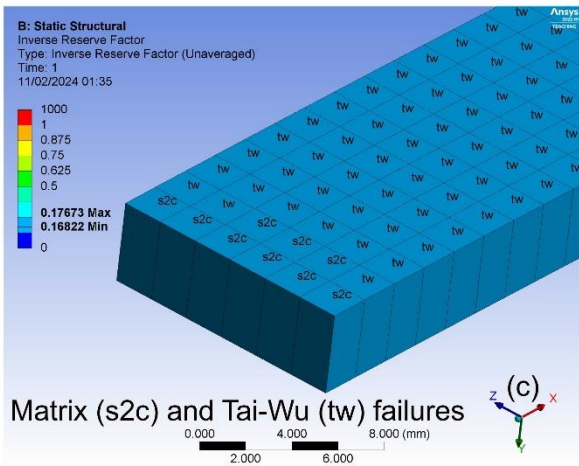
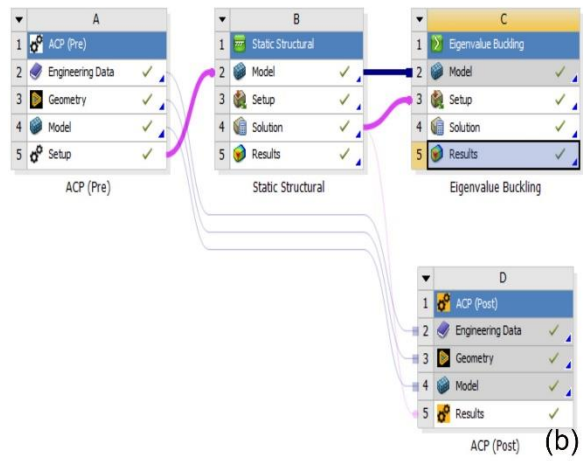
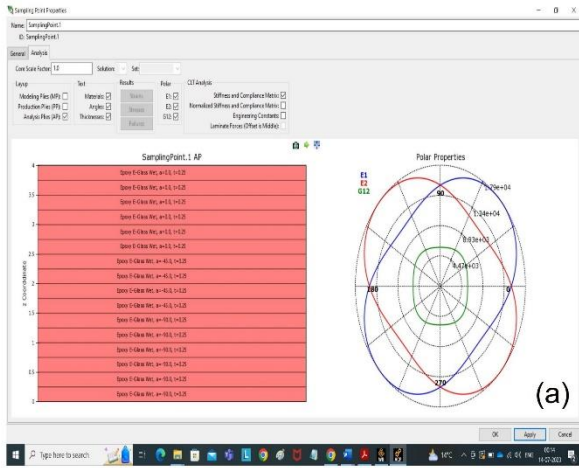


Figure 85. Composite laminates configuration and Identified failure criteria, (a) Plies construction, (b) Ansys setup, (c) Laminate 1, (d) Laminate 2, (e) Laminate 3 and (f) Laminate 4 (reference laminate).

Table 29. Optimization results at various ply orientations

Description	Plies	Ply stacking sequence	Inverse reserve factor			Buckling load factor			Critical buckling load			Laminate weight	
			(IRF-Ansys)	IRF CLT	Error	BLF Ansys	BLF CLT	Error	N _{cr} Ansys	N _{cr} CLT	Error		
Ansys results	24	[(90) ₈ / (45) ₈ / (0) ₈]	0.104	0.185	0.081	2.396	2.68	0.284	592	672	80	5.73E-06	
	25	[(45) ₃ / (-45) ₉ / (45) ₃ / (0) ₁₀]	0.111	0.300	0.189	2.545	2.73	0.185	636	684	48	5.73E-06	
	27	[(0) ₄ / (90) ₃ / (45) ₁₀ / (0) ₁₀]	0.040	0.084	0.044	4.615	2.73	1.885	1153	684	469	5.75E-06	
Optimized Ply-orientation results	Laminate 1	16	[(90) ₆ / (45) ₄ / (0) ₆]	0.176	0.165	0.011	4.772	2.73	2.042	1193	684	509	1.243E-05
	Laminate 2	16	[(45) ₂ / (-45) ₄ / (45) ₂ / (0) ₈]	0.159	0.479	0.320	6.072	2.75	3.322	1518	689	829	1.243E-05
	Laminate 3	16	[(0) ₁ / (90) ₂ / (45) ₇ / (0) ₆]	0.106	0.107	0.011	6.369	2.85	3.519	1592	712	880	1.243E-05
	Laminate 4 (Random orientation)	16	[(45) ₁ / (-45) ₁ / (90) ₂ / (0) ₃ / (90) ₂ / (0) ₃ / (90) ₂ / (45) ₁ / (-45) ₁]	0.180	0.086	0.094	4.540	2.69	1.85	1135	673	462	1.243E-05

A novel optimization method was developed specifically for laminates with composite stacking sequences, aiming to address two critical industrial requirements. Firstly, it enables the handling of multiple load factor cases, thereby expanding the number of objective functions and constraints involved. Secondly, it deals with the diverse and intricate concepts and rules governing stacking sequences. Building upon the MOGAs approach, the evolutionary algorithm devised in this study demonstrated high efficiency in managing numerous objective functions and constraints, reaching several hundred in number. The conception rules were integrated within the evolution and reproduction operators of the genetic algorithm, ensuring that only permissible solutions adhering to these rules were considered during the process. This proposed strategy is particularly suitable for post-processing tasks, facilitating sorting and further design reduction efforts.

The post-processing phase focused on three criteria: minimizing the inverse reserve factor, minimizing the load factor, and ultimately minimizing the number of plies. When compared to conventional design methods, the proposed strategy showed significant

improvements across these criteria. The optimal results are presented in Table 29, where the minimum number of plies is 24, the IRF value is 0.1044, the weight of the laminate is $5.73 \times 10^{-6} \text{ kg/m}^3$, and the buckling load factor is 2.3960. The ultimate compressive strength for the reference laminate was 155.2908 MPa. Comparison of the results showed that Laminate 1 exhibited the highest F_{max} and ultimate compressive strength, while Laminate 3 had the lowest values in both parameters. Laminate 2 had the smallest thickness and area, resulting in lower F_{max} and ultimate compressive strength compared to the other laminates. Surface fracture analysis identified fiber and matrix cracks, providing valuable insights for optimizing the stacking sequence and orientation of plies to enhance the laminate's resistance to buckling and improve overall structural performance in real-world applications.

In summary, the analysis highlights the significance of advanced numerical simulations and optimization techniques in tailoring composite laminates for specific performance criteria, thereby enhancing structural efficiency in various engineering applications. These findings underscore the substantial influence of material composition and laminate design on their mechanical properties, rendering the identified optimal stacking sequences valuable for future applications in UAV and automobile structures.

8. Summary

The doctoral dissertation concerns the optimization methodology for ultra lightweight composite structure which is useful to construct the UAVs structures (TS17). The doctoral dissertation work presents an innovative method for optimizing stacking sequences in lightweight composite structures utilizing multi-objective evolutionary algorithms. Within the optimization framework, I have effectively integrated engineering design standards relevant to stacking sequence design as constraints or additional objectives. Furthermore, I have introduced a novel initiation technique grounded in mechanical principles to improve the optimization process. I showcased the application of this methodology by optimizing composite laminates, taking into account parameters such as weight, inverse reserve factor, and buckling load factor.

8.1 Conclusion

The findings presented in this doctoral dissertation confirm the hypothesis proposed in this research. The suitability of the optimized ultra-lightweight structure for creating lightweight UAVs has been validated, highlighting its eco-friendly and biodegradable qualities. During this PhD research, results were methodically derived, covering optimization approaches, Ansys analysis, manufacturing processes, and laboratory testing procedures.

Case study _1

In this study, three design cases were evaluated, each focusing on different composite materials: epoxy-jute, epoxy-glass, and a sandwich structure.

- ✚ For the epoxy-jute composite, notable deformation ranging from 0.022 mm to 2.038 mm was observed across various design instances. Von Mises stress values fluctuated between 5.569 MPa and 57.754 MPa, indicating variable stress levels within the material. Maximum strain values suggested localized strain within the composite, with relatively low failure index values indicating minimal likelihood of failure under the applied load. Additionally, the composite exhibited a high buckling load factor, indicative of resistance to buckling, and moderate strength ratio results, suggesting a balanced strength-to-weight ratio.

- ✚ Comparatively, the epoxy-glass composite displayed lower levels of deformation, ranging from 0.022 mm to 2.302 mm. Von Mises stress values were similar to the epoxy-jute composite, while maximum strain values were higher. Nonetheless, low failure index values and a high buckling load factor suggested minimal likelihood of failure and resistance to buckling, respectively. Moderate strength ratio values indicated a comparable strength-to-weight ratio to the epoxy-jute composite.
- ✚ In the case of the sandwich structure, it exhibited the highest deformation among the three designs, with values ranging from 1.984 mm to 2.302 mm. Von Mises stress values indicated varying stress concentrations, while maximum strain values surpassed those of the composite designs. Low failure index values implied minimal likelihood of failure, though the buckling load factor was comparatively low, suggesting lesser resistance to buckling. However, moderate strength ratios indicated a balanced strength-to-weight ratio.

This study's findings can be compared to prior research, and it is recommended to explore alterations in geometric shapes, fiber orientations, and ply stacking sequences to mitigate structural failures in T-joints, particularly at the interfaces of the stringer, base plate, and web.

Case study _2 (Approach_1)

An FEM study was performed on composite corrugated sandwich panels using ANSYS software. The research focused on optimizing factors such as corrugated core thickness, angle, and height. The focus of this study is on the physical robustness and structural integrity. Afterwards, an evaluation of the specific energy absorption is conducted to evaluate the effectiveness of the sandwich panels. The deformation-time curves of all seven sandwich panels during local indentation demonstrate a consistent pattern: initially, the force increases linearly, reaches a maximum, and thereafter drops gradually. After analyzing all the results from the simulated 3-point bending tests, the most desirable outcome is picked for further investigation. This outcome, observed on corrugated core composite sandwich panel C2, shows little deformation and indentation.

Case study _2 (Approach_2)

The performance of epoxy-jute composite, epoxy-glass composite, and sandwich structures was evaluated through design examples involving deformation and stress analysis.

- ✚ The epoxy-jute composite exhibited moderate deformation and stress values across all design scenarios. Although it generally performs adequately, further adjustments may be necessary to enhance its mechanical properties for specific applications.
- ✚ In contrast, the epoxy-glass composite displayed reduced deformation and stress levels, indicating superior structural integrity and load-bearing capacity. These findings highlight its suitability for applications requiring increased strength and durability.
- ✚ The sandwich structure demonstrated a balanced distribution of deformation and stress, leveraging the advantages of its composite composition. With its enhanced stiffness-to-weight ratio and resistance to bending and buckling, it presents an attractive option for lightweight structural systems.

In summary, each composite structure exhibited unique mechanical properties and performance characteristics when subjected to the prescribed stress conditions. The majority of failures were seen in places such as the stringers, baseplate, and web surface that is joined to both stringers and connected to the base plate. In the end, the boundary connections used on the base plate resulted in failure, namely in the crucial area surrounding the circular hole. The findings have significant ramifications for the development and enhancement of natural composite materials in engineering applications. The findings of this study indicate that the sandwich structure experiences a shear stress of 28.889 MPa and von Mises stresses of 57.754 MPa, which are higher than those observed in design cases 1 and 2. Furthermore, design case 3 is deemed suitable for aerospace applications. Further inquiry and testing may be necessary to authenticate and improve the findings of this study.

Case study _2_(Approach_3)

The objective of the structural testing in this study was to assess the integrity of individual cell samples following characterization and evaluation for solar performance. Static testing was chosen as a suitable method to represent the types of loads that could lead to

failure of embedded solar cells or arrays, as opposed to flexural testing. Common sources of damage for UAV wings during assembly, disassembly, or landing include impacts with objects, drops, or mishandling. Out-of-plane stress testing was primarily aimed at simulating these impact failures under static conditions. The structural static tests were conducted using Ansys, and four laminates with different configurations were analyzed in this research. The highest stress was observed in laminate_1, while the minimum deformation was noted in laminate_4. Laminate_2 demonstrated the best results when compared to all evaluated laminates. These simulation results hold promise for future applications in UAV wing design.

Case study_3

Comparison in between Sandwich structure vs Sandwich structure with hat shaped stiffeners the several factors.

- ✚ **Structural behaviour:** Case 2 (Sandwich Structure) generally exhibits more predictable and consistent mechanical responses with increasing thickness under both compression and shear loads.
- ✚ **Stress distribution:** Case 3 (Sandwich Core with Hat-Shaped Stiffener) shows more varied stress distributions with thickness, likely due to the presence of stiffeners affecting load distribution.

Application considerations: The choice between these structures would depend on specific application requirements for stiffness, load distribution, and mechanical performance under different loading conditions. Case 2 might be preferred for uniform stress distribution and predictable behaviour, while Case 3 could offer advantages in terms of weight savings and tailored stiffness characteristics with the inclusion of stiffeners. The fabrication and testing strategy is presented in Fig.17 and Fig18.

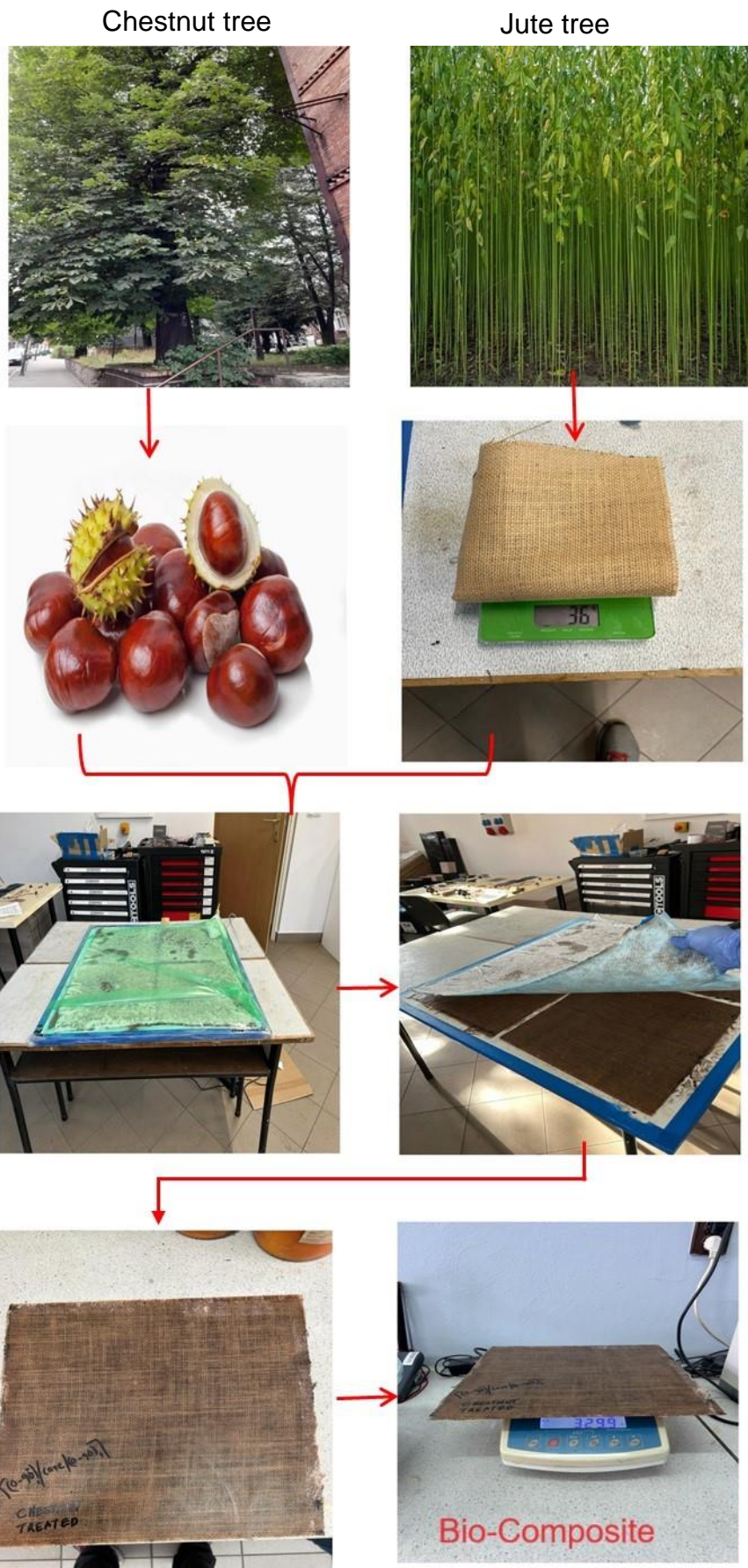


Figure.86 Bio-Composite sandwich structure fabrication strategy for TS17 UAV wing

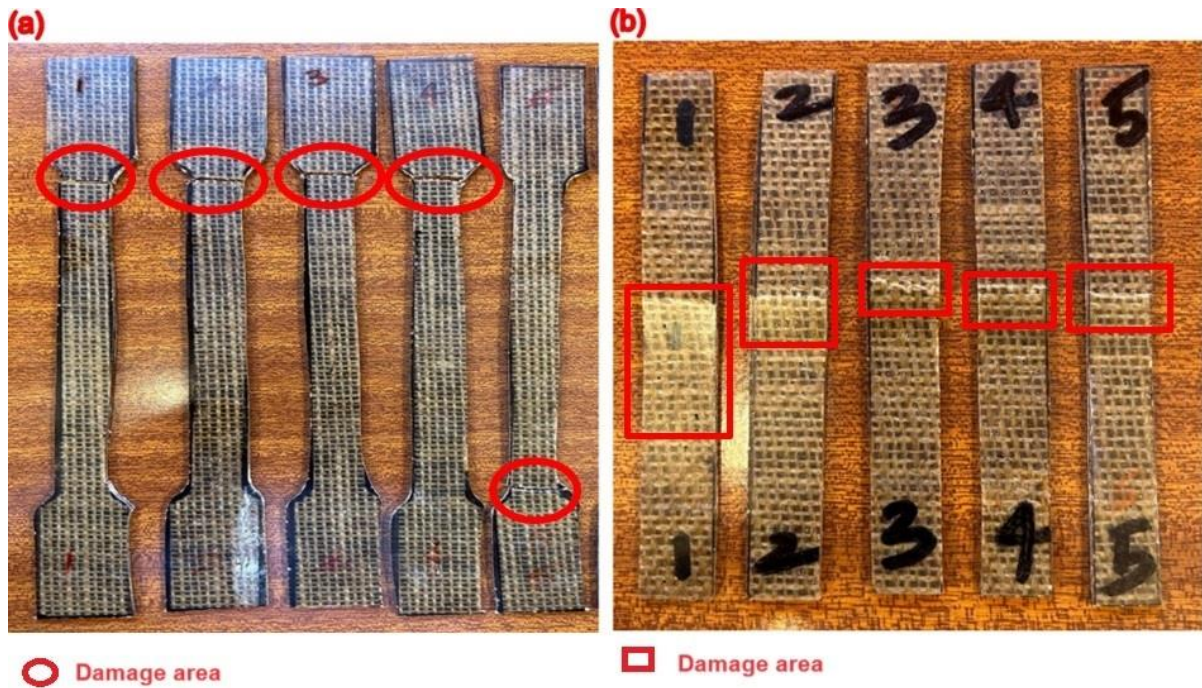


Figure.87 Bio-Composite mechanical testing, (a) Tensile test, (b) Compression test.

The obtained results (Case_2) align with the initial design criteria. Furthermore, there is ongoing work to refine the structure by exploring changes in stacking sequence and ply orientation. These refinements aim to enhance structural rigidity and stability, ensuring optimal performance in the intended application.

The bio-composite sandwich structure is composed of two biomaterials: natural fibers (Jute) and Chestnut, with Chestnut serving as the core material in the construction. This composite material is eco-friendly, lightweight, easily degradable, and contributes to reducing the environmental impact associated with global warming.

Moreover, it offers load bearable stiffness compared to traditional materials. The material is cost-effective compared to alternatives like carbon fiber and glass fiber, facilitates easy fabrication, and can be molded into desired shapes according to specific requirements.

Plie Optimization

In this study, diverse materials with varying strengths and ply sequences were investigated, accounting for thickness variations. Through Ansys simulations, maximum stress, strain, deformation, and shear stress were analyzed for different ply configurations. Particularly, natural reinforced fiber composite (Jute) laminates were scrutinized, revealing that mechanical properties, especially maximum stress, peaked in the longitudinal direction with varying fiber orientations. The study showcased the

superiority of hybrid natural-fiber-reinforced composites over natural fibers, particularly at specific configurations, offering promising prospects for UAV wing construction. The combination of jute and glass fiber with epoxy resin composite, especially at a 45° ply orientation and 3 mm thickness, demonstrated notable mechanical properties. Despite the linear elastic behavior of natural fibers, a substantial increase in material yield strength was observed when natural fibers were combined with synthetic ones. Laboratory testing is imperative to validate these simulation findings. Nevertheless, based on the results, it was concluded that natural hybrid composites hold promise for prototype UAV structure fabrication. Recommendations for future work include fabricating test specimens according to ASTM standards and conducting further analyses based on laboratory tests. If corroborated through testing, this material could revolutionize UAV manufacturing applications.

Structural optimization method results

This study presents a novel optimization method tailored for laminates with composite stacking sequences, addressing two critical industrial needs. Firstly, it allows handling multiple load factor cases, expanding the scope of objective functions and constraints. Secondly, it navigates the intricate concepts and rules governing stacking sequences. Leveraging the MOGAs approach, our evolutionary algorithm efficiently managed numerous objective functions and constraints, integrating conception rules within its operators to ensure adherence to stacking sequence regulations. This strategy proves particularly effective for post-processing tasks, streamlining sorting and design reduction efforts.

The post-processing phase prioritized minimizing the inverse reserve factor, load factor, and the number of plies. Compared to conventional methods, our approach yielded significant improvements across these criteria. Optimal results, presented in Table 2, demonstrate the efficacy of the proposed strategy, with Laminate 1 exhibiting the highest F_{max} and ultimate compressive strength. Surface fracture analysis provided valuable insights for optimizing stacking sequences, enhancing laminate resistance to buckling, and improving structural performance.

In summary, this analysis underscores the importance of advanced numerical simulations and optimization techniques in tailoring composite laminates for specific performance

criteria. The identified optimal stacking sequences hold promise for enhancing structural efficiency in various engineering applications, particularly in UAV and automobile structures, by emphasizing the influence of material composition and laminate design on mechanical properties.

8.2 Future work

From a future perspective, the optimized methodology holds promise for fabricating UAV structures. Specifically, hybrid composites can be utilized in wing construction, while bio-composites are suitable for fuselage components. However, in this research, bio-composites were explored for use throughout the UAV's parts. This study has the potential to catalyze significant advancements in both the automobile and aerospace industries. Further research is necessary to transition this work into real-world applications, including fabrication and flight testing.

References

- [1] Jones RM. *Mechanics of composite materials*. 2nd edn., Materials Science and Engineering Series, Taylor & Francis Group, 1999.
- [2] Kassapoglou C. *Design and Analysis of Composite Structures: With Applications to Aerospace Structures*. Aerospace Series, Wiley, 2011.
- [3] B. C. Hoskin. *Composite materials for aircraft structures*. B. C. Hoskin, Ed, and A. A. Baker, Ed, New York, American Institute of Aeronautics and Astronautics, Inc., 1986, 245, 1986.
- [4] R. M. Jones. *Mechanics of composite materials*. CRC Press, 1998.
- [5] D. Gay, S. V. Hoa, and S. W. Tsai. *Composite materials: design and applications*. CRC press, 2002.
- [6] J. N. Reddy. *Mechanics of laminated composite plates: theory and analysis, volume 1*. CRC press Boca Raton, 1997.
- [7] R. Kumpati, W. Skarka, S.K. Ontipuli, Current Trends in Integration of Non - destructive Testing Methods for Engineered Materials Testing, *Sensors* 21 (2021) 6175. <https://doi.org/10.3390/s21186175>
- [8] Kumpati, R.; Skarka, W.; Skarka, M. Ansys-Based Evaluation of Natural Fiber and Hybrid Fiber-Reinforced Composites. *Sustainability* 2022, *14*, 15992. <https://doi.org/10.3390/su142315992>
- [9] Ramesh Kumpati, Wojciech Skarka, Anna Dolata, Maciej Dyzia, Michał Skarka, Kamil Zenowicz, Enhancement of the stability of composite sandwich material for unmanned aerial vehicle wing panel. *MECHANICS AND MATERIALS IN DESIGN Theory- International Conference M2D2022, Funchal/Portugal, Experiments and Applications in Engineering-2022, Proceedings M2D2022 - 9th International Conference on Mechanics and Materials in Design Funchal/Portugal 26-30 June 2022*, Editors J.F. Silva Gomes and S.A. Meguid, pp.127-136 https://paginas.fe.up.pt/~m2d/proceedings_m2d2022/
- [10] Kumpati, R.; Skarka, W.; Skarka, M.; Brojan, M. Enhanced Optimization of Composite Laminates: Multi-Objective Genetic Algorithms with Improved Ply-Stacking Sequences. *Materials* 2024, *17*, 887. <https://doi.org/10.3390/ma17040887>.
- [11] Wojciech Skarka, Ramesh Kumpati, Michał Skarka, Failure analysis of a composite structural spar and rib-to-skin joints, *Procedia Structural Integrity*, Volume 54, 2024, Pages 490-497, ISSN 2452-3216, <https://doi.org/10.1016/j.prostr.2024.01.111>.

- [12] Ramesh Kumpati, Wojciech Skarka, Michał Skarka, Design optimization and failure analysis of natural composite sandwich T-joints under pulling load conditions, *Engineering Failure Analysis*, Volume 164, 2024, 108672, ISSN 1350-6307, <https://doi.org/10.1016/j.engfailanal.2024.108672>.
- [13] Bažant ZP, Cedolin L. *Stability of Structures: Elastic, Inelastic, Fracture and Damage Theories*. World Scientific, 2010.
- [14] G. Allaire. *Shape optimization by the homogenization method*, volume 146. Springer, 2002
- [15] M. P. Bendsoe. *Optimization of structural topology, shape, and material*. Springer, 1995.
- [16] A. Henrot and M. Pierre. *Variation et Optimisation des formes, Une analyse géométrique*, volume 48 of *Mathématiques et Applications*. Springer, 2005.
- [17] J. Sokolowski and J.-P. Zolesio. *Introduction to shape optimization*. Springer, 1992.
- [18] O. Pironneau. *Optimal shape design for elliptic systems*. Springer, 1984.
- [19] M. Bendsøe. Optimal shape design as a material distribution problem. *Structural and Multidisciplinary Optimization*, 1(4):193{202, 1989.
- [20] G. Allaire. *Conception optimale de structures*, volume 58. Springer, 2006.
- [21] P. Christensen and A. Klarbring. *An introduction to structural optimization*, volume 153. Springer, 2009.
- [22] M. Bendsoe and O. Sigmund. *Topology optimization: theory, methods and applications*. Springer, 2004.
- [23] B. Mohammadi and O. Pironneau. *Applied shape optimization for fluids*, volume 28. Oxford University Press Oxford, 2001.
- [24] F. Murat and L. Tartar. Calcul des variations et homogénéisation, In *les méthodes de l'homogénéisation: théorie et applications en physique*. Coll. Dir. Etudes et Recherches EDF, (57):319{369, 1985.
- [25] L. Tartar. An introduction to the homogenization method in optimal design. *Optimal Shape Design*, pages 47{156, 2000.
- [26] L. Tartar. *The general theory of homogenization: a personalized introduction*, volume 7. Springer, 2009.
- [27] R. V. Kohn and G. Strang. Optimal design and relaxation of variational problems; Parts I, II, III. *Communications on Pure and Applied Mathematics*, 39(1):113{137, 1986.

- [28] A. Cherkaev. Variational methods for structural optimization, volume 140. Springer, 2000
- [29] L. Gibiansky and A. V. Cherkaev. Design of composite plates of extremal rigidity. In Topics in the mathematical modelling of composite materials, pages 95{137. Springer, 1997.
- [30] K. Lurie and A. Cherkaev. Effective characteristics of composite materials and the optimal design of structural elements. In Topics in the mathematical modelling of composite materials, pages 175{271. Springer, 1997.
- [31] M. Bendsoe and N. Kikuchi. Generating optimal topologies in structural design using a homogenization method. Computer methods in applied mechanics and engineering, 71(2):197{224, 1988.
- [32] M. Stolpe and K. Svanberg. An alternative interpolation scheme for minimum compliance topology optimization. Structural and Multidisciplinary Optimization, 22(2):116{124, 2001.
- [33] J. Guest, J. Prévost, and T. Belytschko. Achieving minimum length scale in topology optimization using nodal design variables and projection functions. International Journal for Numerical Methods in Engineering, 61(2):238{254, 2004.
- [34] L. Ambrosio and G. Buttazzo. An optimal design problem with perimeter penalization. Calculus of Variations and Partial Differential Equations, 1(1):55{69, 1993.
- [35] G. Michailidis. Manufacturing Constraints and Multi-Phase Shape and Topology Optimization via a Level-Set Method. PhD thesis, Ecole Polytechnique, <http://tel.archivesouvertes.fr/docs/00/93/73/06/PDF/thesis.pdf>, 2014.
- [36] G. I. Rozvany. A critical review of established methods of structural topology optimization. Structural and Multidisciplinary Optimization, 37(3):217{237, 2009.
- [37] Pedersen P. On optimal orientation of orthotropic materials. Structural optimization 1989; 1(2):101–106.
- [38] Pedersen P. Bounds on elastic energy in solids of orthotropic materials. Structural optimization 990; 2(1):55–63.
- [39] Hornlein H, Kočvara M, Werner R. Material optimization: bridging the gap between conceptual and preliminary design. Aerospace Science and Technology 2001; 5(8):541–554.
- [40] Sigmund O, Torquato R. Design of materials with extreme thermal expansion using a

- three-phase topology optimization method. *Journal of the Mechanics and Physics of Solids* 1997; 45(6):1037–1067.
- [41] Stegmann J, Lund E. Discrete material optimization of general composite shell structures. *International Journal for Numerical Methods in Engineering* 2005; 62(14):2009–2027.
- [42] Lund E, Stegmann J. On structural optimization of composite shell structures using a discrete constitutive parametrization. *Wind Energy* 2005; 8(1):109–124.
- [43] Hvejsel CF, Lund E, Stolpe M. Optimization strategies for discrete multi-material stiffness optimization. *Structural and Multidisciplinary Optimization* 2011; 44(2):149–163.
- [44] Hvejsel CF, Lund E. Material interpolation schemes for unified topology and multimaterial optimization. *Structural and Multidisciplinary Optimization* 2011; 43(6):811–825.
- [45] Bendsoe M, Sigmund O. *Topology Optimization: Theory, Methods and Applications*. 2nd edn., Springer-Verlag, Berlin, 2003.
- [46] Rietz A. Sufficiency of a finite exponent in SIMP (power law) methods. *Structural and Multidisciplinary Optimization* 2001; 21:159–163.
- [47] Stolpe M, Svanberg K. An alternative interpolation scheme for minimum compliance topology optimization. *Structural and Multidisciplinary Optimization* 2001; 22:116–124.
- [48] Lund E. Buckling topology optimization of laminated multi-material composite shell structures. *Composite Structures* 2009; 91(2):158–167.
- [49] Sorensen S, Sorensen R, Lund E. DMTO - a method for Discrete Material and Thickness Optimization of laminated composite structures. *Structural and Multidisciplinary Optimization* 2014; 50(1):25–47.
- [50] Bruyneel M. SFP-a new parameterization based on shape functions for optimal material selection: application to conventional composite plies. *Structural and Multidisciplinary Optimization* 2011; 43(1):17–27.

- [51] Gao T, Zhang W, Duysinx P. A bi-value coding parameterization scheme for the discrete optimal orientation design of the composite laminate. *International Journal for Numerical Methods in Engineering* 2012; 91(1):98–114.
- [52] Timoshenko, S. P., & Gere, J. M. (1961). *Theory of elastic stability*. McGraw-Hill Education.
- [53] Budynas, R. G., & Nisbett, J. K. (2014). *Shigley's mechanical engineering design* (10th ed.). McGraw-Hill Education.
- [54] Cook, R. D., Malkus, D. S., Plesha, M. E., & Witt, R. J. (2001). *Concepts and applications of finite element analysis* (4th ed.). John Wiley & Sons.
- [55] Reddy, J. N. (2006). *An introduction to the finite element method* (3rd ed.). McGraw-Hill Education.
- [56] Ashwell, D. G., & Jones, N. (2006). *Engineering analysis with ANSYS software*. Butterworth-Heinemann.
- [57] Fenner, R. T. (1996). *Engineering analysis of smart material systems*. John Wiley & Sons.
- [58] Chajes, M. J. (1998). *Structural analysis: a historical approach*. Cambridge University Press.
- [59] Norris, C. H., & Wilkins, M. L. (2009). *Buckling of bars, plates, and shells*. CRC Press.
- [60] Megson, T. H. G. (1999). *Structural and stress analysis* (2nd ed.). Butterworth-Heinemann.
- [61] Nielsen, S. R. K. (2004). *Introduction to engineering analysis*. Prentice Hall
- [62] Lindgaard E, Lund E. Nonlinear buckling optimization of composite structures. *Computer Methods in Applied Mechanics and Engineering* 2010; 199(37-40):2319–2330.
- [63] Lindgaard E, Lund E, Rasmussen K. Nonlinear buckling optimization of composite structures considering "worst" shape imperfections. *International Journal of Solids and Structures* 2010; 47(22-23):3186–3202.
- [64] Lindgaard E, Lund E. A unified approach to nonlinear buckling optimization of composite structures. *Computers & Structures* 2011; 89(3-4):357–370.

- [65] Lindgaard E, Lund E. Optimization formulations for the maximum nonlinear buckling load of composite structures. *Structural and Multidisciplinary Optimization* 2011; 43(5):631–646.
- [66] Lindgaard E, Dahl J. On compliance and buckling objective functions in topology optimization of snap-through problems. *Structural and Multidisciplinary Optimization* 2013;47(3):409–421.
- [67] Lindgaard E. Buckling Optimization of Composite Structures. PhD Thesis, Department of Mechanical and Manufacturing Engineering, Aalborg University, Denmark 2010. Special report no. 69.
- [68] Brendel B, Ramm E. Linear and nonlinear stability analysis of cylindrical shells. *Computers & Structures* 1980; 12(4):549–558.
- [69] Al Rashid A, Khan SA, Al-Ghamdi SG, Koç M (2020) Additive manufacturing: Technology, applications, markets, and opportunities for the built environment. *Autom Constr* 118(October).
- [70] Al Rashid A, Imran R, Khalid MY (2020) Determination of opening stresses for railway steel under low cycle fatigue using digital image correlation. *Theor Appl Fract Mech* 108(April).
- [71] Al Rashid A, Khalid MY, Imran R, Ali U, Koc M (2020) Utilization of banana fiber-reinforced hybrid composites in the sports industry. *Mater* 13(14):3167. <https://doi.org/10.3390/ma13143167>
- [72] Thilagavathi G, Pradeep E, Kannaian T, Sasikala L (2010) Development of natural fiber nonwovens for application as car interiors for noise control. *J Ind Text* 39(3):267–278. <https://doi.org/10.1177/1528083709347124>
- [73] Vasile S, Langenhove VL (2004) Automotive industry a high potential market for nonwovens sound insulation. *J Text Apparel Technol Manag* 3(4):1–5
- [74] Sanjay MR, Arpitha GR, Yogesha B (2015) Study on mechanical properties of natural - glass fibre reinforced polymer hybrid composites: a review. *Mater Today Proc* 2(4–5):2959–2967. <https://doi.org/10.1016/j.matpr.2015.07.264>
- [75] Hossain R, Islam A, Van Vuurea A, Verpoest I (2013) Tensile behavior of environment friendly jute epoxy laminated composite. *Procedia Eng* 56:782–788. <https://doi.org/10.1016/j.proeng.2013.03.196>
- [76] A.N. Shah, S.C. Lakkad, Mechanical properties of jute-reinforced plastics, *Fibre Science and Technology*, Volume 15, Issue 1, 1981, Pages 41–46, ISSN 0015-0568, [https://doi.org/10.1016/0015-0568\(81\)90030-0](https://doi.org/10.1016/0015-0568(81)90030-0).
- [77] Zewdie Alemayehu, Ramesh Babu Nallamothe, Mekonnen Liben, Seshu Kishan Nallamothe, Anantha Kamal Nallamothe, Experimental investigation on characteristics

- of sisal fiber as composite material for light vehicle body applications, *Materials Today: Proceedings*, Volume 38, Part 5, 2021, Pages 2439-2444, ISSN 2214-7853, <https://doi.org/10.1016/j.matpr.2020.07.386>.
- [78] Ramesh M, Palanikumar K, Reddy KH (2013) Comparative Evaluation on Properties of Hybrid Glass Fiber- Sisal / Jute Reinforced Epoxy Composites. *Procedia Eng* 51(NUiCONE 2012):745–750.
- [79] Braga RA, Magalhaes PAA Jr (2015) Analysis of the mechanical and thermal properties of jute and glass fiber as reinforcement epoxy hybrid composites. *Mater Sci Eng C* 56:269–273. <https://doi.org/10.1016/j.msec.2015.06.031>
- [80] Ajith Gopinath, M. Senthil Kumar, A. Elayaperumal, Experimental Investigations on Mechanical Properties Of Jute Fiber Reinforced Composites with Polyester and Epoxy Resin Matrices, *Procedia Engineering*, Volume 97, 2014, Pages 2052-2063, ISSN 1877-7058.
- [81] T. Munikenche Gowda, A.C.B. Naidu, Rajput Chhaya, Some mechanical properties of untreated jute fabric-reinforced polyester composites, *Composites Part A: Applied Science and Manufacturing*, Volume 30, Issue 3, 1999, Pages 277-284, ISSN 1359-835X.
- [82] I.K. Varma, S.R. Anantha Krishnan, S. Krishnamoorthy, Composites of glass/modified jute fabric and unsaturated polyester resin, *Composites*, Volume 20, Issue 4, 1989, Pages 383-388, ISSN 0010-4361, [https://doi.org/10.1016/0010-4361\(89\)90664-2](https://doi.org/10.1016/0010-4361(89)90664-2).
- [83] Mohan, R., Kishore, Shridhar, M.K. et al. Compressive strength of jute-glass hybrid fibre composites. *J Mater Sci Lett* 2, 99–102 (1983). <https://doi.org/10.1007/BF00722222>
- [84] Zhang J, Chaisombat K, He S, Wang CH (2012) Hybrid composite laminates reinforced with glass/carbon woven fabrics for lightweight load bearing structures. *Mater Des* 36:75–80. <https://doi.org/10.1016/j.matdes.2011.11.006>
- [85] Ashraf, M.A.; Zwawi, M.; Taqi Mehran, M.; Kanthasamy, R.; Bahadar, A. Jute Based Bio and Hybrid Composites and Their Applications. *Fibers* 2019, 7, 77. <https://doi.org/10.3390/fib7090077>
- [86] K. Sabeel Ahmed, S. Vijayarangan, Experimental Characterization of Woven Jute-Fabric-Reinforced Isothalic Polyester Composites. *Journal of Applied Polymer Science*, Vol. 104, 2650–2662 (2007). DOI 10.1002/app.25652
- [87] Elbadry EA, Aly-HassanMS, Hamada H (2012) Mechanical properties of natural jute fabric/jute mat fiber reinforced polymer matrix hybrid composites. *Adv Mech Eng* 2012:381–388. <https://doi.org/10.1155/2012/354547>
- [88] Khondker OA, Ishiaku US, Nakai A, Hamada H (2005) Tensile, flexural and impact properties of jute fibre-based thermosetting composites. *Plast Rubber Compos* 34(10):450–462. <https://doi.org/10.1179/174328905X66199>

- [89] Yang B, He L, Gao Y (2018) Simulation on impact response of FMLs: effect of fiber stacking sequence, thickness, and incident angle. *IEEE J Sel Top Quantum Electron* 25(3):621–631. <https://doi.org/10.1515/secm-2016-0226>
- [90] Ullah H, Harland AR, Silberschmidt VV (2012) Experimental and numerical analysis of damage in woven gfrp composites under large-deflection bending. *Appl Compos Mater* 19(5):769–783. <https://doi.org/10.1007/s10443-011-9242-7>
- [91] Vinšová L, Urban T (2017) Testing of mechanical properties of thick-walled carbon fiber composite for FEM simulations. *Mater Today Proc* 4(5):5989–5994. <https://doi.org/10.1016/j.matpr.2017.06.083>
- [92] Soliman E, Al-Haik M, Taha MR (2012) On and off-axis tension behaviour of fiber reinforced polymer composites incorporating multi-walled carbon nanotubes. *J Compos Mater* 46(14):1661–1675.
- [93] Rasheed A, Khalid FA (2014) Fabrication and properties of CNTs reinforced polymeric matrix nanocomposites for sports applications *IOP Conf Ser Mater Sci Eng*, vol. 60, no. 1, doi: <https://doi.org/10.1088/1757-899X/60/1/012009>
- [94] Zannat M, Roy R, Sultana MN (2017) Jute-Glass Fiber Based Composite for Engineering Application. *Jute-Glass Fiber Based Compos Eng Appl* 4(August):510–515
- [95] Zannat M, Roy R, Sultana MN (2017) Jute-Glass Fiber Based Composite for Engineering Application. *Jute-Glass Fiber Based Compos Eng Appl* 4(August):510–515
- [96] Gibson, R.F. *Principles of Composite Material Mechanics*, 4th ed.; CRC Press: Boca Raton, FL, USA, 2016.
- [97] Jones, R.M. *Mechanics of Composite Materials*; CRC Press: Boca Raton, FL, USA, 1999.
- [98] Baker, A.A. *Composite Materials for Aircraft Structures*; AIAA Ed.: Reston, VA, USA, 2008.
- [99] Bismarck, A.; Mishra, S.; Lampke, T. Plant fibers as reinforcement for green composites. In *Natural Fibers, Biopolymers, and Biocomposites*; CRC Press: Boca Raton, FL, USA, 2005; Volume 1, pp. 37–108.
- [100] Mohanty, A.K.; Misra, M.; Hinrichsen, G. Biofibres, biodegradable polymers and bio composites: An overview. *Macromol. Mater. Eng.* **2000**, 276–277, 1–24.
- [101] Laurin, F.; Carrere, N.; Maire, J.F. A multi-scale progressive failure approach for composite laminates based on thermodynamic viscoelastic and damage models. *Compos. Part A* **2007**, 38, 198–209.
- [102] Xie, Y.J.; Yan, H.G.; Liu, Z.M. Buckling optimization of hybrid-fiber multilayer sandwich cylindrical shells under external lateral pressure. *Compos. Sci. Technol.* **1996**, 56, 1349–1353.

- [103] Prasanth, K.C. Optimal design of composite cylindrical shells subject to compression buckling strength. *Multidiscip. Model. Mater. Struct.* **2023**, *19/5*, 829–847.
- [104] Tennyson, R.C.; Hansen, J.S. Optimum design for buckling of laminated cylinders, collapse. In *The Buckling of Structures in Theory and Practice*; Thompson, J.M.T., Hunt, G.W., Eds.; Cambridge University Press: Cambridge, UK, 1983.
- [105] Chapter 5—Design and Analysis. In *Military-Handbook-17-3F*; AREA CMPS: Glendale, CA, USA, 2017; pp. 68–71.
- [106] Basem, E.; Tawfik, H.L.; Ahmed, E.; Tarek, E. Weight reduction and strengthening of marine hatch covers by using composite materials. *Int. J. Nav. Archit. Ocean Eng.* **2017**, *9*, 185–198.
- [107] Deb, K. *Multi-Objective Optimization Using Evolutionary Algorithms*; John Wiley & Sons: Hoboken, NJ, USA, 2001.
- [108] Coello, C.; Carlos, A. Evolutionary algorithms for solving multi-objective problems. In *Genetic and Evolutionary Computation*; Springer: Berlin/Heidelberg, Germany, 2007.
- [109] Lairedj, A.; Bouazza, M.; Amara, K.; Chabani, A. Behaviors of simply supported cross-ply rectangular symmetric laminates plates with consideration of prebuckling in-plane deformation. *Acta Mech. Slovaca* **2015**, *19*, 6–12.
- [110] Gopalan, V.; Suthenthiraveerappa, V.; David, J.S.; Subramanian, J.; Annamalai, A.R.; Jen, C.-P. Experimental and Numerical Analyses on the Buckling Characteristics of Woven Flax/Epoxy Laminated Composite Plate under Axial Compression. *Polymers* **2021**, *13*, 995.
- [111] Jones, R.M. *Mechanics of Composite Materials*; CRC Press Inc.: New York, NY, USA, 2015; ISBN 9781560327127.
- [112] EL-Wazerya, M.S.E.; EL-Elamya, M.I.E.; Zoalfakarb, S.H. Mechanical Properties of Glass Fiber Reinforced Polyester Composites. *Int. J. Appl. Sci. Eng.* **2017**, *14*, 121–131.
- [113] Adams.; Daniel, F.; Ronald, A.A. *Understanding Mechanics of Composite Materials*; CRC Press: Boca Raton, FL, USA, 2013.
- [114] Barbero, E.J. *Introduction to Composite Materials Design*, 3rd ed.; CRC Press: Boca Raton, FL, USA, 2017. <https://doi.org/10.1201/9781315296494>.
- [115] Udit B and Rakesh K. Failure of Alternate Honeycomb Core Sandwich Panels AIAA SciTech Forum 2019.
- [116] Bruno C, Christophe B, Malo G. Review of composite sandwich structure in aeronautic applications. *Composites Part C, Open Access* 1 (2020) 100004
- [117] K. R. Venkatesan, A. Rai, and A. Chattopadhyay. Finite element-based damage and failure analysis of honeycomb core sandwich composite structures for space applications. AIAA SciTech Forum (2020).

- [118] Moslem N, Eslami-Farsani R. Design and characterization of a multilayered hybrid cored-sandwich panel stiffened by a thin-walled lattice structure. *Thin-Walled Structures* 161 (2021) 107514
- [119] Yongqiang Li, Wenkai Yao, Tao Wang. Free flexural vibration of thin-walled honeycomb sandwich cylindrical shells. *Thin-Walled Structures* 157 (2020) 107032
- [120] Xinyun Zhang, Kangwen Sun , Dongdong Xu, and Shijun Guo:, Lightweight Photovoltaic Composite Structure on Stratospheric Airships, *Advances in Materials Science and Engineering Volume 2018, Article ID 1294205, 13 pages* <https://doi.org/10.1155/2018/1294205>
- [121] Olivier Montagnier , Laurent Bovet:, Optimisation of a Solar-Powered high altitude long endurance UAV, Flight Dynamics Team, Research centre of the French Air Force, Base Aérienne 701, 13661 Salon air, France
- [122] Octavian Narcis Ionescu , Ileana Cernica , Elena Manea , Catalin Parvulescu, Alin Istrate ,Gabriela Ionescu and Mirela Petruta Sucheai:, Integration of Micro Structured Photovoltaic Cells into the Ultra-LightWing Structure for Extended Range Unmanned Aerial Vehicles, *Appl. Sci.* 2021, 11, 10890. <https://doi.org/10.3390/app112210890>
- [123] Rouxel, Quentin & Dubos, Pierre-Antoine & Khazaie, Shahram & Lucas, Simon & CASARI, Pascal. (2020). EXPERIMENTAL AND NUMERICAL STUDY OF THE COMPOSITE WING STRUCTURE EMBEDDING SOLAR CELLS.
- [124] Hulun Guo, Jinjin Yuan, Krzysztof Kamil Żur, Flutter and divergence zones of perovskite solar cell-based panels of aircraft wings in subsonic airflow, *Aerospace Science and Technology*, Volume 145, 2024, 108841, ISSN 1270-9638, <https://doi.org/10.1016/j.ast.2023.108841>.
- [125] Olivier Montagnier and Laurent Bovet, OPTIMISATION OF A SOLAR-POWERED HIGH ALTITUDE LONG ENDURANCE UAV WITH COMPOSITE WINGS, 3 RD EUROPEAN CONFERENCE FOR AEROSPACE SCIENCES.
- [126] L. Zhao, Z. Fang, F. Liu, M. Shan, J. Zhang, A modified stiffness method considering effects of hole tensile deformation on bolt load distribution in multi-bolt composite joints, *Compos B Eng* 171 (2019) 264–271. <https://doi.org/10.1016/j.compositesb.2019.05.010>.
- [127] N.M. Chowdhury, W.K. Chiu, J. Wang, P. Chang, Experimental and finite element studies of bolted, bonded and hybrid step lap joints of thick carbon fibre/epoxy panels used in aircraft structures, *Compos B Eng* 100 (2016) 68–77. <https://doi.org/10.1016/j.compositesb.2016.06.061>.
- [128] F. Liu, X. Lu, L. Zhao, J. Zhang, N. Hu, J. Xu, An interpretation of the load distributions in highly torqued single-lap composite bolted joints with bolt-hole clearances, *Compos B Eng* 138 (2018) 194–205. <https://doi.org/10.1016/j.compositesb.2017.11.027>.

- [129] H.-S. Li, R.-J. Gu, X. Zhao, Global sensitivity analysis of load distribution and displacement in multi-bolt composite joints, *Compos B Eng* 116 (2017) 200–210. <https://doi.org/10.1016/j.compositesb.2017.01.058>.
- [130] Rama, A.; Mohan, R.; Arvind, N. A scatter search algorithm for stacking sequence optimization of laminated composites. *Compos. Struct.* 2005, 70, 383–402.
- [131] K. Ganesan, C. Kailasanathan, N. Rajini, Sikiru O. Ismail, Nadir Ayrilmis, Faruq Mohammad, Hamad A. Al-Lohedan, Ahmed M. Tawfeek, Zuheir A. Issa, Daifallah M. Aldhayan, Assessment on hybrid jute/coir fibers reinforced polyester composite with hybrid fillers under different environmental conditions, *Construction and Building Materials*, Volume 301, 2021,124117, ISSN 0950-0618, <https://doi.org/10.1016/j.conbuildmat.2021.124117>.
- [132] Laurin, F.; Carrere, N.; Maire, J.F. A multi-scale progressive failure approach for composite laminates based on thermodynamic viscoelastic and damage models. *Compos. Part A* 2007, 38, 198–209. Udit B
- [133] A. Goumghar, M. Assarar, W. Zouari, K. Azouaoui, A. El Mahi, R. Ayad, Study of the fatigue behaviour of hybrid flax-glass/epoxy composites, *Compos Struct* 294 (2022) 115790. <https://doi.org/10.1016/j.compstruct.2022.115790>.
- [134] A. Alawar, A.M. Hamed, K. Al-Kaabi, Characterization of treated date palm tree fiber as composite reinforcement, *Compos B Eng* 40 (2009) 601–606. <https://doi.org/10.1016/j.compositesb.2009.04.018>.
- [135] G. Kelly, Quasi-static strength and fatigue life of hybrid (bonded/bolted) composite single-lap joints, *Compos Struct* 72 (2006) 119–129. <https://doi.org/10.1016/j.compstruct.2004.11.002>.
- [136] Y. Liu, S. Lemanski, X. Zhang, D. Ayre, H.Y. Nezhad, A finite element study of fatigue crack propagation in single lap bonded joint with process-induced disbond, *Int J Adhes Adhes* 87 (2018) 164–172. <https://doi.org/10.1016/j.ijadhadh.2018.10.005>.
- [137] Boucher R. J., 1984, “History of Solar Flight,” AIAA/SAE/ASME 20th Joint Propulsion Conference, 1984, Cincinnati, Ohio.
- [138] POLNOR-LEADER, https://polnor-leader.eu/?page_id=250&lang=en, Accessed: 25.03.2022.
- [139] M. Peciak, W. Skarka, Assessment of the Potential of Electric Propulsion for General Aviation Using Model-Based System Engineering (MBSE) Methodology. *Aerospace*, 2022, 9, 74. <https://doi.org/10.3390/aerospace9020074>.
- [124] K. Mateja, W. Skarka, Towards energetic autonomy of UAV. *Advances in Transdisciplinary Engineering*, 2020, Vol. 12, pp. 423-432. DOI: <https://doi.org/10.3233/ATDE200102>.
- [125] W. Skarka, Model-Based Design and Optimization of Electric Vehicles, *Advances in Transdisciplinary Engineering*, 2018, Vol. 7, pp. 566-575.
- [130] R. Niestroj, T. Rogala, W. Skarka, An Energy Consumption Model for Designing an AGV Energy Storage System with a PEMFC Stack. *Energies* 2020, 13, 3435.

- [131] W. Skarka, A. Jałowicki, Automation of a Thin-Layer Load-Bearing Structure Design on the Example of High Altitude Long Endurance Unmanned Aerial Vehicle (HALE UAV), *Applied Sciences*, 2021, 11(6), 2645.
- [132] Miao, Y., Zhou, E., Wang, Y., and Cheeseman, B. A. (2008). Mechanics of textile composites: Micro-geometry. *Compos. Sci. Technol.* 68 (7), 1671–1678. doi:10.1016/j.compscitech.2008.02.018
- [133] Sun, Q., Meng, Z., Zhou, G., Lin, S.-P., Kang, H., Keten, S., et al. (2018). Multi-scale computational analysis of unidirectional carbon fiber reinforced polymer composites under various loading conditions. *Compos. Struct.* 196, 30–43. doi:10.1016/j.compstruct.2018.05.025
- [134] Sun, Q., Zhou, G., Meng, Z., Jain, M., and Su, X. (2021). An integrated computational materials engineering framework to analyze the failure behaviors of carbon fiber reinforced polymer composites for lightweight vehicle applications. *Compos. Sci. Technol.* 202, 108560. doi:10.1016/j.compscitech.2020.108560
- [135] Tian, W.; Qi, L.; Liang, J.; Chao, X.; Zhou, J. Evaluation for elastic properties of metal matrix composites with randomly distributed fibers: Two-step mean-field homogenization procedure versus FE homogenization method. *J. Alloy. Compd.* 2016, 658, 241–247. [CrossRef]
- [136] Adumitroaie, A.; Barbero, E.J. Beyond plain weave fabrics–I. Geometrical model. *Compos. Struct.* 2011, 93, 1424–1432.
- [137] Gilioli, A.; Manes, A.; Giglio, M. Evaluation of the effects of the numerical modelling choices on the simulation of a tensile test on CFRP composite. *Procedia Struct. Integr.* 2018, 8, 33–42. *Appl. Sci.* 2020, 10, 6542 13 of 14
- [138] Hale, P.; Ng, E.G. Non-linear material characterization of CFRP with FEM utilizing cohesive surface considerations validated with effective tensile test fixturing. *Mater. Today Commun.* 2020, 23, 100872.
- [139] Li, H.X. Limit analysis of composite materials with anisotropic microstructures: A homogenization approach. *Mech. Mater.* 2011, 43, 574–585.
- [140] Muflikhun, M.A.; Chua, A.Y. Load-displacement experimental data from axial tensile loading of CFRP-SPCC hybrid laminates. *Data Brief* 2020, 29, 105306.
- [141] Babu, K.P.; Mohite, P.M.; Upadhyay, C.S. Development of an RVE and its stiffness predictions based on mathematical homogenization theory for short fibre composites. *Int. J. Solids Struct.* 2018, 130, 80–104.
- [142] Qi, Z.; Liu, Y.; Chen, W. An approach to predict the mechanical properties of CFRP based on cross-scale simulation. *Compos. Struct.* 2019, 210, 339–347. [CrossRef]
- [143] Gao, J.; Shakoor, M.; Domel, G.; Merzkirch, M.; Zhou, G.; Zeng, D.; Su, X.; Liu, W.K. Predictive multiscale modeling for Unidirectional Carbon Fiber Reinforced Polymers. *Compos. Sci. Technol.* 2020, 186, 107922.

- [144] Mustafa, G.; Suleman, A.; Crawford, C. Probabilistic micromechanical analysis of composite material stiffness properties for a wind turbine blade. *Compos. Struct.* 2015, 131, 905–916.
- [145] Lee, S.P.; Jin, J.W.; Kang, K.W. Probabilistic analysis for mechanical properties of glass/epoxy composites using homogenization method and Monte Carlo simulation. *Renew. Energy* 2014, 65, 219–226. [CrossRef]
- [146] Kamiński, M.; Kazimierczak, M. 2D versus 3D probabilistic homogenization of the metallic fiber-reinforced composites by the perturbation-based stochastic Finite Element Method. *Compos. Struct.* 2014, 108, 1009–1018.
- [147] Tan, H.; Huang, Y.; Liu, C.; Geubelle, P.H. The Mori–Tanaka method for composite materials with nonlinear interface debonding. *Int. J. Plast.* 2005, 21, 1890–1918. *Appl. Sci.* 2020, 10, 6542 14 of 14
- [148] Klusemann, B.; Svendsen, B. Homogenization methods for multi-phase elastic composites. *Tech. Mech. Sci. J. Fundam. Appl. Eng. Mech.* 2010, 30, 374–386.

Abstract

Unmanned Aerial Vehicles (UAVs) have had a significant increase in popularity in recent times, being utilized in many industrial and recreational applications. Military operations, recording movies and pictures from above, keeping an eye on dangers like fires, mapping land, evaluating crops, and search and rescue operations are just some of the many things that these devices can be used for. The intended function of a UAV can differ based on its design, shape, method of power transmission, and duration of flight. The scientific topic addresses the complexity of constructing laminated composite structures, requiring careful specification of various variables for each ply and consideration of multiple design criteria such as mass, stiffness, and buckling. Traditional design approaches frequently produce inferior solutions because they rely on engineering heuristics. This study promotes rational analysis and design methodologies, which enable an automated and optimized design process that continuously improves to efficiently satisfy operational requirements.

The major goal is to use optimization approaches based on classical laminate theory to discover the most effective stacking sequence, resulting in higher performance metrics while drastically reducing the overall weight of the composite structure. This weight reduction is critical for increasing UAV endurance and fuel efficiency, as lighter structures use less energy during flight. The doctoral dissertation includes two case studies: T-joint structural analysis and sandwich core optimization approaches.

During work related to the doctoral thesis, four distinctive T-joint geometrical models were developed and analysed with different material, thickness, and shape, which were included in the doctoral dissertation as one of the case studies. The study involved the fabrication and optimization of a prototype bio-composite material with a focus on environmental sustainability.

The optimized results from the genetic algorithm by Ansys were also verified with laboratory tests. The results achieved are suitable for aerospace applications and especially designed for UAV structures. This eco-friendly material enhances the structural integrity of composites while aligning with broader initiatives aimed at reducing the environmental impact of aerospace engineering.

Streszczenie

Popularność bezzałogowych statków powietrznych (UAV) znacznie wzrosła w ostatnim czasie, ponieważ są wykorzystywane w wielu zastosowaniach przemysłowych i rekreacyjnych. Operacje wojskowe, nagrywanie filmów i zdjęć z góry, monitorowanie zagrożeń takich jak pożary, sporządzanie map terenu, ocena upraw oraz akcje poszukiwawczo-ratownicze to tylko niektóre z wielu rzeczy, do których można wykorzystać te urządzenia. Zamierzona funkcja UAV może się różnić w zależności od jego konstrukcji, kształtu, sposobu przenoszenia mocy i czasu trwania lotu. Temat naukowy dotyczy złożoności konstruowania laminowanych konstrukcji kompozytowych, wymagającej dokładnego określenia różnych zmiennych dla każdej warstwy i uwzględnienia wielu kryteriów projektowych, takich jak masa, sztywność i wyboczenie. Tradycyjne podejścia do projektowania często dają gorsze rozwiązania, ponieważ opierają się na heurystyce inżynierskiej. Badanie to promuje racjonalne metodologie analizy i projektowania, które umożliwiają zautomatyzowany i zoptymalizowany proces projektowania, który jest stale ulepszany, aby skutecznie spełniać wymagania operacyjne.

Głównym celem jest zastosowanie podejść optymalizacyjnych opartych na klasycznej teorii laminatów w celu odkrycia najbardziej efektywnej kolejności układania, co skutkuje wyższymi parametrami wydajności przy jednoczesnym drastycznym zmniejszeniu całkowitej masy konstrukcji kompozytowej. Ta redukcja masy ma kluczowe znaczenie dla zwiększenia wytrzymałości UAV i zużycia paliwa, ponieważ lżejsze konstrukcje zużywają mniej energii podczas lotu. Rozprawa doktorska obejmuje dwa studia przypadków: analizę strukturalną połączeń typu T oraz metody optymalizacji rdzenia warstwowego.

W trakcie prac związanych z rozprawą doktorską opracowano i przeanalizowano cztery wyróżniające się modele geometryczne złącza T, różniące się materiałem, grubością i kształtem, które uwzględniono w rozprawie doktorskiej jako jedno ze studiów przypadku. Badanie obejmowało wytworzenie i optymalizację prototypowego materiału biokompozytowego, ze szczególnym uwzględnieniem zrównoważenia środowiskowego.

Zoptymalizowane wyniki algorytmu genetycznego firmy Ansys zostały również zweryfikowane w testach laboratoryjnych. Uzyskane wyniki nadają się do zastosowań

lotniczych i są specjalnie zaprojektowane dla konstrukcji UAV. Ten ekologiczny materiał zwiększa integralność strukturalną kompozytów, wpisując się jednocześnie w szersze inicjatywy mające na celu zmniejszenie wpływu inżynierii lotniczej na środowisko.